Homogenization for the multiple scale analysis of musculoskeletal mineralized tissues

Homogenisierung für die Multiskalen-Analyse von muskuloskelettalem mineralisiertem Gewebe

Zur Erlangung des Grades eines Doktors der Naturwissenschaften (Dr. rer. nat.)
genehmigte Dissertation von Diplom-Mathematikerin Sara Tiburtius aus Berlin
2015 — Darmstadt — D 17

TECHNISCHE
UNIVERSITÄT
DARMSTADT

Fachbereich Mathematik
Forschungsbereich Numerik und
Wissenschaftliches Rechnen

Homogenization for the multiple scale analysis of musculoskeletal mineralized tissues
Homogenisierung für die Multiskalen-Analyse von muskuloskelettalem mineralisiertem Gewebe

Genehmigte Dissertation von Diplom-Mathematikerin Sara Tiburtius aus Berlin

1. Gutachten: Prof. Dr. Jens Lang
2. Gutachten: Quentin Grimal, PhD

Tag der Einreichung: 17.10.2014
Tag der Prüfung: 26.01.2015

Darmstadt — D 17

Zusammenfassung

In dieser Arbeit entwickeln wir Multiskalen-Modelle für zwei wichtige Vertreter von muskuloskelettalem mineralisisertem Gewebe: der mineralisierten Sehne des Truthahns (kurz mineralisierte Sehne) und dem Osteon. Unter der Verwendung von Homogenisierungmethoden simulieren wir ihre elastischen Eigenschaften auf verschiedenen Längenskalen. Wir verfolgen zwei Ziele: zum einen suchen wir Homogenisierungsmethoden, die die grobskaligen elastischen Eigenschaften der untersuchten Gewebearten numerisch genau sowie in einer realistischen Zeit vorhersagen, zum anderen suchen wir diejenigen Modellparameter, die die elastischen Eigenschaften der untersuchten Materialien maßgeblich bestimmen.

Im ersten Kapitel dieser Arbeit geben wir eine kurze Einleitung in das Thema. Im zweiten Kapitel stellen wir die für diese Arbeit nötigen Grundlagen vor. Unsere Modelle beruhen auf den Randwertproblemen der statischen linearen Elastizität. Wir präsentieren verschiedene Randwertprobleme und klären Existenz und Eindeutigkeit dieser. Um die grobskaligen elastischen Eigenschaften unser Materialien zu bestimmen, benötigen wir Homogenisierungsmethoden. Wir verwenden die Mori-Tanaka Methode, die Selbstkonsistenz-Methode, verschiedene Methoden aus der Homogenisierung periodischer Materialien und die repräsentative Volumenelement basierende Homogenisierungsmethode mit Verschiebungs- oder Spannungs-Randbedingungen. Diese und weitere Homogenisierungmethoden stellen wir im dritten Kapitel vor. Unsere Implementierung der Homogenisierungsmethoden ist im Fokus des vierten Kapitels.

Mithilfe der Mori-Tanaka Methode und der Selbstkonsistenz-Methode sagen wir die grobskaligen elastischen Eigenschaften der mineralisierten Sehne vorher. Um die numerische Genauigkeit dieser beiden Homogenisierungsmethoden zu untersuchen, führen wir verschiedene Tests durch. Eine Beschreibung dieser Tests sowie die Ergebnisse dieser Tests präsentieren wir im fünften Kapitel. Wir stellen fest, daß sich die numerische Genauigkeit der Mori-Tanaka Methode um eine Größenordnung verbessert, wenn wir den Toolparameter der Mori-Tanaka Methode um eine Größenordnung verkleinern. Ähnliches gilt für die Selbstkonsistenz-Methode. Ebenfalls im fünften Kapitel fixieren wir Defaultwerte für die Toolparameter derart, daß die Vorhersagen beider Homogenisierungsmethoden eine ausreichende numerische Genauigkeit haben. Im sechsten Kapitel schließlich stellen wir unser Multiskalen-Modell der mineralisierten Sehne vor. Unter Verwendung einer globalen Sensitivitätsanalyse (Elementary Effects Method) und einer Parameterstudie unseres Modells identifizierten wir diejenigen Parameter, die die elastischen Eigenschaften der mineralisierten Sehne maßgeblich bestimmen. Dies sind die Mikroporosität sowie verschiedene Parameter, die die Form und den Volumenanteil des in der mineralisierten Sehne enthaltenen Minerals charakterisieren. Zum Schluss validierten wir unser Modell, indem wir unsere vorhergesagten elastischen Eigenschaften mit experimentellen Daten, gemessen von unseren Projektpartnern der Charité Berlin, vergleichen. Wir beobachten eine sehr gute Übereinstimmung dieser Daten, der relative Fehler ist zwischen 6 und 8 Prozent.

Im siebten Kapitel entwickeln wir ein Zweiskalen-Modell für das Osteon. Wir verwenden die repräsentative Volumenelement basierende Homogenisierungsmethode mit Verschiebungs-Randbedingungen. Wir führen eine Konvergenzanalyse dieser Homogenisierungsmethode sowie einen Vergleich verschiedener Homogenisierungsmethoden durch. Basierend auf einer lokalen Parameterstudie unseres Osteon Modells bestimmen wir die Parameter, die die elastischen Eigenschaften des Osteons maßgeblich bestimmen. Dies sind der Typ und die Anzahl, der in einem Osteon enthaltenen lamellären Einheiten. Da im Gegensatz zur mineralisierten Sehne keine experimentellen Daten unserer Projektpartner zur Verfügung stehen, vergleichen wir unser Modell mit entsprechenden Daten aus der Literatur. Unsere vorhergesagten Steifigkeiten stimmen gut mit den Daten aus der Literatur überein.

Im letzten Kapitel dieser Arbeit ziehen wir Schlussfolgerungen.

Abstract

Using multiscale models and homogenization methods the elastic properties of two important musculoskeletal mineralized tissues, the mineralized turkey leg tendon (in short mineralized tendon) and the osteon, are modeled and simulated at different length scales. Our first aim is to find homogenization methods which predict the apparent elastic properties of the investigated tissues numerical accurate as well as are computationally efficient. Our second aim is to find the key parameters determining the elastic properties of the investigated tissues.

After a short introduction (first chapter), we present the background required for this work (second chapter). Our models are based on the boundary value problems of static linear elasticity. We state different boundary value problems and recall existence and uniqueness results of them. In the third chapter we introduce the homogenization methods employed in this thesis. These are: the Mori-Tanaka method, the self-consistent method, some homogenization methods for periodic materials, and the representative volume element based homogenization method with displacement and traction boundary conditions. We describe the implementation of these homogenization methods in the fourth chapter.

In order to predict the coarse-scale elastic properties of the mineralized tendon we employ the Mori-Tanka and the self-consistent method. In the fifth chapter we perform various numerical tests for the building unit of the mineralized tendon to clarify the numerical accuracy and the computational efficiency of the employed homogenization methods. We show that the numerical accuracy of the Mori-Tanaka method improves about one order of magnitude, if we decrease the tool parameter of the Mori-Tanaka method about one order of magnitude. Similar applies to the self-consistent method. Furthermore, we fix tool parameters of the homogenization methods such that the predicted coarse-scale elastic properties are numerical accurate. In the sixth chapter we present our multiscale model of the mineralized tendon. Performing a global sensitivity analysis (Elementary Effects method) and a parametric study of our model we investigate the essential parameters influencing the elastic properties of the mineralized tendon. These are: the microporosity and different parameters, describing the shape and the volume fraction of the mineral within the mineralized tendon. Finally, we compare our model elastic properties with experimentally derived elastic properties, given by our project partners from the Charité Berlin. We find a very good agreement, we have small relative errors of 6-8%.

In the seventh chapter we develop a multiscale model for the osteon. We employ the RVE-based homogenization method with displacement boundary conditions. We perform a convergence analysis of our method as well as compare different homogenization methods with each other. Performing a parametric study of the osteon model we determine the key parameters influencing the apparent elastic properties of the osteon. These are: the type of the circular lamellar units contained in an osteon and the numbers of the circular lamellar units. Since there is, in contrast to the mineralized tendon, no experimental data available by our colleagues, we compare our model with data found in the literature. Our predicted elastic properties agree well with the data found in the literature.

In the last chapter of this work we draw conclusions.

Acknowledgements

First of all, I am grateful to my supervisors Dr. Alf Gerisch and Prof. Dr. Jens Lang - without their guidance and help this dissertation would not been possible.

Then, I also want to thank Prof. Dr. Kay Raum for his valuable contributions to physical aspects of the MTLT and the osteon. Moreover, I enjoyed fruitful discussions on homogenization methods, theoretical physics and other issues with Dr. Quentin Grimal and Dr. Peter Varga.

Due to preliminary work of Dr. Alf Gerisch, Prof. Dr. Kay Raum and Dr. Quentin Grimal, the following tools were available

- the RVE-based homogenization method with displacement and traction boundary conditions. This method was implemented by Dr. Alf Gerisch and Prof. Dr. Kay Raum (Raum et al., 2010).
- the AHF method and the Matlab function BuildEshelbyAndHillTensors. These methods were implemented by Dr. Quentin Grimal (Parnell and Grimal, 2009).

All persons mentioned above, permitted me to use these tools. I appreciate this very much.

Special thanks go to my colleagues. They discussed with me numerical aspects of the finite element method and the homogenization methods. Moreover, I say thanks to Eli Duenisch, who helped me to implement some homogenization methods and to set up the parametric study, performed for the osteon model in Chapter 7.

Last but not least, many thanks to my family and all my friends who supported me over the last five years.

This thesis was supported by the Deutsche Forschungsgemeinschaft (SPP 1420 grant GE 1894/3).

List of abbreviations

Symbol	Description
axi	axial direction (parallel to tendon long axis)
AHA	asymptotic homogenization method for arbitrary materials
AHF	asymptotic homogenization method for fibril-reinforced materials
cLU	circular LU
CIR	circumferential MTLT tissue
col	collagen
DMB	degree of mineralization of bone
EB	embedding box of the osteon
ES	extrafibrillar space
ha	hydroxyapatite
HC	Haversian canal
INT	interstitial MTLT tissue
LU	lamellar unit
MCF	mineralized collagen fibril
MCFB	mineralized collagen fibril bundle
MMT	musculoskeletal mineralized tissue
mp	micropores
MT	Mori-Tanaka method
MTLT	mineralized turkey leg tendon
np	nanopores
pmma	polymethylmethacrylate
ROI	region of interest
RVE	representative volume element
SAM	scanning acoustic microscopy
SC	self-consistent method
SR-μCT	synchrotron radiation micro-computed tomography
trv	transverse direction (perpendicular to tendon long axis)

Nomenclature

$\cdot, :, \otimes, \times, \langle \cdot, \cdot \rangle$	scalar product, double contraction, tensor product, vector product, inner product
$\lvert V \rvert, \lvert \boldsymbol{T} \rvert, \lVert \cdot \rVert_m$	volume of volume element V, absolute value of tensor $\boldsymbol{T}$, norm on Sobolev space $H^m(\Omega, \mathbb{R}^n)$ with $m, n \in \mathbb{N}$
$\nabla, \frac{\partial u}{\partial y}$, div	nabla operator, partial derivative of $u = u(x, y)$ with respect to y, divergence operator
α_{MCF}	ratio of MCF mineral to total mineral (mineral distribution parameter)
β	angle between the x_1-axis and the radial direction
γ	orientation of the MCFBs within the cLU
Γ_Ω, Γ_V	boundary of domain Ω or volume element V
δ_{ij}	Kronecker delta
$\boldsymbol{\varepsilon}, \boldsymbol{\varepsilon}_t, \boldsymbol{\varepsilon}_0, \bar{\boldsymbol{\varepsilon}}, \check{\boldsymbol{\varepsilon}}$	strain tensor, eigenstrain tensor, strain of the homogeneous reference material, difference in strain of some heterogeneous material as compared to the homogeneous reference material, constant strain
$\theta_{i-1,i}$	change in orientation of the MCFB from sublamella sl_{i-1} to sublamella sl_i of a cLU
λ	first Lamé coefficient
μ	second Lamé coefficient
$\mu^*_{(i,j)}$	sensitivity measure describing the overall influence of parameter p_i on stiffness component $C_j = C_j(p_i, \dots)$
ν	Poisson's ratio
ρ	density
$\boldsymbol{\sigma}, \boldsymbol{\sigma}_0, \bar{\boldsymbol{\sigma}}$	stress tensor, stress tensor of the homogeneous reference material, difference in stress of some heterogeneous material as compared to the homogeneous reference material
$\sigma_{(i,j)}$	sensitivity measure characterizing linear versus nonlinear effects of parameter p_i on stiffness component $C_j = C_j(p_i, \dots)$
$\tau_{\text{cLU}}, \tau_i$	thickness of a cLU, thickness of a sublamella sl_i of a cLU
$\boldsymbol{\phi}$	deformation tensor
$\Omega, \overline{\Omega}$	domain, closure of Ω
$a(u, v)$	bilinear form
a_1, a_2, a_3	semi-axes of an ellipsoidal inclusion
aE	absolute L^2 error
ar_A	aspect ratio of a spheroidal inclusion made of material A
A, A_i	composite material A consists of homogeneous phases A_i
$\mathcal{B}_\mathcal{V}$	basis of space $\mathcal{V}$
$\boldsymbol{C}, \boldsymbol{C}_A, C^A_\nu$	fine-scale stiffness tensor, apparent stiffness tensor (A refers to either our material or the employed homogenization method), component of $\boldsymbol{C}_A$ in direction ν

$C^m(\Omega, \mathbb{R}^n)$ ..... space of m times continuously differentiable functions $f : \Omega \to \mathbb{R}^n$

$C^\infty_{\text{per}}(V)$ ..... set of functions $f : V \to \mathbb{R}^n$ which are infinitely differentiable on V and are V-periodic

D^T_ν ..... maximum relative error of the predicted acoustic impedance with respect to a linear regression model of the experimental data for tissue type $T \in \{\text{CIR}, \text{INT}, \dots \text{CIR/INT}\}$ in direction $\nu \in \{\text{axi}, \text{trv}\}$

DMB^{MCFB} ..... DMB of MCFB tissue

DMB ..... experimental DMB

$\boldsymbol{e}_i$ ..... orthogonal unit vectors of $\mathbb{R}^n$; $i = 1, \dots, n$

E ..... Young's modulus

G, G_{ij} ..... shear modulus, shear modulus in the $\boldsymbol{e}_i\,\boldsymbol{e}_j$-plane

$\mathcal{G}_{\boldsymbol{C}}$ ..... symmetry group of the stiffness tensor $\boldsymbol{C}$

h ..... mesh size

h_{Os}, h_{HC} ..... height of the osteon, height of the HC

$H^m(\Omega, \mathbb{R}^n)$ ..... Sobolev space of L^2-functions $f : \Omega \to \mathbb{R}^n$ which have a weak derivative up to order $m \in \mathbb{N}$

$H^{1/2}(\Gamma_\Omega, \mathbb{R}^n)$ ..... set of traces

$H^1_{\text{per}}(V, \mathbb{R}^n)$ ..... closure of $C^\infty_{\text{per}}(V)$ with respect to the H^1-norm

$\mathbf{id}$, $\mathbf{Id}$, $\mathbf{Id^s}$ ..... second-order identity tensor in $\text{Lin}(\mathbb{R}^n)$, fourth-order identity tensor in $\mathbb{L}\text{in}(\mathbb{R}^n)$, fourth-order identity tensor in $\mathbb{S}\text{ym}(\mathbb{R}^n)$

K ..... bulk modulus

$\boldsymbol{K}_i^{(\boldsymbol{\varepsilon},A)}$, $\boldsymbol{K}_i^{(\boldsymbol{\sigma},A)}$ ..... phase strain concentration tensor of phase A_i, phase stress concentration tensor of phase A_i

$\widetilde{l}_1, \widetilde{l}_2, \widetilde{l}_3$ ..... size of the LU along the x_1, the x_2 and the x_3-axis

l_f, l_m, l_c ..... characteristic size of the fine, the meso and the coarse scale

L_1, L_2, L_3 ..... size of the embedding box of an osteon along the x_1, x_2 and x_3-axis

$L^2(\Omega, \mathbb{R}^n)$ ..... space of quadratic Lebesgue integrable functions $f : \Omega \to \mathbb{R}^n$

$\text{Lin}(\mathcal{V}, \mathcal{W}), \text{Lin}(\mathcal{V})$. set of linear functions $f : \mathcal{V} \to \mathcal{W}$, where $\mathcal{V}$ and $\mathcal{W}$ are inner product spaces, $\text{Lin}(\mathcal{V}) \coloneqq \text{Lin}(\mathcal{V}, \mathcal{V})$

$\mathbb{L}\text{in}(\mathcal{V})$ ..... set of linear functions $f : \text{Lin}(\mathcal{V}) \to \text{Lin}(\mathcal{V})$

$LG_k(T)$ ..... Lagrangian grid of order k on a tetrahedral element T

$\boldsymbol{M}$, $\boldsymbol{M}_A$ ..... fine-scale compliance tensor, apparent compliance tensor of material A

$\mathcal{M}_V(f)$ ..... mean value of function f over volume element V

n_{cLU} ..... number of cLUs in an osteon

n_{terms} ..... number of terms in the multipole expansion of the AHF method

$\mathcal{O}$ ..... group of orthogonal second-order tensors

p ..... convergence order of an iterative method

$\boldsymbol{P}$, $\boldsymbol{P}_i^M$ ..... Hill tensor of an inclusion phase, Hill tensor of inclusion phase A_i used for homogenization method M

$\mathbb{P}_k$ ..... space of polynomials in three variables of degree less or equal to k

Q	asymptotic error constant of an iterative method
r_{Os}, r_{HC}	radius of the osteon, radius of the HC
rE, raE, mrE	relative error, mixed absolute-relative error, maximum relative error
$\mathbf{ref}(\boldsymbol{n})$	reflection about the plane with normal $\boldsymbol{n}$
$\mathbf{rot}(\alpha, \boldsymbol{n})$	rotation by an angle $0 < \alpha \leq \pi$ around an axis in direction $\boldsymbol{n}$
rRMSE_{ν}^{T}	relative root mean square error of the predicted acoustic impedance with respect to experimentally assessed values for tissue type $T \in \{\mathrm{CIR}, \mathrm{INT}, \mathrm{CIR/INT}\}$ in direction ν
$\mathbb{R}^n$, $\mathbb{R}^{n\times m}$	n-dimensional space of real number, $n \times m$-dimensional space of real numbers
$\mathcal{R}$	set of rigid displacements
s	scale ratio l_m/l_c
sl_i	ith sublamella of a cLU
$\boldsymbol{S}$	Eshelby tensor of an inclusion embedded in the homogeneous reference material
$\mathcal{S}_A$	model of composite material A
$\mathrm{Sym}(\mathcal{V})$	set of symmetric second-order tensors in $\mathrm{Lin}(\mathcal{V})$
$\mathbb{S}\mathrm{ym}(\mathcal{V})$	set of fourth-order tensors in $\mathbb{L}\mathrm{in}(\mathcal{V})$ which obey minor and major symmetries
t	time
$\boldsymbol{t}$	traction
$\mathrm{tol}_{\mathrm{int}}$, $\mathrm{tol}_{\mathrm{nls}}$	integration tolerance for the Hill tensor, nonlinear solver tolerance of the self-consistent method
$\mathcal{T}_h$	mesh with mesh size h
$\boldsymbol{u}$, $\boldsymbol{u}^s$, $\boldsymbol{u}_0$, $\bar{\boldsymbol{u}}$	displacement tensor, fine-scale displacement tensor which depends on the scale ratio s, displacement tensor of the homogeneous reference material, difference in displacement of some heterogeneous material as compared to the homogeneous reference material
$\boldsymbol{u_0}$, $\boldsymbol{u_1}$, $\boldsymbol{u_2}$	zero, first and second-order term of the asymptotic expansion of $\boldsymbol{u}^s$
$U_{\mathcal{M}(\boldsymbol{\varepsilon})}, U_{\boldsymbol{\varepsilon}}$	coarse-scale strain energy density, fine-scale strain energy density
vf_B^A	volume fraction of material B in (composite) material A
$\widetilde{\mathrm{vf}}_{\mathrm{mp}}$	experimental microporosity of MTLT tissue derived from light microscopy images
V, V_i	volume element of domain Ω filled with composite material A or phase A_i
$\mathcal{V}$	inner product space, vector space or function space
$W_{\mathcal{M}_V(\boldsymbol{\varepsilon})}, W_{\boldsymbol{\varepsilon}}$	coarse-scale strain energy, fine-scale strain energy
$W^1_{\mathrm{per}}(V)$	quotient space of $H^1_{\mathrm{per}}(V, \mathbb{R}^n)$
$\boldsymbol{x}$, $\boldsymbol{y}$, $\boldsymbol{z}$	material point in Ω, point in the coordinate system associated to the fine scale, point in the coordinate system associated to the coarse scale
Z, Z_{ν}^{A}	predicted acoustic impedance, predicted acoustic impedance of material A in direction ν
$\widetilde{Z}, \widetilde{Z}_i$	experimental acoustic impedance, experimental acoustic impedance of ROI i
$\mathbb{Z}$	space of integer numbers

Contents

1 Introduction

We start by explaining the context in which this thesis is set, and present the research questions addressed by it. This is followed by an overview of the thesis structure. Finally, we cite our publications and give an acknowledgment.

1.1 Scope of this thesis

Musculoskeletal mineralized tissues (MMTs) like bone tissue, tendon, dentin, and cartilage are fascinating materials. They consist of the same constituents: collagen, mineral, water and non-collageneous proteins, but nevertheless fulfill different tasks and resist various forces. Bone tissue for instance sustains compression forces very well, but pulling or shear forces let the bone break quickly. In contrast the tendon is capable of withstanding high tension forces, but do not resist compression forces well.

MMTs are hierarchically structured materials (Weiner and Wagner, 1998; Hellmich et al., 2004; Fratzl and Weinkamer, 2007; Nikolov and Raabe, 2008; Hamed et al., 2010; Raum et al., 2011). The cylindrically shaped mineralized collagen fibril (MCF), having an average diameter of $50 - 100$ nm and a substantially longer length, is their single essential building block (Weiner and Wagner, 1998). Depending on the particular MMT type the MCF is organized in different patterns across many length scales. As a consequence thereof the elastic properties of an MMT at a certain length scale (coarse scale) are determined by the structural (composition and organization) and the material properties at underlying scales (fine scales). This hierarchical organization of the MMTs demands a multiscale analysis of the MMTs materials properties, in particular of its elastic properties.

Usually, the elastic properties of the MMTs are modeled based on the equations of linear elasticity. Since any appropriate model of the MMT needs to include the MMTs' complex characteristic fine-scale properties, finding an analytical solution of the equations of linear elasticity is difficult, if not impossible. Therefore, one aims at finding approximate solutions. Solving the equations of linear elasticity numerically using some discretization technique such as finite elements, finite differences or others, requires an extremely fine mesh to resolve the fine-scale structure of MMTs. The resulting computational costs are high and are beyond todays computing capacity (Zohdi and Wriggers, 2008).

Tools such as multiscale models and homogenization help to resolve this issue. One establishes a sequence of submodels, each specifying the coarse-scale or apparent elastic properties of some characteristic pattern of the MMT. Following a bottom-up approach, the output of submodels, representing patterns at finer scales, serves as input for those characterizing patterns at coarser scales. This yields a multiscale model of the MMT. Homogenization methods predict approximations to the apparent elastic properties. In the past, three main homogenization theories have been developed, which we call periodic homogenization, RVE-based homogenization and Eshelby-based homogenization henceforth. To name only a few number of homogenization methods in this context: the asymptotic homgenization technique, in particular the AHF method (Parnell and Grimal, 2009) and the AHA method, the RVE-based homogenization method with traction and displacement boundary conditions (Zohdi and Wriggers, 2008), the Voigt and the Reuss techniques (Voigt, 1888; Reuss, 1929), the Dilute method, the Mori-Tanaka method (Mori and Tanaka, 1973), and the self-consistent method (Hill, 1965).

The main focus of this thesis is on modeling and simulation of (apparent) elastic properties of MMTs. We develop multiscale models combined with appropriate homogenization techniques, which predict the apparent elastic properties of different MMTs at different scales. Two important examples of MMTs are considered (i) mineralized turkey leg tendon (MTLT) tissue, a simply structured MMT, that consists of unidirectionally aligned MCF bundles (MCFBs), (ii) osteonal tissue, a more advanced MMT, which consists of gradually rotated MCFBs. The MTLT can be seen as a very simplified model of bone, which has a similar composition but more complex structure. Osteons are a basic structural unit of bone.

Studies on MTLT and osteonal tissue can form the basis for studies on other MMTs. Clearly, other MMTs will be more difficult to investigate and hence MTLT and osteons constitute appropriate starting points.

Existing studies on the modeling and simulation of the elastic properties of the MTLT, the osteon and other MMTs, usually, pursue two different aims. Some authors consider their model with a given fixed set of parameters and focus mainly on explaining (their) experimental data. Others analyze only the influence of the input parameters on the model output and do not at all compare their model predictions with experimental data. We think that both of these aims are equally important and will address both in the development of our MMT models. Beyond this, we also consider central numerical aspects, such as accuracy, numerical efficiency and convergence (accuracy of predictions as tool parameters are made stricter), which in most publications on MMTs merely play a minor role.

The main research questions addressed in this thesis are

1. Are our employed homogenization methods accurate and computationally efficient? How does the accuracy of the predictions of the homogenization methods change when the tool parameters are made stricter?
2. In which way do our model predictions depend on the choice of the homogenization method?
3. Which parameters essentially determine the elastic properties of the investigated MMTs? How do these essential parameters influence the coarse-scale elastic properties of the investigated MMTs?
4. How well compare our model predictions with experimental or model data available in the literature?

1.2 Outline of this thesis

We assume that MMTs consists of perfectly bonded heterogeneities. Furthermore, we restrict ourself here to model MMTs as linear elastic materials. Therefore, we base all our considerations on boundary value problems in static and dynamic linear elasticity. An important concept in linear elasticity is that of a tensor. That is why we start this thesis in Chapter 2 defining a tensor, introducing operations on tensors, as well as listing important properties of tensors. Additionally, we describe in Chapter 2 boundary value problems in static and dynamic linear elasticity, existence and uniqueness results for them, as well as techniques to solve them numerically, i.e. the Galerkin finite element methods.

Homogenization in general, requirements to successfully apply it, and the theoretical background and methods of periodic, RVE-based and Eshelby-based homogenization are in the focus of Chapter 3. The implementation of the homogenization methods, employed for our MTLT and osteon model, is described in Chapter 4. In Chapter 5 we assess accuracy and computational efficiency of the homogenization methods employed for the MTLT model. This is done based on the building unit of MMTs.

In Chapters 6 and 7 we model and simulate the coarse-scale elastic properties of the MTLT and the osteon, respectively. For both tissues, we start by reviewing the structural organization of each tissue and formulating tissue-type adapted research questions and tasks. Then, we present our multiscale models. In particular, we describe the model parameters, explain how to derive them and justify our choice of homogenization method. Note that we employ Eshelby-based homogenization methods (Mori-Tanaka method, self-consistent method) for our MTLT model, while RVE-based and periodic homogenization techniques (RVE-based homogenization with traction and displacement boundary conditions and the AHA method) for our osteon model. In order to answer our research questions regarding the determining parameters of the MMTs' apparent elastic properties, we perform a global sensitivity analysis (in case of the MTLT model) and a local parametric study. Finally, we compare the model predictions with experimental data, discuss our results with respect to our posed research questions and give future tasks.

In case of the MTLT, our project partners provided experimentally-derived data (structural and elastic properties) of the MTLT at the coarse and the fine scale. We briefly review their data and their findings in Chapter 6. Based on the experimental fine-scale properties we determine reasonable model parameters;

the coarse-scale elastic properties we use to validate our MTLT model. The collaboration with our project partners resulted in a paper (Tiburtius et al., 2014), in which the experimental data of our project partners and the majority of our results in Chapter 6 were published, see Section 1.3 for details.

This thesis ends with a brief overall conclusion in Chapter 8. Mainly, this is a summary of the conclusions stated at the end of each result chapter, i.e. Chapters 5, 6 and 7.

1.3 Publications

As mentioned before, the majority of our results in Chapter 6 were published in Tiburtius et al. (2014). This paper was a joint work together with our project partners of the Charité Berlin (Susanne Schrof, Ference Molnár and Prof. Dr. Kay Raum), Dr. Peter Varga, Dr. Quentin Grimal, Dr. Alf Gerisch and Dr. Françoise Peyrin.

The modeling part and the numerical analysis of the MTLT model was performed by me, while my colleagues in the lab of Kay Raum derived the experimental data. I am grateful to Prof. Dr. Kay Raum, Susanne Schrof and Ference Molnár, who discussed with me issues, such as how to incorporate the experimental data into the MTLT model and how to interpret the experimental data. Images showing the experimental data of our project partners are given with the permission of Prof. Dr. Kay Raum. This includes the following images: all subimages in Fig. 6.2, Fig. 6.8, Fig. 6.9 and Fig. 7.1

I have also benefited from many discussions with Dr. Alf Gerisch, Dr. Quentin Grimal and Dr. Peter Varga on modeling aspects and the results of our study.

2 Linear elasticity and the finite element method

The description of linear elasticity makes extensive use of various tensors and tensor fields. We, therefore, start this chapter introducing tensors and tensor fields and describing our notation of them. In Section 2.1 we inductively construct zeroth-, first-, second- and fourth-order tensors on $\mathbb{R}^n$. Higher-order tensors do not appear in the context of linear elasticity, and hence we do not consider them here. Also in Section 2.1, we consider tensor fields on $\mathbb{R}^n$. Furthermore, we introduce the most important operations on tensors and tensor fields in linear elasticity, and give important properties for tensors and tensor fields. Finally, we discuss different representations of symmetric second-order tensors and fourth-order tensors which possess minor and major symmetries. Thereby we focus on those representations which are frequently used in the context of linear elasticity: the Voigt, the Kelvin and the Mandel notation. All three representations will be of importance for the computational handling of fourth-order tensors when implementing homogenization methods.

In Section 2.2 we turn to boundary value problems in static and dynamic linear elasticity. We begin by reviewing the quantities entering these boundary value problems. Afterwards, we state the governing equations (Newton's second law, constitutive law) and discuss the form of the constitutive law for different material symmetries. Finally, we specify three types of boundary conditions, namely traction, displacement and periodic boundary conditions. All of them play an important role in homogenization, see Chapter 3 for details.

Section 2.3 focuses on the weak formulation of the boundary value problems in static and dynamic linear elasticity. We begin by introducing the most important function spaces as needed to setup the weak formulation. Afterwards, we explicitly state the pure-displacement weak formulation of our boundary value problems. Finally, we briefly review theorems concerning the existence and uniqueness of weak solutions to these weak formulations.

Finally, in Section 2.4 we turn to the finite element method. We discuss the Galerkin approach and address its main ideas and concepts in application to our boundary value problems. The section concludes with error bounds for the finite element approximation.

There is a large amount of literature available on tensors, linear elasticity and finite element methods. A general introduction into tensors and tensor algebra, with emphasis on continuum mechanics, is given, for instance, by Sändig (2005) or Gurtin (1981). Another useful, but more elaborated reference on tensors is Moakher (2008). For linear elasticity we follow mainly the books of Braess (1997) and Ciarlet (1988), the lecture notes of Sändig (2005), and a paper of Oleĭnik et al. (1992). For the finite element methods we mainly review results from the books of Braess (1997), Ciarlet (1978) and Brenner and Scott (2008); Brenner and Carstensen (2004).

2.1 Tensors on $\mathbb{R}^n$ and tensor fields

Tensors are linear maps over an underlying inner product space $\mathcal{V}$. They are mathematical objects which do not change under basis transformations in $\mathcal{V}$. Due to this invariance to basis changes in $\mathcal{V}$, they are a useful tool when expressing physical laws. Any tensor can be represented, with respect to a basis of $\mathcal{V}$, by its components. These components are no longer invariant to basis changes in $\mathcal{V}$. The number of indices needed to uniquely refer to a component is referred to as the order of a tensor. In the following, we assume that $\mathcal{V}$ is a finite dimensional inner product space, and consider the basis of $\mathcal{V}$ to be orthonormal. The latter means that we deal with so-called Cartesian tensors only.

Usually, we represent a vector or a tensor using symbolic notation. Thereby, we denote vectors, first- and second-order tensors by bold lowercase Roman or Greek letters (for example $\boldsymbol{u}$, $\boldsymbol{\sigma}$) and indicate fourth-order tensors by bold uppercase Roman letters (for example $\boldsymbol{C}$). Also we use index notation, i.e. we describe tensors through their components. We denote these components with the same letter as the

tensor, but give them in lightface type (for example u_i, σ_{ij}, C_{ijkl}). When we employ index notation, we adopt Einstein's summation convention, i.e. over repeated indices of different tensors is implicitly summed. Furthermore, we will, except in a few occasions, refer to a tensor and its representation in Voigt, Kelvin or Mandel notation by the same symbol.

In the following let $\mathcal{V}$ and $\mathcal{W}$ refer to real vector spaces of finite dimension n and m. Both vector spaces are equipped with some inner product, denoted $\langle\cdot,\cdot\rangle$. A typical example is $\mathcal{V} = \mathbb{R}^n$, where $\langle \boldsymbol{v}_1, \boldsymbol{v}_2\rangle$ refers to the dot product of two vectors $\boldsymbol{v}_1, \boldsymbol{v}_2 \in \mathcal{V}$. Moreover, let $\{\boldsymbol{e}_1, \boldsymbol{e}_2, \cdots, \boldsymbol{e}_n\}$, in short $\{\boldsymbol{e}_i\}$, denote some arbitrary orthonormal basis of $\mathcal{V}$. We introduce the following sets

Definition 2.1.1 *The sets $Lin(\mathcal{V},\mathcal{W})$, $Lin(\mathcal{V})$, $\mathbb{L}in(V)$ and $\mathbb{R}^{n\times m}$ are defined by*

$$Lin(\mathcal{V},\mathcal{W}) := \{f \mid f : \mathcal{V} \to \mathcal{W} \text{ is linear}\}, \tag{2.1}$$
$$Lin(\mathcal{V}) := Lin(\mathcal{V},\mathcal{V}), \tag{2.2}$$
$$\mathbb{L}in(\mathcal{V}) := \{f \mid f : Lin(\mathcal{V}) \to Lin(\mathcal{V}) \text{ is linear}\}, \tag{2.3}$$
$$\mathbb{R}^{n\times m} := \{\boldsymbol{A} \mid \boldsymbol{A} \text{ is a } n\times m \text{ matrix with components } A_{ij} \in \mathbb{R}\}, \tag{2.4}$$

respectively.

Zeroth-order tensors: Any zeroth-order tensor $\boldsymbol{t}$ is a linear map from $\mathbb{R}$ to $\mathbb{R}$, but also can be viewed of as a real scalar.
First-order tensors: Any first-order tensor $\boldsymbol{t}$ is a linear map $\boldsymbol{t} : \mathcal{V} \to \mathbb{R}$ with $\boldsymbol{v} \mapsto \boldsymbol{t}[\boldsymbol{v}]$. Equivalently, a first-order tensor can be thought of as a vector in $\mathbb{R}^n$. With respect to the basis $\{\boldsymbol{e}_i\}$ of $\mathcal{V}$, we can give $\boldsymbol{t}$ by

$$\boldsymbol{t} = t_i\,\boldsymbol{e}_i, \quad t_i = \langle \boldsymbol{t}, \boldsymbol{e}_i\rangle, \tag{2.5}$$

where $t_i \in \mathbb{R}$ are the components of $\boldsymbol{t}$.

Second-order tensors: Second-order tensors $\boldsymbol{t}$ are linear maps from $\mathcal{V}$ to $\mathcal{V}$ with $\boldsymbol{v} \mapsto \boldsymbol{t}[\boldsymbol{v}]$, that is $\boldsymbol{t} \in \mathrm{Lin}(\mathcal{V})$. Any second-order tensor can be thought of as a matrix in $\mathbb{R}^{n\times n}$. An important example of a second-order tensor is $\boldsymbol{e}_i \otimes \boldsymbol{e}_j$[1]. This tensor maps a vector $\boldsymbol{v} \in \mathcal{V}$ to another vector $(\boldsymbol{e}_i \otimes \boldsymbol{e}_j)[\boldsymbol{v}] = \langle \boldsymbol{v}, \boldsymbol{e}_j\rangle\,\boldsymbol{e}_i$. The set

$$\mathcal{B}_{\mathrm{Lin}} = \{\boldsymbol{e}_i \otimes \boldsymbol{e}_j\}_{1\le i,j\le n} \tag{2.6}$$

forms a basis of $\mathrm{Lin}(\mathcal{V})$. Hence, $\boldsymbol{t} \in \mathrm{Lin}(\mathcal{V})$ has the representation

$$\boldsymbol{t} = t_{ij}\,\boldsymbol{e}_i \otimes \boldsymbol{e}_j, \quad t_{ij} = \langle \boldsymbol{e}_i, \boldsymbol{t}[\boldsymbol{e}_j]\rangle, \tag{2.7}$$

where t_{ij} are the components of $\boldsymbol{t}$. On $\mathrm{Lin}(\mathcal{V})$ we define the inner product and the induced norm, respectively, by

$$\langle \boldsymbol{t}, \tilde{\boldsymbol{t}}\rangle = t_{ij}\tilde{t}_{ij} \quad \text{and} \quad \|\boldsymbol{t}\| = \sqrt{t_{ij}t_{ij}}. \tag{2.8}$$

Note that the basis $\mathcal{B}_{\mathrm{Lin}}$ is orthonormal with respect to the inner product (2.8).

Fourth-order tensors: Any fourth-order tensor $\boldsymbol{T}$ is a linear map from $\mathrm{Lin}(\mathcal{V})$ to $\mathrm{Lin}(\mathcal{V})$ with $\boldsymbol{t} \mapsto \boldsymbol{T}[\boldsymbol{t}]$, that is $\boldsymbol{T} \in \mathbb{L}\mathrm{in}(\mathcal{V})$. We denote by $\boldsymbol{e}_i \otimes \boldsymbol{e}_j \otimes \boldsymbol{e}_k \otimes \boldsymbol{e}_l$ the fourth-order tensor which maps $\boldsymbol{t} \in \mathrm{Lin}(\mathcal{V})$ to another tensor $\langle \boldsymbol{t}, \boldsymbol{e}_k \otimes \boldsymbol{e}_l\rangle\,\boldsymbol{e}_i \otimes \boldsymbol{e}_j \in \mathrm{Lin}(\mathcal{V})$. The set

$$\mathcal{B}_{\mathbb{L}\mathrm{in}} = \{\boldsymbol{e}_i \otimes \boldsymbol{e}_j \otimes \boldsymbol{e}_k \otimes \boldsymbol{e}_l\}_{1\le i,j,k,l\le n} \tag{2.9}$$

[1] In general, the symbol $\otimes$ denotes the so-called tensor product. See Eq. (2.18) for a definition.

forms a basis of $\mathbb{L}\mathrm{in}(\mathcal{V})$. Hence, $\boldsymbol{T} \in \mathbb{L}\mathrm{in}(\mathcal{V})$ has the representation

$$\boldsymbol{T} = T_{ijkl}\, \boldsymbol{e}_i \otimes \boldsymbol{e}_j \otimes \boldsymbol{e}_k \otimes \boldsymbol{e}_l, \quad T_{ijkl} = \langle \boldsymbol{e}_i \otimes \boldsymbol{e}_j, \boldsymbol{T}[\boldsymbol{e}_k \otimes \boldsymbol{e}_l] \rangle, \tag{2.10}$$

where $\langle \cdot, \cdot \rangle$ denotes the inner product on $\mathrm{Lin}(\mathcal{V})$. On $\mathbb{L}\mathrm{in}(\mathcal{V})$ we define the inner product and the induced norm, respectively, by

$$\langle \boldsymbol{T}, \boldsymbol{S} \rangle = T_{ijkl} S_{ijkl} \quad \text{and} \quad \|\boldsymbol{T}\| = \sqrt{T_{ijkl} T_{ijkl}}. \tag{2.11}$$

Note that the basis $\mathcal{B}_{\mathbb{L}\mathrm{in}}$ is orthonormal with respect to the inner product (2.11).

Tensor fields: Tensor fields are functions from a domain $\Omega \subset \mathbb{R}^3$ on the set of tensors of order k. In this thesis we mainly consider zeroth-, first-, second- and fourth-order tensor fields on $\mathbb{R}^3$, i.e. it holds that $k = 0$, $k = 1$, $k = 2$ and $k = 4$, respectively. Important first-order and second-order tensor fields in the context of linear elasticity, are the displacement $\boldsymbol{u}$ and the stress $\boldsymbol{\sigma}$, respectively.

We denote tensor fields following the notation of tensors described above. In particular, we use lowercase Roman or Greek letters, bold lowercase Roman/Greek letters, or bold uppercase Roman letters to denote zeroth-order, first/second-order or fourth-order tensor fields, respectively. The value of a tensor field at $\boldsymbol{x}$, a tensor, is formally given by $\boldsymbol{f}(\boldsymbol{x})$. However, in order to shorten notation we may omit the $\boldsymbol{x}$-dependency of the tensor $\boldsymbol{f}(\boldsymbol{x})$ and refer to it then to as $\boldsymbol{f}$.

2.1.1 Operations on tensors and tensor fields

We set $\mathcal{V} = \mathbb{R}^n$ in the following. Simple tensor operations on $\mathrm{Lin}(\mathbb{R}^n)$ and $\mathbb{L}\mathrm{in}(\mathbb{R}^n)$ are the addition, the subtraction, the scalar multiplication and the scalar division. These operations are performed componentwise. This means, in particular, for the addition and the subtraction, that these operations are only defined for two tensors of the same order.

A crucial tensor operation in linear elasticity is the double contraction. This operation is denoted by the symbol : and involves summing over two indices. As operands we allow any two tensors which have an order equal or higher to two. In the context of linear elasticity, we encounter the following double contractions

$$\boldsymbol{t} : \tilde{\boldsymbol{t}} = t_{ij} \tilde{t}_{ij} = \langle \boldsymbol{t}, \tilde{\boldsymbol{t}} \rangle, \tag{2.12}$$

$$(\boldsymbol{T} : \boldsymbol{t})_{ij} = T_{ijkl} t_{kl} = (\boldsymbol{T}[\boldsymbol{t}])_{ij}, \tag{2.13}$$

$$(\boldsymbol{T} : \widetilde{\boldsymbol{T}})_{ijkl} = T_{ijmn} \widetilde{T}_{mnkl}, \tag{2.14}$$

where $\boldsymbol{t}, \tilde{\boldsymbol{t}} \in \mathrm{Lin}(\mathbb{R}^n)$ and $\boldsymbol{T}, \widetilde{\boldsymbol{T}} \in \mathbb{L}\mathrm{in}(\mathbb{R}^n)$. It is worth to note here that the double contraction of two second-order tensors, as defined by Eq. (2.12), satisfies the requirements of an inner product.

For the double contractions, defined by Eq. (2.12), Eq. (2.13) and Eq. (2.14), the following properties holds

$$\boldsymbol{t} : \tilde{\boldsymbol{t}} = \tilde{\boldsymbol{t}} : \boldsymbol{t}, \qquad (a\boldsymbol{t}) : \tilde{\boldsymbol{t}} = a(\boldsymbol{t} : \tilde{\boldsymbol{t}}), \qquad \boldsymbol{t} : \boldsymbol{t} \geq 0,\ \boldsymbol{t} : \boldsymbol{t} = 0 \Leftrightarrow \boldsymbol{t} = 0, \tag{2.15}$$

$$\boldsymbol{t} : (\tilde{\boldsymbol{t}} + \hat{\boldsymbol{t}}) = \boldsymbol{t} : \tilde{\boldsymbol{t}} + \boldsymbol{t} : \hat{\boldsymbol{t}}, \qquad (a\boldsymbol{T}) : \boldsymbol{t} = a(\boldsymbol{T} : \boldsymbol{t}), \qquad \boldsymbol{T} : (\boldsymbol{t} + \tilde{\boldsymbol{t}}) = \boldsymbol{T} : \boldsymbol{t} + \boldsymbol{T} : \tilde{\boldsymbol{t}}, \tag{2.16}$$

$$(a\boldsymbol{T}) : \widetilde{\boldsymbol{T}} = a(\boldsymbol{T} : \widetilde{\boldsymbol{T}}), \tag{2.17}$$

where $a \in \mathbb{R}$, $\boldsymbol{t}, \tilde{\boldsymbol{t}}, \hat{\boldsymbol{t}} \in \mathrm{Lin}(\mathbb{R}^n)$ and $\boldsymbol{T}, \widetilde{\boldsymbol{T}} \in \mathbb{L}\mathrm{in}(\mathbb{R}^n)$. Note that the double contraction of two second-order tensors is commutative, however, the double contraction of two fourth-order tensors is not, in general $\boldsymbol{T} : \widetilde{\boldsymbol{T}} \neq \widetilde{\boldsymbol{T}} : \boldsymbol{T}$.

Another important tensor operation is the simple contraction. As the name suggests, this operation involves summation over only one index. We denote this operation by a blank and encounter the following single contractions

$$(\boldsymbol{t}\,\tilde{\boldsymbol{t}})_{ij} = t_{ik}\tilde{t}_{kj}, \quad (\boldsymbol{t}\,\boldsymbol{r})_i = t_{ik}\,r_k = (\boldsymbol{t}[\boldsymbol{r}])_i, \quad \forall \boldsymbol{r} \in \mathbb{R}^n, \quad \forall \boldsymbol{t}, \tilde{\boldsymbol{t}} \in \mathrm{Lin}(\mathbb{R}^n).$$

The operations $\boldsymbol{t}\,\tilde{\boldsymbol{t}}$ and $\boldsymbol{t}\,\boldsymbol{r}$ coincides with the standard matrix-matrix and the matrix-vector product of linear algebra, respectively.

Besides the double and the single contraction, we encounter the tensor product of a first-order or a second-order tensor with a first-order tensor

$$(\boldsymbol{r} \otimes \tilde{\boldsymbol{r}})_{ij} \coloneqq r_i\tilde{r}_j \quad \text{and} \quad (\boldsymbol{t} \otimes \tilde{\boldsymbol{r}})_{ijk} \coloneqq t_{ij}\tilde{r}_k \quad \forall \boldsymbol{r}, \tilde{\boldsymbol{r}} \in \mathbb{R}^n, \quad \forall \boldsymbol{t} \in \mathrm{Lin}(\mathbb{R}^n). \tag{2.18}$$

Finally, we introduce for two first-order tensors $\boldsymbol{r}, \tilde{\boldsymbol{r}} \in \mathbb{R}^n$, the dot product and the cross product, respectively, by

$$\boldsymbol{r} \cdot \tilde{\boldsymbol{r}} \coloneqq r_i\tilde{r}_i, \quad (\boldsymbol{r} \times \tilde{\boldsymbol{r}})_i \coloneqq \gamma_{ijk}\,r_j\,\tilde{r}_k. \tag{2.19}$$

where γ_{ijk} refers to the Levi-Civita symbol (Ciarlet, 1988, see the definition of the *orientation tensor* on page 5). Note that the dot product $\boldsymbol{r} \cdot \tilde{\boldsymbol{r}}$ is an inner product on $\mathbb{R}^n$.

2.1.2 Tensor properties, special tensors, and tensor derivatives

We list different properties of tensors and special tensors used throughout this thesis. Furthermore, we introduce tensor derivatives and the mean of a tensor.

Symmetric second-order tensors

Let us note first, that the transpose of $\boldsymbol{t} \in \mathrm{Lin}(\mathbb{R}^n)$ and $\boldsymbol{T} \in \mathbb{L}\mathrm{in}(\mathbb{R}^n)$, denoted $\boldsymbol{t}^T$ and $\boldsymbol{T}^T$, is uniquely defined via

$$\begin{aligned} \boldsymbol{u} \cdot (\boldsymbol{t}^T\boldsymbol{v}) &= \boldsymbol{v} \cdot (\boldsymbol{t}\,\boldsymbol{u}), \quad \forall\, \boldsymbol{u}, \boldsymbol{v} \in \mathbb{R}^n, \\ \boldsymbol{u} : (\boldsymbol{T}^T : \boldsymbol{v}) &= \boldsymbol{v} : (\boldsymbol{T} : \boldsymbol{u}), \quad \forall\, \boldsymbol{u}, \boldsymbol{v} \in \mathrm{Lin}(\mathbb{R}^n), \end{aligned}$$

respectively.

A second-order tensor $\boldsymbol{t}$ is said to be symmetric if $\boldsymbol{t}^T = \boldsymbol{t}$, that is $t_{ij} = t_{ji}$. We denote the set of all symmetric second-order tensors by

$$\mathrm{Sym}(\mathbb{R}^n) \coloneqq \{\boldsymbol{t} \mid \boldsymbol{t} \in \mathrm{Lin}(\mathbb{R}^n), \boldsymbol{t} \text{ is symmetric}\}.$$

The set $\mathrm{Sym}(\mathbb{R}^n)$ is an inner product subspace of $\mathrm{Lin}(\mathbb{R}^n)$ of dimension $N = n(n+1)/2$. An orthonormal basis of $\mathrm{Sym}(\mathbb{R}^n)$ is given by the set of symmetric second-order tensors

$$\mathcal{B}_{\mathrm{Sym}} = \{\, 2^{-\frac{1}{2}(1+\delta_{ij})}\,(\boldsymbol{e}_i \otimes \boldsymbol{e}_j + \boldsymbol{e}_j \otimes \boldsymbol{e}_i)\,\}_{1 \le i \le j \le n}\,, \tag{2.20}$$

where δ_{ij} refers to the Kronecker delta. Note that the factor $2^{-\frac{1}{2}(1+\delta_{ij})}$ is crucial in defining an orthonormal basis.

Minor and major symmetric fourth-order tensors

For fourth-order tensors $\boldsymbol{T}$ we distinguish two symmetries: we say that $\boldsymbol{T}$ possesses minor symmetries if

$T_{ijkl} = T_{jikl} = T_{ijlk}$, and refer to the property $T_{ijkl} = T_{klij}$ as major symmetry. We denote the set of all fourth-order tensors in $\mathbb{L}\mathrm{in}(\mathbb{R}^n)$ that possess major and minor symmetries, by

$$\mathbb{S}\mathrm{ym}(\mathbb{R}^n) := \{\boldsymbol{T} \mid \boldsymbol{T} \in \mathbb{L}\mathrm{in}(\mathbb{R}^n), \boldsymbol{T} \text{ is major and minor symmetric}\}.$$

The set $\mathbb{S}\mathrm{ym}(\mathbb{R}^n)$ forms an inner product subspace of $\mathbb{L}\mathrm{in}(\mathbb{R}^n)$ of dimension $M := N(N+1)/2$. An orthonormal basis of $\mathbb{S}\mathrm{ym}(\mathbb{R}^n)$ is denoted by $\mathcal{B}_{\mathbb{S}\mathrm{ym}}$, see Eq. (2.36) for details.

Identity tensors
Let $\mathbf{id} \in \mathrm{Lin}(\mathbb{R}^n)$ and $\mathbf{Id} \in \mathbb{L}\mathrm{in}(\mathbb{R}^n)$ denote the identity tensor of order two and four, respectively. They map any tensor, $\boldsymbol{t} \in \mathbb{R}^n$ or $\boldsymbol{T} \in \mathrm{Lin}(\mathbb{R}^n)$, onto itself, i.e.

$$\begin{aligned} \mathbf{id}[\boldsymbol{t}] &= \mathbf{id}\,\boldsymbol{t} = \boldsymbol{t}, \quad \forall\, \boldsymbol{t} \in \mathbb{R}^n, \\ \mathbf{Id}[\boldsymbol{t}] &= \mathbf{Id} : \boldsymbol{t} = \boldsymbol{t}, \quad \forall\, \boldsymbol{t} \in \mathrm{Lin}(\mathbb{R}^n). \end{aligned}$$

With respect to the orthonormal bases $\mathcal{B}_{\mathrm{Lin}}$ and $\mathcal{B}_{\mathbb{L}\mathrm{in}}$, the identity tensors $\mathbf{id}$ and $\mathbf{Id}$ have the components

$$\mathrm{id}_{ij} = \delta_{ij}, \quad \mathrm{Id}_{ijkl} = \delta_{ik}\delta_{jl}, \tag{2.21}$$

respectively. Obviously, $\mathbf{id}$ is symmetric, i.e. $\mathbf{id} \in \mathrm{Sym}(\mathbb{R}^n)$. The fourth-order tensor $\mathbf{Id}$ satisfies major but no minor symmetries, thus $\mathbf{Id} \notin \mathbb{S}\mathrm{ym}(\mathbb{R}^n)$. For this reason, it is useful to define a special identity tensor within $\mathbb{S}\mathrm{ym}(\mathbb{R}^n)$. This tensor maps every symmetric second-order tensor onto itself, i.e.

$$\mathbf{Id}^{\mathrm{s}}[\boldsymbol{t}] = \mathbf{Id}^{\mathrm{s}} : \boldsymbol{t} = \boldsymbol{t}, \quad \forall\, \boldsymbol{t} \in \mathrm{Sym}(\mathbb{R}^n).$$

With respect to the orthonormal basis $\mathcal{B}_{\mathbb{S}\mathrm{ym}}$, the identity tensor $\mathbf{Id}^{\mathrm{s}}$ has the components

$$\mathrm{Id}^{\mathrm{s}}_{ijkl} = \frac{1}{2}(\delta_{ik}\delta_{jl} + \delta_{il}\delta_{jk}). \tag{2.22}$$

Positive definite tensor, determinant and inverse tensor
A second-order tensor $\boldsymbol{t}$ is called positive definite if $t_{ij}\, r_i\, r_j > 0$ holds for all $0 \neq \boldsymbol{r} \in \mathbb{R}^n$. Likewise, we say that a fourth-order tensor $\boldsymbol{T}$ is positive definite if $T_{ijkl}\, d_{ij}\, d_{kl} > 0$ holds for all $0 \neq \boldsymbol{d} \in \mathrm{Lin}(\mathbb{R}^n)$.

The determinant of a second-order tensor $\boldsymbol{t} \in \mathrm{Lin}(\mathbb{R}^n)$, denoted $\det \boldsymbol{t}$, is the determinant of the corresponding matrix representation.

A tensor $\boldsymbol{t} \in \mathrm{Lin}(\mathbb{R}^n)$ is said to be invertible if there exists a tensor $\boldsymbol{t}^{-1} \in \mathrm{Lin}(\mathbb{R}^n)$ satisfying the condition

$$\boldsymbol{t}^{-1}\boldsymbol{t} = \boldsymbol{t}\,\boldsymbol{t}^{-1} = \mathbf{id}. \tag{2.23}$$

The tensor $\boldsymbol{t}^{-1}$ is uniquely defined and is called inverse of $\boldsymbol{t}$. The inverse of $\boldsymbol{t}$ exists if and only if the determinant of $\boldsymbol{t}$ is nonzero. Note that every positive definite second-order tensor has a positive determinant and thus is invertible.

A fourth-order tensor $\boldsymbol{T}^{-1} \in \mathbb{S}\mathrm{ym}(\mathbb{R}^n)$, if it exists, will be named the inverse of the fourth-order tensor $\boldsymbol{T} \in \mathbb{S}\mathrm{ym}(\mathbb{R}^n)$, if

$$\boldsymbol{T} : \boldsymbol{T}^{-1} = \boldsymbol{T}^{-1} : \boldsymbol{T} = \mathbf{Id}^{\mathrm{s}}. \tag{2.24}$$

Orthogonal
A second-order tensor $\boldsymbol{t} \in \mathrm{Lin}(\mathbb{R}^n)$ is said to be orthogonal if $\boldsymbol{t}^T\boldsymbol{t} = \boldsymbol{t}\,\boldsymbol{t}^T = \mathbf{id}$.

Eigenvalue and eigentensor
Finally, we briefly consider the eigenvalue problem for fourth-order tensors in $\mathbb{S}\mathrm{ym}(\mathbb{R}^n)$. It is defined as

$$\boldsymbol{T} : \boldsymbol{t} = \lambda \boldsymbol{t}, \tag{2.25}$$

where $\lambda \in \mathbb{R}$ and $\boldsymbol{t} \in \mathrm{Sym}(\mathbb{R}^n)$ denote the eigenvalue and the corresponding eigentensor, respectively.

Mean of a tensor field
The mean of the kth-order tensor field $\boldsymbol{h}$ ($k = 1, 2$) over the volume element $V \subset \mathbb{R}^3$, is denoted by $\mathcal{M}_V(\boldsymbol{h})$, and is given by

$$\mathcal{M}_V(\boldsymbol{h}) := \frac{1}{|V|} \int_V \boldsymbol{h}(\boldsymbol{x}) \, \mathrm{d}\boldsymbol{x}, \tag{2.26}$$

respectively.

Nabla operator and divergence of a tensor field
Let us denote by g, $\boldsymbol{h}$ and $\boldsymbol{k}$ a zeroth-, a first- and a second-order tensor field, respectively. In what follows, we assume that these tensor fields are sufficiently smooth, so that derivatives can be taken. Moreover, let $\{\boldsymbol{e}_i\}$ and $\{\boldsymbol{e}_i \otimes \boldsymbol{e}_j\}$ be some fix orthonormal basis of $\mathbb{R}^3$ and $\mathrm{Lin}(\mathbb{R}^3)$, respectively.

The partial derivative of g with respect to x_i is denoted $\frac{\partial g}{\partial x_i}$. The nabla operator $\nabla := (\frac{\partial}{\partial x_1}, \frac{\partial}{\partial x_2}, \frac{\partial}{\partial x_3})^T$, applied to g and $\boldsymbol{h}$, respectively, yields

$$\nabla g := \frac{\partial g}{\partial x_i} \boldsymbol{e}_i \equiv \begin{pmatrix} \frac{\partial g}{\partial x_1} \\ \frac{\partial g}{\partial x_2} \\ \frac{\partial g}{\partial x_3} \end{pmatrix}, \quad \nabla \boldsymbol{h} := \frac{\partial h_i}{\partial x_j} \boldsymbol{e}_i \otimes \boldsymbol{e}_j \equiv \begin{pmatrix} \frac{\partial h_1}{\partial x_1} & \frac{\partial h_1}{\partial x_2} & \frac{\partial h_1}{\partial x_3} \\ \frac{\partial h_2}{\partial x_1} & \frac{\partial h_2}{\partial x_2} & \frac{\partial h_2}{\partial x_3} \\ \frac{\partial h_3}{\partial x_1} & \frac{\partial h_3}{\partial x_2} & \frac{\partial h_3}{\partial x_3} \end{pmatrix}. \tag{2.27}$$

Finally, we introduce the divergence of a second-order tensor field $\boldsymbol{k}$. This tensor has order one, is denoted div $\boldsymbol{k}$, and is defined by

$$\mathrm{div}\, \boldsymbol{k} = \frac{\partial k_{j_1 i}}{\partial x_i} \boldsymbol{e}_{j_1}, \tag{2.28}$$

see, for instance, Ciarlet (1988) or Cioranescu and Donato (1999).

V-periodicity
Let $h : \Omega \to \mathbb{R}$ be a zeroth-order tensor field, let $\{\boldsymbol{e}_1, \boldsymbol{e}_2, \boldsymbol{e}_3\}$ be the standard basis of $\mathbb{R}^3$ and let $V = (0, l_1) \times (0, l_2) \times (0, l_3) \subset \mathbb{R}^3$. The tensor field h is V-periodic if and only if

$$h(\boldsymbol{x} + m\, l_i \boldsymbol{e}_i) = h(\boldsymbol{x}) \quad \text{for} \quad \forall\, \boldsymbol{x} \in \mathbb{R}^3, \quad \forall m \in \mathbb{Z}, \quad \forall\, i \in \{1, 2, 3\} \qquad (\text{no summation over } i). \tag{2.29}$$

Likewise, we call a kth-order tensor field on $\mathbb{R}^3$ V-periodic if all its components are V-periodic.

It is worth to note the following property of V-periodic tensor fields

Theorem 2.1.2 *For any V-periodic and differentiable first or second-order tensor field $\boldsymbol{h}$ the mean of $\nabla \boldsymbol{h}$ over the volume element V is zero, i.e. $\mathcal{M}_V(\nabla \boldsymbol{h}) = 0$.*

Proof. See Cioranescu and Donato (1999) for details. □

Theorem 2.1.2 follows from partial integration and the divergence theorem.

2.1.3 Voigt, Kelvin and Mandel notation of symmetric second-order tensors and minor and major symmetric fourth-order tensors

Any second-order tensor $\boldsymbol{t} \in \mathrm{Sym}(\mathbb{R}^n)$ can be represented as a first-order tensor in $\mathbb{R}^N$ where $N = n/(n+1)$. Likewise, any fourth-order tensor $\boldsymbol{T} \in \mathbb{S}\mathrm{ym}(\mathbb{R}^n)$ can be described as a second-order tensor in $\mathrm{Sym}(\mathbb{R}^N)$. In particular, the latter representation has the advantage that we can think of the double contraction $\boldsymbol{T} : \boldsymbol{t}$ as a matrix-vector product. This fact makes the implementation of double contractions much easier. In what follows, we review the Kelvin, the Mandel and the Voigt notation. Thereby, we follow mainly Moakher (2008), Mehrabadi and Cowin (1990) and Helnwein (2001).

Before we start, let us introduce the following invertible maps $\Psi : I \times I \to K$, with the index sets $I \times I = \{(i,j) \,|\, 1 \le i \le j \le n\}$ and $K = \{1, 2, \ldots, N\}$ with $N = n(n+1)/2$. For $n = 3$ we have, for instance, the two maps Ψ_1 and Ψ_2, defined in Table 2.1.

Table 2.1.: Index maps $\Psi_1, \Psi_2 : I \times I \to K$ for $n = 3$.

(i,j)	$(1,1)$	$(2,2)$	$(3,3)$	$(2,3)$	$(1,3)$	$(1,2)$
$\Psi_1(i,j)$	1	2	3	4	5	6
$\Psi_2(i,j)$	1	2	3	5	6	4

Symmetric second-order tensors

Let us define

$$\tilde{\boldsymbol{e}}_{\Psi(i,j)} = 2^{-\frac{1}{2}(1+\delta_{ij})}(\boldsymbol{e}_i \otimes \boldsymbol{e}_j + \boldsymbol{e}_j \otimes \boldsymbol{e}_i), \quad 1 \le i \le j \le n \qquad \text{(no summation)}. \tag{2.30}$$

The set $\{\tilde{\boldsymbol{e}}_a\}_{1 \le a \le N}$ spans the vector space $\tilde{\mathcal{V}} := \mathrm{Sym}(\mathbb{R}^n)$, compare Eq. (2.20), and is an orthonormal basis of $\tilde{\mathcal{V}}$. Therefore, any $\boldsymbol{t} \in \mathrm{Sym}(\mathbb{R}^n)$ has the representation

$$\boldsymbol{t} \equiv \tilde{\boldsymbol{t}} = \tilde{t}_a \tilde{\boldsymbol{e}}_a, \quad 1 \le a \le N \quad \text{with} \quad \tilde{t}_{\psi(i,j)} = 2^{\frac{1}{2}(1+\delta_{ij})} t_{ij}, \tag{2.31}$$

where t_{ij} is given by Eq. (2.7). In other words, any second-order tensor $\boldsymbol{t} \in \mathrm{Sym}(\mathbb{R}^n)$ can be represented as a first-order tensor $\tilde{\boldsymbol{t}} \in \mathbb{R}^N$ (Moakher, 2008).

We say that $\boldsymbol{t} \in \mathrm{Sym}(\mathbb{R}^3)$ is given in Kelvin notation[2], when representing $\boldsymbol{t}$ as the tensor $\tilde{\boldsymbol{t}}$ using the map $\Psi = \Psi_1$. Furthermore, $\boldsymbol{t} \in \mathrm{Sym}(\mathbb{R}^3)$ is said to be given in Mandel notation, when referring to the tensor $\tilde{\boldsymbol{t}}$ obtained when using the map $\Psi = \Psi_2$.

Besides the Kelvin and the Mandel notation, we also employ the Voigt notation for a tensor $\boldsymbol{t} \in \mathrm{Sym}(\mathbb{R}^3)$. Using this notation we represent the stress tensor, $\boldsymbol{\sigma}$, and the strain tensor, $\boldsymbol{\varepsilon}$, as

$$\tilde{\boldsymbol{\sigma}} = \tilde{\sigma}_a \tilde{\boldsymbol{e}}_a, \quad 1 \le a \le N, \quad \tilde{\boldsymbol{e}}_a \in \mathcal{B}'_{\mathrm{Sym}}, \quad \text{and} \quad \tilde{\sigma}_{\psi_1(i,j)} = \sigma_{ij}, \tag{2.32}$$

$$\tilde{\boldsymbol{\varepsilon}} = \tilde{\varepsilon}_a \tilde{\boldsymbol{e}}_a, \quad 1 \le a \le N, \quad \tilde{\boldsymbol{e}}_a \in \mathcal{B}''_{\mathrm{Sym}}, \quad \text{and} \quad \tilde{\varepsilon}_{\psi_1(i,j)} = 2^{1-\delta_{ij}} \varepsilon_{ij}, \tag{2.33}$$

respectively, with $\mathcal{B}'_{\mathrm{Sym}}$ and $\mathcal{B}''_{\mathrm{Sym}}$ bases of $\mathrm{Sym}(\mathbb{R}^n)$ given by

$$\mathcal{B}'_{\mathrm{Sym}} = \{\tilde{\boldsymbol{e}}_a\}_{1 \le a \le N}, \quad \text{with} \quad \tilde{\boldsymbol{e}}_{\Psi_1(i,j)} = \boldsymbol{e}_i \otimes \boldsymbol{e}_j + \boldsymbol{e}_j \otimes \boldsymbol{e}_i\,, \tag{2.34}$$

$$\mathcal{B}''_{\mathrm{Sym}} = \{\tilde{\boldsymbol{e}}_a\}_{1 \le a \le N}, \quad \text{with} \quad \tilde{\boldsymbol{e}}_{\Psi_1(i,j)} = 2^{-(1-\delta_{ij})}(\boldsymbol{e}_i \otimes \boldsymbol{e}_j + \boldsymbol{e}_j \otimes \boldsymbol{e}_i)\,. \tag{2.35}$$

[2] Mehrabadi and Cowin (1990) and others coined the term "Kelvin notation" after the inventor of this notation, Lord Kelvin. However, this term was not used by Moakher (2008).

Since the basis vectors in $\mathcal{B}'_{\text{Sym}}$ and $\mathcal{B}''_{\text{Sym}}$ are not normalized with respect to the inner product of $\text{Sym}(\mathbb{R}^n)$, neither the basis $\mathcal{B}'_{\text{Sym}}$ nor $\mathcal{B}''_{\text{Sym}}$ is orthonormal. Thus, the objects $\tilde{\boldsymbol{\sigma}}$ and $\tilde{\boldsymbol{\varepsilon}}$ represent no first-order Cartesian tensor. Nevertheless, we can associate with these object the vectors $(\tilde{\sigma}_1, \tilde{\sigma}_2, \cdots, \tilde{\sigma}_N)^T$ and $(\tilde{\varepsilon}_1, \tilde{\varepsilon}_2, \cdots, \tilde{\varepsilon}_N)^T$, respectively.

Minor and major symmetric fourth-order tensors

We define

$$\hat{\boldsymbol{e}}_{a\,b} = \tilde{\boldsymbol{e}}_a \otimes \tilde{\boldsymbol{e}}_b, \tag{2.36}$$

where $\tilde{\boldsymbol{e}}_a$ and $\tilde{\boldsymbol{e}}_b$ are given as in Eq. (2.30) and $1 \leq a \leq b \leq N$. The set $\{\hat{\boldsymbol{e}}_{ab}\}_{1\leq a\leq b\leq N}$ spans the vector space $\hat{\mathcal{V}} = \mathbb{S}\text{ym}(\mathbb{R}^n)$ and is an orthonormal basis of $\mathbb{S}\text{ym}(\mathbb{R}^n)$. Any tensor $\boldsymbol{T} \in \mathbb{S}\text{ym}(\mathbb{R}^n)$ has the representation

$$\boldsymbol{T} \equiv \hat{\boldsymbol{T}} = \hat{T}_{ab}\,\hat{\boldsymbol{e}}_{ab}, \quad 1 \leq a \leq b \leq N \quad \text{with} \quad \hat{T}_{\psi(i,j)\psi(k,l)} = 2^{1-\frac{1}{2}(\delta_{ij}+\delta_{kl})}\,T_{ijkl}, \tag{2.37}$$

where T_{ijkl} is given by Eq. (2.10). Note that $\hat{T}_{ab} = \hat{T}_{ba}$, i.e. $\hat{\boldsymbol{T}} \in \text{Sym}(\mathbb{R}^N)$. Thus, any fourth-order tensor $\boldsymbol{T} \in \mathbb{S}\text{ym}(\mathbb{R}^n)$ can be viewed as a second-order tensor $\hat{\boldsymbol{T}} \in \text{Sym}(\mathbb{R}^N)$ (Moakher, 2008).

We say that $\boldsymbol{T} \in \mathbb{S}\text{ym}(\mathbb{R}^3)$ is given in Kelvin or Mandel notation, if $\Psi = \Psi_1$ or $\Psi = \Psi_2$, respectively. Using the Voigt notation we can represent the tensor $\boldsymbol{T} \in \mathbb{S}\text{ym}(\mathbb{R}^3)$ as a matrix $\hat{\boldsymbol{T}}$ with components $\hat{T}_{\Psi_1(i,j)\Psi_1(k,l)} = T_{ijkl}$. Note that the components of $\hat{\boldsymbol{T}}$ form no Cartesian tensor, since the basis with respect to which the components were given, is not orthonormal.

Equivalent operations on symmetric second-order and fourth-order tensors which possess minor and major symmetries

The following theorem enables us to translate some operations on symmetric fourth-order to corresponding operations on second-order tensors, see Moakher (2008) for details.

Theorem 2.1.3 *Let $n = 3$ and $N = 6$. Furthermore, let $\boldsymbol{S}$ and $\boldsymbol{T}$ be two fourth-order tensors in $\mathbb{S}\text{ym}(\mathbb{R}^n)$, and $\tilde{\boldsymbol{S}} \in \text{Sym}(\mathbb{R}^N)$ and $\tilde{\boldsymbol{T}} \in \text{Sym}(\mathbb{R}^N)$ their corresponding second-order tensors in Kelvin or Mandel notation. Finally, let $\boldsymbol{u}$ be a second-order tensor in $\text{Sym}(\mathbb{R}^n)$ and $\tilde{\boldsymbol{u}} \in \mathbb{R}^N$ its corresponding first-order tensor in Kelvin or Mandel notation. It holds that*

1. *The second-order tensor $\boldsymbol{S} : \boldsymbol{u}$ corresponds to the first-order tensor $\tilde{\boldsymbol{S}}\tilde{\boldsymbol{u}}$.*
2. *$\langle \boldsymbol{S}, \boldsymbol{T} \rangle = \langle \tilde{\boldsymbol{S}}, \tilde{\boldsymbol{T}} \rangle$ and $\|\boldsymbol{S}\| = \sqrt{\langle \boldsymbol{S}, \boldsymbol{S} \rangle} = \sqrt{\tilde{\boldsymbol{S}} : \tilde{\boldsymbol{S}}} = \left\|\tilde{\boldsymbol{S}}\right\|$,*
3. *If $\boldsymbol{u}$ is an eigentensor of $\boldsymbol{T}$ and λ an eigenvalue of $\boldsymbol{T}$, then, $\tilde{\boldsymbol{u}}$ is an eigentensor of $\tilde{\boldsymbol{T}}$ and λ is an eigenvalue of $\tilde{\boldsymbol{T}}$, respectively.*

Note that we have no such correspondences when using the Voigt notation.

2.2 Boundary value problems in linear elasticity

In this section we present different boundary value problems appearing in linear elasticity. We start introducing basic notions of linear elasticity, move then to the equations of linear elasticity and, finally, review the different boundary conditions employed in this thesis.

2.2.1 Deformation, (rigid) displacement, stress and strain in static linear elasticity

Here, we consider the material under the influence of time-independent forces. Below, we describe the deformation, the strain and the stress of the material arising from these forces.

Let Ω be a domain in $\mathbb{R}^3$, i.e. a bounded connected open non-empty subset of $\mathbb{R}^3$ which has a Lipschitz-continuous boundary Γ_Ω. Usually, the closure of Ω, denoted $\overline{\Omega}$, represents the volume of $\mathbb{R}^3$ occupied by our material before any forces were applied to the material. A point $\boldsymbol{x} \in \overline{\Omega}$ is called a material point, while arbitrary points $\boldsymbol{x} \in \mathbb{R}^3$ are referred to as spatial points.

Under the impact of a stationary force $\overline{\Omega}$ changes. We describe this change by the deformation, a map $\boldsymbol{\phi} : \overline{\Omega} \to \mathbb{R}^3$ for which we assume it is continuously differentiable and bijective. Moreover, $\boldsymbol{\phi}$ shall be orientation preserving, i.e. the determinant of $\nabla\boldsymbol{\phi}$ in every material point is positive.

Based on the deformation $\boldsymbol{\phi}$, we can define the displacement $\boldsymbol{u}$ by $\boldsymbol{\phi} = \mathbf{id} + \boldsymbol{u}$. The displacement $\boldsymbol{u}$ is a first-order tensor field. It can be given with respect to either the reference configuration, i.e. $\boldsymbol{x} \in \overline{\Omega}$, or to the deformed configuration (Euler configuration), i.e. $\boldsymbol{x} \in \boldsymbol{\phi}(\overline{\Omega})$. Unless stated otherwise, we from now on assume that any vector or tensor field is given over the reference configuration.

Given two material points $\boldsymbol{x}$ and $\boldsymbol{x}+\boldsymbol{z}$ and a deformation $\boldsymbol{\phi}$, we consider the difference between $\boldsymbol{\phi}(\boldsymbol{x})$ and $\boldsymbol{\phi}(\boldsymbol{x}+\boldsymbol{z})$, i.e.

$$\left\|\boldsymbol{\phi}(\boldsymbol{x}+\boldsymbol{z}) - \boldsymbol{\phi}(\boldsymbol{x})\right\| = \boldsymbol{z}^T\,\nabla\boldsymbol{\phi}^T\nabla\boldsymbol{\phi}\,\boldsymbol{z} + o(\|\boldsymbol{z}^2\|),$$

where o is the little-o Landau symbol. For small $\|\boldsymbol{z}^2\|$ the expression $\nabla\boldsymbol{\phi}^T\nabla\boldsymbol{\phi}$ is a measure for the distortion of the material under $\boldsymbol{\phi}$. This measure gives the identity for deformations which translate or rotate the material, but do not change the shape of it, see for instance Sändig (2005). Since it would be desirable to have a measure returning for any of these deformations zero, we introduce the second-order tensor field

$$\hat{\boldsymbol{\varepsilon}} = \frac{1}{2}(\mathbf{id} - \nabla\boldsymbol{\phi}^T\nabla\boldsymbol{\phi}) = \frac{1}{2}\left(\mathbf{id} - (\mathbf{id} + \nabla\boldsymbol{u}^T + \nabla\boldsymbol{u} + \nabla\boldsymbol{u}^T\nabla\boldsymbol{u})\right) \tag{2.38}$$

$$= \frac{1}{2}(\nabla\boldsymbol{u}^T + \nabla\boldsymbol{u} + \nabla\boldsymbol{u}^T\nabla\boldsymbol{u}), \tag{2.39}$$

where we made use of $\nabla\boldsymbol{\phi} = \mathbf{id} + \nabla\boldsymbol{u}$ in Eq. (2.38).

So far, we provided basic notions of elasticity for arbitrary displacements. However, in linear elasticity, we only consider displacements for which $\|\nabla\boldsymbol{u}^T\|$ is small. For these it is justified to linearize $\hat{\boldsymbol{\varepsilon}}$, i.e. to neglect $\nabla\boldsymbol{u}^T\nabla\boldsymbol{u}$ in Eq. (2.39). In summary, we measure the distortion of a material by the so-called linearized strain tensor field

$$\boldsymbol{\varepsilon} : \Omega \to \mathrm{Lin}(\mathbb{R}^3), \quad \boldsymbol{x} \mapsto \boldsymbol{\varepsilon}(\boldsymbol{x}) = \frac{1}{2}\left(\nabla\boldsymbol{u}(\boldsymbol{x}) + (\nabla\boldsymbol{u}(\boldsymbol{x}))^T\right). \tag{2.40}$$

Instead of $\boldsymbol{\varepsilon}(\boldsymbol{x})$ we shall also write $\boldsymbol{\varepsilon}(\boldsymbol{u})$, in order to emphasize that the strain is a function of the displacement $\boldsymbol{u}$. With respect to the basis $\mathcal{B}_{\mathrm{Lin}}$ (Eq. (2.6)) the strain tensor $\boldsymbol{\varepsilon}(\boldsymbol{x})$ has the representation $\boldsymbol{\varepsilon}(\boldsymbol{x}) = \varepsilon_{ij}(\boldsymbol{x})\,\boldsymbol{e}_i \otimes \boldsymbol{e}_j$. Finally, note that the tensor $\boldsymbol{\varepsilon}(\boldsymbol{x})$ is symmetric for all $\boldsymbol{x} \in \Omega$.

For specific displacements, the so-called rigid displacements, it holds that $\boldsymbol{\varepsilon}(\boldsymbol{x}) = 0$. The set of rigid displacements, denoted $\mathcal{R}$, is a linear space which is characterized by

$$\mathcal{R} = \{\boldsymbol{r} \mid \boldsymbol{r}(\boldsymbol{x}) = \boldsymbol{q}\,\boldsymbol{x} + \boldsymbol{b}, \quad \boldsymbol{q} \in \mathbb{R}^{3\times3} \text{ such that } \boldsymbol{q}^T = -\boldsymbol{q}, \quad \boldsymbol{x} \in \mathbb{R}^3, \quad \boldsymbol{b} \in \mathbb{R}^3 \text{ constant } \}. \tag{2.41}$$

Note that the set $\mathcal{R}$ plays a crucial role for establishing the uniqueness of solutions to the boundary value problems of linear elasticity, see Section 2.3.3.

When a volume or a surface force is applied to a material, neighboring material points exert internal forces on each other. The second-order stress tensor field, $\boldsymbol{\sigma}$, is a measure of these. Its existence is given

by Cauchy's theorem. In the following we describe this theorem and consequences of it for materials in equilibrium.

Let there act some volume force $\boldsymbol{f}$ on Ω, represented by $\boldsymbol{f} : \Omega \to \mathbb{R}^3, \boldsymbol{x} \mapsto \boldsymbol{f}(\boldsymbol{x})$. We refer to the area force, acting onto a plane whose orientation is given by the unit normal $\boldsymbol{n}$ and which goes through $\boldsymbol{x} \in \Omega$, as the traction, and denote it by $\boldsymbol{t} = \boldsymbol{t}(\boldsymbol{x}, \boldsymbol{n})$. Furthermore, we denote the set of all unit normals $\boldsymbol{n}$ by $\mathcal{N}_3$. Cauchy's theorem states that, if the Euler-Cauchy stress principle holds, the traction $\boldsymbol{t}$ depends linearly on $\boldsymbol{n}$, i.e. at each material point $\boldsymbol{x} \in \Omega$ there exists a tensor $\boldsymbol{\sigma}(\boldsymbol{x})$, the so-called stress tensor, such that $\boldsymbol{t} = \boldsymbol{\sigma}(\boldsymbol{x})\boldsymbol{n}$ (Ciarlet, 1988).

Theorem 2.2.1 (Cauchy's theorem) *Let V be some small connected volume in Ω and Γ_V its boundary. Let the following properties be satisfied:*

- *the volume force $\boldsymbol{f}$ is continuous on $\overline{\Omega}$,*
- *the Euler-Cauchy stress principle*

$$\int_V \boldsymbol{f}(\boldsymbol{x})\,\mathrm{d}\boldsymbol{x} + \int_{\Gamma_V} \boldsymbol{t}(\boldsymbol{x},\boldsymbol{n})\,\mathrm{d}\boldsymbol{s} = 0, \quad \int_V \boldsymbol{x} \times \boldsymbol{f}(\boldsymbol{x})\,\mathrm{d}\boldsymbol{x} + \int_{\Gamma_V} \boldsymbol{x} \times \boldsymbol{t}(\boldsymbol{x},\boldsymbol{n})\,\mathrm{d}\boldsymbol{s} = 0,$$

  and the law of conservation of mass holds for every volume V,
- *for each $\boldsymbol{n} \in \mathcal{N}_3$ the traction $\boldsymbol{t}(\cdot, \boldsymbol{n})$ is continuously differentiable on $\overline{\Omega}$,*
- *for each $\boldsymbol{x} \in \overline{\Omega}$ the traction $\boldsymbol{t}(\boldsymbol{x}, \cdot)$ is continuous on $\mathcal{N}_3$.*

Then there exists a continuously differentiable second-order tensor field, $\boldsymbol{\sigma}$, the so-called stress, such that

1. $\boldsymbol{t}(\boldsymbol{x},\boldsymbol{n}) = \boldsymbol{\sigma}(\boldsymbol{x})\boldsymbol{n} \quad \forall\, \boldsymbol{x} \in \Omega,\ \forall\, \boldsymbol{n} \in \mathcal{S}_3,$
2. $\boldsymbol{\sigma}(\boldsymbol{x})$ *is symmetric* $\quad \forall \boldsymbol{x} \in \overline{\Omega},$
3. $\operatorname{div} \boldsymbol{\sigma}(\boldsymbol{x}) = -\boldsymbol{f}(\boldsymbol{x})$ *is satisfied* $\forall\, \boldsymbol{x} \in \Omega.$

With respect to $\mathcal{B}_{\mathrm{Lin}}$ the stress tensor $\boldsymbol{\sigma}(\boldsymbol{x})$ has the representation $\boldsymbol{\sigma}(\boldsymbol{x}) = \sigma_{ij}(\boldsymbol{x})\boldsymbol{e}_i \otimes \boldsymbol{e}_j$. Thereby, the components $\sigma_{ii}(\boldsymbol{x})$ for $i = 1,2,3$ (normal stresses) represent the stresses which are normal to the surface, and $\sigma_{ij}(\boldsymbol{x})$ with $i \neq j$ (shear stresses) those which lie within the surface; see Fig. 2.1 for an illustration.

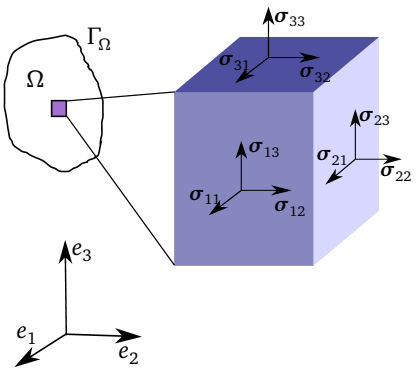

Figure 2.1.: Components of the stress tensor, $\boldsymbol{\sigma}(\boldsymbol{x})$, in material point $\boldsymbol{x} \in \Omega$. Components are given with respect to the basis $\mathcal{B}_{\mathrm{Lin}}$; the purple cuboid represents the material point $\boldsymbol{x} \in \Omega$.

2.2.2 Equations of motion, equations of equilibrium

Let $t \in [0, T_e]$, where $T_e \geq 0$, denote the time in the following. For a time-dependent body or volume force, $\boldsymbol{f} = \boldsymbol{f}(\boldsymbol{x}, t)$, Newton's second law applies. According to this law, a material point $\boldsymbol{x}$ experiences an acceleration $\partial^2 \boldsymbol{u}/\partial t^2$ which is proportional to the net force acting on the material. Expressing the net force based on the stress and the volume force, Newton's second law reads

$$\operatorname{div}_{\boldsymbol{x}} \boldsymbol{\sigma}(\boldsymbol{x}, t) = -\boldsymbol{f}(\boldsymbol{x}, t) + \rho(\boldsymbol{x}, t) \frac{\partial^2 \boldsymbol{u}}{\partial t^2}(\boldsymbol{x}, t), \quad \boldsymbol{x} \in \Omega,\, t \in [0, T_e]. \tag{2.42}$$

Here, ρ is the density of the material and $\operatorname{div}_{\boldsymbol{x}} \boldsymbol{\sigma}$ denotes the divergence of $\boldsymbol{\sigma}$ with respect to $\boldsymbol{x}$. Equations (2.42) are also called equations of motion.

If the material is in equilibrium, then $\frac{\partial^2 \boldsymbol{u}}{\partial t^2} = 0$, and Eq. (2.42) simplifies to

$$\operatorname{div} \boldsymbol{\sigma}(\boldsymbol{x}) = -\boldsymbol{f}(\boldsymbol{x}), \quad \boldsymbol{x} \in \Omega. \tag{2.43}$$

The latter equations are referred to as the equations of equilibrium.

2.2.3 Hooke's law, Hooke's inverse law, strain energy

The equations of equilibrium or motion do not yet completely characterize the behavior of a material. We, moreover, need to specify the relationship between stress and strain. In linear elasticity this relationship is linear and is given by Hooke's law. It reads in tensor and index notation, respectively,

$$\boldsymbol{\sigma}(\boldsymbol{x}) = \boldsymbol{C}(\boldsymbol{x}) : \boldsymbol{\varepsilon}(\boldsymbol{x}), \quad \sigma_{ij}(\boldsymbol{x}) = C_{ijkl}(\boldsymbol{x})\, \varepsilon_{kl}(\boldsymbol{x}), \tag{2.44}$$

where $\boldsymbol{C}(\boldsymbol{x})$ is a fourth-order tensor, usually called stiffness tensor or elasticity tensor. We sometimes write $\boldsymbol{\sigma}(\boldsymbol{u}) := \boldsymbol{C} : \boldsymbol{\varepsilon}(\boldsymbol{u})$ in order to emphasize the dependency of $\boldsymbol{\sigma}$ on the displacement $\boldsymbol{u}$. It is worth to note here, that Eq. (2.44) is a matrix-vector relation, when representing the tensors, $\boldsymbol{\sigma}(\boldsymbol{x})$, $\boldsymbol{C}(\boldsymbol{x})$ and $\boldsymbol{\varepsilon}(\boldsymbol{x})$, using one of the three notations introduced in Section 2.1.3 (Kelvin, Voigt and Mandel notation), see Appendix A for details.

If the stiffness tensor $\boldsymbol{C}(\boldsymbol{x})$ is the same for all $\boldsymbol{x} \in \Omega$, the material is referred to as homogeneous, otherwise as heterogeneous. The properties of homogeneity and heterogeneity depend on the length scale. For example, concrete is a homogeneous material at the coarse scale, while when zoomed inside, it is heterogeneous.

The strain energy of a linear elastic material occupying the domain Ω is denoted by $W_{\boldsymbol{\varepsilon}}$. It is defined as the energy stored in an linear elastic body due to deformation, and is given by

Definition 2.2.2 (Strain energy (density)) *The strain energy is defined by*

$$W_{\boldsymbol{\varepsilon}} = \int_{\Omega} U_{\boldsymbol{\varepsilon}}(\boldsymbol{x})\, \mathrm{d}\boldsymbol{x}, \tag{2.45}$$

where $U_{\boldsymbol{\varepsilon}}(\boldsymbol{x})$ is the strain energy density given by

$$U_{\boldsymbol{\varepsilon}}(\boldsymbol{x}) = \frac{1}{2} \boldsymbol{\varepsilon}(\boldsymbol{x}) : \boldsymbol{C}(\boldsymbol{x}) : \boldsymbol{\varepsilon}(\boldsymbol{x}). \tag{2.46}$$

For any $\boldsymbol{x} \in \Omega$ and $\boldsymbol{\varepsilon}(\boldsymbol{x}) \neq 0$ the strain energy density has to be positive, i.e. $U_{\boldsymbol{\varepsilon}}(\boldsymbol{x}) > 0$. Thus it is required that the stiffness tensor $\boldsymbol{C}(\boldsymbol{x})$ is positive definite and hence invertible. We denote the inverse of $\boldsymbol{C}(\boldsymbol{x})$ by $\boldsymbol{M}(\boldsymbol{x})$ and call it compliance tensor. This tensor is positive definite, since the inverse of a positive definite tensor is positive definite too. Hooke's inverse law reads in tensor and index notation, respectively,

$$\boldsymbol{\varepsilon}(\boldsymbol{x}) = \boldsymbol{M}(\boldsymbol{x}) : \boldsymbol{\sigma}(\boldsymbol{x}), \quad \varepsilon_{ij}(\boldsymbol{x}) = M_{ijkl}(\boldsymbol{x})\, \varepsilon_{kl}(\boldsymbol{x}). \tag{2.47}$$

2.2.4 Symmetries of the stiffness tensor

We consider the stiffness tensor, the strain and the stress tensor in some fix arbitrary material point $\boldsymbol{x} \in \Omega$. To this end, we omit in this section the tensor's dependency on $\boldsymbol{x}$.

Any stiffness tensor obeys minor and major symmetries, for a proof see below. Moreover, the stiffness tensor might exhibit further symmetries, these depend on the given material. To this end, we consider the symmetry groups of a stiffness tensor (Bóna et al., 2004; Buryachenko, 2007) and classify the stiffness tensor according to these as either isotropic, transverse isotropic, orthotropic or anisotropic. For each such class we give the explicit form of the stiffness tensor (Bower, 2010).

Minor and major symmetries

For arbitrary fix indices, $o, p \in \{1,2,3\}$, we define $\boldsymbol{\varepsilon^{op}} = \delta_{io}\delta_{jp}$ where $i, j \in \{1,2,3\}$. Moreover, we set $\boldsymbol{\sigma^{op}} = \boldsymbol{C} : \boldsymbol{\varepsilon^{op}}$. We assume that $\boldsymbol{\sigma^{op}}$ is a stress tensor, therefore, $\boldsymbol{\sigma^{op}}$ needs to be symmetric (Theorem 2.2.1). Then

$$0 = \sigma_{ij}^{op} - \sigma_{ji}^{op} = C_{ijkl}\varepsilon_{kl}^{op} - C_{jikl}\varepsilon_{kl}^{op} = C_{ijop} - C_{jiop}.$$

Since o and p where chosen arbitrary, the stiffness tensor $\boldsymbol{C}$ obeys the symmetries $C_{ijkl} = C_{jikl}$.

Major symmetries of the stiffness tensor ($C_{ijkl} = C_{klij}$) follows considering the stiffness tensor as a function of the strain energy density $U_{\boldsymbol{\varepsilon}}$ (see Definition 2.2.2), i.e.

$$C_{ijkl} = \frac{\partial^2 U_{\boldsymbol{\varepsilon}}}{\partial \varepsilon_{ij} \partial \varepsilon_{kl}}.$$

Assuming that $U_{\boldsymbol{\varepsilon}}$ is smooth, the order of the differentiation does not matter. Hence, $C_{ijkl} = C_{klij}$.

Finally, by virtue of the major symmetries and the symmetry $C_{ijkl} = C_{jikl}$, we have

$$C_{ijkl} = C_{klij} = C_{lkij} = C_{ijlk}. \tag{2.48}$$

In summary, $\boldsymbol{C}$ obeys minor and major symmetries. These symmetries reduces the number of different components of $\boldsymbol{C}$ from $3^4 = 81$ to 21.

Isotropy, transverse isotropy, orthotropy, anisotropy

Any orthogonal tensor $\boldsymbol{q} \in \mathrm{Sym}(\mathbb{R}^3)$ is called a symmetry of $\boldsymbol{C}$, if

$$C_{ijkl} = q_{im}q_{jn}q_{ko}q_{lp}C_{mnop}. \tag{2.49}$$

The set of symmetries $\boldsymbol{q}$ of $\boldsymbol{C}$ forms a group which is referred to as the symmetry group of $\boldsymbol{C}$, denoted $\mathcal{G}_{\boldsymbol{C}}$. Note that $\mathcal{G}_{\boldsymbol{C}}$ is a group with respect to simple contraction, that is two elements $\boldsymbol{q}$, $\tilde{\boldsymbol{q}}$ of $\mathcal{G}_{\boldsymbol{C}}$ form a new one by $\boldsymbol{q}\,\tilde{\boldsymbol{q}}$. Moreover, $\mathcal{G}_{\boldsymbol{C}}$ is a subgroup of $\mathcal{O}$, the group of orthogonal second-order tensors. Any symmetry group $\mathcal{G}_{\boldsymbol{C}}$ contains the unit element $\mathbf{id}$, as well as the point symmetry, $-\mathbf{id}$. Moreover, it possibly contains the elements

$$\mathbf{rot}(\alpha, \boldsymbol{e}): \text{ rotation by an angle } 0 < \alpha \leq \pi \text{ around an axis in direction } \boldsymbol{e},$$
$$\mathbf{ref}(\boldsymbol{e}): \text{ reflection about the plane with normal vector } \boldsymbol{e},$$

where $\boldsymbol{e} \in \{\boldsymbol{e}_1, \boldsymbol{e}_2, \boldsymbol{e}_3\}$ denotes the standard unit basis vectors of $\mathbb{R}^3$. Depending on the symmetry group, the stiffness tensor $\boldsymbol{C}$ is characterized by a specific number of parameters, the so-called elastic constants.

Here, we consider stiffness tensors that have 2, 5, 9 or 21 elastics constants; the corresponding stiffness tensors are said to be isotropic, transversely isotropic, orthotropic or anisotropic, respectively. The corresponding symmetries we call isotropy, transverse isotropy, orthotropy and anisotropy, respectively. It is important to keep in mind that all these symmetries depend on the length scale. For instance, a material which is anisotropic on one length scale may be isotropic on another (usually coarser) length scale.

Isotropy
The symmetry group of an isotropic stiffness tensor is given by $\mathcal{G}_{\boldsymbol{C}} = \mathcal{O}$. Thus, the elastic properties of an isotropic material are independent of the direction. The stiffness tensor of an isotropic material is characterized by the two Lamé coefficients, λ and μ, and reads in Voigt notation

$$\boldsymbol{C} = \begin{bmatrix} \lambda+2\mu & \lambda & \lambda & 0 & 0 & 0 \\ \lambda & \lambda+2\mu & \lambda & 0 & 0 & 0 \\ \lambda & \lambda & \lambda+2\mu & 0 & 0 & 0 \\ 0 & 0 & 0 & \mu & 0 & 0 \\ 0 & 0 & 0 & 0 & \mu & 0 \\ 0 & 0 & 0 & 0 & 0 & \mu \end{bmatrix}. \tag{2.50}$$

Besides the Lamé coefficients, other elastic constants, such as the Young's modulus E and the Poisson's ratio ν are used to characterize $\boldsymbol{C}$. While E gives the ratio of stress to strain along an axis, the Poisson's ratio ν is the ratio of the strain normal to the applied load to the strain in direction of the applied load. Besides the Young's modulus and the Poisson's ratio we often use the bulk and the shear modulus, denoted by K and G, respectively. The bulk modulus K measures the material's resistance to uniform compression (inward forces) and the shear modulus, G, gives the ratio of shear stress to the shear strain. Formulas for converting (λ, μ) to (E, ν) or (K, G), are given in Bower (2010).

Materials that are isotropic at the coarse scale are, for instance, glass, metal or concrete.

Transverse isotropy
Transverse isotropic stiffness tensors have the symmetry group $\mathcal{G}_{\boldsymbol{C}} = \{\pm\mathbf{id}, \pm\mathbf{rot}(\alpha, \boldsymbol{e}_i)\}$ with $0 < \alpha \leq \pi$ and $\boldsymbol{e}_i$ one of the three vectors of $\{\boldsymbol{e}_1, \boldsymbol{e}_2, \boldsymbol{e}_3\}$. Considering $\boldsymbol{e}_3$ the symmetry axis, rotating a transverse isotropic material about this axis by some arbitrary angle α, its stiffness tensor will not change. The stiffness tensor of a transverse isotropic material is characterized by the following five elastic constants: the Young's modulo in direction of $\boldsymbol{e}_1$ and $\boldsymbol{e}_3$, denoted by E_1 and E_3, respectively, the Poisson's ratio in the $\boldsymbol{e}_1\boldsymbol{e}_2$-plane and the $\boldsymbol{e}_1\boldsymbol{e}_3$-plane, denoted by ν_{12} and ν_{13}, respectively, and the shear modulus in the $\boldsymbol{e}_2\boldsymbol{e}_3$-plane, denoted by G_{23}.

The stiffness tensor reads in Voigt notation

$$\boldsymbol{C} = \begin{bmatrix} C_{11} & C_{12} & C_{13} & 0 & 0 & 0 \\ C_{12} & C_{11} & C_{13} & 0 & 0 & 0 \\ C_{13} & C_{13} & C_{33} & 0 & 0 & 0 \\ 0 & 0 & 0 & C_{44} & 0 & 0 \\ 0 & 0 & 0 & 0 & C_{44} & 0 \\ 0 & 0 & 0 & 0 & 0 & \dfrac{C_{11}-C_{12}}{2} \end{bmatrix}, \tag{2.51}$$

with

$$C_{11} = \frac{E_1 - E_3\nu_{13}^2}{A}, \quad C_{12} = \frac{E_1\nu_{12} + E_3\nu_{13}^2}{A}, \quad C_{13} = \frac{(1+\nu_{12})\,E_3\,\nu_{13}}{A}, \quad C_{33} = \frac{E_3 - E_3\nu_{12}^2}{A}, \quad C_{44} = G_{23},$$

where $\quad A = -\dfrac{(1+\nu_{12})\cdot(E_1(\nu_{12}-1) + 2\,E_3\,\nu_{13}^2)}{E_1}.$

Finally, we introduce an essential parameter quantifying the rate of anisotropy of a transverse isotropic elastic material. We call this parameter the anisotropy ratio, denote it by AR, and define $\mathrm{AR} = C_{33}/C_{11}$.

Important material which have the former described type of symmetry at the coarse scale are composites that consist of uniaxially-aligned fibres embedded in some homogeneous matrix. These composites are designed to withstand high loads in the direction parallel to the fibres. One such example of this type of composite is the building unit of bone, i.e. the mineralized collagen fibril, see Chapter 6.

Orthotropy
A material is said to be orthotropic, if it has the symmetry group $\mathcal{G}_{\boldsymbol{C}} = \{\pm\mathbf{id}, \pm\mathbf{ref}(\boldsymbol{e}_1), \pm\mathbf{ref}(\boldsymbol{e}_2), \pm\mathbf{ref}(\boldsymbol{e}_3)\}$. Due to the symmetries in $\mathcal{G}_{\boldsymbol{C}}$, we can mirror the material with respect to the $\boldsymbol{e}_1\boldsymbol{e}_2$, $\boldsymbol{e}_1\boldsymbol{e}_3$ and $\boldsymbol{e}_2\boldsymbol{e}_3$-plane without changing its elastic properties. In order to fully characterize an orthotropic stiffness tensor $\boldsymbol{C}$ it requires nine independent elastic constants. These are: the Young's moduli in direction $\boldsymbol{e}_1$, $\boldsymbol{e}_2$ or $\boldsymbol{e}_3$, denoted, E_1, E_2 and E_3, respectively, the Poisson's ratios in the $\boldsymbol{e}_1\boldsymbol{e}_2$, $\boldsymbol{e}_1\boldsymbol{e}_3$ and $\boldsymbol{e}_2\boldsymbol{e}_3$-plane, denoted, respectively, ν_{12}, ν_{13} and ν_{23}, and, finally, the shear moduli in the $\boldsymbol{e}_1\boldsymbol{e}_2$, $\boldsymbol{e}_1\boldsymbol{e}_3$ and $\boldsymbol{e}_2\boldsymbol{e}_3$-plane, denoted, respectively, G_{12}, G_{13} and G_{23}. Based on the elastic constants we can give the stiffness tensor of an orthotropic material in Voigt notation as

$$\boldsymbol{C} = \begin{bmatrix} C_{11} & C_{12} & C_{13} & 0 & 0 & 0 \\ C_{12} & C_{22} & C_{23} & 0 & 0 & 0 \\ C_{13} & C_{23} & C_{33} & 0 & 0 & 0 \\ 0 & 0 & 0 & C_{44} & 0 & 0 \\ 0 & 0 & 0 & 0 & C_{55} & 0 \\ 0 & 0 & 0 & 0 & 0 & C_{66} \end{bmatrix}, \tag{2.52}$$

with

$$C_{11} = \frac{1-\nu_{23}\nu_{32}}{E_2 E_3 B}, \quad C_{12} = \frac{\nu_{21}+\nu_{31}\nu_{23}}{E_2 E_3 B}, \quad C_{13} = \frac{\nu_{31}+\nu_{21}\nu_{32}}{E_2 E_3 B}, \quad C_{22} = \frac{1-\nu_{31}\nu_{13}}{E_1 E_3 B},$$
$$C_{23} = \frac{\nu_{32}+\nu_{31}\nu_{12}}{E_1 E_3 B}, \quad C_{33} = \frac{1-\nu_{12}\nu_{21}}{E_1 E_2 B}, \quad C_{44} = G_{23}, \quad C_{55} = G_{13}, \quad C_{66} = G_{12},$$

where $$B = \frac{(1-\nu_{12}\nu_{21}-\nu_{23}\nu_{32}-\nu_{13}\nu_{31}-2\nu_{12}\nu_{23}\nu_{31})}{E_1 E_2 E_3}.$$

A well-known material that is orthotropic at the coarse scale is wood.

Anisotropy
Anisotropic materials have the smallest symmetry group, that is $\mathcal{G}_{\boldsymbol{C}} = \{\pm\mathbf{id}\}$. Their stiffness tensor is fully occupied and is given in Voigt notation by

$$\boldsymbol{C} = \begin{bmatrix} C_{11} & C_{12} & C_{13} & C_{14} & C_{15} & C_{16} \\ C_{12} & C_{22} & C_{23} & C_{24} & C_{25} & C_{26} \\ C_{13} & C_{23} & C_{33} & C_{34} & C_{35} & C_{36} \\ C_{14} & C_{24} & C_{34} & C_{44} & C_{45} & C_{46} \\ C_{15} & C_{25} & C_{35} & C_{45} & C_{55} & C_{56} \\ C_{16} & C_{26} & C_{36} & C_{46} & C_{56} & C_{66} \end{bmatrix}. \tag{2.53}$$

Materials which have this type of symmetry at the coarse scale are bone or brushed metals.

2.2.5 Boundary value problems in static and dynamic linear elasticity

We present different boundary value problems considered in this thesis.

The equations of static linear elasticity include the equations of equilibrium, Hooke's law and the equations for the linearized strain. They read

Problem 2.2.3 (Equations of static linear elasticity) *Find* $\boldsymbol{u} = \boldsymbol{u}(\boldsymbol{x})$ *such that*

$$\begin{aligned} \operatorname{div} \boldsymbol{\sigma}(\boldsymbol{x}) &= -\boldsymbol{f}(\boldsymbol{x}), \quad \boldsymbol{x} \in \Omega, \\ \boldsymbol{\sigma}(\boldsymbol{x}) &= \boldsymbol{C}(\boldsymbol{x}) : \boldsymbol{\varepsilon}(\boldsymbol{x}), \\ \boldsymbol{\varepsilon}(\boldsymbol{x}) &= \frac{1}{2}\left(\nabla \boldsymbol{u}(\boldsymbol{x}) + (\nabla \boldsymbol{u}(\boldsymbol{x}))^T\right), \end{aligned}$$

where $\boldsymbol{\sigma}$ *is the stress,* $\boldsymbol{f}$ *some volume force applied to domain* Ω*,* $\boldsymbol{C}$ *the stiffness tensor and* $\boldsymbol{\varepsilon}$ *the strain, see Sections 2.2.1 and 2.2.3 for a definition of these quantities.*

We supplement Problem 2.2.3 with either displacement or traction boundary conditions, i.e. we consider the following boundary value problems

Problem 2.2.4 (Displacement boundary value problem in static linear elasticity)
Find $\boldsymbol{u} = \boldsymbol{u}(\boldsymbol{x})$ *such that* $\boldsymbol{u}$ *satisfies Problem 2.2.3 supplemented with displacement boundary conditions*

$$\boldsymbol{u}(\boldsymbol{x}) = \boldsymbol{u}_0(\boldsymbol{x}), \quad \boldsymbol{x} \in \Gamma_\Omega, \tag{2.54}$$

where $\boldsymbol{u}_0 : \Gamma_\Omega \to \mathbb{R}^3$.

Problem 2.2.5 (Traction boundary value problem in static linear elasticity)
Find $\boldsymbol{u} = \boldsymbol{u}(\boldsymbol{x})$ *such that* $\boldsymbol{u}$ *satisfies Problem 2.2.3 supplemented with traction boundary conditions*

$$\boldsymbol{\sigma}(\boldsymbol{x})\boldsymbol{n}(\boldsymbol{x}) = \boldsymbol{g}(\boldsymbol{x}), \quad \boldsymbol{x} \in \Gamma_\Omega, \tag{2.55}$$

and the integral constraints

$$\mathcal{M}_\Omega(\boldsymbol{u}(\boldsymbol{x})) = \boldsymbol{b}. \tag{2.56}$$

Here, $\boldsymbol{n}$ *is the outward normal in point* $\boldsymbol{x} \in \Gamma_\Omega$*,* $\boldsymbol{g} : \Gamma_\Omega \to \mathbb{R}^3$*, and* $\boldsymbol{b}$ *is an arbitrary constant vector in* $\mathbb{R}^3$.

Besides displacement boundary conditions (2.54) and traction boundary conditions (2.55), we supplement Problem 2.2.3 also with periodic boundary conditions. These boundary conditions arise in periodic homogenization, see Chapter 3. In that respect, we consider a brick-shaped domain $V = (0, l_1) \times (0, l_2) \times (0, l_3)$ with $V \subset \Omega \subset \mathbb{R}^3$ and $0 < l_i \in \mathbb{R}$ for $i = 1, 2, 3$. Moreover, we enforce the displacement to be V-periodic (Section 2.1.2). In summary, our periodic boundary value problem reads

Problem 2.2.6 (Periodic boundary value problem in static linear elasticity) *Find* $\boldsymbol{u} = \boldsymbol{u}(\boldsymbol{x})$ *such that* $\boldsymbol{u}$ *satisfies Problem 2.2.3 supplemented with periodic boundary conditions*

$$\boldsymbol{u}(\boldsymbol{x}) - \boldsymbol{p}^{kl}(\boldsymbol{x}) \quad V\text{-periodic}, \tag{2.57}$$

and the integral constraints

$$\mathcal{M}_V(\boldsymbol{u}(\boldsymbol{x}) - \boldsymbol{p}^{kl}(\boldsymbol{x})) = 0, \tag{2.58}$$

where $p_m^{kl}(\boldsymbol{x}) := x_l\, \delta_{mk}$ *for* $k, l, m = 1, 2, 3$ *and* $\boldsymbol{x} \in V$.

Problems 2.2.4, 2.2.5 and 2.2.6 have a weak solution $\boldsymbol{u}$ in some appropriate function space, see Section 2.3 for details.

Although this thesis deals primarily with the equations of static linear elasticity, we also consider the equations of dynamic linear elasticity. The latter include the equations of motion, Hooke's law and the equations for the linearized strain. Supplemented with initial conditions and boundary conditions these equations read

Problem 2.2.7 (Initial displacement-boundary value problem in dynamic linear elasticity)
Find $\boldsymbol{u} = \boldsymbol{u}(\boldsymbol{x})$ *such that*

$$\begin{aligned}
\operatorname{div} \boldsymbol{\sigma}(\boldsymbol{x},t) &= -\boldsymbol{f}(\boldsymbol{x},t) + \rho(\boldsymbol{x}) \frac{\partial^2 \boldsymbol{u}}{\partial t^2}(\boldsymbol{x},t), \quad (\boldsymbol{x},t) \in \Omega \times [0,T_e], \\
\boldsymbol{\sigma}(\boldsymbol{x},t) &= \boldsymbol{C}(\boldsymbol{x}) : \boldsymbol{\varepsilon}(\boldsymbol{x},t), \\
\boldsymbol{\varepsilon}(\boldsymbol{x},t) &= \frac{1}{2}\left(\nabla \boldsymbol{u}(\boldsymbol{x},t) + (\nabla \boldsymbol{u}(\boldsymbol{x},t))^T\right), \\
\boldsymbol{u}(\boldsymbol{x},0) &= \boldsymbol{u}_0(\boldsymbol{x}), \quad \frac{\partial \boldsymbol{u}}{\partial t}(\boldsymbol{x},0) = \boldsymbol{v}(\boldsymbol{x}), \quad \boldsymbol{x} \in \Omega, \\
\boldsymbol{u}(\boldsymbol{x},t) &= \boldsymbol{u}_1(\boldsymbol{x},t), \quad (\boldsymbol{x},t) \in \Gamma_\Omega \times [0,T_e]
\end{aligned} \tag{2.59}$$

where $\boldsymbol{\sigma}$ *is the stress,* $\boldsymbol{f}$ *some volume force applied to domain* Ω*,* ρ *the density,* T_e *a final time,* $\boldsymbol{\varepsilon}$ *the strain, and* $\boldsymbol{u}_0, \boldsymbol{v} : \Omega \to \mathbb{R}^3$ *and* $\boldsymbol{u}_1 : \Gamma_\Omega \times [0,T_e] \to \mathbb{R}^3$*.*

In this thesis we will consider Problem 2.2.7 in a specific setting. We assume that the volume force $\boldsymbol{f}$ and the displacement $\boldsymbol{u}$ are time-harmonic, i.e. they take the form $\tilde{\boldsymbol{f}}(\boldsymbol{x})\exp(i\omega t)$ and $\tilde{\boldsymbol{u}}(\boldsymbol{x})\exp(i\omega t)$, where ω denotes the frequency, respectively. Under this assumptions Problem 2.2.7 simplifies to some time-independent boundary value problem, the so-called Navier's equation for time-harmonic waves. Theorems concerning the existence and uniqueness of solutions to this boundary value problem are given, for instance, in Eringen and Suhubi (1975).

2.3 Weak formulation of boundary value problems in static linear elasticity

In this section we present the weak formulation of the displacement, the traction and the periodic boundary value problem in static linear elasticity (Problems 2.2.4, 2.2.5 and 2.2.6). In Section 2.3.1 we introduce the function spaces in which these weak formulations are posed, the Sobolev spaces. Then, we state these weak formulations explicitly in Section 2.3.2. Finally, in Section 2.3.3 we briefly review theorems concerning the existence and uniqueness of weak solutions to these weak formulations.

For a general introduction to Sobolev spaces we refer the reader to Ciarlet (2013). Existence and uniqueness results stated in Section 2.3.3 can be viewed in detail in Oleĭnik et al. (1992) and Cioranescu and Donato (1999).

In what follows, we assume that $\Omega \subset \mathbb{R}^3$ is a domain. Recall that this means that Ω is a bounded connected open non-empty subset of $\mathbb{R}^3$, which has a Lipschitz-continuous boundary Γ_Ω. Moreover, we consider the boundary Γ_Ω to have a positive measure, and assume that there is given a brick-shaped subset V of Ω.

2.3.1 Lebesgue and Sobolev spaces

We use the standard Lebesgue space $L^2(\Omega, \mathbb{R}^n)$, that is

$$L^2(\Omega,\mathbb{R}^n) := \left\{ \boldsymbol{u} \,\middle|\, \boldsymbol{u} : \boldsymbol{x} \in \Omega \mapsto \boldsymbol{u}(\boldsymbol{x}) = \left(u_1,\dots,u_n\right)^T \in \mathbb{R}^n \text{ such that } \int_\Omega \boldsymbol{u}(\boldsymbol{x}) \cdot \boldsymbol{u}(\boldsymbol{x})\,\mathrm{d}\boldsymbol{x} = \sum_{i=1}^n \int_\Omega u_i^2\,\mathrm{d}\boldsymbol{x} < \infty \right\}. \tag{2.60}$$

Usually, we consider $L^2(\Omega, \mathbb{R}^n)$ for $n = 1, 3$. Equipped with the norm and the scalar product

$$\|\boldsymbol{u}\|_0 := \sqrt{\langle \boldsymbol{u}, \boldsymbol{u} \rangle_0}, \qquad \text{and} \qquad \langle \boldsymbol{u}, \boldsymbol{v} \rangle_0 := \int_\Omega \boldsymbol{u} \cdot \boldsymbol{v} \, \mathrm{d}\boldsymbol{x} = \sum_{i=1}^{n} \int_\Omega u_i \, v_i \, \mathrm{d}\boldsymbol{x} \quad \forall \boldsymbol{v} \in L^2(\Omega, \mathbb{R}^n), \tag{2.61}$$

the set $L^2(\Omega, \mathbb{R}^n)$ is a Hilbert space.

Let there be given a multiindex $\alpha = (\alpha_1, \alpha_2, \alpha_3) \in \mathbb{N}^3$ with $|\alpha| := \sum_{i=1}^{3} \alpha_i \geq 1$. We call $v \in L^2(\Omega, \mathbb{R})$ the αth weak partial derivative of $u \in L^2(\Omega, \mathbb{R})$, if

$$\int_\Omega v \, w \, \mathrm{d}\boldsymbol{x} = (-1)^{|\alpha|} \int_\Omega u \, \frac{\partial^{|\alpha|} w}{\partial \boldsymbol{x}^\alpha} \, \mathrm{d}\boldsymbol{x} \quad \forall \, w \in C_c^\infty(\Omega, \mathbb{R}). \tag{2.62}$$

Here, $C_c^\infty(\Omega, \mathbb{R})$ denotes the set of functions $h : \Omega \to \mathbb{R}$ which are continuous, infinitely differentiable and have compact support in Ω. If v exists, it is uniquely defined by relation (2.62) and is denoted $\frac{\partial^{|\alpha|} u}{\partial \boldsymbol{x}^\alpha}$. For multi-dimensional valued functions $\boldsymbol{u} \in L^2(\Omega, \mathbb{R}^n)$ we define the αth weak partial derivative of $\boldsymbol{u}$ componentwise and denote it by $\frac{\partial^{|\alpha|} \boldsymbol{u}}{\partial \boldsymbol{x}^\alpha}$.

Analogously as for continuous and sufficiently smooth functions in Section 2.1.2, we introduce the nabla operator ∇ for functions $\boldsymbol{u} \in L^2(\Omega, \mathbb{R}^n)$. Thereby, we replace the standard derivative by the weak derivative, defined by Eq. (2.62).

Besides the Lebesgue space $L^2(\Omega, \mathbb{R}^n)$, we use the Sobolev spaces

$$H^m(\Omega, \mathbb{R}) := \left\{ u \,\middle|\, u \in L^2(\Omega, \mathbb{R}), \, \frac{\partial^{|\alpha|} u}{\partial \boldsymbol{x}^\alpha} \in L^2(\Omega, \mathbb{R}) \quad \forall |\alpha| \leq m \right\}, \tag{2.63}$$

$$H^m(\Omega, \mathbb{R}^n) := \left(H^m(\Omega, \mathbb{R}) \right)^n, \tag{2.64}$$

where $m, n \in \mathbb{N}$ and $m \geq 1$. The by far most important Sobolev space in this thesis is $H^1(\Omega, \mathbb{R}^3)$. Defining a scalar product on $H^1(\Omega, \mathbb{R}^n)$ by

$$\langle \boldsymbol{u}, \boldsymbol{v} \rangle_1 := \int_\Omega \boldsymbol{u} \cdot \boldsymbol{v} \, \mathrm{d}\boldsymbol{x} + \int_\Omega \nabla \boldsymbol{u} : \nabla \boldsymbol{v} \, \mathrm{d}\boldsymbol{x}, \tag{2.65}$$

the set $H^1(\Omega, \mathbb{R}^n)$ is a Hilbert space with respect to the induced norm $\|\boldsymbol{u}\|_1 = \sqrt{\langle \boldsymbol{u}, \boldsymbol{u} \rangle_1}$. Besides the norm $\|\cdot\|_1$, we equip $H^1(\Omega, \mathbb{R}^n)$ with the semi-norm

$$|\boldsymbol{u}|_1 = \sqrt{\int_\Omega \nabla \boldsymbol{u} : \nabla \boldsymbol{u} \, \mathrm{d}\boldsymbol{x}} \quad . \tag{2.66}$$

A norm and a semi-norm on $H^m(\Omega, \mathbb{R}^n)$, where $m \geq 2$, are given by

$$\|\boldsymbol{u}\|_m := \left(\sum_{|\alpha| \leq m} \left\| \frac{\partial^{|\alpha|} \boldsymbol{u}}{\partial \boldsymbol{x}^\alpha} \right\|_0^2 \right)^{\frac{1}{2}}, \qquad |\boldsymbol{u}|_m := \left(\sum_{|\alpha| = m} \left\| \frac{\partial^{|\alpha|} \boldsymbol{u}}{\partial \boldsymbol{x}^\alpha} \right\|_0^2 \right)^{\frac{1}{2}}, \tag{2.67}$$

respectively. The set $H^m(\Omega, \mathbb{R}^n)$ is a Hilbert space with respect to the norm $\|\cdot\|_m$.

In what follows, we want to consider boundary values of functions $\boldsymbol{u} \in H^1(\Omega, \mathbb{R}^n)$. To this end, we introduce the trace operator and the trace

Theorem 2.3.1 *Let denote $C^0(\overline{\Omega}, \mathbb{R}^n)$ the set of continuous functions $\boldsymbol{u} : \overline{\Omega} \to \mathbb{R}^n$. There exists a linear continuous operator γ with*

$$\gamma : H^1(\Omega, \mathbb{R}^n) \to H^{1/2}(\Gamma_\Omega, \mathbb{R}^n), \quad \gamma : \boldsymbol{u} \mapsto \gamma(\boldsymbol{u}),$$

such that for any $\boldsymbol{u} \in H^1(\Omega, \mathbb{R}^n) \cap C^0(\overline{\Omega}, \mathbb{R}^n)$ one has $\gamma(\boldsymbol{u})[\boldsymbol{x}] = \boldsymbol{u}(\boldsymbol{x})$ for all $\boldsymbol{x} \in \Gamma_\Omega$. We denote by $H^{1/2}(\Gamma_\Omega, \mathbb{R}^n)$ the set that contains the functions $\gamma(\boldsymbol{u})$. Equipped with the norm

$$\|\boldsymbol{v}\|_{1/2} = \inf\left\{\|\boldsymbol{u}\|_1 \mid \boldsymbol{u} \in H^1(\Omega, \mathbb{R}^n), \boldsymbol{v} = \gamma(\boldsymbol{u})\right\} \tag{2.68}$$

the set $H^{1/2}(\Gamma_\Omega, \mathbb{R}^n)$ is a Hilbert space. The operator γ and the function $\gamma(\boldsymbol{u})$ are referred to as trace operator and trace, respectively.

Now, using the trace of some function $\boldsymbol{u} \in H^1(\Omega, \mathbb{R}^n)$ we can describe the boundary values of $\boldsymbol{u}$ through the function $\gamma(\boldsymbol{u})$ in $H^{1/2}(\Gamma_\Omega, \mathbb{R}^n)$. Note that, as it is customary, we shall henceforth omit the symbol γ and write, for instance, "$\boldsymbol{u} = \boldsymbol{u}_0$, $\boldsymbol{x} \in \Gamma_\Omega$" while strictly meaning "$\gamma(\boldsymbol{u}) = \boldsymbol{u}_0$" where $\boldsymbol{u}_0 \in H^{1/2}(\Gamma_\Omega, \mathbb{R}^n)$.

An important space in the context of displacement boundary conditions is $H^1_{\Gamma_\Omega}(\overline{\Omega}, \mathbb{R}^n)$. This space contains all functions which satisfy displacement boundary conditions, i.e.

$$H^1_{\Gamma_\Omega}(\overline{\Omega}, \mathbb{R}^3) := \left\{\boldsymbol{u} | \boldsymbol{u} \in H^1(\Omega, \mathbb{R}^n), \boldsymbol{u} = \boldsymbol{u}_0 \text{ for } \boldsymbol{x} \in \Gamma_\Omega, \boldsymbol{u}_0 \in H^{1/2}(\Gamma_\Omega, \mathbb{R}^n)\right\} \tag{2.69}$$

Finally, we consider function spaces suitable when periodic boundary conditions apply to the boundary of V. To this end, we introduce

$$C^\infty_{\text{per}}(V) := \{\boldsymbol{u} \mid \boldsymbol{u} : V \to \mathbb{R}^n,\ \boldsymbol{u} \text{ is infinitely differentiable on } V,\ \boldsymbol{u} \text{ is } V\text{-periodic}\}, \tag{2.70}$$

$$H^1_{\text{per}}(V, \mathbb{R}^n) := \text{closure of } C^\infty_{\text{per}}(V) \text{ with respect to the } H^1\text{-norm}, \tag{2.71}$$

$$W^1_{\text{per}}(V, \mathbb{R}^n) := H^1_{\text{per}}(V, \mathbb{R}^n)/\mathbb{R}^n. \tag{2.72}$$

Denoting by $[\boldsymbol{u}]$ the equivalence class represented by $\boldsymbol{u} \in H^1_{\text{per}}(V, \mathbb{R}^n)$, we define a norm on $W^1_{\text{per}}(V, \mathbb{R}^n)$ by

$$\|[\boldsymbol{u}]\|_{W^1_{\text{per}}(V, \mathbb{R}^n)} = \|\nabla \boldsymbol{u}\|_0 . \tag{2.73}$$

The set $W^1_{\text{per}}(V, \mathbb{R}^n)$ equipped with the norm $\|[\boldsymbol{u}]\|_{W^1_{\text{per}}(V, \mathbb{R}^n)}$ is a Hilbert space (Cioranescu and Donato, 1999).

2.3.2 Weak formulation

In this section we present the weak formulation of the boundary value problems in static linear elasticity, i.e. Problems 2.2.4, 2.2.5 and 2.2.6. Depending on whether we express these equations in terms of one or more of the quantities, displacement, strain and stress, different weak formulations arise. Here, we focus on the pure-displacement weak formulation. This formulation, besides others, is implemented in the finite element software employed in this thesis.

Let denote $\mathcal{V} \subseteq H^1(\Omega, \mathbb{R}^3)$ some function space. In order to setup the weak formulation, we multiply the equations of equilibrium (Eq. (2.43)) with an arbitrary function $\boldsymbol{v} \in \mathcal{V}$, and integrate over Ω, to obtain

$$\int_\Omega (\operatorname{div} \boldsymbol{\sigma}(\boldsymbol{u})) \cdot \boldsymbol{v} \, \mathrm{d}\boldsymbol{x} = -\int_\Omega \boldsymbol{f} \cdot \boldsymbol{v} \, \mathrm{d}\boldsymbol{x}. \tag{2.74}$$

We assume that $\boldsymbol{f} \in L^2(\Omega, \mathbb{R}^3)$, so that the integral on the right-hand side of Eq. (2.74) exists. Using the identity

$$(\operatorname{div} \boldsymbol{\sigma}(\boldsymbol{u})) \cdot \boldsymbol{v} = \operatorname{div}(\boldsymbol{\sigma}(\boldsymbol{u})\, \boldsymbol{v}) - \boldsymbol{\sigma}(\boldsymbol{u}) : \nabla \boldsymbol{v},$$

as well as employing the divergence theorem, the left-hand side of Eq. (2.74) becomes

$$\begin{aligned}\int_\Omega (\operatorname{div} \boldsymbol{\sigma}(\boldsymbol{u})) \cdot \boldsymbol{v} \, \mathrm{d}\boldsymbol{x} &= \int_\Omega \operatorname{div}(\boldsymbol{\sigma}(\boldsymbol{u})\, \boldsymbol{v}) \, \mathrm{d}\boldsymbol{x} - \int_\Omega \boldsymbol{\sigma}(\boldsymbol{u}) : \nabla \boldsymbol{v} \, \mathrm{d}\boldsymbol{x} = \int_{\Gamma_\Omega} (\boldsymbol{\sigma}(\boldsymbol{u})\, \boldsymbol{v}) \cdot \boldsymbol{n} \, \mathrm{d}\boldsymbol{s} - \int_\Omega \boldsymbol{\sigma}(\boldsymbol{u}) : \nabla \boldsymbol{v} \, \mathrm{d}\boldsymbol{x} \\ &= \int_{\Gamma_\Omega} (\boldsymbol{\sigma}(\boldsymbol{u})\boldsymbol{n}) \cdot \boldsymbol{v} \, \mathrm{d}\boldsymbol{s} - \int_\Omega \boldsymbol{\sigma}(\boldsymbol{u}) : \boldsymbol{\varepsilon}(\boldsymbol{v}) \, \mathrm{d}\boldsymbol{x}. \end{aligned} \tag{2.75}$$

Note that $\boldsymbol{\sigma}(\boldsymbol{u}) : \nabla \boldsymbol{v} = \boldsymbol{\sigma}(\boldsymbol{u}) : \boldsymbol{\varepsilon}(\boldsymbol{v})$ holds, since the strain $\boldsymbol{\varepsilon}(\boldsymbol{v})$ is the symmetric part of $\nabla \boldsymbol{v}$. Moreover, the surface integral in Eq. (2.75) exists, if $\boldsymbol{\sigma}(\boldsymbol{u})\boldsymbol{n} =: \boldsymbol{g} \in H^{1/2}(\Gamma_\Omega, \mathbb{R}^3)$.

Inserting Eq. (2.75) in Eq. (2.74), substituting Hooke's law and multiplying the resulting equation with minus one, we obtain the following weak formulation

$$\begin{aligned} &\text{find } \boldsymbol{u} \in \mathcal{V} \text{ such that} \\ &\int_\Omega (\boldsymbol{C} : \boldsymbol{\varepsilon}(\boldsymbol{u})) : \boldsymbol{\varepsilon}(\boldsymbol{v}) \, \mathrm{d}\boldsymbol{x} = \int_{\Gamma_\Omega} \boldsymbol{g} \cdot \boldsymbol{v} \, \mathrm{d}\boldsymbol{s} + \int_\Omega \boldsymbol{f} \cdot \boldsymbol{v} \, \mathrm{d}\boldsymbol{x} \quad \forall \boldsymbol{v} \in \mathcal{V}. \end{aligned} \tag{2.76}$$

In summary, we can state

Problem 2.3.2 *Let $\boldsymbol{f} \in L^2(\Omega, \mathbb{R}^3)$, $\boldsymbol{g} \in H^{1/2}(\Gamma_\Omega, \mathbb{R}^3)$. The weak formulation of Problems 2.2.4, 2.2.5 and 2.2.6 is given by*

$$\begin{aligned} &\textit{find } \boldsymbol{u} \in \mathcal{V} \textit{ such that} \\ &a(\boldsymbol{u}, \boldsymbol{v}) = G(\boldsymbol{v}) + F(\boldsymbol{v}) \qquad \forall \boldsymbol{v} \in \mathcal{V}, \end{aligned} \tag{2.77}$$

with bilinear form

$$a : \mathcal{V} \times \mathcal{V} \to \mathbb{R}, \quad a(\boldsymbol{u}, \boldsymbol{v}) = \int_\Omega (\boldsymbol{C} : \boldsymbol{\varepsilon}(\boldsymbol{u})) : \boldsymbol{\varepsilon}(\boldsymbol{v}) \mathrm{d}\boldsymbol{x}, \tag{2.78}$$

and linear forms G and F

$$G : \mathcal{V} \to \mathbb{R} \quad \textit{with} \quad G(\boldsymbol{v}) = \int_{\Gamma_\Omega} \boldsymbol{g} \cdot \boldsymbol{v} \, \mathrm{d}\boldsymbol{s}, \tag{2.79}$$

$$F : \mathcal{V} \to \mathbb{R} \quad \textit{with} \quad F(\boldsymbol{v}) = \int_\Omega \boldsymbol{f} \cdot \boldsymbol{v} \, \mathrm{d}\boldsymbol{x}, \tag{2.80}$$

respectively. Here, $\mathcal{V}$ and the linear form (2.79) *depend on the type of boundary conditions prescribed on Γ_Ω, see Section 2.3.3.*

A function $\boldsymbol{u}$ which fulfills Problem 2.3.2 is said to be a weak solution of the corresponding boundary value problem.

Note that the bilinear form (2.78) as well as the linear forms, (2.79) and (2.80), are only functions of the displacement $\boldsymbol{u}$. In this sense, Problem 2.3.2 is called the pure-displacement weak formulation of the equations of static linear elasticity.

2.3.3 Existence and uniqueness results

In this section we present different theorems showing that a weak solution of each of the three Problems 2.2.4, 2.2.5 and 2.2.6 exists and is unique in some suitable function space.

Theorem 2.3.3 *Let $\boldsymbol{u} \in H^1(\Omega, \mathbb{R}^3)$ satisfies displacement boundary conditions $\boldsymbol{u} = \boldsymbol{u}_0$ on Γ_Ω, where $\boldsymbol{u}_0 \in H^{1/2}(\Gamma_\Omega, \mathbb{R}^3)$. For any such $\boldsymbol{u}$ it holds that $G(\boldsymbol{u}) = 0$ in Problem 2.3.2. Moreover, Problem 2.3.2 has a solution $\boldsymbol{u}$ in $H^1_{\Gamma_\Omega}(\overline{\Omega}, \mathbb{R}^3)$ which is unique and satisfies the estimate*

$$\|\boldsymbol{u}\|_1 \leq c \left(\left\| \boldsymbol{f} \right\|_0 + \left\| \boldsymbol{u}_0 \right\|_{1/2} \right), \tag{2.81}$$

where the constant $c = c(\Omega)$ depends on the domain Ω.

Proof. For a detailed proof we refer the reader to Oleĭnik et al. (1992). □

The proof of Oleĭnik et al. (1992) makes use of Korn's first inequality in $H^1(\Omega, \mathbb{R}^3)$ and of the Lax-Milgram theorem, both given below.

Theorem 2.3.4 (Korn's first inequality) *There exists a constant $c = c(\Omega) > 0$, such that*

$$\|\boldsymbol{\varepsilon}(\boldsymbol{v})\|_0^2 + \|\boldsymbol{v}\|_0^2 \geq c \|\boldsymbol{v}\|_1^2 \quad \forall \boldsymbol{v} \in H^1(\Omega, \mathbb{R}^3). \tag{2.82}$$

Theorem 2.3.5 (Lax-Milgram theorem) *Let $\mathcal{V}$ be a Hilbert space and let $\|\cdot\|_{\mathcal{V}}$ denote its induced norm. Moreover, let $a : \mathcal{V} \times \mathcal{V} \to \mathbb{R}$ be a bilinear form which is bounded and $\mathcal{V}$-elliptic, i.e. there exist constants $c_1, c_2 > 0$ such that*

$$|a(\boldsymbol{u}, \boldsymbol{v})| \leq c_1 \|\boldsymbol{u}\|_{\mathcal{V}} \|\boldsymbol{v}\|_{\mathcal{V}} \quad \forall \boldsymbol{u}, \boldsymbol{v} \in \mathcal{V}, \tag{2.83}$$

$$a(\boldsymbol{v}, \boldsymbol{v}) \geq c_2 \|\boldsymbol{v}\|_{\mathcal{V}}^2 \quad \forall \boldsymbol{v} \in \mathcal{V}, \tag{2.84}$$

holds. Then for any bounded linear form $F, G : \mathcal{V} \to \mathbb{R}$ the weak problem

$$\begin{aligned} &\text{find } \boldsymbol{u} \in \mathcal{V} \text{ such that} \\ &a(\boldsymbol{u}, \boldsymbol{v}) = F(\boldsymbol{v}) + G(\boldsymbol{v}) \quad \forall \boldsymbol{v} \in \mathcal{V}, \end{aligned} \tag{2.85}$$

has a unique solution $\boldsymbol{u}$ in $\mathcal{V}$.

Theorem 2.3.6 *Let traction boundary conditions $\boldsymbol{\sigma}\,\boldsymbol{n} = \boldsymbol{g}$, where $\boldsymbol{g} \in H^{1/2}(\Gamma_\Omega, \mathbb{R}^3)$, be prescribed on Γ_Ω. Suppose that*

$$G(\boldsymbol{r}) + F(\boldsymbol{r}) = 0 \tag{2.86}$$

holds for any rigid displacement $\boldsymbol{r} \in \mathcal{R} \subset H^1(\Omega, \mathbb{R}^3)$. Then there exists a solution $\boldsymbol{u}$ of Problem 2.3.2 in $H^1(\Omega, \mathbb{R}^3)/\mathcal{R}$, which is unique and satisfies

$$\|\boldsymbol{\varepsilon}(\boldsymbol{u})\|_0 \leq c \left(\left\| \boldsymbol{f} \right\|_0 + \left\| \boldsymbol{g} \right\|_{1/2} \right). \tag{2.87}$$

Here, the constant $c = c(\Omega)$ depends only on the domain Ω.

Proof. For a detailed proof we refer the reader to Oleĭnik et al. (1992). Nevertheless, we briefly review this proof below. □

Let us note first, that the space of rigid displacements $\mathcal{R}$ coincides with the kernel of the bilinear form (2.78), i.e. with the set of all $\boldsymbol{u} \in H^1(\Omega, \mathbb{R}^3)$ for which $a(\boldsymbol{u}, \boldsymbol{v}) = 0$ for all $\boldsymbol{v} \in H^1(\Omega, \mathbb{R}^3)$. Clearly, $\emptyset \neq \mathcal{R} \subset H^1(\Omega, \mathbb{R}^3)$. Together with Eq. (2.86) this implies that $\boldsymbol{r} \in \mathcal{R}$ satisfies Eq. (2.77).

Consider some closed subspace of $H^1(\Omega, \mathbb{R}^3)$, denoted $\tilde{\mathcal{V}}$, for which $\tilde{\mathcal{V}} \cap \mathcal{R} = \emptyset$ and $\tilde{\mathcal{V}} \cup \mathcal{R} = H^1(\Omega, \mathbb{R}^3)$ holds. Such a subspace $\tilde{\mathcal{V}}$ exists (Oleĭnik et al., 1992) and it is easy to see that the premises of the Lax-Milgram theorem holds in $\tilde{\mathcal{V}}$. Thus, there exists a solution of Problem 2.3.2 which is unique and lies in $\tilde{\mathcal{V}}$.

Since $H^1(\Omega, \mathbb{R}^3) = \tilde{\mathcal{V}} \cup \mathcal{R}$, there exists some solution of the weak problem in $H^1(\Omega, \mathbb{R}^3)$, which, however, is only unique up to additive rigid displacements. In order to find some function space $\mathcal{V}$, in which the solution is unique, one modularizes all that elements from $H^1(\Omega, \mathbb{R}^3)$ which belong to $\mathcal{R}$. In other words, one searches for a solution in the quotient space $H^1(\Omega, \mathbb{R}^3)/\mathcal{R}$.

Theorem 2.3.7 *Let V be a brick-shaped subset of domain Ω. Moreover, let periodic boundary conditions* (2.57) *be satisfied. Suppose that*

$$\int_V \boldsymbol{f} \, \mathrm{d}\boldsymbol{x} = 0 \tag{2.88}$$

holds. Then, for any $\boldsymbol{v}$ it holds that $G(\boldsymbol{v}) = 0$ in Problem 2.3.2. Moreover, Problem 2.3.2 has a unique solution $\boldsymbol{u}$ in $W^1_{\mathrm{per}}(V, \mathbb{R}^3)$, and this solution satisfies

$$\|\boldsymbol{u}\|_1 \leq c \left\|\boldsymbol{f}\right\|_0, \tag{2.89}$$

where c denotes some constant.

Proof. A detailed proof of Theorem 2.3.7 is given in Cioranescu and Donato (1999) or Oleĭnik et al. (1992). The proof of Oleĭnik et al. (1992) rests upon the Lax-Milgram theorem and is quite similar to the proof of Theorem 2.3.6. Below we present a rough sketch of the proof. □

The kernel of the bilinear form (2.78) in $H^1_{\mathrm{per}}(V, \mathbb{R}^3)$ is $\mathcal{R} = \mathbb{R}^3$. Again, there exists some subspace $\tilde{\mathcal{V}}$ for which $\tilde{\mathcal{V}} \cap \mathcal{R} = \emptyset$ and $\tilde{\mathcal{V}} \cup \mathcal{R} = H^1_{\mathrm{per}}(V, \mathbb{R}^3)$ holds. By the Lax-Milgram theorem a unique solution in $\tilde{\mathcal{V}}$ exists (Cioranescu and Donato, 1999; Oleĭnik et al., 1992). For $\boldsymbol{r} \in \mathcal{R}$ the right-hand side of Eq. (2.77) becomes

$$G(\boldsymbol{r}) + F(\boldsymbol{r}) = F(\boldsymbol{r}) = \int_V \boldsymbol{f} \cdot \boldsymbol{r} \, \mathrm{d}\boldsymbol{x} = \boldsymbol{r} \cdot \int_V \boldsymbol{f} \, \mathrm{d}\boldsymbol{x} = 0. \tag{2.90}$$

Note in the above equation that $G(\boldsymbol{r}) = 0$ holds, because $\boldsymbol{r}$ is V-periodic. Finally, we obtain a unique solution in the quotient space $W^1_{\mathrm{per}}(V, \mathbb{R}^3) = H^1_{\mathrm{per}}(V, \mathbb{R}^3)/\mathbb{R}^3$.

2.4 Galerkin finite element methods

In this section we briefly present the idea of the Galerkin finite element methods. We demonstrate this method applying it to the weak formulation of the equations of static linear elasticity (Problem 2.3.2). We close this section showing an error estimate for the approximation found by the Galerkin finite element methods.

For a detailed introduction and discussion of the Galerkin finite element methods we refer the reader to the literature (Braess, 1997; Ciarlet, 1978; Brenner and Scott, 2008; Brenner and Carstensen, 2004).

In what follows, we assume that Ω is a polyhedral domain in $\mathbb{R}^3$. Moreover, we denote by $\mathcal{V}$ the functions space in which we search for a unique solution of Problem 2.3.2. Finally, $\mathbb{P}_k$ is said to be the space of polynomials in three variables of degree $\leq k$.

2.4.1 Basic formulation

Galerkin finite element methods search for an approximate solution of Problem 2.3.2 in some finite dimensional space $\mathcal{V}_h$. The approximate solution, denoted $\boldsymbol{u}_h$, is called finite element approximation, and $\mathcal{V}_h$ is said to be the finite element space. In this thesis we employ conforming finite element methods, thus $\mathcal{V}_h \subset \mathcal{V}$.

In order to construct $\mathcal{V}_h$, we partition our domain Ω into a set of polyhedrals. This partition, denoted $\mathcal{T}_h$, must fulfill the following conditions

(i) each polyhedral $T \in \mathcal{T}_h$ is a closed nonempty subset of Ω (the *elements*),

(ii) $\overline{\Omega} = \bigcup_{T \in \mathcal{T}_h} T$,

(iii) the intersection of two different elements of $\mathcal{T}_h$ equals either the empty set, a common vertex, a common edge or a common face of the two elements.

Then $\mathcal{T}_h$ is said to be a mesh of the domain Ω. Denoting by h_T the maximum edge length of element $T \in \mathcal{T}_h$, we introduce the mesh size $h := \max_{T \in \mathcal{T}_h} h_T$. The latter parameter represents the mesh resolution.

We use tetrahedral elements T. On each such element we introduce a Lagrangian grid of order k, denoted $LG_k(T)$ in the following. Roughly spoken, a Lagrangian grid is a regular arrangement of points $\boldsymbol{x} \in \mathbb{R}^3$ in T such as seen in Fig. 2.2. More precisely, we set $LG_k(T) = \{\boldsymbol{x}_1, \boldsymbol{x}_2, \ldots, \boldsymbol{x}_M\}$ where $\boldsymbol{x}_i$ for $i = 1, \ldots, M$ represents a point (*node*) on the edges of T as marked in Fig. 2.2. Note that M depends on the order k.

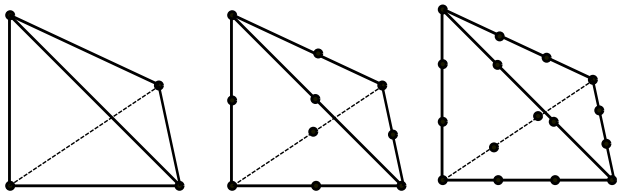

Figure 2.2.: Lagrangian grid of order $k = 1$, $k = 2$ and $k = 3$, respectively, shown in the left, middle and right sub image. Small circles represent the nodes of T.

Given values $p(\boldsymbol{x}_i)$ for all $\boldsymbol{x}_i \in LG_k(T)$, we can uniquely define a function $p \in \mathbb{P}_k$. A basis of $\mathbb{P}_k$ is given by the set $\{\boldsymbol{\Phi}_i\}_{i=1,\ldots,M}$, where $\boldsymbol{\Phi}_i$ is a polynomial of order $\leq k$, which is one for $\boldsymbol{x}_i \in LG_k(T)$ but zero in any other point of $LG_k(T)$. These basis functions are also called *shape functions*. The triple $(T, \{\boldsymbol{\Phi}_i\}, LG_k(T))$ is said to be a tetrahedral Lagrange element of order k. In this thesis we employ tetrahedral Lagrange elements of order one or two.

Given a mesh $\mathcal{T}_h$ and a Lagrange element of order k, we construct a finite element space $\mathcal{V}_h$ such that any function $\boldsymbol{v}_h \in \mathcal{V}_h$ satisfies the following properties

- it is continuous on $\overline{\Omega}$,
- its restriction to each element $T \in \mathcal{T}_h$ is a polynomial of order $\leq k$,
- for all elements $T \in \mathcal{T}_h$ it is completely determined by its values in all nodes.

It can be shown that $\mathcal{V}_h \subset \mathcal{V}$, see for instance Ciarlet (1978, Theorem 2.2.3). This relies on the fact that condition (iii) holds for mesh $\mathcal{T}_h$.

Finally, the finite element method becomes

$$\begin{aligned} &\text{find } \boldsymbol{u}_h \in \mathcal{V}_h \text{ such that} \\ &a(\boldsymbol{u}_h, \boldsymbol{v}_h) = G(\boldsymbol{v}_h) + F(\boldsymbol{v}_h) \qquad \forall \boldsymbol{v}_h \in \mathcal{V}_h, \end{aligned} \tag{2.91}$$

where a, G and F denote the bilinear form and the two linear forms defined in Problem 2.3.2, respectively. Note that, there exists a unique solution to problem (2.91) in $\mathcal{V}_h$, since there exists one for Problem 2.3.2 in $\mathcal{V}$ and it holds that $\mathcal{V}_h \subset \mathcal{V}$.

Using the representation $\boldsymbol{u}_h = \sum_{i=1}^{M} u_i \boldsymbol{\Phi}_i$, problem (2.91) can be transformed to the linear system

$$\boldsymbol{A}_h \boldsymbol{u}_h = \boldsymbol{b}_h. \tag{2.92}$$

Here, $(\boldsymbol{A}_h)_{ij} = a(\boldsymbol{\Phi}_i, \boldsymbol{\Phi}_j)$, $\boldsymbol{u}_h = (u_1, \ldots, u_M)$ and $(\boldsymbol{b}_h)_j = G(\boldsymbol{\Phi}_j) + F(\boldsymbol{\Phi}_j)$ for $i, j = 1, \ldots, M$.

2.4.2 Error estimates

In the following, we present estimates for the error $\boldsymbol{u} - \boldsymbol{u}_h$ in the finite element approximation of the solution $\boldsymbol{u} \in \mathcal{V} \subseteq H^m(\Omega, \mathbb{R}^3)$ to Problem 2.3.2, where $\boldsymbol{u} = \boldsymbol{u}_0$ on Γ_Ω with $\boldsymbol{u}_0 \in H^{1/2}(\Gamma_\Omega, \mathbb{R}^3)$.

We consider a family of meshes, denoted $\{\mathcal{T}_h\}$, where each $\mathcal{T}_h$ is defined as in Section 2.4.1 and the mesh size h goes to zero. This family of meshes is assumed to be shape regular.

Definition 2.4.1 *A family of meshes $\{\mathcal{T}_h\}$ is shape regular, if there exists a positive constant $c \in \mathbb{R}$ such that*

$$R_T \leq c\, r_T \quad \forall T \in \mathcal{T}_h \in \{\mathcal{T}_h\}, \tag{2.93}$$

where R_T and r_T denote the outer and inner radius of T, respectively. Here, the outer radius is the radius of the smallest ball containing T and the inner radius is the radius of the largest ball in T.

By this property, we ensure that the shape of the elements does not degenerate with refinement of the mesh.

Let us denote by $\mathcal{V}_h \subset \mathcal{V}$ the finite element space, which was composed by Lagrange elements of order k on mesh $\mathcal{T}_h$, and $\boldsymbol{u}_h$ is the solution of problem (2.91) in $\mathcal{V}_h$. We are interested in the error of $\boldsymbol{u}_h$ for a family of shape regular meshes $\{\mathcal{T}_h\}$, as h goes to zero. To this end, we aim for an error estimate of type $\left\|\boldsymbol{u} - \boldsymbol{u}_h\right\| \leq c\, h^p$ with p as large as possible and a constant c independent of the mesh size h. Usually, c will depend on the norm in use, the order of the shape functions and the regularity of $\boldsymbol{u}$.

For Lagrange elements of order one and two we have the following error estimates

Theorem 2.4.2 *Let a family of shape regular meshes $\{\mathcal{T}_h\}$ be given. Using tetrahedral Lagrange elements of order $k = 1$ or $k = 2$ and assuming that $\boldsymbol{u} \in H^{k+1}(\Omega, \mathbb{R}^3)$, the following error estimate holds*

$$\left\|\boldsymbol{u} - \boldsymbol{u}_h\right\|_0 \leq c\, h^{k+1} |\boldsymbol{u}|_{k+1}. \tag{2.94}$$

Proof. See, for instance, Braess (1997). □

3 Homogenization

In the context of linear elasticity, we consider homogenization from three different viewpoints: periodic homogenization, RVE-based homogenization and Eshelby-based homogenization. In Section 3.1 we briefly review all viewpoints. Then, in Section 3.2, we move to the minimum requirements that are necessary to successfully employ homogenization. Subsequent to this, in Section 3.3, we introduce the apparent/effective stiffness tensor in Eshelby-based and RVE-based homogenization and discuss when the apparent and the effective stiffness tensor coincide.

In Section 3.4, Section 3.5 and Section 3.6 we review different methods in periodic, RVE-based and Eshelby-based homogenization. We start by explaining the general approach of the asymptotic homogenization method in periodic homogenization. We apply this method to the equations of static and dynamic linear elasticity, which gives rise to the AHA and the AHF method. Then, we move to the RVE-based homogenization method using displacement or traction boundary conditions. Finally, we focus on Eshelby-based homogenization methods and similar techniques and consider the Voigt and the Reuss technique, as well as the Dilute, the Mori-Tanaka and the self-consistent method. We end this chapter comparing the apparent stiffness tensors predicted by the different methods in Section 3.7.

There is a large amount of literature available on homogenization in the context of linear elasticity. A nice overview on periodic homogenization is given by Cioranescu and Donato (1999), Allaire (2010) or Sanchez-Palencia (1986). For a general introduction into RVE-based homogenization we refer the reader to Nemat-Nasser and Hori (1999), Mura (1987) and Zohdi and Wriggers (2008). An overview of Eshelby-based homogenization techniques and similar methods can be found, for instance, in Nemat-Nasser and Hori (1999), Gross and Seelig (2007), Zaoui (1997) and Zohdi and Wriggers (2008).

3.1 Homogenization from different viewpoints

The concept of homogenization is known in a variety of fields. In chemistry and biology it describes the generation of a homogeneous material, i.e. a similar and uniform structure or material, from a number of components. For instance, the homogenization of milk aims to reduce the size of the fat molecules in milk in order to prevent the cream from separating out. Thereby, one increases the durability of milk.

In the context of continuum mechanics the purpose of homogenization is to describe the coarse-scale properties (strain, stress, stiffness) of materials with many small heterogeneities. Obviously, the coarse-scale properties of such materials depend on the material's composition, its structure, and its elastic properties at finer length scales. As a consequence thereof, the strain and the stress of the material show, depending on the length scale, different orders of oscillation. That is, they change smoothly at the coarse scale, while rapidly at finer scales. In this context the scales are often referred to as slow (slow variation of stress and strain) or as fast (highly oscillating stress and strain).

Finding the coarse-scale properties of any material by "properly averaging" over the material's properties at finer scale is what we call homogenization. We consider here three different approaches to homogenization: two physically motivated ones, leading to so-called RVE-based and Eshelby-based homogenization methods, and a more mathematical one, resulting in periodic homogenization methods. Note that RVE-based homogenization in the engineering literature is also referred to as "coarse-scaling". All approaches are described in more detail in the following subsections. See Fig. 3.1 for an illustration of the homogenization process from the three viewpoints of RVE-based, periodic and Eshelby-based homogenization.

In what follows, we consider a domain $\Omega \subseteq \mathbb{R}^3$ occupied by some material A with many small heterogeneities. Homogenization, in particular, predicts the coarse-scale elastic properties of this material. We denote this coarse-scale stiffness tensor by $\boldsymbol{C}_I$, where I refers to either our material, i.e. $I = A$,

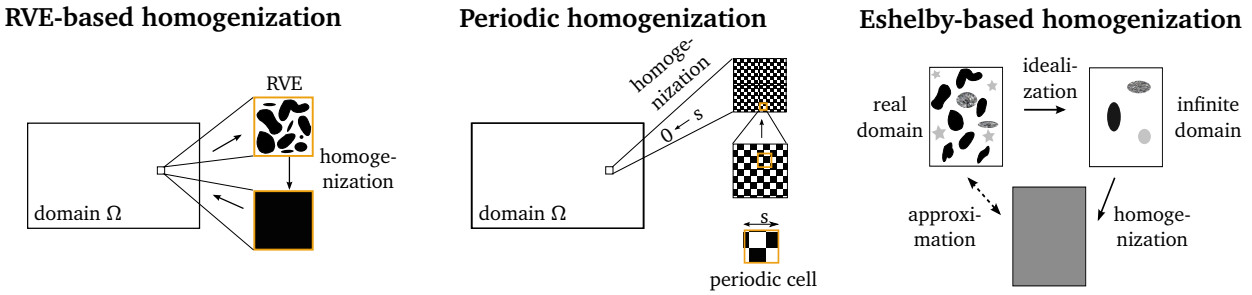

Figure 3.1.: The process of homogenization from the three viewpoints of RVE-based, periodic and Eshelby-based homogenization; corresponding images are depicted from left to right.

or the homogenization method that was used to obtain the coarse-scale elastic properties of our material. Throughout this chapter, where we introduce different homogenization methods, we will mainly employ I to refer to the homogenization method. However, in Chapters 5, 6 and 7, where we predict the coarse-scale elastic properties of different MMTs, we prefer to indicate by I the type of MMT or its substructures.

Periodic homogenization

In periodic homogenization it is assumed that the material is periodic, i.e. the material's heterogeneities are distributed in a periodic manner. Then the domain $\Omega \subset \mathbb{R}^3$ consists of a repeating periodic cell (unit cell), denoted V, of size s. In particular, this implies that the fine-scale stiffness tensor $\boldsymbol{C}^s$ of our material A changes periodically over Ω, i.e. $\boldsymbol{C}^s$ is V-periodic (Eq. (2.29)). The idea of periodic homogenization is to analyze the limit of a family of dynamic linear elastic boundary value problems (Problem 2.2.7), i.e.

$$\begin{aligned} &\operatorname{div}_{\boldsymbol{z}}(\boldsymbol{C}^s(\boldsymbol{z}) : \boldsymbol{\varepsilon}(\boldsymbol{u}^s(\boldsymbol{z},t))) = -\boldsymbol{f}(\boldsymbol{z},t) + \rho \frac{\partial^2 \boldsymbol{u}^s(\boldsymbol{z},t)}{\partial t^2}, \quad \boldsymbol{z} \in \Omega,\ t \in [0,T_0], \\ &+ \text{ appropriate initial and boundary conditions,} \end{aligned} \tag{3.1}$$

where the density ρ depends also on s. The corresponding displacement, also depending on s, is denoted by $\boldsymbol{u}^s$. In general, solving Eq. (3.1) numerically, any method, such as finite elements or finite differences, will require a mesh size that must be smaller than s. If s is too small, the resulting mesh will be very fine and the corresponding discrete problems are costly or even impossible to solve because the CPU time as well as the memory storage are too large. Assuming that the sequence of displacements $\boldsymbol{u}^s$ converges to a limit $\boldsymbol{u}$ as $s \to 0$, one looks for a homogenized boundary value problem of the form

$$\begin{aligned} &\operatorname{div}_{\boldsymbol{z}}(\boldsymbol{C}_A : \boldsymbol{\varepsilon}(\boldsymbol{u}(\boldsymbol{z},t))) = -\boldsymbol{f}(\boldsymbol{z},t) + \rho_A \frac{\partial^2 \boldsymbol{u}(\boldsymbol{z},t)}{\partial t^2}, \quad \boldsymbol{z} \in \Omega,\ t \in [0,T_0], \\ &+ \text{ appropriate initial and boundary conditions,} \end{aligned} \tag{3.2}$$

where $\boldsymbol{C}_A$ and ρ_A are the coarse-scale stiffness tensor and the coarse-scale density, respectively. As usual in the literature, we call these quantities effective stiffness tensor and effective density, respectively. Note that, Eq. (3.2) is easier to solve numerically than Eq. (3.1), since $\boldsymbol{C}_A$ is constant throughout Ω.

Famous periodic homogenization techniques are the asymptotic homogenization method, Tartar's oscillating test functions method, and the methods based on two-scale convergence. For a detailed introduction into periodic homogenization see, for instance, the books of Cioranescu and Donato (1999) and Sanchez-Palencia (1986), or the lecture notes of Allaire (2010).

RVE-based homogenization

RVE-based homogenization methods are motivated by experimental tests. For example, in tensile tests a uniform load in direction v is applied to a heterogeneous sample of material A and the resulting change of the geometry is measured. Then the coarse-scale stress σ_A, the coarse-scale strain ε_A and the Young's modulus E_A of a coarse-scale isotropic material A, are given by

$$\sigma_A = F/S, \quad \varepsilon_A = \Delta L/L \quad \text{and} \quad \sigma_A = E_A \varepsilon_A,$$

where F is the external load, S the area to which the external load was applied to, L the sample length after applying the load, and ΔL the difference in sample length before and after applying the load.

Similarly as for the experimental tests described before, we can determine the coarse-scale stress, strain and stiffness tensor of any material A in a computational way. To this end, we model the elastic behavior of material A based on the equations of static linear elasticity (Problem 2.2.3) and assume that specific boundary conditions are prescribed on the material. Since it is generally too expensive to solve these equations on the whole domain Ω occupied by our material, we solve them for a small volume element $V \subset \Omega$. This element, if representative for the material, is called representative volume element (RVE) in the following, see Section 3.3 for a precise definition. We approximate the coarse-scale strain and the coarse-scale stress by the respective averages of strain and stress over V, and call the resulting quantities average stress and average strain, respectively. The linear operator $\boldsymbol{C}_A$ relating the average stress and the average strain, is the so-called apparent stiffness tensor. To this end, the RVE-based homogenization method applies six specific boundary conditions on the RVE and solves each of the resulting boundary value problems numerically. Based on the solutions of these six problems one derives the average stresses and the average strains. Finally, these are used to set up a linear system with the apparent stiffness tensor $\boldsymbol{C}_A$ as unknown.

Note that, in general, the apparent stiffness tensor $\boldsymbol{C}_A$ depends on the size of the volume element V, its position within Ω, as well as on the boundary conditions applied on V. However, this is not the case, if our material possesses the property of statistical homogeneity, V is an RVE and $\boldsymbol{C}_A$ is independent of the applied boundary conditions, see Section 3.3 for details. In particular, then, $\boldsymbol{C}_A$ is the same in any coarse-scale point of our material. Following the notion of Huet (1990), we refer to $\boldsymbol{C}_A$ then as "effective stiffness tensor" rather than calling it "apparent stiffness tensor".

Eshelby-based homogenization and similar homogenization theories

Eshelby-based homogenization methods and similar techniques idealize the material under examination. This approach allows to analytically compute the coarse-scale stiffness tensor for the idealized material, which serves as approximation or bound to the unknown coarse-scale stiffness tensor of our material under examination. The coarse-scale stiffness tensor derived by this procedure we call apparent stiffness tensor and denote it by $\boldsymbol{C}_A$.

Eshelby-based homogenization methods idealize our material under examination by an infinite composite A of n homogeneous constituents (phases) having a specific shape and distribution. These methods rely on the matrix inclusion problem of Eshelby (Eshelby, 1957). Well-known methods are: the Dilute approximation, the Mori-Tanaka method (Mori and Tanaka, 1973), and the self-consistent method (Hill, 1965). A review of these and other Eshelby-based homogenization methods can be found, for instance, in Nemat-Nasser and Hori (1999) or Zaoui (2002).

Famous homogenization methods, which idealize the material under examination in a similar, however, different way than Eshelby-based homogenization methods, are: the Voigt and Reuss techniques (Voigt, 1888; Reuss, 1929), and the Hashin-Shtrikman bounds (Hashin and Shtrikman, 1963), see Section 3.6.1 for details.

3.2 Basic assumptions in homogenization: existence of scales, scale separation

There are three basic assumptions in periodic, RVE-based and Eshelby-based homogenization. First of all, we assume that there exist at least three length scales:

- the coarse scale. This scale is characterized by the size l_c of the material domain Ω. Here the small heterogeneities of the material are "invisible" and the field variables of the body change smoothly.

- the meso scale. At this scale we perform the homogenization. This scale is characterized by the parameter l_m, which represents either the size of the periodic cell or the RVE. Within the periodic cell or the RVE the material's heterogeneities are visible and the field variables of the body change rapidly at this scale.

- the fine scale. This scale is characterized by the size of the material's heterogeneities, l_f. The field variables of the body change rapidly at this scale.

Sometimes, the coarse and the fine scale are also termed macro and micro scale, respectively. In this thesis we prefer to use the more accurate terms coarse and fine scale, respectively. This is because we study MMTs, whose material properties vary from the nanometer up to the millimeter scale, and it seems to be confusing to refer to the nanometer scale as micro scale.

Secondly, we assume that l_f is much larger than the size of single molecules. Therefore, we can model the material's elastic behavior and properties using the equations of continuum mechanics (linear elasticity), and do not need to take into account molecular dynamics.

Thirdly, we assume that the coarse and the finer scales are well-separated. In RVE-based homogenization, we require that $l_f \ll l_m < l_c$. In periodic homogenization we demand $l_m \ll l_c$. Here, the size of the heterogeneities l_f is of no importance, in particular $l_m \sim l_f$. That is why we use the terms meso scale and fine scale in periodic homogenization synonymously. Defining the scale ratio, $s := l_m/l_c$, we can express the assumption of scale separation in periodic homogenization also by $s \ll 1$. In Eshelby-based homogenization there exists no meso scale, and the coarse and the fine scales are separated by construction. The coarse scale is represented by an infinite material, while the heterogeneities, are finite ellipsoidal inclusions.

Scale separation is important as otherwise we can find no description of the material's coarse-scale behavior which is independent of the fine-scale structure. Consider, for example, the homogenization which enables us to display an image on a screen (Parnell, 2004). When we watch the image on the screen our brain is unable to resolve the fine-scale structure of the screen, the pixels, and we see a homogenized image. The length scale of a pixel, l_f, is much smaller than the length scale of the image on the screen, l_m. Moreover, we usually observe the screen from a distance l_c, greater than l_m. Note that if we are too close to the screen, i.e. $l_m \sim l_c$, we cannot see the whole image.

3.3 Apparent and effective properties in Eshelby-based and RVE-based homogenization

We start by introducing the apparent stiffness tensor in Eshelby-based and RVE-based homogenization (Section 3.3.1). Hereinafter, in Section 3.3.2 we specify the concept of the RVE and discuss different requirements on the RVE or our material to obtain effective rather than apparent properties. In Section 3.3.3 we give the Hill-Mandel condition. This condition ensures that the homogeneous and the heterogeneous material are energetically equivalent. Finally, in Section 3.3.4 we state two important theorems in RVE-based homogenization.

3.3.1 Apparent stiffness and apparent compliance tensor

Given some arbitrary volume element $V \subset \Omega$, not necessarily an RVE, we define the coarse scale variables: the average strain, $\mathcal{M}_V(\boldsymbol{\varepsilon})$, and the average stress, $\mathcal{M}_V(\boldsymbol{\sigma})$, by

$$\mathcal{M}_V(\boldsymbol{\varepsilon}) := \frac{1}{|V|}\int_V \boldsymbol{\varepsilon}(\boldsymbol{x})\,\mathrm{d}\boldsymbol{x}, \tag{3.3}$$

$$\mathcal{M}_V(\boldsymbol{\sigma}) := \frac{1}{|V|}\int_V \boldsymbol{\sigma}(\boldsymbol{x})\,\mathrm{d}\boldsymbol{x}, \tag{3.4}$$

respectively, where $|V|$ is the volume of V. Note that Eqs. (3.3) and (3.4) have to be understood componentwise. Moreover, note that $\mathcal{M}_V(\boldsymbol{\varepsilon})$ and $\mathcal{M}_V(\boldsymbol{\sigma})$ are second-order tensor fields, because $\boldsymbol{\varepsilon}$ and $\boldsymbol{\sigma}$ are so.

We assume that a linear relationship between the average stress and the average strain hold, i.e.

$$\mathcal{M}_V(\boldsymbol{\sigma}) = \boldsymbol{C}_A : \mathcal{M}_V(\boldsymbol{\varepsilon}), \tag{3.5}$$

where the apparent stiffness tensor $\boldsymbol{C}_A$ is unknown. Likewise, we introduce the apparent compliance tensor $\boldsymbol{M}_A$ over

$$\mathcal{M}_V(\boldsymbol{\varepsilon}) = \boldsymbol{M}_A : \mathcal{M}_V(\boldsymbol{\sigma}). \tag{3.6}$$

Note that the tensors, $\boldsymbol{C}_A$ and $\boldsymbol{M}_A$, depend on the size of V, the location of V within Ω, and the boundary conditions applied on V.

The RVE-based homogenization method derives $\boldsymbol{C}_A$ based on Eq. (3.5), see Section 3.5 for details.

Eshelby-based homogenization methods as well as Voigt and Reuss techniques idealize the material under investigation to an infinite composite A, which consists of n homogeneous and perfectly bonded phases A_i, $i \in \{1,\dots,n\}$, with corresponding domains V_i, stiffness tensors $\boldsymbol{C}_i$, compliance tensors $\boldsymbol{M}_i$, and volume fractions vf_i. In order to derive an explicit equation for $\boldsymbol{C}_A$ and $\boldsymbol{M}_A$, we assume that two fourth-order tensors, $\boldsymbol{K}_i^{(\boldsymbol{\varepsilon},A)}$ and $\boldsymbol{K}_i^{(\boldsymbol{\sigma},A)}$, exist such that

$$\mathcal{M}_{V_i}(\boldsymbol{\varepsilon}) = \boldsymbol{K}_i^{(\boldsymbol{\varepsilon},A)} : \mathcal{M}_V(\boldsymbol{\varepsilon}), \tag{3.7}$$

$$\mathcal{M}_{V_i}(\boldsymbol{\sigma}) = \boldsymbol{K}_i^{(\boldsymbol{\sigma},A)} : \mathcal{M}_V(\boldsymbol{\sigma}), \tag{3.8}$$

where $i \in \{1,\dots,n\}$. These tensors exist if we impose additionally assumptions on the structural organization of A, as done for the Dilute method in Section 3.6.5, for the Mori-Tanaka method in Section 3.6.6 and for the self-consistent method in Section 3.6.7. Then, $\boldsymbol{K}_i^{(\boldsymbol{\varepsilon},A)}$ is said to be the phase strain concentration tensor, while $\boldsymbol{K}_i^{(\boldsymbol{\sigma},A)}$ is called phase stress concentration tensor.

Making use of Eq. (3.4) and Eq. (3.7), we can split the average stress $\mathcal{M}_V(\boldsymbol{\sigma})$ as follows:

$$\begin{aligned}\mathcal{M}_V(\boldsymbol{\sigma}) &= \frac{1}{|V|}\int_V \boldsymbol{\sigma}(\boldsymbol{x})\,\mathrm{d}\boldsymbol{x} = \sum_{i=1}^{n}\frac{|V_i|}{|V|}\left(\frac{1}{|V_i|}\int_{V_i}\boldsymbol{\sigma}(\boldsymbol{x})\,\mathrm{d}\boldsymbol{x}\right) = \sum_{i=1}^{n}\mathrm{vf}_i\mathcal{M}_{V_i}(\boldsymbol{\sigma}) = \sum_{i=1}^{n}\mathrm{vf}_i\mathcal{M}_{V_i}(\boldsymbol{C}_i:\boldsymbol{\varepsilon})\\ &= \sum_{i=1}^{n}\mathrm{vf}_i\,\boldsymbol{C}_i : \mathcal{M}_{V_i}(\boldsymbol{\varepsilon}) = \sum_{i=1}^{n}\mathrm{vf}_i\,\boldsymbol{C}_i : (\boldsymbol{K}_i^{(\boldsymbol{\varepsilon},A)} : \mathcal{M}_V(\boldsymbol{\varepsilon})) = \left(\sum_{i=1}^{n}\mathrm{vf}_i\,\boldsymbol{C}_i : \boldsymbol{K}_i^{(\boldsymbol{\varepsilon},A)}\right) : \mathcal{M}_V(\boldsymbol{\varepsilon}).\end{aligned} \tag{3.9}$$

In Eq. (3.9) we exploit Hooke's law and the identity $\mathcal{M}_{V_i}(\boldsymbol{C}_i : \boldsymbol{\varepsilon}) = \boldsymbol{C}_i : \mathcal{M}_{V_i}(\boldsymbol{\varepsilon})$. The latter is valid because $\boldsymbol{C}_i$ is constant throughout each phase. Comparing Eq. (3.9) to Eq. (3.5) we can give the apparent stiffness tensor $\boldsymbol{C}_A$ as function of the phase strain concentration tensors

$$\boldsymbol{C}_A = \sum_{i=1}^{n}\mathrm{vf}_i\,\boldsymbol{C}_i : \boldsymbol{K}_i^{(\boldsymbol{\varepsilon},A)}. \tag{3.10}$$

Similarly, we can use Eq. (3.3) and Eq. (3.8), to split the average strain $\mathcal{M}_V(\boldsymbol{\varepsilon})$ as follows

$$\mathcal{M}_V(\boldsymbol{\varepsilon}) = \left(\sum_{i=1}^{n} \mathrm{vf}_i \, \boldsymbol{M}_i : \boldsymbol{K}_i^{(\boldsymbol{\sigma},A)} \right) : \mathcal{M}_V(\boldsymbol{\sigma}) \,. \tag{3.11}$$

Comparing Eq. (3.11) to Eq. (3.6), we obtain the apparent compliance tensor as function of the phase stress concentration tensors

$$\boldsymbol{M}_A = \sum_{i=1}^{n} \mathrm{vf}_i \, \boldsymbol{M}_i : \boldsymbol{K}_i^{(\boldsymbol{\sigma},A)} \,. \tag{3.12}$$

All Eshelby-based homogenization methods, the Reuss technique, and the Voigt technique, introduced in Section 3.6, will be based on Eq. (3.10) or Eq. (3.12).

3.3.2 Apparent versus effective properties for RVE-based homogenization methods

For RVE-based homogenization methods we call our coarse-scale properties *effective* rather than *apparent*, if

- the volume element V is equal or larger than the RVE,
- the material is statistically homogeneous,
- the coarse-scale stiffness tensor $\boldsymbol{C}_A$ is independent of the boundary conditions applied on V (this holds if Eq. (3.5) holds for all feasible pairs of $(\boldsymbol{\sigma}, \boldsymbol{\varepsilon})$),

see below for a definition of the RVE and the property of statistical homogeneity. In particular, the coarse-scale stiffness tensor $\boldsymbol{C}_A$ is said to be the effective stiffness tenor. An effective stiffness tensor, in contrast to an apparent stiffness tensor, is homogeneous at the coarse scale. Using the RVE-based homogenization method we aim generally to find effective rather than apparent stiffness tensors. However, except for in a few occasions, the materials under investigation in this thesis will be not statistically homogeneous. Thus, generally, the coarse-scale elastic properties derived will be apparent and not effective.

RVE: There exist different concepts of RVEs see, for instance, Nemat-Nasser and Hori (1999) for an overview of them. In this thesis we consider a volume element V an RVE if it is a "representative" part of the material, i.e. it can be assumed that the properties of the RVE reflect those of the whole material. As such its size, l_m, needs to be large compared to the characteristic length of the heterogeneities, l_f, but also small to the characteristic size of the material l_c. In other words, the scale separation needs to be sufficient, i.e. $l_f \ll l_m \ll l_c$.

Statistical homogeneity A material which is heterogeneous at the fine scale, can be heterogeneous or homogeneous at the coarse scale. In general, the apparent stiffness tensor of a material which is heterogeneous at the coarse scale, will differ in any two coarse-scale points. However, if the material possesses the property of statistical homogeneity the apparent stiffness tensor is constant throughout the material.

There exists different definitions of the property of statistically homogeneity. For instance, Nemat-Nasser and Hori (1999) define a composite material to be statistically homogeneous if the probability of finding a phase at a point does not depend on the point itself. In this thesis, we rely on the definition presented in Parnell (2004). According to this definition a material is statistically homogeneous if the statistical distribution of the heterogeneities within any RVE is the same. As a consequence thereof, each RVE, wherever it may be located within the material, has the same average stress, average strain and apparent stiffness tensor. In particular, the apparent stiffness tensor of the material will be homogeneous at the coarse scale.

3.3.3 Hill-Mandel condition for the RVE-based homogenization method

Homogenization of a statistically homogeneous material over an RVE may be also thought of as the process of replacing a complex heterogeneous material by a simple 'energetically equivalent' homogeneous one. A simple but important condition under which the homogeneous and the heterogeneous material are energetically equivalent, is the Hill-Mandel condition, compare Nemat-Nasser and Hori (1999, section 2.3).

Let there be given a statistically homogeneous material, an RVE V and some boundary conditions prescribed on the boundary Γ_V. The most important boundary conditions in the context of RVE-based homogenization are

$$\boldsymbol{u} = \breve{\boldsymbol{\varepsilon}}\,\boldsymbol{x}, \quad \boldsymbol{x} \in \Gamma_V, \tag{3.13a}$$

$$\boldsymbol{\sigma}\,\boldsymbol{n} = \boldsymbol{t} = \breve{\boldsymbol{\sigma}}\,\boldsymbol{n}, \quad \boldsymbol{x} \in \Gamma_V, \tag{3.13b}$$

where we assume that $\breve{\boldsymbol{\varepsilon}}$ and $\breve{\boldsymbol{\sigma}}$ are constant strain and stress tensors, respectively.

The Hill-Mandel condition requires that the coarse-scale strain energy $W_{\mathcal{M}_V(\boldsymbol{\varepsilon})}$ equals the average of the fine-scale strain energy $\mathcal{M}_V(W_{\boldsymbol{\varepsilon}})$, i.e $W_{\mathcal{M}_V(\boldsymbol{\varepsilon})} = \mathcal{M}_V(W_{\boldsymbol{\varepsilon}})$. It follows

$$\mathcal{M}_V(\boldsymbol{\varepsilon}) : \mathcal{M}_V(\boldsymbol{\sigma}) = \mathcal{M}_V(\boldsymbol{\varepsilon} : \boldsymbol{\sigma}), \tag{3.14}$$

where we recall that the strain energy was defined in Definition 2.2.2, we make use of Hooke's law at the coarse scale, $\boldsymbol{C}_A : \mathcal{M}_V(\boldsymbol{\varepsilon}) = \mathcal{M}_V(\boldsymbol{\sigma})$, we employ Hooke's law at the fine scale, $\boldsymbol{C} : \boldsymbol{\varepsilon} = \boldsymbol{\sigma}$ and multiply the resulting equations by $2/|V|$. Interpreting Eq. (3.14), we can say that the Hill-Mandel condition requires that the product of the average stress and the average strain equals the average of the product of stress and strain.

It was Hill (1967), who proved that the boundary conditions of type (3.13a) and (3.13b) fulfill the Hill-Mandel condition. A straight forward application of the Hill-Mandel condition together with a reasoning similar as in Section 2.2.3 and Section 2.2.4, shows that the apparent stiffness tensor derived is positive definite and fulfills minor and major symmetries.

3.3.4 Average stress and average strain theorem

Following Zohdi and Wriggers (2008) we state the average strain theorem and the average stress theorem below. Note that these theorems are valid irrespective of whether the volume element V is an RVE.

Theorem 3.3.1 (Average strain theorem) *Let V contain perfectly bonded heterogeneities. Moreover, let $\boldsymbol{u}$ satisfy the equations of static linear elasticity (Problem 2.2.3) on V, with displacement boundary conditions* (3.13a) *on boundary Γ_V. Then the average strain is given by*

$$\mathcal{M}_V(\boldsymbol{\varepsilon}) = \breve{\boldsymbol{\varepsilon}}.$$

Proof. We make use of the relations

$$\int_V \nabla \boldsymbol{t}\, \mathrm{d}\boldsymbol{x} = \int_{\Gamma_V} \boldsymbol{t} \otimes \boldsymbol{n}\, \mathrm{d}\boldsymbol{s} \quad \text{and} \quad \int_V (\nabla \boldsymbol{t})^T\, \mathrm{d}\boldsymbol{x} = \int_{\Gamma_V} \boldsymbol{n} \otimes \boldsymbol{t}\, \mathrm{d}\boldsymbol{s}, \tag{3.15}$$

where $\boldsymbol{t}, \boldsymbol{n} \in \mathbb{R}^3$ and $\otimes$ denotes the tensor product of two first-order tensors, defined by Eq. (2.18). Note that Eq. (3.15) follows, when applying the divergence theorem to the tensors $T_{ijk} = t_i\, \mathrm{id}_{\mathrm{jk}}$ and $T_{ijk} = t_j\, \mathrm{id}_{\mathrm{ik}}$.

The proof of Theorem 3.3.1 is a straightforward two-fold application of the divergence theorem. Prescribing boundary conditions of type (3.13a) on the boundary Γ_V, we obtain

$$\begin{aligned}\mathcal{M}_V(\boldsymbol{\varepsilon}) &= \frac{1}{|V|}\int_V \boldsymbol{\varepsilon}\,\mathrm{d}\boldsymbol{x} = \frac{1}{|2V|}\int_V \left(\nabla\boldsymbol{u} + (\nabla\boldsymbol{u})^T\right)\mathrm{d}\boldsymbol{x} \\ &= \frac{1}{|2V|}\int_{\Gamma_V} (\boldsymbol{u}\otimes\boldsymbol{n} + \boldsymbol{n}\otimes\boldsymbol{u})\,\mathrm{d}\boldsymbol{s} = \frac{1}{|2V|}\int_{\Gamma_V} ((\check{\boldsymbol{\varepsilon}}\,\boldsymbol{x})\otimes\boldsymbol{n} + \boldsymbol{n}\otimes(\check{\boldsymbol{\varepsilon}}\,\boldsymbol{x}))\,\mathrm{d}\boldsymbol{s} \\ &= \frac{1}{|2V|}\int_V \left(\nabla(\check{\boldsymbol{\varepsilon}}\,\boldsymbol{x}) + (\nabla(\check{\boldsymbol{\varepsilon}}\,\boldsymbol{x}))^T\right)\mathrm{d}\boldsymbol{x} = \frac{1}{|V|}\int_V \check{\boldsymbol{\varepsilon}}\,\mathrm{d}\boldsymbol{x} = \check{\boldsymbol{\varepsilon}}.\end{aligned} \tag{3.16}$$

Here, we make use of the definition of the strain (see Eq. (2.40)) and the relations (3.15). Finally, we insert in Eq. (3.16) the displacement boundary conditions (3.13a). □

It is worth to note here that, if the heterogeneities within V are not perfectly bonded, some discontinuity terms enter Eq. (3.16). Then $\mathcal{M}_V(\boldsymbol{\varepsilon}) \neq \check{\boldsymbol{\varepsilon}}$, see Zohdi and Wriggers (2008) for details.

Theorem 3.3.2 (Average stress theorem) *Let $\boldsymbol{u}$ satisfy the equations of static linear elasticity (Problem 2.2.3) on V, with traction boundary conditions* (3.13b) *on boundary Γ_V. Then the average stress is given by*

$$\mathcal{M}_V(\boldsymbol{\sigma}) = \check{\boldsymbol{\sigma}} + \frac{1}{|V|}\int_V \boldsymbol{f}\otimes\boldsymbol{x}\,\mathrm{d}\boldsymbol{x}.$$

Proof. Consider the identity

$$\operatorname{div}(\boldsymbol{\sigma}\otimes\boldsymbol{x}) = \boldsymbol{\sigma}\,\nabla\boldsymbol{x} + \operatorname{div}\boldsymbol{\sigma}\otimes\boldsymbol{x} = \boldsymbol{\sigma} - \boldsymbol{f}\otimes\boldsymbol{x}. \tag{3.17}$$

This identity follows from $\operatorname{div}\boldsymbol{\sigma} = -\boldsymbol{f}$ and $\nabla\boldsymbol{x} = \mathbf{id}$. Then

$$\begin{aligned}\mathcal{M}_V(\boldsymbol{\sigma}) &= \frac{1}{|V|}\int_V \boldsymbol{\sigma}\,\mathrm{d}\boldsymbol{x} = \frac{1}{|V|}\int_V \operatorname{div}(\boldsymbol{\sigma}\otimes\boldsymbol{x})\,\mathrm{d}\boldsymbol{x} + \frac{1}{|V|}\int_V \boldsymbol{f}\otimes\boldsymbol{x}\,\mathrm{d}\boldsymbol{x} \\ &= \frac{1}{|V|}\int_{\Gamma_V} (\boldsymbol{\sigma}\otimes\boldsymbol{x})\boldsymbol{n}\,\mathrm{d}\boldsymbol{s} + \frac{1}{|V|}\int_V \boldsymbol{f}\otimes\boldsymbol{x}\,\mathrm{d}\boldsymbol{x} = \frac{1}{|V|}\int_{\Gamma_V} (\check{\boldsymbol{\sigma}}\otimes\boldsymbol{x})\boldsymbol{n}\,\mathrm{d}\boldsymbol{s} + \frac{1}{|V|}\int_V \boldsymbol{f}\otimes\boldsymbol{x}\,\mathrm{d}\boldsymbol{x} \\ &= \frac{1}{|V|}\int_V \operatorname{div}(\check{\boldsymbol{\sigma}}\otimes\boldsymbol{x})\,\mathrm{d}\boldsymbol{x} + \frac{1}{|V|}\int_V \boldsymbol{f}\otimes\boldsymbol{x}\,\mathrm{d}\boldsymbol{x} = \frac{1}{|V|}\int_V \check{\boldsymbol{\sigma}}\,\mathrm{d}\boldsymbol{x} + \frac{1}{|V|}\int_V \boldsymbol{f}\otimes\boldsymbol{x}\,\mathrm{d}\boldsymbol{x} \\ &= \check{\boldsymbol{\sigma}} + \frac{1}{|V|}\int_V \boldsymbol{f}\otimes\boldsymbol{x}\,\mathrm{d}\boldsymbol{x}.\end{aligned}$$

Here, we first use the identity (3.17), employ then the divergence theorem and insert the traction boundary conditions (3.13b). Finally, we apply the divergence theorem again, and make use of $\operatorname{div}(\check{\boldsymbol{\sigma}}\otimes\boldsymbol{x}) = \check{\boldsymbol{\sigma}}$, which holds since $\check{\boldsymbol{\sigma}}$ is constant throughout V. □

3.4 Methods in periodic homogenization

We first present the general idea of the asymptotic homogenization method (Section 3.4.1). Hereinafter, we apply this formalism to the equations of static and dynamic linear elasticity. In doing so, we mainly follow Cioranescu and Donato (1999), Auriault et al. (2010), Sanchez-Palencia (1986) and Francu (1982). For both types of equations we obtain homogenized problems, whose effective stiffness

tensors depends on so-called cell problems. The main difficulty of solving the homogenized problems lies in finding the solutions to the cell problems.

In Section 3.4.2 we consider the equations of static linear elasticity for arbitrary periodic materials. For these materials, in general, no explicit formula of the cell problem solution exists, and hence the corresponding cell problems needs to be solved numerically. To this end, we present a numerical approach to which we will refer to as *AHA method* in the following. Note that AHA stands for Asymptotic Homogenization method for Arbitrary periodic materials.

Finally, in Section 3.4.3 we move to fibre-reinforced periodic materials. For these materials exist semi-analytical formulas for the cell problem solutions. We review the results of Parnell and Abrahams (2008, 2006) who determined the effective properties of fibre-reinforced periodic materials, applying the asymptotic homogenization formalism to the equations of dynamic linear elasticity. In order to distinguish the latter approach from the AHA method, we call it the *AHF method*, where AHF stands for Asymptotic Homogenization method for Fibre-reinforced periodic materials, in the following.

Before we start, let us recall the basic assumptions in periodic homogenization. We assume that our material A is periodic with periodic cell V. Moreover, we let the local stiffness tensor to be V-periodic, see Section 3.1 for details.

3.4.1 Basics of the asymptotic homogenization method

Assuming that a coarse and a fine scale (meso scale) exists, we define two coordinate systems, $\mathcal{Z}$ and $\mathcal{Y}$, associated with the coarse and the fine scale, respectively. The coordinates of $\mathcal{Z}$ and $\mathcal{Y}$ are given respectively by

$$z_i, \quad y_i = \frac{z_i}{s}, \quad \text{for } i = 1,2,3, \tag{3.18}$$

where $s = l_m/l_c$ refers to the scale ratio. Note that we consider $\boldsymbol{z}$ and $\boldsymbol{y}$ to be independent variables. The idea of the asymptotic homogenization method is to approximate the displacement $\boldsymbol{u}^s(\boldsymbol{z},t)$ in the equations of dynamic (static) linear elasticity (Eq. (3.1)) by an asymptotic expansion

$$\boldsymbol{u}^s(\boldsymbol{z},t) = \boldsymbol{u}(\boldsymbol{z},\boldsymbol{y},t) = \boldsymbol{u_0}(\boldsymbol{z},\boldsymbol{y},t) + \frac{1}{s}\boldsymbol{u_1}(\boldsymbol{z},\boldsymbol{y},t) + \frac{1}{s^2}\boldsymbol{u_2}(\boldsymbol{z},\boldsymbol{y},t) + \frac{1}{s^3}\boldsymbol{u_3}(\boldsymbol{z},\boldsymbol{y},t) + \dots . \tag{3.19}$$

We assume that the unknown functions $\boldsymbol{u_i} : \Omega \times V \times \mathbb{R} \to \mathbb{R}^3$, $i = 0,1,2,3,\dots$ are smooth and V-periodic in the variable $\boldsymbol{y}$. Since $\boldsymbol{C}^s(\boldsymbol{z})$ is V-periodic, we have $\boldsymbol{C}^s(\boldsymbol{z}) = \boldsymbol{C}(\boldsymbol{z}/s) = \boldsymbol{C}(\boldsymbol{y})$.

Before we start, we note that for any function $\boldsymbol{\Psi}^s(\boldsymbol{z},t) = \boldsymbol{\Psi}(\boldsymbol{z},\boldsymbol{y},t)$ the matrix $\nabla\boldsymbol{\Psi}^s(\boldsymbol{z},t)$ is given by

$$\nabla_{\boldsymbol{z}}\boldsymbol{\Psi}^s(\boldsymbol{z},t) = \nabla_{\boldsymbol{z}}\boldsymbol{\Psi}(\boldsymbol{z},\boldsymbol{y},t) + \frac{1}{s}\nabla_{\boldsymbol{y}}\boldsymbol{\Psi}(\boldsymbol{z},\boldsymbol{y},t), \tag{3.20}$$

where $\nabla_{\boldsymbol{z}}\boldsymbol{\Psi}$ and $\nabla_{\boldsymbol{y}}\boldsymbol{\Psi}$ denote the matrix of partial derivatives of Ψ with respect to the variables $\boldsymbol{z}$ and $\boldsymbol{y}$, respectively. Likewise, a similar relation holds for the divergence of $\boldsymbol{\Psi}^s(\boldsymbol{z},t)$

$$\operatorname{div}_{\boldsymbol{z}}\boldsymbol{\Psi}^s(\boldsymbol{z},t) = \operatorname{div}_{\boldsymbol{z}}\boldsymbol{\Psi}(\boldsymbol{z},\boldsymbol{y},t) + \frac{1}{s}\operatorname{div}_{\boldsymbol{y}}\boldsymbol{\Psi}(\boldsymbol{z},\boldsymbol{y},t). \tag{3.21}$$

Inserting the asymptotic expansion (3.19) into the equations of dynamic (static) linear elasticity (Eq. (3.1)) and making use of Eq. (3.20) and Eq. (3.21) for $\boldsymbol{\Psi}^s = \boldsymbol{u}^s$, we obtain an equation with terms of different order in s. Equating terms of equal-order with zero, gives rise to a cascade of equations for $\boldsymbol{u_i}$.

Homogenized equations of static linear elasticity: We now apply the asymptotic homogenization

technique, described above, to the equations of static linear elasticity (Problem 2.2.3) on some arbitrary periodic material. Solving successively the corresponding cascade of equations, we obtain the homogenized problem

$$\operatorname{div}_z \left(\boldsymbol{C}_A : \nabla_z \boldsymbol{u}_0(\boldsymbol{z}) \right) = -\boldsymbol{f}(\boldsymbol{z}), \quad \boldsymbol{z} \in \Omega, \tag{3.22}$$

$$+ \text{ appropriate boundary conditions}, \tag{3.23}$$

where the stiffness tensor $\boldsymbol{C}_A$ is given by

$$(\boldsymbol{C}_A)_{ijkl} := \mathcal{M}_V \left(C_{ijmn}(\boldsymbol{y}) \frac{\partial w_m^{kl}(\boldsymbol{y})}{\partial y_n} \right) \quad \text{for} \quad \boldsymbol{y} \in V, \quad i,j,k,l,m,n = 1,2,3, \tag{3.24}$$

and $\boldsymbol{w}^{kl}$ is the solution of cell problem CP^{kl}

$$\begin{aligned} &\operatorname{div}_y \left(\boldsymbol{C}(\boldsymbol{y}) : \nabla_y \boldsymbol{w}^{kl}(\boldsymbol{y}) \right) = 0, \quad \boldsymbol{y} \in V, \\ &\boldsymbol{w}^{kl}(\boldsymbol{y}) - \boldsymbol{p}^{kl}(\boldsymbol{y}) \qquad V\text{-periodic}, \\ &\mathcal{M}_V(\boldsymbol{w}^{kl}(\boldsymbol{y}) - \boldsymbol{p}^{kl}(\boldsymbol{y})) = 0, \end{aligned} \tag{3.25}$$

with $p_m^{kl}(\boldsymbol{y}) := y_l \, \delta_{mk}$. For any combination of k and l, cell problem CP^{kl} admits a unique weak solution in $W^1_{\text{per}}(V)$ (Theorem 2.3.7).

In order to determine $\boldsymbol{C}_A$ it is sufficient to solve six out of the nine cell problems (3.25). This is because $\boldsymbol{C}_A$ satisfies minor symmetries, i.e. $(\boldsymbol{C}_A)_{ijkl} = (\boldsymbol{C}_A)_{ijlk}$, and, hence, the solutions of the cell problems CP^{kl} and CP^{lk} determine the same components of $\boldsymbol{C}_A$. We consider here the cell problems CP^{kl} for which $k \leq l$ holds, i.e. we solve the cell problems CP^{kl} with $(k,l) = (1,1)$, $(1,2)$, $(1,3)$, $(2,2)$, $(2,3)$, $(3,3)$. For simplicity in notation, the solutions, strains and stresses of these cell problems, i.e. $\boldsymbol{w}^{kl}$, $\boldsymbol{\varepsilon}(\boldsymbol{w}^{kl})$ and $\boldsymbol{\sigma}(\boldsymbol{w}^{kl})$, are respectively denoted, by $\boldsymbol{w}_i$, $\boldsymbol{\varepsilon}_i := \boldsymbol{\varepsilon}(\boldsymbol{w}_i)$ and $\boldsymbol{\sigma}_i := \boldsymbol{\sigma}(\boldsymbol{w}_i)$, where $i = \Psi_1(k,l) \in \{1,2,\ldots,6\}$ with the index map Ψ_1 given by Table 2.1. In summary, we consider the cell problems

$$\begin{aligned} &\operatorname{div}_y \left(\boldsymbol{C}(\boldsymbol{y}) : \nabla_y \boldsymbol{w}_i(\boldsymbol{y}) \right) = 0, \quad \boldsymbol{y} \in V, \\ &\widetilde{\boldsymbol{w}}_i(\boldsymbol{y}) \qquad V\text{-periodic} \\ &\mathcal{M}_V(\widetilde{\boldsymbol{w}}_i(\boldsymbol{y})) = 0. \end{aligned} \tag{3.26}$$

with $i \in \{1,2,\ldots,6\}$, and $\widetilde{\boldsymbol{w}}_i(\boldsymbol{y})$ given by

$$\begin{aligned} &\widetilde{\boldsymbol{w}}_1(\boldsymbol{y}) = \boldsymbol{w}_1(\boldsymbol{y}) - y_1 \boldsymbol{e}_1, \quad \widetilde{\boldsymbol{w}}_2(\boldsymbol{y}) = \boldsymbol{w}_2(\boldsymbol{y}) - y_2 \boldsymbol{e}_2, \quad \widetilde{\boldsymbol{w}}_3(\boldsymbol{y}) = \boldsymbol{w}_3(\boldsymbol{y}) - y_3 \boldsymbol{e}_3, \\ &\widetilde{\boldsymbol{w}}_4(\boldsymbol{y}) = \boldsymbol{w}_4(\boldsymbol{y}) - y_3 \boldsymbol{e}_2, \quad \widetilde{\boldsymbol{w}}_5(\boldsymbol{y}) = \boldsymbol{w}_5(\boldsymbol{y}) - y_3 \boldsymbol{e}_1, \quad \widetilde{\boldsymbol{w}}_6(\boldsymbol{y}) = \boldsymbol{w}_6(\boldsymbol{y}) - y_2 \boldsymbol{e}_1, \end{aligned} \tag{3.27}$$

where $\boldsymbol{e}_1, \boldsymbol{e}_2$ and $\boldsymbol{e}_3$ denote the vectors $(1,0,0)^T$, $(0,1,0)^T$ and $(0,0,1)^T$, respectively.

Note that the stiffness tensor $\boldsymbol{C}_A$ neither depends on the chosen domain Ω nor on the boundary conditions prescribed on the boundary of Ω. In view of the RVE-based or the Eshelby-based homogenization (Section 3.3.1), it thus makes sense to speak of $\boldsymbol{C}_A$ as effective rather than as apparent stiffness tensor.

Furthermore, note that $\boldsymbol{C}_A$ is constant throughout Ω, it is positive definite and satisfies minor and major symmetries (Cioranescu and Donato, 1999). The equation for determining $\boldsymbol{C}_A$, i.e. Eq. (3.24), can be reformulated to

$$(\boldsymbol{C}_A)_{mnkl} = \mathcal{M}_V \left((\boldsymbol{C}(\boldsymbol{y}) : \boldsymbol{\varepsilon}_i)_{mn} \right) = \mathcal{M}_V \left((\boldsymbol{\sigma}_i)_{mn} \right), \quad m,n = 1,2,3, \quad i = \Psi_1(k,l) = 1,2,\ldots,6. \tag{3.28}$$

Finally, it is worth to note that

$$\mathcal{M}_V\left(\boldsymbol{\sigma}_i\right) = \boldsymbol{C}_A : \mathcal{M}_V\left(\boldsymbol{\varepsilon}_i\right) \quad \text{with} \quad \mathcal{M}_V\left((\boldsymbol{\varepsilon}_{\Psi_1(k,l)})_{mn}\right) = \frac{1}{2}(\delta_{ln}\delta_{km} + \delta_{lm}\delta_{kn}), \quad i = \Psi_1(k,l) = 1,2,\ldots,6, \tag{3.29}$$

holds, see Appendix B for a proof. In line with the RVE-based homogenization theory (Section 3.3.1), we call $\mathcal{M}_V(\boldsymbol{\sigma}_i)$ average stress and $\mathcal{M}_V(\boldsymbol{\varepsilon}_i)$ average strain. Representing all average stresses and average strains in Voigt notation, we collect the corresponding vectors, denoted again by $\mathcal{M}_V(\boldsymbol{\sigma}_i)$ and $\mathcal{M}_V(\boldsymbol{\varepsilon}_i)$, in two matrices, $\left[\mathcal{M}_V(\boldsymbol{\sigma}_1),\ldots,\mathcal{M}_V(\boldsymbol{\sigma}_6)\right]$ and $\left[\mathcal{M}_V(\boldsymbol{\varepsilon}_1),\ldots,\mathcal{M}_V(\boldsymbol{\varepsilon}_6)\right]$. Then, the first relations in Eq. (3.29) read in compact form

$$\left[\mathcal{M}_V(\boldsymbol{\sigma}_1),\ldots,\mathcal{M}_V(\boldsymbol{\sigma}_6)\right] = \boldsymbol{C}_A\left[\mathcal{M}_V(\boldsymbol{\varepsilon}_1),\ldots,\mathcal{M}_V(\boldsymbol{\varepsilon}_6)\right], \tag{3.30}$$

where $\boldsymbol{C}_A$ is unknown and given in Voigt notation. Due to the second relations in Eq. (3.29), which read in compact form $\left[\mathcal{M}_V(\boldsymbol{\varepsilon}_1),\ldots,\mathcal{M}_V(\boldsymbol{\varepsilon}_6)\right] = \mathbf{id}$ with $\mathbf{id}$ the identity matrix in $\mathbb{R}^{6\times6}$, Eq. (3.30) becomes

$$\left[\mathcal{M}_V(\boldsymbol{\sigma}_1),\ldots,\mathcal{M}_V(\boldsymbol{\sigma}_6)\right] = \boldsymbol{C}_A. \tag{3.31}$$

Note that although equation $\left[\mathcal{M}_V(\boldsymbol{\varepsilon}_1),\ldots,\mathcal{M}_V(\boldsymbol{\varepsilon}_6)\right] = \mathbf{id}$ holds analytically, it may not hold numerically. This is because, we compute $\mathcal{M}_V(\boldsymbol{\varepsilon}_1)$ to $\mathcal{M}_V(\boldsymbol{\varepsilon}_6)$ using the finite element method and numerical integration.

Homogenized equations of dynamic linear elasticity: We now apply the asymptotic homogenization method to the equations of dynamic linear elasticity (Problem 2.2.7). Therefore, we consider some periodic material A and assume that zero volume forces apply to it. Moreover, we let time-harmonic waves of low frequency ω propagate through our material, i.e. we assume that the displacement $\boldsymbol{u}^s$ takes a periodic or sinusoidal form, i.e. it is given by $\boldsymbol{u}^s(\boldsymbol{z},t) = \tilde{\boldsymbol{u}}(\boldsymbol{z})\exp(i\omega t)$, where $\tilde{\boldsymbol{u}}(\boldsymbol{z})$ denotes some function independent of t. By construction, $\nabla\boldsymbol{u}^s$ and $\partial^2\boldsymbol{u}^s/\partial t^2$ become $\nabla\boldsymbol{u}^s = \nabla\tilde{\boldsymbol{u}}(\boldsymbol{z})\exp(i\omega t)$ and $\partial^2\boldsymbol{u}^s/\partial t^2 = -\omega^2\boldsymbol{u}^s$, respectively. Hence, all terms in Eq. (3.1) include the nonzero factor $\exp(i\omega t)$, which we suppress henceforth. The resulting displacement in Eq. (3.1) is a function of the spatial variable $\boldsymbol{z}$ only and is denoted again by $\boldsymbol{u}^s$.

Substituting the second time derivative of the displacement into Eq. (3.1) we obtain

$$\operatorname{div}(\boldsymbol{C}^s(\boldsymbol{z}) : \nabla\boldsymbol{u}^s(\boldsymbol{z})) = -\omega^2\rho^s(\boldsymbol{z})\,\boldsymbol{u}^s(\boldsymbol{z}), \quad \boldsymbol{z}\in\Omega, \tag{3.32}$$

where we set $\boldsymbol{C}^s(\boldsymbol{z}) = \boldsymbol{C}(\boldsymbol{y})$, $\rho^s(\boldsymbol{z}) = \rho(\boldsymbol{y})$ and $\boldsymbol{u}^s(\boldsymbol{z}) = \boldsymbol{u}(\boldsymbol{z},\boldsymbol{y})$. Non-dimensionalizing Eq. (3.32) and inserting the asymptotic expansion (3.19) into Eq. (3.32), one proceeds analogous to the equations of static linear elasticity. This yields the homogenized problem (Parnell and Abrahams, 2008)

$$\operatorname{div}(\boldsymbol{C}_A : \nabla\boldsymbol{u_0}(\boldsymbol{z})) = -\rho_A\,\boldsymbol{u_0}(\boldsymbol{z}), \quad \boldsymbol{z}\in\Omega, \tag{3.33}$$

where $\boldsymbol{C}_A$ and ρ_A denote the effective stiffness tensor and the effective density, respectively. Note that, analogous to the equations of static linear elasticity, $\boldsymbol{C}_A$ in Eq. (3.33) is determined based on some cell problems, see Parnell and Abrahams (2008) for details.

3.4.2 AHA method

In general, that is for arbitrary periodic material, there is no analytical formula for the solution to the cell problem CP^{kl} of the homogenized equations of static linear elasticity, defined in (3.25). It is natural to approximate that solution numerically. In order to obtain an approximation to the effective stiffness tensor $\boldsymbol{C}_A$, given by (3.24), we perform the following steps

- Fix some periodic cell V.
- For $k \leq l$ solve cell problems CP^{kl} (problem (3.26)) on V numerically (finite elements, finite differences, ...). This yields approximate solutions $\boldsymbol{w}_i$, $i = 1, 2, \ldots, 6$ to cell problems CP^{kl}, with corresponding stresses $\boldsymbol{\sigma}_i = \boldsymbol{\sigma}(\boldsymbol{w}_i)$ and strains $\boldsymbol{\varepsilon}_i = \boldsymbol{\varepsilon}(\boldsymbol{w}_i)$.
- Compute the average stresses $\mathcal{M}_V(\boldsymbol{\sigma}_i)$ and the average strains $\mathcal{M}_V(\boldsymbol{\varepsilon}_i)$ for $i = 1, 2, \ldots, 6$. Represent all of them as vectors using Voigt notation.
- Setup the linear system (3.30) and solve it for $\boldsymbol{C}_A$.

We refer to this approach as AHA method, where AHA stands for Asymptotic Homogenization method for Arbitrary periodic materials. The effective stiffness tensor, derived by this approach, is denoted by $\boldsymbol{C}_{\text{AHA}}$ in the following.

3.4.3 AHF method

On domains Ω which are occupied by fibre-reinforced periodic materials, there exist semi-analytical solutions to cell problems of the homogenized equations of dynamic linear elasticity (Section 3.4.1). To this end we shortly review the results of Parnell and Abrahams (2008, 2006) and Parnell and Grimal (2009).

Parnell and Abrahams (2008) assume that only waves with low frequencies ω travel through the composite. They consider some periodic material A, which consists of two phases and occupies the domain Ω. A typical periodic cell V is of size l_m and is made up of a hexagonal matrix phase, A_0, in which several infinitely long cylinders, A_1, at arbitrary locations are embedded. Both phases are linear elastic and isotropic with corresponding Lamé coefficients, μ_0, λ_0 and μ_1, λ_1. The phases A_0 and A_1 have the densities, ρ_0 and ρ_1, and occupy the domains, V_0 and V_1, respectively. It holds that $V_0 \cup V_1 \coloneqq V$. The fine scale of material A is characterized by the size of the periodic cell, l_m, the material's coarse scale is characterized by the wavelength of the wave traveling through the material, denoted by l_c and given by $l_c = 1/\omega$. Finally, it is assumed that the y_3-axis of the three-dimensional fine-scale Cartesian coordinate system $\mathcal{Y}$ is parallel to the cylinder.

The scale ratio is given by

$$s \coloneqq \sqrt{\frac{\rho_0 \, l_m^2}{l_c^2 \, \mu_0}}.$$

Since by assumption only waves with low frequencies travel through the composite, i.e. $l_m \ll l_c$, the scale separation is sufficient. Thus, the asymptotic homogenization technique can be applied.

Employing this technique, as described in Section 3.4.1, a number of cell problems arise. The nontrivial ones were treated by Parnell and Abrahams (2008, 2006) using complex variable theory and multipole expansions[1] in specific V-periodic functions. These authors truncated the multipole expansions at a finite number of terms, n_{terms}, yielding a truncated system of equations for the solutions to the cell problems. Assuming that the cylinders have circular cross sections, the even terms of the multipole expansions are zero (Parnell and Abrahams, 2006). Hence, n_{terms} takes odd values only. Solving a linear system for these terms the truncated multipole expansion can be determined.

[1] The wave field resulting from a point source (multipole) may be expanded in a series in terms of a parameter which gets small as the distance of the source increases. This technique is called multipole expansion (Michaels, 1984; Kushch, 2013).

Having solved the cell problems, a homogenized problem of type (3.33) was derived. This problem is equivalent to the equations of dynamic linear elasticity for a homogeneous transverse isotropic elastic composite. Its transverse isotropic effective stiffness tensor $\boldsymbol{C}_A$ is given by,

$$\begin{aligned}
(\boldsymbol{C}_A)_{11} &= (1-\mathrm{vf})(q_0+2m_0)+\mathrm{vf}(q_1+2m_1)\\
&\quad +[(q_1-q_0)+2(m_1-m_0)]Q_1+(q_1-q_0)Q_2,\\
(\boldsymbol{C}_A)_{12} &= (1-\mathrm{vf})q_0+\mathrm{vf}\,q_1+(q_1-q_0)Q_1\\
&\quad +[(q_1-q_0)+2(m_1-m_0)]Q_2,\\
(\boldsymbol{C}_A)_{13} &= (1-\mathrm{vf})q_0+\mathrm{vf}\,q_1+(q_1-q_0)(Q_1-Q_2),\\
(\boldsymbol{C}_A)_{33} &= (1-\mathrm{vf})(q_0+2m_0)+\mathrm{vf}(q_1+2m_1)+(q_1-q_0)Q_3,\\
(\boldsymbol{C}_A)_{44} &= (1-\mathrm{vf})m_0+\mathrm{vf}\,m_1+(m_1-m_0)Q_4,
\end{aligned} \tag{3.34}$$

where $\mathrm{vf}=|V_1|/|V|$ refers to the volume fraction of phase A_1; compare Parnell and Abrahams (2008) or Parnell and Grimal (2009). The quantities Q_i for $i=1,2,3,4$ refer to line integrals of the solutions to the cell problems, and the two quantities, $q(\boldsymbol{y})$ and $m(\boldsymbol{y})$, are given by

$$q(\boldsymbol{y})=\begin{cases} q_0=\frac{\lambda_0}{\mu_0} & \boldsymbol{y}\in V_0\\ q_1=\frac{\lambda_1}{\mu_0} & \boldsymbol{y}\in V_1\end{cases} \quad \text{and} \quad m(\boldsymbol{y})=\begin{cases} m_0=1 & \boldsymbol{y}\in V_0\\ m_1=\frac{\mu_1}{\mu_0} & \boldsymbol{y}\in V_1\end{cases}, \tag{3.35}$$

respectively. In what follows, we call the approach described above AHF method, where AHF stands for Asymptotic Homogenization method for Fibre-reinforced materials. The effective stiffness tensor derived by this method, is denoted by $\boldsymbol{C}_{\mathrm{AHF}}$.

3.5 Methods in RVE-based homogenization

In this section we focus on the RVE-based homogenization method, introduced in Section 3.1. We briefly present the method's approach and discuss this method for different boundary conditions. In particular, we look at displacement boundary conditions (3.13a) and traction boundary conditions (3.13b).

Let there be given some brick-shaped volume element V, not necessarily an RVE. In order to obtain the apparent stiffness tensor, $\boldsymbol{C}_A$, defined by Eq. (3.5), we setup a linear system for $\boldsymbol{C}_A$ as described below.

We numerically solve six different boundary value problems in static linear elasticity (Problem 2.2.4 or Problem 2.2.5). More precisely, we solve

$$\begin{aligned}
\mathrm{div}(\boldsymbol{\sigma})&=0, \quad \boldsymbol{x}\in V,\\
\boldsymbol{\sigma}&=\boldsymbol{C}:\boldsymbol{\varepsilon},\\
\boldsymbol{\varepsilon}&=\frac{1}{2}(\nabla\boldsymbol{u}+\nabla\boldsymbol{u}^T),
\end{aligned} \tag{3.36a}$$

with boundary conditions of type either

$$\boldsymbol{u}_i=\breve{\boldsymbol{\varepsilon}}_i\,\boldsymbol{x}, \quad \boldsymbol{x}\in\Gamma_V, \tag{3.36b}$$

or

$$\boldsymbol{t}_i=\breve{\boldsymbol{\sigma}}_i\,\boldsymbol{n}, \quad \boldsymbol{x}\in\Gamma_V, \tag{3.36c}$$

where $i=1,2,\ldots,6$, and $\breve{\boldsymbol{\varepsilon}}_i=\breve{\boldsymbol{\sigma}}_i$ are constant second-order tensors, given by

$$\begin{aligned}
\breve{\boldsymbol{\varepsilon}}_1&=\begin{pmatrix}\beta&0&0\\0&0&0\\0&0&0\end{pmatrix}, \quad \breve{\boldsymbol{\varepsilon}}_2=\begin{pmatrix}0&0&0\\0&\beta&0\\0&0&0\end{pmatrix}, \quad \breve{\boldsymbol{\varepsilon}}_3=\begin{pmatrix}0&0&0\\0&0&0\\0&0&\beta\end{pmatrix},\\
\breve{\boldsymbol{\varepsilon}}_4&=\begin{pmatrix}0&0&0\\0&0&\beta\\0&\beta&0\end{pmatrix}, \quad \breve{\boldsymbol{\varepsilon}}_5=\begin{pmatrix}0&0&\beta\\0&0&0\\\beta&0&0\end{pmatrix}, \quad \breve{\boldsymbol{\varepsilon}}_6=\begin{pmatrix}0&\beta&0\\\beta&0&0\\0&0&0\end{pmatrix}.
\end{aligned} \tag{3.37}$$

Here, $\beta \neq 0$ is some arbitrary constant in $\mathbb{R}$. Note that the equations of static linear elasticity completed with traction boundary conditions (3.36c) admit a weak solution which is only unique up to rigid displacements $\boldsymbol{r} \in \mathcal{R}$, see Section 2.3 for details. We fix this degree of freedom, enforcing that

$$\mathcal{M}_V(\boldsymbol{u}_i) = 0. \tag{3.38}$$

Numerically solving the boundary value problems stated above, yields for each problem (i = 1, 2,. . . ,6) the approximate fine-scale displacements, $\boldsymbol{u}_i$, the approximate fine-scale strains, $\boldsymbol{\varepsilon}_i$, and the approximate fine-scale stresses, $\boldsymbol{\sigma}_i$. Based on Eq. (3.3) and Eq. (3.4) and, we derive the corresponding average strains $\mathcal{M}_V(\boldsymbol{\varepsilon}_i)$ and average stresses $\mathcal{M}_V(\boldsymbol{\sigma}_i)$, respectively. Now, since Eq. (3.5) should hold for any pair $(\mathcal{M}_V(\boldsymbol{\sigma}_i), \mathcal{M}_V(\boldsymbol{\varepsilon}_i))$ with $i = 1, 2, \ldots, 6$, we gain that the unknown apparent stiffness tensor $\boldsymbol{C}_A$, satisfies

$$\mathcal{M}_V(\boldsymbol{\sigma}_i) = \boldsymbol{C}_A : \mathcal{M}_V(\boldsymbol{\varepsilon}_i), \quad i = 1, 2, \ldots, 6. \tag{3.39}$$

These conditions can be summarized in a single compact linear system for the unknown $\boldsymbol{C}_A$. To this end, recall that any symmetric second-order tensor can be represented as a six-dimensional column vector using the Voigt notation, see Section 2.1.3. In particular, we can represent $\mathcal{M}_V(\boldsymbol{\sigma}_i)$ and $\mathcal{M}_V(\boldsymbol{\varepsilon}_i)$ as vectors. We denote these vectors by the same symbols, and collect them in two matrices, $\left[\mathcal{M}_V(\boldsymbol{\sigma}_1), \ldots, \mathcal{M}_V(\boldsymbol{\sigma}_6)\right]$ and $\left[\mathcal{M}_V(\boldsymbol{\varepsilon}_1), \ldots, \mathcal{M}_V(\boldsymbol{\varepsilon}_6)\right]$, and arrive at the following linear system

$$\left[\mathcal{M}_V(\boldsymbol{\sigma}_1), \ldots, \mathcal{M}_V(\boldsymbol{\sigma}_6)\right] = \boldsymbol{C}_A \left[\mathcal{M}_V(\boldsymbol{\varepsilon}_1), \ldots, \mathcal{M}_V(\boldsymbol{\varepsilon}_6)\right]. \tag{3.40}$$

Here, the apparent stiffness tensor $\boldsymbol{C}_A$ is given in Voigt notation.

We emphasize that $\boldsymbol{C}_A$, derived based on linear system (3.40), in general, depends on whether we prescribe boundary conditions of type (3.36b) or (3.36c) on the boundary Γ_V. We next discuss these two boundary conditions and the corresponding simplifications of the linear system (3.40).

If displacement boundary conditions of type (3.36b) are prescribed on the boundary Γ_V, the average strain $\mathcal{M}_V(\boldsymbol{\varepsilon}_i)$ is known for all $i = 1, 2, \ldots, 6$. Indeed, Theorem 3.3.1 states that $\mathcal{M}_V(\boldsymbol{\varepsilon}_i) = \breve{\boldsymbol{\varepsilon}}_i$ for all i. Hence, the linear system (3.40) simplifies to

$$\left[\mathcal{M}_V(\boldsymbol{\sigma}_1), \ldots, \mathcal{M}_V(\boldsymbol{\sigma}_6)\right] = \boldsymbol{C}_A \begin{bmatrix} \beta & 0 & 0 & 0 & 0 & 0 \\ 0 & \beta & 0 & 0 & 0 & 0 \\ 0 & 0 & \beta & 0 & 0 & 0 \\ 0 & 0 & 0 & 2\beta & 0 & 0 \\ 0 & 0 & 0 & 0 & 2\beta & 0 \\ 0 & 0 & 0 & 0 & 0 & 2\beta \end{bmatrix}. \tag{3.41}$$

In the following, we will denote the solution of linear system (3.41) also by $\boldsymbol{C}_{\mathrm{d}}$.

If traction boundary conditions of type (3.36c) are prescribed on the boundary Γ_V, the average stress $\mathcal{M}_V(\boldsymbol{\sigma}_i)$ is known for all $i = 1, 2, \ldots, 6$. Indeed, Theorem 3.3.2 states that $\mathcal{M}_V(\boldsymbol{\sigma}_i) = \breve{\boldsymbol{\sigma}}_i$ for all i. Thus, the linear system (3.40) simplifies to

$$\begin{bmatrix} \beta & 0 & 0 & 0 & 0 & 0 \\ 0 & \beta & 0 & 0 & 0 & 0 \\ 0 & 0 & \beta & 0 & 0 & 0 \\ 0 & 0 & 0 & \beta & 0 & 0 \\ 0 & 0 & 0 & 0 & \beta & 0 \\ 0 & 0 & 0 & 0 & 0 & \beta \end{bmatrix} = \boldsymbol{C}_A \left[\mathcal{M}_V(\boldsymbol{\varepsilon}_1), \ldots, \mathcal{M}_V(\boldsymbol{\varepsilon}_6)\right]. \tag{3.42}$$

In the following, we will denote the solution of linear system (3.42) also by $\boldsymbol{C}_{\mathrm{t}}$.

It is worth to note here, that $\boldsymbol{C}_{\mathrm{d}} - \boldsymbol{C}_{\mathrm{t}}$ is an indicator for whether the volume element V is an RVE. This is because of Eq. (3.76), presented in Section 3.7.

3.6 Methods in Eshelby-based homogenization and Voigt and Reuss techniques

Voigt and Reuss techniques (Voigt, 1888; Reuss, 1929) idealize the material under investigation such that the resulting apparent stiffness tensors are functions of the stiffness tensors of the material's constituents, their compliance tensors and their volume fractions; see Section 3.6.1 for details.

Eshelby-based homogenization methods idealize the material under investigation as an infinite composite A which consists of n homogeneous and perfectly bonded phases A_i, $i \in \{1,\dots,n\}$. In Section 3.6.2 we consider A to be a composite consisting of a matrix and a single heterogeneity. We reduce this problem to the matrix-inclusion problem stated by Eshelby (1957). The latter result is subject of Section 3.6.3. It has been reformulated since 1957 and we give it as in Gross and Seelig (2007) or Weinberger and Cai (2004). Hereinafter, in Section 3.6.4, we generalize to N-phase composites. Finally, we present various Eshelby-based homogenization techniques: the Dilute method, the Mori-Tanaka method (Mori and Tanaka, 1973), and the self-consistent method (Hill, 1965). For each method we briefly describe the corresponding assumptions on A and give the resulting apparent stiffness tensor, $\boldsymbol{C}_A$.

3.6.1 Voigt and Reuss techniques

Two well known techniques go back to Voigt (1888) and Reuss (1929). We present these techniques for the case of a two-phase composite.

Consider a composite A, which consists of the phases A_1 and A_2. The phase A_1, the phase A_2 and the composite A occupy the domains Ω_1, Ω_2 and $\Omega = \Omega_1 \cup \Omega_2$, respectively. We set $\mathrm{vf}_1 = |\Omega_1|/|\Omega|$, and $\mathrm{vf}_2 = |\Omega_2|/|\Omega|$. The stiffness tensor of phase A_1 and phase A_2 are denoted by $\boldsymbol{C}_1$ and $\boldsymbol{C}_2$, respectively.

Given that boundary conditions $\boldsymbol{u} = \breve{\boldsymbol{\varepsilon}}\,\boldsymbol{x}$ are prescribed on the boundary of Ω, Voigt assumed that the strain inside of each phase is constant and equals $\breve{\boldsymbol{\varepsilon}}$. This gives $\mathcal{M}_{\Omega_i}(\boldsymbol{\varepsilon}) = \breve{\boldsymbol{\varepsilon}}$ for $i = 1,2$. Using these equations and Theorem 3.3.1, we obtain $\mathcal{M}_{\Omega_i}(\boldsymbol{\varepsilon}) = \breve{\boldsymbol{\varepsilon}} = \mathcal{M}_{\Omega}(\boldsymbol{\varepsilon})$ for $i = 1,2$. Hence, the phase strain concentration tensor of A_i, defined by Eq. (3.7) and denoted $\boldsymbol{K}_i^{(\boldsymbol{\varepsilon},A)}$, is given by $\boldsymbol{K}_i^{(\boldsymbol{\varepsilon},A)} = \mathbf{Id}^{\mathbf{s}}$ for $i = 1,2$. Substituting $\boldsymbol{K}_i^{(\boldsymbol{\varepsilon},A)}$ into Eq. (3.10), we obtain the apparent stiffness tensor

$$\boldsymbol{C}_{\mathrm{Voigt}} = \mathrm{vf}_1\,\boldsymbol{C}_1 + \mathrm{vf}_2\,\boldsymbol{C}_2\,. \tag{3.43}$$

Note that $\boldsymbol{C}_{\mathrm{Voigt}}$ is the volume average of the phase stiffness tensors.

Given a material for which boundary conditions $\boldsymbol{t} = \breve{\boldsymbol{\sigma}}\,\boldsymbol{n}$ apply on the boundary, Reuss considered the stress inside each phase as constant and equal to $\breve{\boldsymbol{\sigma}}$. This gives $\mathcal{M}_{\Omega_i}(\boldsymbol{\sigma}) = \breve{\boldsymbol{\sigma}}$ for $i = 1,2$. Using these equations and Theorem 3.3.2 (in the absence of volume forces), we obtain $\mathcal{M}_{\Omega_i}(\boldsymbol{\sigma}) = \breve{\boldsymbol{\sigma}} = \mathcal{M}_{\Omega}(\boldsymbol{\sigma})$. Hence, the phase stress concentration tensor of A_i, defined by Eq. (3.8) and denoted $\boldsymbol{K}_i^{(\boldsymbol{\sigma},A)}$, is given by $\boldsymbol{K}_i^{(\boldsymbol{\sigma},A)} = \mathbf{Id}^{\mathbf{s}}$ for $i = 1,2$. Inserting $\boldsymbol{K}_i^{(\boldsymbol{\sigma},A)}$ into Eq. (3.12) gives

$$(\boldsymbol{C}_{\mathrm{Reuss}})^{-1} = \mathrm{vf}_1\,(\boldsymbol{C}_1)^{-1} + \mathrm{vf}_2\,(\boldsymbol{C}_2)^{-1}\,. \tag{3.44}$$

3.6.2 Two-phase composite made of a matrix and a single heterogeneity

Consider a composite, denoted MH, which consists of a matrix phase, denoted M, into which a single ellipsoidal heterogeneity, denoted H, is embedded. The composite MH, the heterogeneity H and the matrix M occupy the (infinite) domains $\Omega \subset \mathbb{R}^3$, $\Omega_H \subset \Omega$ and $\Omega_M = \Omega \setminus \Omega_H$, respectively. We set $\mathrm{vf}_H = |\Omega_H|/|\Omega|$ and $\mathrm{vf}_M = |\Omega_M|/|\Omega|$, then $\mathrm{vf}_H + \mathrm{vf}_M = 1$. The fine-scale stiffness tensor of composite MH reads

$$\boldsymbol{C} = \begin{cases} \boldsymbol{C}_H & \text{for } \boldsymbol{x} \in \Omega_H, \\ \boldsymbol{C}_0 & \text{for } \boldsymbol{x} \in \Omega_M, \end{cases} \tag{3.45}$$

where $\boldsymbol{C}_H$ and $\boldsymbol{C}_0$ are homogeneous stiffness tensors. Furthermore, consider a second composite, denoted REF, which consists of the matrix M only and has thus the stiffness tensor $\boldsymbol{C}_0$. This composite is also called homogeneous reference material in the engineering literature. The elastic behavior (in the absence of volume forces) of the composite MH and REF is respectively modeled, by

$$\text{MH} \begin{cases} \operatorname{div}\boldsymbol{\sigma} = 0, & \boldsymbol{x} \in \Omega, \\ \boldsymbol{\sigma} = \boldsymbol{C} : \boldsymbol{\varepsilon}, & \\ \boldsymbol{u} = \check{\boldsymbol{\varepsilon}}_0 \boldsymbol{x}, & \text{at infinity}, \end{cases} \qquad \text{REF} \begin{cases} \operatorname{div}\boldsymbol{\sigma}_0 = 0, & \boldsymbol{x} \in \Omega, \\ \boldsymbol{\sigma}_0 = \boldsymbol{C}_0 : \boldsymbol{\varepsilon}_0, & \\ \boldsymbol{u}_0 = \check{\boldsymbol{\varepsilon}}_0 \boldsymbol{x}, & \text{at infinity}, \end{cases} \tag{3.46}$$

where $\check{\boldsymbol{\varepsilon}}_0$ denotes some constant strain at infinity.

We aim to determine the apparent elastic properties of the composite MH. Instead of treating composite MH directly, we consider a matrix-inclusion composite, denoted MI, whose elastic behavior and elastic properties are equivalent, however, easier to determine than to those of MH. In the following, we assume that:

1. the matrix-inclusion composite MI consists of a matrix $\Omega \setminus \Omega_H$, occupying an infinite domain, into which a single ellipsoidal inclusion Ω_H, i.e. a subdomain of the matrix which has the same stiffness as the matrix, is embedded,
2. boundary conditions $\boldsymbol{u} = \check{\boldsymbol{\varepsilon}}_0 \boldsymbol{x}$, where $\check{\boldsymbol{\varepsilon}}_0$ is a constant strain, apply on the composite MI at infinity.

In order to simulate the heterogeneity some suitable, however, yet unknown strain, $\boldsymbol{\varepsilon}_t$, is introduced in Ω_H, the so-called eigenstrain. We determine a suitable eigenstrain $\boldsymbol{\varepsilon}_t$, comparing the composites MH and REF to each other. The difference in displacement, strain and stress of the composites MH and REF is denoted by $\bar{\boldsymbol{u}} := \boldsymbol{u} - \boldsymbol{u}_0$, $\bar{\boldsymbol{\varepsilon}} := \boldsymbol{\varepsilon} - \boldsymbol{\varepsilon}_0$ and $\bar{\boldsymbol{\sigma}} := \boldsymbol{\sigma} - \boldsymbol{\sigma}_0$, respectively. Making use of Hooke's law, $\bar{\boldsymbol{\sigma}}$ reads

$$\begin{aligned} \bar{\boldsymbol{\sigma}} = \boldsymbol{\sigma} - \boldsymbol{\sigma}_0 = \boldsymbol{C} : \boldsymbol{\varepsilon} - \boldsymbol{C}_0 : (\boldsymbol{\varepsilon} - \bar{\boldsymbol{\varepsilon}}) &= \boldsymbol{C}_0 : \bar{\boldsymbol{\varepsilon}} + (\boldsymbol{C} - \boldsymbol{C}_0) : \boldsymbol{\varepsilon} \\ &= \boldsymbol{C}_0 : \bar{\boldsymbol{\varepsilon}} + \boldsymbol{C}_0 : \underbrace{\boldsymbol{C}_0^{-1} : (\boldsymbol{C} - \boldsymbol{C}_0) : \boldsymbol{\varepsilon}}_{=: -\boldsymbol{\varepsilon}_t}. \end{aligned} \tag{3.47}$$

Here $\boldsymbol{C}_0^{-1}$ exists since $\boldsymbol{C}_0$ is positive definite by definition. By construction of $\bar{\boldsymbol{u}}$, $\bar{\boldsymbol{\varepsilon}}$ and $\bar{\boldsymbol{\sigma}}$, the following boundary value problem holds

$$\begin{aligned} \operatorname{div}\bar{\boldsymbol{\sigma}} = 0, &\qquad \boldsymbol{x} \in \mathbb{R}^3, \\ \bar{\boldsymbol{\sigma}} = \boldsymbol{C}_0 (\bar{\boldsymbol{\varepsilon}} - \boldsymbol{\varepsilon}_t), & \\ \bar{\boldsymbol{u}} = 0, &\qquad \text{at infinity}. \end{aligned} \tag{3.48}$$

Given that the eigenstrain $\boldsymbol{\varepsilon}_t$ is constant in Ω_H, boundary value problem (3.48) was solved by Eshelby (1957). Applying Eshelby's results (Section 3.6.3) to our composite MI, we find that $\bar{\boldsymbol{\varepsilon}}$ is constant and given by $\bar{\boldsymbol{\varepsilon}} = \boldsymbol{S} : \boldsymbol{\varepsilon}_t$, where $\boldsymbol{\varepsilon}_t$ is defined by Eq. (3.47) and $\boldsymbol{S}$ denotes the constant Eshelby tensor.

Finally, we derive the apparent stiffness tensor of composite MH. Therefore, we make use of Eq. (3.10) and determine the phase strain concentration tensors of the heterogeneity H and the matrix M, both defined by Eq. (3.7) and denoted by, $\boldsymbol{K}_H^{(\boldsymbol{\varepsilon},\mathrm{MH})}$ and $\boldsymbol{K}_M^{(\boldsymbol{\varepsilon},\mathrm{MH})}$, respectively. Based on the results found in the preceding paragraphs, we determine $\boldsymbol{K}_H^{(\boldsymbol{\varepsilon},\mathrm{MH})}$. The strain $\boldsymbol{\varepsilon}$ inside the heterogeneity ($\boldsymbol{x} \in \Omega_H$) reads

$$\begin{aligned} \boldsymbol{\varepsilon} = \boldsymbol{\varepsilon}_0 + \bar{\boldsymbol{\varepsilon}} = \boldsymbol{\varepsilon}_0 + \boldsymbol{S} : \boldsymbol{\varepsilon}_t = \boldsymbol{\varepsilon}_0 - \boldsymbol{S} : \boldsymbol{C}_0^{-1} : (\boldsymbol{C} - \boldsymbol{C}_0) : \boldsymbol{\varepsilon} &= \boldsymbol{\varepsilon}_0 - \boldsymbol{S} : \boldsymbol{C}_0^{-1} : (\boldsymbol{C}_H - \boldsymbol{C}_0) : \boldsymbol{\varepsilon} \\ &= \mathcal{M}_\Omega(\boldsymbol{\varepsilon}) - \boldsymbol{S} : \boldsymbol{C}_0^{-1} : (\boldsymbol{C}_H - \boldsymbol{C}_0) : \boldsymbol{\varepsilon}. \end{aligned} \tag{3.49}$$

Here, we make use of $\bar{\boldsymbol{\varepsilon}} = \boldsymbol{S} : \boldsymbol{\varepsilon}_t$, substitute then the eigenstrain $\boldsymbol{\varepsilon}_t$ given by Eq. (3.47) into Eq. (3.49) and, finally, employ $\boldsymbol{\varepsilon}_0 = \check{\boldsymbol{\varepsilon}}_0 = \mathcal{M}_\Omega(\boldsymbol{\varepsilon})$. Note that $\check{\boldsymbol{\varepsilon}}_0 = \mathcal{M}_\Omega(\boldsymbol{\varepsilon})$ holds because homogeneous displacement

boundary conditions (3.13a) are prescribed on the boundary of composite MH (Theorem 3.3.1). Taking the mean over Ω_H in Eq. (3.49) and comparing the resulting equation to Eq. (3.7), we find $\boldsymbol{K}_H^{(\boldsymbol{\varepsilon},\mathrm{MH})}$ to be

$$\boldsymbol{K}_H^{(\boldsymbol{\varepsilon},\mathrm{MH})} = \left(\mathbf{Id}^{\mathbf{s}} + \boldsymbol{S} : \boldsymbol{C}_0^{-1} : (\boldsymbol{C}_H - \boldsymbol{C}_0)\right)^{-1}. \tag{3.50}$$

In order to determine the phase strain concentration tensor $\boldsymbol{K}_M^{(\boldsymbol{\varepsilon},\mathrm{MH})}$, we note that

$$\begin{aligned}\mathcal{M}_\Omega(\boldsymbol{\varepsilon}) &= \mathrm{vf}_H\, \mathcal{M}_{\Omega_H}(\boldsymbol{\varepsilon}) + \mathrm{vf}_M\, \mathcal{M}_{\Omega_M}(\boldsymbol{\varepsilon}) = \mathrm{vf}_H\, \boldsymbol{K}_H^{(\boldsymbol{\varepsilon},\mathrm{MH})} : \mathcal{M}_\Omega(\boldsymbol{\varepsilon}) + \mathrm{vf}_M\, \boldsymbol{K}_M^{(\boldsymbol{\varepsilon},\mathrm{MH})} : \mathcal{M}_\Omega(\boldsymbol{\varepsilon}) \\ &= (\mathrm{vf}_H\, \boldsymbol{K}_H^{(\boldsymbol{\varepsilon},\mathrm{MH})} + \mathrm{vf}_M\, \boldsymbol{K}_M^{(\boldsymbol{\varepsilon},\mathrm{MH})}) : \mathcal{M}_\Omega(\boldsymbol{\varepsilon})\end{aligned}$$

holds. Then, it holds that $\mathrm{vf}_M\, \boldsymbol{K}_M^{(\boldsymbol{\varepsilon},\mathrm{MH})} = \mathbf{Id}^{\mathbf{s}} - \mathrm{vf}_H\, \boldsymbol{K}_H^{(\boldsymbol{\varepsilon},\mathrm{MH})}$. Finally, substituting $\boldsymbol{K}_H^{(\boldsymbol{\varepsilon},\mathrm{MH})}$, defined by Eq. (3.50), and $\mathrm{vf}_M\, \boldsymbol{K}_M^{(\boldsymbol{\varepsilon},\mathrm{MH})}$, into Eq. (3.10), the apparent stiffness tensor $\boldsymbol{C}_{MH}$ of the composite MH reads

$$\begin{aligned}\boldsymbol{C}_{MH} &= \mathrm{vf}_H \boldsymbol{C}_H : \boldsymbol{K}_H^{(\boldsymbol{\varepsilon},\mathrm{MH})} + \mathrm{vf}_M\, \boldsymbol{C}_0 : \boldsymbol{K}_M^{(\boldsymbol{\varepsilon},\mathrm{MH})} = \mathrm{vf}_H \boldsymbol{C}_H : \boldsymbol{K}_H^{(\boldsymbol{\varepsilon},\mathrm{MH})} + \boldsymbol{C}_0 : (\mathbf{Id}^{\mathbf{s}} - \mathrm{vf}_H\, \boldsymbol{K}_H^{(\boldsymbol{\varepsilon},\mathrm{MH})}) \\ &= \boldsymbol{C}_0 + \mathrm{vf}_H(\boldsymbol{C}_H - \boldsymbol{C}_0) : \boldsymbol{K}_H^{(\boldsymbol{\varepsilon},\mathrm{MH})} \\ &= \boldsymbol{C}_0 + \mathrm{vf}_H(\boldsymbol{C}_H - \boldsymbol{C}_0) : \left(\mathbf{Id}^{\mathbf{s}} + \boldsymbol{S} : \boldsymbol{C}_0^{-1} : (\boldsymbol{C}_H - \boldsymbol{C}_0)\right)^{-1}.\end{aligned} \tag{3.51}$$

3.6.3 Eshelby's result on matrix-inclusion composites and the Hill tensor

Consider a homogeneous linear elastic material which occupies the infinite domain $\Omega \subseteq \mathbb{R}^3$ and has the stiffness tensor $\boldsymbol{C}_0$. Let there be some inclusion, i.e. a subdomain $\Omega_I \subset \Omega$ which undergoes a change of size and shape which is caused, for instance, by thermal expansion of the subdomain or mismatch of different parts of the material.

Given that the inclusion is ellipsoidal and displacement boundary conditions (3.13a) apply at infinity, Eshelby (1957) proved that the strain inside the inclusion is constant and depends on the eigenstrain (Nemat-Nasser and Hori, 1999; Mura, 1987)

Theorem 3.6.1 *Let the displacement $\bar{\boldsymbol{u}}$ fulfill the boundary value problem*

$$\begin{aligned}\operatorname{div} \bar{\boldsymbol{\sigma}} &= 0 \qquad \boldsymbol{x} \in \Omega, \\ \bar{\boldsymbol{\sigma}} &= \boldsymbol{C}_0 : (\bar{\boldsymbol{\varepsilon}} - \boldsymbol{\varepsilon}_t), \\ \bar{\boldsymbol{u}} &= 0 \quad \textit{at infinity}.\end{aligned}$$

Furthermore, let the eigenstrain $\boldsymbol{\varepsilon}_t$ be constant in Ω_I and zero elsewhere. Then the strain $\bar{\boldsymbol{\varepsilon}}$ inside the inclusion is constant and is given by

$$\bar{\boldsymbol{\varepsilon}} = \boldsymbol{S} : \boldsymbol{\varepsilon}_t. \tag{3.52}$$

The fourth-order tensor $\boldsymbol{S}$ is called Eshelby tensor and has the following properties: (i) it is completely defined by the semi-axes of the ellipsoidal inclusion I and the stiffness tensor $\boldsymbol{C}_0$ of the matrix, (ii) it possesses minor but, in general, no major symmetries, i.e. $S_{ijkl} = S_{jikl} = S_{ijlk}$ and $S_{ijkl} \neq S_{klij}$.

Besides the Eshelby tensor $\boldsymbol{S}$ also the Hill tensor, denoted $\boldsymbol{P}$, plays an important role for Eshelby-based homogenization methods. It is defined by

$$\boldsymbol{S} = \boldsymbol{P} : \boldsymbol{C}_0. \tag{3.53}$$

Considering a three-dimensional Cartesian coordinate system, whose axes x_i with $i = 1, 2, 3$ are aligned with the principal axes of the inclusion, and denoting by a_i the length of the semi-axis in direction x_i, the Hill tensor reads (Masson, 2008; Ghahremani, 1977)[2]

$$P_{ijkl} = \frac{1}{4\pi} \int_{\theta=0}^{\pi} \int_{\eta=0}^{2\pi} N_{ijkl}(a_1, a_2, a_3, \theta, \eta, \boldsymbol{C}_0) \sin\theta \, \mathrm{d}\theta \, \mathrm{d}\eta, \tag{3.54a}$$

where

$$N_{ijkl}(a_1, a_2, a_3, \theta, \eta, \boldsymbol{C}_0) = \frac{1}{4} \left(B^{-1}_{jk} x_i x_l + B^{-1}_{ik} x_j x_l + B^{-1}_{jl} x_i x_k + B^{-1}_{il} x_j x_k \right), \tag{3.54b}$$

with

$$B_{ik} = (\boldsymbol{C}_0)_{ijkl} \, x_j \, x_l, \quad x_1 = \frac{\sin\theta \cos\eta}{a_1}, \quad x_2 = \frac{\sin\theta \sin\eta}{a_2}, \quad x_3 = \frac{\cos\theta}{a_3}. \tag{3.54c}$$

Closed formulas for the integrals in P_{ijkl} are only available if the inclusion has a specific shape (spheroidal, cylindrical) and the stiffness tensor $\boldsymbol{C}_0$ is isotropic or transverse isotropic. For a review of these cases, and the corresponding expressions for the Hill tensor, see Mura (1987) or Suvorov and Dvorak (2002). For more general matrix-inclusion composites the integrals in P_{ijkl} usually need to be evaluated numerically.

Note that the Hill tensor depends only on ratios of the semi axes, rather than on the absolute values of the a_i. This is because of the property (Barthélémy, 2009)

$$\boldsymbol{N}(\lambda a_1, \lambda a_2, \lambda a_3, \theta, \eta, \boldsymbol{C}_0) = \boldsymbol{N}(a_1, a_2, a_3, \theta, \eta, \boldsymbol{C}_0), \quad \forall \, \lambda \neq 0. \tag{3.55}$$

In this thesis we are mainly interested in prolate spheroidal inclusions, i.e. those for which $a_1 = a_2 \leq a_3$. In our case $a_3 \geq 1$. We usually normalize a_1 and a_2, i.e. $a_1 = a_2 = 1$, and refer to the resulting a_3 as aspect ratio, denoted ar in the following. Then, the Hill tensor is a function of the stiffness tensor $\boldsymbol{C}_0$ and the aspect ratio ar only, i.e. $\boldsymbol{P} = \boldsymbol{P}(\boldsymbol{C}_0, \mathrm{ar})$.

Finally, note that the Hill tensor $\boldsymbol{P}$, in contrast to the Eshelby tensor $\boldsymbol{S}$, obeys both, minor and major symmetries.

3.6.4 n-phase composite

Let there be given a composite A that consists of n homogeneous and perfectly bonded phases, A_i where $i = 1, \ldots, n$, with corresponding stiffness tensors $\boldsymbol{C}_i$, compliance tensors $\boldsymbol{M}_i$, and volume fractions vf_i. Furthermore, let phases A_1 to A_{n-1} be ellipsoidal heterogeneities, and let phase A_n be either an ellipsoidal heterogeneity or a matrix into which the phases A_1 to A_{n-1} are embedded. In the latter case, we call A_n matrix phase. Furthermore, we assume that each phase A_i occupies the domain Ω_i. The union of all phase domains is the infinite domain $\Omega \subseteq \mathbb{R}^3$. Hence, the volume fraction of the i-th phase is given by $\mathrm{vf}_i = |\Omega_i|/|\Omega|$. Additionally, we have $\sum_{i=1}^{n} \mathrm{vf}_i = 1$.

In order to determine the apparent stiffness tensor $\boldsymbol{C}_A$ of the n-phase composite, we make use of the results of Sections 3.6.2 and 3.6.3. To this end, we setup for each heterogeneity A_i of the n-phase composite A an equivalent matrix-inclusion composite MH_i. Thereby, we assume that the composite MH_i consists of some inclusion phase $\tilde{A}_i$, which occupies the same domain and has the same stiffness as phase

[2] The formulas given in Masson (2008) and Ghahremani (1977) differ formally about the factor $\frac{1}{a_1}$. However, because of property (3.55) with $\lambda = \frac{1}{a_1}$, the two formulas coincide.

A_i, and is embedded into some material with stiffness $\boldsymbol{C}_0$. The elastic behavior (in the absence of volume forces) of the n-phase composite A and the composite MH_i is respectively modeled, by

$$\mathrm{A}\ \begin{cases} \operatorname{div}\boldsymbol{\sigma} = 0, & \boldsymbol{x}\in\Omega, \\ \boldsymbol{\sigma} = \boldsymbol{C} : \boldsymbol{\varepsilon}, & \\ \boldsymbol{u} = \breve{\boldsymbol{\varepsilon}}\,\boldsymbol{x}, & \text{at infinity}, \end{cases} \qquad \mathrm{MH}_i\ \begin{cases} \operatorname{div}\tilde{\boldsymbol{\sigma}} = 0, & \boldsymbol{x}\in\Omega, \\ \tilde{\boldsymbol{\sigma}} = \tilde{\boldsymbol{C}}_i : \tilde{\boldsymbol{\varepsilon}}, & \\ \tilde{\boldsymbol{u}} = \breve{\boldsymbol{\varepsilon}}_0\,\boldsymbol{x}, & \text{at infinity}, \end{cases} \tag{3.56}$$

where $\breve{\boldsymbol{\varepsilon}}$ and $\breve{\boldsymbol{\varepsilon}}_0$ are, not necessarily equal, constant strains at infinity, and the stiffness tensors $\boldsymbol{C}$ and $\tilde{\boldsymbol{C}}_i$ are respectively given by

$$\boldsymbol{C} = \begin{cases} \boldsymbol{C}_1 & \boldsymbol{x}\in\Omega_1 \\ \vdots & \\ \boldsymbol{C}_n & \boldsymbol{x}\in\Omega_n \end{cases} \qquad \tilde{\boldsymbol{C}}_i = \begin{cases} \boldsymbol{C}_i & \boldsymbol{x}\in\Omega_i \\ \boldsymbol{C}_0 & \boldsymbol{x}\in\Omega\setminus\Omega_i \end{cases} \tag{3.57}$$

with $\boldsymbol{C}_0$ some homogeneous stiffness. Finally, we assume that for each inclusion phase it holds that

$$\mathcal{M}_{\Omega_i}(\boldsymbol{\varepsilon}) = \mathcal{M}_{\Omega_i}(\tilde{\boldsymbol{\varepsilon}}). \tag{3.58}$$

The strain $\breve{\boldsymbol{\varepsilon}}_0$ and the stiffness $\boldsymbol{C}_0$ can be chosen at will. Their choice expresses how inclusion phases of the same type, and also of other types, interact among each other. Here, we consider three scenarios:

1. $\breve{\boldsymbol{\varepsilon}}_0 = \breve{\boldsymbol{\varepsilon}}$ and $\boldsymbol{C}_0 = \boldsymbol{C}_n$ (A_n is a matrix phase). Under these assumptions the inclusion of composite MH_i "feels" only the strain $\breve{\boldsymbol{\varepsilon}}$ at infinity. Thus, we neglect any interactions among the heterogeneities. This scenario is only justified, if the volume fraction vf_i of each phase A_i ($i = 1,\dots,n-1$) is small.

2. $\breve{\boldsymbol{\varepsilon}}_0 = \mathcal{M}_{\Omega_n}(\boldsymbol{\varepsilon})$ and $\boldsymbol{C}_0 = \boldsymbol{C}_n$ (A_n is a matrix phase). Under these assumptions the inclusion of composite MH_i "feels" the average strain of the matrix phase A_n at infinity.

3. $\breve{\boldsymbol{\varepsilon}}_0$ is fixed by assumptions (3.58) for $i = 1,\dots,n$ ($A_1, A_2, \dots, A_n$ are inclusion phases) and $\boldsymbol{C}_0$ is given by $\boldsymbol{C}_0 = \boldsymbol{C}_A$. Under these assumptions each inclusion phase senses other inclusion phases through the effective material.

For each scenario we determine $\boldsymbol{C}_A$ based on Eq. (3.10). Therefore, we need to find the phase strain concentration tensor of each phase A_i, denoted $\boldsymbol{K}_i^{(\boldsymbol{\varepsilon},A)}$ and defined by (compare Eq. (3.7)),

$$\mathcal{M}_{\Omega_i}(\boldsymbol{\varepsilon}) = \boldsymbol{K}_i^{(\boldsymbol{\varepsilon},A)} : \mathcal{M}_{\Omega}(\boldsymbol{\varepsilon}) = \boldsymbol{K}_i^{(\boldsymbol{\varepsilon},A)} : \breve{\boldsymbol{\varepsilon}}. \tag{3.59}$$

If A_i is the heterogeneity phase, by assumption, it holds that $\mathcal{M}_{\Omega_i}(\boldsymbol{\varepsilon}) = \mathcal{M}_{\Omega_i}(\tilde{\boldsymbol{\varepsilon}})$. Making use of the results, presented in Section 3.6.2 and Eq. (3.50), the average strain $\mathcal{M}_{\Omega_i}(\tilde{\boldsymbol{\varepsilon}})$ of each inclusion phase $\tilde{A}_i$ is given by

$$\mathcal{M}_{\Omega_i}(\tilde{\boldsymbol{\varepsilon}}) = (\mathbf{Id}^{\mathbf{s}} + \boldsymbol{P}_i : (\boldsymbol{C}_i - \boldsymbol{C}_0))^{-1} : \mathcal{M}_{\Omega}(\tilde{\boldsymbol{\varepsilon}}), \tag{3.60}$$

where $\boldsymbol{P}_i = \boldsymbol{P}_i(\boldsymbol{C}_0, \mathrm{ar}_i)$ is the Hill tensor of the inclusion phase $\tilde{A}_i$, with ar_i the aspect ratio of $\tilde{A}_i$.

Scenario 1: Substituting $\breve{\boldsymbol{\varepsilon}}_0 = \breve{\boldsymbol{\varepsilon}}$ and $\mathcal{M}_{\Omega_i}(\tilde{\boldsymbol{\varepsilon}}) = \mathcal{M}_{\Omega_i}(\boldsymbol{\varepsilon})$ ($i = 1,\dots,n-1$) into Eq. (3.60), and comparing the resulting equation to Eq. (3.59), the phase strain concentration tensor $\boldsymbol{K}_i^{(\boldsymbol{\varepsilon},A)}$ of the heterogeneity phase A_i ($i = 1, 2, n-1$) is given by

$$\boldsymbol{K}_i^{(\boldsymbol{\varepsilon},A)} = (\mathbf{Id}^{\mathbf{s}} + \boldsymbol{P}_i : (\boldsymbol{C}_i - \boldsymbol{C}_n))^{-1}. \tag{3.61}$$

Note that $\boldsymbol{K}_i^{(\boldsymbol{\varepsilon},A)}$ as given in Eq. (3.61) equals the phase strain concentration tensor of the heterogeneity phase of the two-phase composite MH in Section 3.6.2. Proceeding similar as in Section 3.6.2, the phase strain concentration tensor $\boldsymbol{K}_n^{(\boldsymbol{\varepsilon},A)}$ of the matrix phase A_n reads

$$\mathrm{vf}_n\, \boldsymbol{K}_n^{(\boldsymbol{\varepsilon},A)} = \mathbf{Id}^{\mathbf{s}} - \sum_{i=1}^{n-1} \mathrm{vf}_i \left(\mathbf{Id}^{\mathbf{s}} + \boldsymbol{P}_i : (\boldsymbol{C}_i - \boldsymbol{C}_n)\right)^{-1}. \tag{3.62}$$

Finally, substituting Eq. (3.61) and Eq. (3.62) into Eq. (3.10), the apparent stiffness tensor $\boldsymbol{C}_A$ of composite A, under the assumptions of scenario 1, reads

$$\boldsymbol{C}_A = \boldsymbol{C}_n + \sum_{i=1}^{n-1} \mathrm{vf}_i (\boldsymbol{C}_i - \boldsymbol{C}_n) : \left(\mathbf{Id}^{\mathbf{s}} + \boldsymbol{P}_i : (\boldsymbol{C}_i - \boldsymbol{C}_n)\right)^{-1}. \tag{3.63}$$

Scenario 2: Firstly, we determine the constant strain $\breve{\boldsymbol{\varepsilon}}_0$ at infinity. To this end, we link $\breve{\boldsymbol{\varepsilon}}_0$ to $\breve{\boldsymbol{\varepsilon}}$ by

$$\begin{aligned} \breve{\boldsymbol{\varepsilon}} = \mathcal{M}_\Omega(\boldsymbol{\varepsilon}) = \sum_{r=1}^{n} \mathrm{vf}_r\, \mathcal{M}_{\Omega_r}(\boldsymbol{\varepsilon}) &= \sum_{r=1}^{n-1} \mathrm{vf}_r\, \mathcal{M}_{\Omega_r}(\tilde{\boldsymbol{\varepsilon}}) + \mathrm{vf}_n\, \mathcal{M}_{\Omega_n}(\boldsymbol{\varepsilon}) \\ &= \left(\sum_{r=1}^{n-1} \mathrm{vf}_r \left(\mathbf{Id}^{\mathbf{s}} + \boldsymbol{P}_r : (\boldsymbol{C}_r - \boldsymbol{C}_n)\right)^{-1} + \mathrm{vf}_n\, \mathbf{Id}^{\mathbf{s}} \right) : \breve{\boldsymbol{\varepsilon}}_0 , \end{aligned} \tag{3.64}$$

where we make use of Theorem 3.3.1, employ the relations $\mathcal{M}_{\Omega_i}(\boldsymbol{\varepsilon}) = \mathcal{M}_{\Omega_i}(\tilde{\boldsymbol{\varepsilon}})$ for $i = 1, \dots n-1$, substitute (3.60), and make use of the relations $\mathcal{M}_\Omega(\tilde{\boldsymbol{\varepsilon}}) = \breve{\boldsymbol{\varepsilon}}_0$ and $\mathcal{M}_{\Omega_n}(\boldsymbol{\varepsilon}) = \breve{\boldsymbol{\varepsilon}}_0$. Solving Eq. (3.64) for $\breve{\boldsymbol{\varepsilon}}_0$, we obtain

$$\breve{\boldsymbol{\varepsilon}}_0 = \left(\sum_{r=1}^{n-1} \mathrm{vf}_r \left(\mathbf{Id}^{\mathbf{s}} + \boldsymbol{P}_r : (\boldsymbol{C}_r - \boldsymbol{C}_n)\right)^{-1} + \mathrm{vf}_n\, \mathbf{Id}^{\mathbf{s}} \right)^{-1} : \breve{\boldsymbol{\varepsilon}}. \tag{3.65}$$

Making use of $\mathcal{M}_{\Omega_i}(\tilde{\boldsymbol{\varepsilon}}) = \mathcal{M}_{\Omega_i}(\boldsymbol{\varepsilon})$ for $i = 1, 2, \dots, n-1$, $\mathcal{M}_\Omega(\tilde{\boldsymbol{\varepsilon}}) = \breve{\boldsymbol{\varepsilon}}_0$ and Eq. (3.65) in Eq. (3.60), and comparing the resulting equation to Eq. (3.59), the phase strain concentration tensor of each heterogeneity phase A_i $(i = 1, \dots, n-1)$ is given by

$$\boldsymbol{K}_i^{(\boldsymbol{\varepsilon},A)} = \left(\mathbf{Id}^{\mathbf{s}} + \boldsymbol{P}_i : (\boldsymbol{C}_i - \boldsymbol{C}_n)\right)^{-1} : \left(\sum_{r=1}^{n-1} \mathrm{vf}_r \left(\mathbf{Id}^{\mathbf{s}} + \boldsymbol{P}_r : (\boldsymbol{C}_r - \boldsymbol{C}_n)\right)^{-1} + \mathrm{vf}_n\, \mathbf{Id}^{\mathbf{s}} \right)^{-1}. \tag{3.66}$$

Substituting Eq. (3.65) into $\mathcal{M}_{\Omega_n}(\boldsymbol{\varepsilon}) = \breve{\boldsymbol{\varepsilon}}_0$ and comparing the resulting equation to Eq. (3.59), the phase strain concentration tensor $\boldsymbol{K}_n^{(\boldsymbol{\varepsilon},A)}$ of the matrix phase A_n reads

$$\boldsymbol{K}_n^{(\boldsymbol{\varepsilon},A)} = \left(\sum_{r=1}^{n-1} \mathrm{vf}_r \left(\mathbf{Id}^{\mathbf{s}} + \boldsymbol{P}_r : (\boldsymbol{C}_r - \boldsymbol{C}_n)\right)^{-1} + \mathrm{vf}_n\, \mathbf{Id}^{\mathbf{s}} \right)^{-1}. \tag{3.67}$$

Finally, we determine the apparent stiffness $\boldsymbol{C}_A$ substituting Eqs. (3.66) and (3.67) into Eq. (3.10). This gives

$$\boldsymbol{C}_A = \left(\sum_{i=1}^{n-1} \mathrm{vf}_i\, \boldsymbol{C}_i : \left(\mathbf{Id}^{\mathbf{s}} + \boldsymbol{P}_i : (\boldsymbol{C}_i - \boldsymbol{C}_n)\right)^{-1} + \mathrm{vf}_n\, \boldsymbol{C}_n \right) : \left(\sum_{r=1}^{n-1} \mathrm{vf}_r \left(\mathbf{Id}^{\mathbf{s}} + \boldsymbol{P}_r : (\boldsymbol{C}_r - \boldsymbol{C}_n)\right)^{-1} + \mathrm{vf}_n\, \mathbf{Id}^{\mathbf{s}} \right)^{-1}. \tag{3.68}$$

Scenario 3 We proceed similar as for scenario 2. Since now A_n is a heterogeneity phase, we employ in Eq. (3.64) the assumption $\mathcal{M}_{\Omega_n}(\boldsymbol{\varepsilon}) = \mathcal{M}_{\Omega_n}(\tilde{\boldsymbol{\varepsilon}})$ (for scenario 2 we used here $\mathcal{M}_{\Omega_n}(\boldsymbol{\varepsilon}) = \breve{\boldsymbol{\varepsilon}}_0$). Moreover, we make use of $\boldsymbol{C}_0 = \boldsymbol{C}_A$. Then, the phase strain concentration tensor of each heterogeneity phase A_i ($i = 1, \ldots, n$) reads

$$\boldsymbol{K}_i^{(\boldsymbol{\varepsilon},A)} = \left(\mathbf{Id}^{\mathbf{s}} + \boldsymbol{P}_i : (\boldsymbol{C}_i - \boldsymbol{C}_A)\right)^{-1} : \left(\sum_{r=1}^{n} \mathrm{vf}_r \left(\mathbf{Id}^{\mathbf{s}} + \boldsymbol{P}_r : (\boldsymbol{C}_r - \boldsymbol{C}_A)\right)^{-1}\right)^{-1}, \tag{3.69}$$

where $\boldsymbol{P}_r = \boldsymbol{P}_r(\boldsymbol{C}_A, \mathrm{ar}_r)$. Inserting Eq. (3.69) into Eq. (3.10), the apparent stiffness $\boldsymbol{C}_A$ of composite A becomes

$$\boldsymbol{C}_A = \sum_{i=1}^{n} \mathrm{vf}_i \, \boldsymbol{C}_i : \left(\mathbf{Id}^{\mathbf{s}} + \boldsymbol{P}_i : (\boldsymbol{C}_i - \boldsymbol{C}_A)\right)^{-1} : \left(\sum_{r=1}^{n} \mathrm{vf}_r \left(\mathbf{Id}^{\mathbf{s}} + \boldsymbol{P}_r : (\boldsymbol{C}_r - \boldsymbol{C}_A)\right)^{-1}\right)^{-1}. \tag{3.70}$$

Eqs. (3.63), (3.68), and (3.70) give rise to the three following Eshelby-based homogenization methods: the Dilute method, the Mori-Tanaka method and the self-consistent method. All these methods are given for the case of a two-phase composite ($n = 2$) in the next three sections.

Note that we henceforth use the terms heterogeneity and inclusion synonymously. This is justified, since we throughout this thesis in general consider only ellipsoidal (spheroidal) heterogeneities. These heterogeneities can be considered in the context of Eshelby's results (Sections 3.6.2 and 3.6.3) as inclusion with some suitable eigenstrain.

3.6.5 Dilute method

Let the composite A consist of an ellipsoidal inclusion phase, A_1, with fixed orientation and aspect ratio ar_1, embedded into a matrix phase, A_2. Furthermore, let the inclusions be as far as apart from each other that there is no interaction among them. This assumption is justified if the volume fraction of the inclusion phase A_1 is very small, i.e. $\mathrm{vf}_1 \leq 0.01$.

Under these assumptions we can make use of the results of scenario 1 in Section 3.6.4. Then, the Dilute method computes the apparent stiffness tensor, $\boldsymbol{C}_{\mathrm{D}}$, as approximation to the effective stiffness of A, by

$$\boldsymbol{C}_{\mathrm{D}} = \boldsymbol{C}_2 + \mathrm{vf}_1(\boldsymbol{C}_1 - \boldsymbol{C}_2) : \left(\mathbf{Id}^{\mathbf{s}} + \boldsymbol{P}^{\mathrm{D}} : (\boldsymbol{C}_1 - \boldsymbol{C}_2)\right)^{-1}, \tag{3.71}$$

where $\boldsymbol{P}^{\mathrm{D}} = \boldsymbol{P}(\boldsymbol{C}_2, \mathrm{ar}_1)$ denotes the Hill tensor of the inclusion phase A_1.

3.6.6 Mori-Tanaka method

In order to generalize to composites where $\mathrm{vf}_1 > 0.01$, we introduce the Mori-Tanaka method (Mori and Tanaka, 1973).

Let the composite A consist of an ellipsoidal inclusion phase, A_1, with fixed orientation and aspect ratio ar_1, which is embedded into a matrix phase, A_2. Moreover, let the inclusions feel the matrix and let them be sufficiently far apart from each other, so that there is no interactions among the inclusions.

Under these assumptions the results of scenario 2 in Section 3.6.4 can be used. The Mori-Tanaka method computes the apparent stiffness tensor, $\boldsymbol{C}_{\mathrm{MT}}$, as approximation to the effective stiffness of A, by

$$\boldsymbol{C}_{\mathrm{MT}} = \left(\mathrm{vf}_1 \, \boldsymbol{C}_1 : \left(\mathbf{Id}^{\mathbf{s}} + \boldsymbol{P}^{\mathrm{MT}} : (\boldsymbol{C}_1 - \boldsymbol{C}_2)\right)^{-1} + \mathrm{vf}_2 \, \boldsymbol{C}_2\right) : \left(\mathrm{vf}_1 \left(\mathbf{Id}^{\mathbf{s}} + \boldsymbol{P}^{\mathrm{MT}} : (\boldsymbol{C}_1 - \boldsymbol{C}_2)\right)^{-1} + \mathrm{vf}_2 \mathbf{Id}^{\mathbf{s}}\right)^{-1}, \tag{3.72}$$

where $\boldsymbol{P}^{\mathrm{MT}} = \boldsymbol{P}^{\mathrm{MT}}(\boldsymbol{C}_2, \mathrm{ar}_1)$ denotes the Hill tensor of phase A_1.

One side effect of choosing $\boldsymbol{C}_0 = \boldsymbol{C}_2$ is that we constantly over or underestimate the role of the matrix. We overestimate it, and with it the apparent stiffness tensor of the composite A, if we choose the matrix to be stiffer than the inclusion. However, we underestimate it, when taking the inclusion to be stiffer than the matrix. For a deeper discussion of the choice $\boldsymbol{C}_2 = \boldsymbol{C}_0$ and its consequences see, for instance, the instructive construction of the Mori-Tanaka method, given in Benveniste (1987).

3.6.7 Self-consistent method

Neither the Dilute, nor the Mori-Tanaka method accounts for inclusion interaction. To this end, we introduce the self-consistent method (Hill, 1965). Additionally, this method comes also into play in situation, where for the material A there exists no well-defined matrix phase.

Let the composite A consist of two ellipsoidal inclusion phases, A_1 and A_2, with fixed orientation and semi-axes. Both inclusions are embedded in the effective material. Hence, each phase "feels" the other phases in the way that it sense them through the overall effective stiffness.

Under these assumptions we make use of the results of scenario 3 in Section 3.6.4. Then, the self-consistent method computes the apparent stiffness tensor, $\boldsymbol{C}_{\mathrm{SC}}$, as approximation to the effective stiffness of A. Since the latter is not known, it is formally replaced by $\boldsymbol{C}_{\mathrm{SC}}$ in Eq. (3.70), yielding a nonlinear system of equations

$$\boldsymbol{C}_{\mathrm{SC}} = \sum_{r=1}^{2} \mathrm{vf}_r \, \boldsymbol{C}_r : \left(\mathbf{Id}^{\mathbf{s}} + \boldsymbol{P}_r^{\mathrm{SC}} : (\boldsymbol{C}_r - \boldsymbol{C}_{\mathrm{SC}})\right)^{-1} : \left(\sum_{s=1}^{2} \mathrm{vf}_s \left(\mathbf{Id}^{\mathbf{s}} + \boldsymbol{P}_s^{\mathrm{SC}} : (\boldsymbol{C}_s - \boldsymbol{C}_{\mathrm{SC}})\right)^{-1}\right)^{-1}, \tag{3.73}$$

where $\boldsymbol{P}_s^{\mathrm{SC}} = \boldsymbol{P}_s^{\mathrm{SC}}(\boldsymbol{C}_A, \mathrm{ar}_s)$ refers to the Hill tensor of phase A_s.

Multiplying Eq. (3.73) by

$$\sum_{s=1}^{2} \mathrm{vf}_s \left(\mathbf{Id}^{\mathbf{s}} + \boldsymbol{P}_s^{\mathrm{SC}} : (\boldsymbol{C}_s - \boldsymbol{C}_{\mathrm{SC}})\right)^{-1}$$

from the right, and bringing all quantities to the left-hand side of the equation, we can reformulate Eq. (3.73) to

$$\sum_{r=1}^{2} \mathrm{vf}_r \, (\boldsymbol{C}_r - \boldsymbol{C}_{\mathrm{SC}}) : \left(\mathbf{Id}^{\mathbf{s}} + \boldsymbol{P}_r^{\mathrm{SC}} : (\boldsymbol{C}_r - \boldsymbol{C}_{\mathrm{SC}})\right)^{-1} = 0. \tag{3.74}$$

Note, that solving the nonlinear system (3.74) for $\boldsymbol{C}_{\mathrm{SC}}$ incurs considerably more computational effort than the direct computation of $\boldsymbol{C}_A$ in the Mori-Tanaka method or the Dilute method.

3.7 Comparison of apparent stiffness tensors predicted using periodic, RVE-based and Eshelby-based homogenization methods

In this section we compare the apparent stiffness tensors predicted by the different homogenization methods, introduced in Sections 3.4, 3.5 and 3.6.

Let $\boldsymbol{C}_A$ denote the effective stiffness tensor of our material A. Moreover, recall that $\boldsymbol{C}_{\mathrm{d}}$, $\boldsymbol{C}_{\mathrm{t}}$ and $\boldsymbol{C}_{\mathrm{AHA}}$ denote the apparent stiffness tensors predicted by the RVE-based homogenization method with homogeneous displacement or traction boundary conditions and the AHA method, respectively. The following inequalities hold

$$\boldsymbol{C}_{\mathrm{t}} \leq \boldsymbol{C}_{\mathrm{AHA}} \leq \boldsymbol{C}_{\mathrm{d}}, \tag{3.75}$$

$$\boldsymbol{C}_{\mathrm{t}} \leq \boldsymbol{C}_A \leq \boldsymbol{C}_{\mathrm{d}}, \tag{3.76}$$

Here, and in the following, two fourth-order tensors A and B are said to be $A \leq B$, if their difference $B - A$ is positive definite. Proofs of the inequalities (3.75) and (3.76) are given, for instance, in Huet (1990) or Hori and Nemat-Nasser (1999).

The Reuss and the Voigt approximations are lower and upper bounds for the unknown effective stiffness tensor of the material under investigation, i.e

$$(\boldsymbol{M}_{\text{Reuss}})^{-1} \leq \boldsymbol{C}_A \leq \boldsymbol{C}_{\text{Voigt}}. \tag{3.77}$$

A proof of statement (3.77) can be found, for instance, in Zohdi and Wriggers (2008, Chapter 4.2). Note that for general heterogeneous materials A, the Reuss and the Voigt technique yields no tight bounds for the effective stiffness tensor $\boldsymbol{C}_A$. The tightest upper and lower bounds known for $\boldsymbol{C}_A$ are the Hashin-Shtrikman bounds (Nemat-Nasser and Hori, 1999).

If composite A consists of ellipsoidal inclusions in an isotropic matrix, the apparent stiffness tensor $\boldsymbol{C}_{\text{MT}}$, predicted using the Mori-Tanaka method, coincides with either the lower or the upper Hashin-Shtrikman bound (Nemat-Nasser and Hori, 1999). The other Hashin-Shtrikman bound can be attained by exchanging the stiffness tensor of the matrix and the inclusion in the Mori-Tanaka method.

4 Implementation

In this chapter we describe the implementation of homogenization methods, introduced in Chapter 3 and employed in Chapters 5 to 7. For each homogenization method we specify its in and output parameters and discuss aspects of the computational realization.

Firstly, in Section 4.1 we consider the AHF method, the AHA method and the RVE-based homogenization method. Next, we move to a self-consistent version of the two latter homogenization methods, these will be employed in Chapter 7. Solving the underlying boundary value problems using a finite elemente software, we give details on employed features of this software and discuss how to implement necessary boundary conditions. Also in Section 4.1, we describe the computational realization of the numerical convergence analysis performed in Chapter 7. Finally, in Section 4.2 we consider the Mori-Tanaka and the self-consistent method.

In this thesis we employed Matlab (MathWorks, 2010-2014) as well as the finite element software Comsol Multiphysics (COMSOL Multiphysics GmbH, 2011-2013). All Matlab as well as Comsol Multiphysics computations conducted in this thesis were performed on a compute server, equipped with 8 x 2.8 GHz dual-core AMD Opteron processors and 128 GB RAM.

Finally, a remark on the notation in use in this chapter: as in Chapter 3 we denote the apparent stiffness tensor of the material A by $\boldsymbol{C}_A$, if the main focus is on the composite A, and otherwise by $\boldsymbol{C}_M$, where M indicates the homogenization method in use.

4.1 AHF method, AHA method and RVE-based homogenization method

AHF method

The AHF method was implemented by Parnell and Grimal (2009). It returns the apparent stiffness $\boldsymbol{C}_{\mathrm{AHF}}$ (Voigt notation) of composite A. Input quantities of the AHF method are

$$\mathrm{vf}, \qquad \boldsymbol{C}_0, \qquad \boldsymbol{C}_1 \qquad \text{and} \qquad n_{\mathrm{terms}}.$$

where $\mathrm{vf} \in [0,1]$ is the volume fraction of the cylindrical phase, $\boldsymbol{C}_0$ and $\boldsymbol{C}_1$ are the isotropic stiffness tensors of the matrix phase and the cylindrical phase, respectively, and n_{terms} is the number of terms in the multipole expansion. Recall that n_{terms} takes odd values only, see Section 3.4.3 for details, and note that the AHF method is implemented for $n_{\mathrm{terms}} \in \{3,5,7,9,11\}$ only.

The computation of $\boldsymbol{C}_{\mathrm{AHF}}$ is fast since the linear system to be solved for $\boldsymbol{C}_{\mathrm{AHF}}$ has only the small dimension n_{terms}. Among the homogenization methods investigated in this thesis, the AHF method is the fastest one but also the least flexible (most restrictive assumptions on the fine-scale structure of A).

AHA method and RVE-based homogenization method

We obtain the apparent stiffness tensor $\boldsymbol{C}_A$ performing the following algorithm

Algorithm 4.1.1 (AHA method and RVE-based homogenization method)

1. *Use the Galerkin finite element methods to numerically solve six boundary value problems of static linear elasticity on domain V (AHA method: problem* (3.26)*, RVE-based homogenization method: problem* (3.36a) *with displacement boundary conditions* (3.36b) *or traction boundary conditions* (3.36c) *on boundary Γ_V). This yields approximate solutions (displacements) to these boundary value problems with corresponding stresses and strains.*

2. *Compute the average of these stresses and strains over V.*
3. *Based on the average stresses and average strains set up a linear equation system for the apparent stiffness tensor of material A. Solve this to obtain the apparent stiffness tensor in Voigt notation (AHA method: $\boldsymbol{C}_{AHA}$, RVE-based homogenization with displacement and traction boundary conditions: $\boldsymbol{C}_d$, $\boldsymbol{C}_t$).*

In order to perform Algorithm 4.1.1, the following quantities have to be given

$$V, \qquad \boldsymbol{C}(\boldsymbol{x}) \qquad \text{and} \qquad \mathcal{T}_h, \tag{4.1}$$

where we denote by $\boldsymbol{C}(\boldsymbol{x})$ the fine-scale stiffness tensor of the material A at point $\boldsymbol{x} \in V$ and by $\mathcal{T}_h$ the mesh on V.

Note that, in contrast to the AHF method, the AHA and the RVE-based homogenization method allow to represent arbitrary fine-scale structures. However, this comes on considerably more computational effort, since we have to employ the finite element method for six different boundary value problems.

Self-consistent AHA method and self-consistent RVE-based homogenization method

We now consider the fine-scale stiffness tensor of composite A, denoted $\boldsymbol{C}(\boldsymbol{x})$, to be known only for some arbitrary shaped subset $\boldsymbol{x} \in W \subset V$, where V is as usual a brick-shaped periodic cell or a brick-shaped volume element. More precisely, we assume that

$$\boldsymbol{C}(\boldsymbol{x}) = \begin{cases} \boldsymbol{C}_1(\boldsymbol{x}) & \text{for } \boldsymbol{x} \in W, \\ \boldsymbol{C}_2 & \text{for } \boldsymbol{x} \in V \setminus W, \end{cases} \tag{4.2}$$

where the stiffness $\boldsymbol{C}_1(\boldsymbol{x})$ is known and the homogeneous stiffness $\boldsymbol{C}_2$ is to be determined. Since W is located completely within V, we will call the set $V \setminus W$ embedding box (EB) in the following.

Domains as described above are of importance for our study of the osteon in Chapter 7. Here, we consider W to be a cylinder, which makes it impossible to implement on the boundary of W periodic boundary conditions as necessary for the AHA method. Therefore, we embed W in a brick-shaped domain V. Furthermore, since we are interested in the apparent elastic properties of the osteon alone, we consider the embedding box to be filled with the effective material of the osteon. Also, in Chapter 7 we want to use the RVE-based homogenization method with traction boundary conditions (3.36c). The osteon consists of a central cylindrical canal (Haversian canal), which may be filled with air. Prescribing traction boundary conditions, in particular, on the top and the bottom of the Haversian canal, we let some surface forces apply to these faces. These will push the air back and force through the canal, a situation which we want to avoid, and thus embed the osteon into its effective material.

In order to handle situations, as given by Eq. (4.2), we introduce the self-consistent AHA method and the self-consistent RVE-based homogenization method. These methods assume that the embedding box consists of the effective material of W, that is $\boldsymbol{C}_2$ equals the effective stiffness tensor of A. Since the latter is not known, we approximate it by some starting value $\boldsymbol{C}^{(0)}$ and iteratively improve this approximation. Note that the term *self-consistent* in the name of the methods pay tribute to the Eshelby-based self-consistent method, for which we similarly assume that the inclusion phases are embedded into the effective material.

The following algorithm is set up

Algorithm 4.1.2 (Self-consistent AHA method and self-consistent RVE-based homogenization method)

1. *Fix some starting value $\boldsymbol{C}^{(0)}$ of the apparent stiffness tensor and some tolerance TOL. Set $\boldsymbol{C}_2 = \boldsymbol{C}^{(0)}$. Fix a positive natural number M specifying the maximum number of iterations allowed for Algorithm 4.1.2.*

2. *For* $k = 1, 2, \ldots$

   a) *Run the AHA method or the RVE-based homogenization using Algorithm 4.1.1. Thereby, pose the underlying boundary value problems on* V*, and average the fine-scale stress and the fine-scale strain over* W*. This yields the apparent stiffness tensor* $\boldsymbol{C}^{(k)}$*. Set* $\boldsymbol{C}_2 = \boldsymbol{C}^{(k)}$*.*

   b) *Stop if* $|\boldsymbol{C}^{(k-1)} - \boldsymbol{C}^{(k)}| < TOL$ *holds componentwise or the number of iterations equals* M*.*

3. $\boldsymbol{C}_A := \boldsymbol{C}^{(k)}$.

Note that we average in step (2a) of Algorithm 4.1.2 only over W and not over V. Thereby, we avoid that the stiffness tensor $\boldsymbol{C}_2$ of the embedding box unintentionally influences the apparent stiffness tensor $\boldsymbol{C}_A$.

Algorithm 4.1.2 returns the apparent stiffness tensor $\boldsymbol{C}_A$ which we also will denote by $\boldsymbol{C}_A^{(\mathrm{sAHA})}$, $\boldsymbol{C}_A^{(\mathrm{sd})}$ and $\boldsymbol{C}_A^{(\mathrm{st})}$ for the self-consistent AHA method, the self-consistent RVE-based homogenization method with displacement boundary conditions and the self-consistent RVE-based homogenization method with traction boundary conditions, respectively. The input quantities of Algorithm 4.1.2 are

$$W, \qquad V, \qquad \boldsymbol{C}(\boldsymbol{x}), \qquad \mathcal{T}_h, \qquad \boldsymbol{C}^{(0)}, \qquad M, \qquad \text{and} \qquad \text{TOL}, \tag{4.3}$$

where the notation is analogously as for the AHA method and the RVE-based homogenization method.

Galerkin finite element method

Both, the (self-consistent) AHA method and the (self-consistent) RVE-based homogenization method, involve solving the equations of static linear elasticity on some domain, numerically. To this end we use the finite element method and employ the software Comsol Multiphysics (COMSOL Multiphysics GmbH, 2011-2013) with the Structural Mechanics Module. This module implements the Ritz-Galerkin approach and utilizes the pure-displacement formulation of the equations of static linear elasticity. In consequence, the displacement is derived directly, while the strain is determined by differentiating the displacement, and the stress results through Hooke's law.

We couple Comsol Multiphysics with Matlab using its so-called "Livelink for Matlab " (COMSOL Multiphysics GmbH, 2011-2013). This allows to write a script which sets up our model, the physics and the solver setting. Scripting

- ensures reproducibility of all our results. This is useful for parameter studies as performed in Chapter 7.
- enables us to write functions outside of Comsol Multiphysics using the Matlab language for them. We made strongly use of this feature when implementing the (self-consistent) AHA method and the (self-consistent) RVE-based homogenization method.
- is useful when post-processing our results. Thereby, we can bypass the cumbersome graphical user interface of Comsol Multiphysics.

Setting up the equations of static linear elasticity in a Matlab script includes several steps: defining the domain and meshing it, specifying the fine-scale stiffness tensor $\boldsymbol{C}$ of the material under investigation, setting up the boundary conditions and defining possible constraints for the solution which guarantee uniqueness of the solution and, finally, setting up the solver for the finite element linear system.

We specify all lengths of our domain in μm. This is advantageous in the chapter on the osteon (Chapter 7). Since the dimension of the osteon is in the μm range we avoid thereby error-prone conversions outside of the script. In order to obtain a consistent set of units for our equations when using μm as

unit for the length, we have to employ the units MPa and MPa $\cdot (\mu\text{m})^{-1}$ for the stiffness tensor and the volume force, respectively.

The equations of static linear elasticity encountered for the (self-consistent) AHA and the (self-consistent) RVE-based homogenization method are completed with three types of boundary conditions: displacement boundary conditions (3.36b), traction boundary conditions (3.36c) and periodic boundary conditions (3.27). Displacement boundary conditions are straightforward to implement, since the weak solution of the displacement boundary value problem in static linear elasticity, i.e. Problem 2.2.4, is unique in $H^1(V, \mathbb{R}^3)$. For traction and periodic boundary conditions, however, we need to enforce some additional integral constraints to obtain uniqueness of the solution in some suitable function space. For a description of how to set up these constraints using Comsol Multiphysics, see the next section.

Discretization of our domain is done via the automatic mesh generator of Comsol Multiphysics. In the following we consider the mesh size h to characterize the maximum possible size of the edges within each tetrahedral element. In other words, no element size (longest edge) exceeds h. Furthermore, we use tetrahedral Lagrange elements of either first or second order.

The finite element linear system is solved employing the iterative solver *biconjugate gradient stabilized method*, in short BiCGstab. Note that we decided against a direct solver because its computational cost and its memory usage in large three-dimensional applications as ours becomes quite enormous. We start our iterative solver with $\boldsymbol{u} = 0$. In order to speed up the convergence of our iterative solver, we employ a preconditioner. Here, we use the method SOR (Successive over-relaxation). The local error of our iterative solver is controlled using a relative tolerance of 10^{-7}; this tolerance is tighter than Comsol Multiphysics defaults.

Traction and periodic boundary conditions

Using traction boundary conditions (3.36c) or periodic boundary conditions as in problem (3.26) we, respectively, enforce the integral constraints

$$\mathcal{M}_V(\boldsymbol{u}) = 0 \quad \text{and} \quad \mathcal{M}_V(\widetilde{\boldsymbol{w}}) = 0, \tag{4.4}$$

where $\boldsymbol{u}$ denotes the solution to the traction boundary value problem, and $\widetilde{\boldsymbol{w}} \in \{\widetilde{\boldsymbol{w}}_1, \widetilde{\boldsymbol{w}}_2, \ldots, \widetilde{\boldsymbol{w}}_6\}$ is defined by Eq. (3.27).

We implement the constraints (4.4) employing the feature *integration coupling* of Comsol Multiphysics. More precisely, we use the operator $\mathcal{F}_{\text{con}}$, defined by

$$\mathcal{F}_{\text{con}} : \mathcal{V} \to \mathbb{R}, \quad \mathcal{F}_{\text{con}}(g) \coloneqq \frac{1}{|V|} \int_V g(\boldsymbol{x}) \, \mathrm{d}\boldsymbol{x} \, . \tag{4.5}$$

Here, $\mathcal{V}$ denotes the set of functions g, which map from V to $\mathbb{R}$. We assume that g is either an individual component of $\boldsymbol{u}$ or $\widetilde{\boldsymbol{w}}$, and replace the constraints (4.4) by the conditions

$$\mathcal{F}_{\text{con}}(u_i) = 0 \quad \text{and} \quad \mathcal{F}_{\text{con}}(\widetilde{w}_i) = 0 \qquad \text{for } i = 1, 2, 3, \tag{4.6}$$

respectively. The conditions in Eq. (4.6) are enforced using point constraints in Comsol Multiphysics.

Periodic boundary conditions in problem (3.26) are realized computationally using the feature *general extrusion model coupling* of Comsol Multiphysics. Generally, this is an operator $\mathcal{F}_{\text{per}}$, defined by

$$\mathcal{F}_{\text{per}} : \mathcal{V}_1 \to \mathcal{V}_2, \quad \mathcal{F}_{\text{per}}(g)[\boldsymbol{x}] \coloneqq g(\phi(\boldsymbol{x})) \quad \forall \boldsymbol{x} \in \Gamma_+, \tag{4.7}$$

which maps functions in the set $\mathcal{V}_1 \coloneqq \{g \,|\, g : \Gamma_- \to \mathbb{R}\}$ to functions in the set $\mathcal{V}_2 \coloneqq \{g \,|\, g : \Gamma_+ \to \mathbb{R}\}$. Here, we denote by Γ_- and Γ_+ two opposite faces of the boundary Γ_V and let $\phi : \Gamma_+ \to \Gamma_-$ be a function

which maps a point on the face Γ_+ to an opposite point on face Γ_-. Note that we have for a box-shaped domain V, in total, three pairs of opposite faces Γ_+, Γ_- and three corresponding functions ϕ.

We use the operator $\mathcal{F}_{\text{per}}$ to replace the periodic boundary conditions in problem (3.26), i.e. the conditions

$$\widetilde{\boldsymbol{w}}|_{\Gamma_+} = \widetilde{\boldsymbol{w}}|_{\Gamma_-} \quad \text{for all three pairs of opposite faces } \Gamma_+, \Gamma_-,$$

by the pointwise constraints on the boundary

$$\widetilde{w}_i\big|_{\Gamma_+} - \mathcal{F}_{\text{per}}(\widetilde{w}_i|_{\Gamma_-}) = 0, \quad i = 1,2,3, \text{ for all three pairs of opposite faces } \Gamma_+, \Gamma_-.$$

Pointwise constraints of such type are discretized in Comsol Multiphysics such that they hold in each Lagrange point of each mesh element. The discretized constraints are then appended to the finite element linear system.

Numerical convergence analysis

We set up a family of shape regular meshes $\{\mathcal{T}_h\}$ for which the mesh size h decreases. As described in the former subsections, we compute for each mesh $\mathcal{T}_h$ an approximate solution $\boldsymbol{u}_h$ to our boundary value problem. In order to quantify the error in $\boldsymbol{u}_h$ with respect to some reference solution, denoted $\boldsymbol{u}_{\text{ref}}$, we use the measure aE, defined by

$$\text{aE}(\boldsymbol{u}_h) = \left(\sum_{j=1}^{3} \left\| (\boldsymbol{u}_h)_j - (\boldsymbol{u}_{\text{ref}})_j \right\|_0^2 \right)^{\frac{1}{2}}. \tag{4.8}$$

Before determining $\text{aE}(\boldsymbol{u}_h)$, we need to interpolate $\boldsymbol{u}_h$, living on mesh $\mathcal{T}_h$, to mesh $\mathcal{T}_{\text{ref}}$. To this end, we employ the feature *join* of Comsol Multiphysics, together with its method *explicit*. Note that this feature performs linear or cubic spline interpolation, when employing Lagrange elements of order one or two, respectively. The join feature expects two data sets as input. The first data set needs to be associated to the mesh $\mathcal{T}_{\text{ref}}$ and the displacement $\boldsymbol{u}_{\text{ref}}$, while the second one has to refer to the mesh $\mathcal{T}_h$ and the displacement $\boldsymbol{u}_h$. Note that the order of the data sets is important; if we change it, we perform a useless interpolation from the finer to the coarser mesh. Given that $\boldsymbol{u}_h$ and $\boldsymbol{u}_{\text{ref}}$ live on the same mesh, we carry out Comsol Multiphysics's volume integration feature to compute the integrals in Eq. (4.8) for $j = 1,2,3$. This feature uses Gaussian quadrature for three-dimensional domains choosing two Gauss points for each direction $\boldsymbol{e}_i$ on each finite element. Thereby, we can exactly integrate polynomials of degree three or less. This is sufficient for our application in Chapter 7, since we use Lagrange elements of order one and two only.

4.2 Mori-Tanaka method and self-consistent method

We implement the Mori-Tanaka and the self-consistent method for general types of composites A. Thereby, we assume that the homogeneous reference material is anisotropic with stiffness $\boldsymbol{C}_0$ (Voigt notation), and we consider the aspect ratios ar_i, $i \in \{1, 2\}$ of the inclusion phase(s) to be larger than one and smaller than infinity.

Under the above assumptions, no closed expressions for the Hill tensors $\boldsymbol{P}^{\text{MT}}$, $\boldsymbol{P}_1^{\text{SC}}$ and $\boldsymbol{P}_2^{\text{SC}}$, or more precisely, for the double integrals in their components (Eq. (3.54a)), are known. Hence, we determine these values numerically. To this end, we employ the Matlab functions *dblquad* and *quadl*. These functions implement adaptive integration of double integrals using the Lobatto four-point rule with a degree of precision of five. Moreover, the absolute error of the approximation is estimated using an eight-point

Lobatto-Kronrod rule of degree of precision of nine. The largest absolute error accepted is characterized by the integration tolerance $\mathrm{tol}_{\mathrm{int}}$. The computation of the Hill tensor was realized in a function called *BuildEshelbyAndHillTensors*. This function was implemented by Dr. Quentin Grimal and slightly modified by us. It has the input quantities

$$\mathrm{ar}, \qquad \boldsymbol{C}_0 \qquad \text{and} \qquad \mathrm{tol}_{\mathrm{int}}, \tag{4.9}$$

and returns the corresponding Hill tensor $\boldsymbol{P}$ in Kelvin notation.

Mori-Tanaka method

Once the Hill tensor is known, the computation of the apparent stiffness tensor $\boldsymbol{C}_{\mathrm{MT}}$ is a straightforward evaluation of Eq. (3.72). We implement the Mori-Tanaka method in a Matlab function called *Mori_Tanaka*. Input quantities of this function are

$$\mathrm{vf}_1, \qquad \mathrm{ar}_1, \qquad \boldsymbol{C}_1, \qquad \boldsymbol{C}_2, \qquad \text{and} \qquad \mathrm{tol}_{\mathrm{int}}. \tag{4.10}$$

The function *Mori_Tanaka* returns the apparent stiffness tensor $\boldsymbol{C}_{\mathrm{MT}}$ in Voigt notation.

In contrast to the self-consistent method, the computation of $\boldsymbol{C}_{\mathrm{MT}}$ is cheap since we need to compute the Hill tensor only once, see the next section.

Self-consistent method

Employing the self-consistent method we need to solve the following nonlinear system

$$\begin{aligned} \boldsymbol{F}(\boldsymbol{C}_A) &:= \boldsymbol{f}(\boldsymbol{C}_A, \boldsymbol{P}_1^{\mathrm{SC}}(\boldsymbol{C}_A), \boldsymbol{P}_2^{\mathrm{SC}}(\boldsymbol{C}_A)) \\ &= \sum_{r=1}^{2} \mathrm{vf}_r \, (\boldsymbol{C}_r - \boldsymbol{C}_A) : \left(\mathbf{Id}^{\mathbf{s}} + \boldsymbol{P}_r^{\mathrm{SC}}(\boldsymbol{C}_A) : (\boldsymbol{C}_r - \boldsymbol{C}_A)\right)^{-1} = 0. \end{aligned} \tag{4.11}$$

Here, we consider all fourth-order tensors to be symmetric and in Kelvin notation and, thus, represent each of them as a matrix. Furthermore, we represent the double contractions of two fourth-order tensors simply as a matrix-matrix product. Therefore, the nonlinear system (4.11) is of dimension 21.

What makes it difficult to solve nonlinear system (4.11) is that the Hill tensor $\boldsymbol{P}_r^{\mathrm{SC}}$ depends on the unknown apparent stiffness tensor $\boldsymbol{C}_A$. In a first attempt, we solved the nonlinear system (4.11) employing a Newton-type algorithm. This algorithm combines the Newton algorithm with some relaxation strategy and is part of the Matlab function *fsolve*. Using this algorithm we obtain reasonable apparent stiffness tensors, yet, the computation time is far too large. The reason for the high computation time lies in the complex form of $\boldsymbol{F}$. Using the Newton-type algorithm we search for a solution of the nonlinear system (4.11) by solving the linearized equation

$$\boldsymbol{F}'(\widetilde{\boldsymbol{C}}^{(m)}) \, \Delta\widetilde{\boldsymbol{C}} = -\boldsymbol{F}(\widetilde{\boldsymbol{C}}^{(m)}) \quad \text{with} \quad \Delta\widetilde{\boldsymbol{C}} = \widetilde{\boldsymbol{C}}^{(m+1)} - \widetilde{\boldsymbol{C}}^{(m)}, \quad m = 1, \ldots, K.$$

Here, $\widetilde{\boldsymbol{C}}^{(m)}$ denotes the mth approximation of the apparent stiffness tensor $\boldsymbol{C}_A$, and $\boldsymbol{F}'(\widetilde{\boldsymbol{C}}^{(m)}) \in \mathbb{R}^{21\times 21}$ is the Jacobian matrix of partial derivatives of $\boldsymbol{F}$ with respect to $\widetilde{\boldsymbol{C}}^{(m)}$. We approximate the Jacobian matrix $\boldsymbol{F}'(\widetilde{\boldsymbol{C}}^{(m)})$ using finite differences. This is expensive because $21+1$ evaluations of $\boldsymbol{F}$ are necessary to determine the whole Jacobian matrix $\boldsymbol{F}'$, and each such evaluation of $\boldsymbol{F}$ requires to compute the two Hill tensors $\boldsymbol{P}_1^{\mathrm{SC}}$ and $\boldsymbol{P}_2^{\mathrm{SC}}$. In total, performing K Newton steps, we have to evaluate $22 \cdot 2 \cdot K$ Hill tensors.

In order to decrease the high number of Hill tensor evaluations and, thus, the costs to compute $\boldsymbol{C}_A$, we approximate our complex nonlinear system (4.11), by a simpler one. Given some approximation of $\boldsymbol{C}_A$, denoted $\boldsymbol{C}^{(k-1)}$, we now solve

$$\boldsymbol{G}(\boldsymbol{C}_A) = \boldsymbol{g}(\boldsymbol{C}_A, \boldsymbol{P}_1^{\mathrm{SC}}(\boldsymbol{C}^{(k-1)}), \boldsymbol{P}_2^{\mathrm{SC}}(\boldsymbol{C}^{(k-1)})) = 0, \quad \text{where} \quad k = 1, 2, \ldots, N. \tag{4.12}$$

Note that, in contrast to the nonlinear system (4.11), the Hill tensors $\boldsymbol{P}_1^{\mathrm{SC}}(\boldsymbol{C}^{(k-1)})$ and $\boldsymbol{P}_2^{\mathrm{SC}}(\boldsymbol{C}^{(k-1)})$ in nonlinear system (4.12), are independent of the unknown $\boldsymbol{C}_A$. Using the Newton-type algorithm we solve the nonlinear system (4.12). This yields a new approximation of $\boldsymbol{C}_A$, which we denote by $\boldsymbol{C}^{(k)}$. Iterating over k, we successively improve $\boldsymbol{G}$. We stop iteration if the maximal component of $|\boldsymbol{C}^{(k)} - \boldsymbol{C}^{(k-1)}|$ is smaller than the so-called nonlinear solver tolerance $\mathrm{tol}_{\mathrm{nls}}$ or the maximum number of iterations is reached.

In summary, we formulate the following algorithm

Algorithm 4.2.1 (Self-consistent method)

1. *Fix a nonlinear solver tolerance $\mathrm{tol}_{\mathrm{nls}}$, an integration tolerance tol_{int} for the Hill tensor computations, and a starting value $\boldsymbol{C}^{(0)}$. Additionally, fix a positive natural number M specifying the maximum number of iterations allowed for Algorithm 4.2.1.*

2. *For $k = 1, 2, \ldots$*

   a) *Employ the function BuildEshelbyAndHillTensors with tol_{int} to derive the Hill Tensors, $\boldsymbol{P}_1^{SC}(\boldsymbol{C}^{(k-1)})$ and $\boldsymbol{P}_2^{SC}(\boldsymbol{C}^{(k-1)})$.*

   b) *Solve the corresponding nonlinear system* (4.12) *using the Newton-type algorithm. This gives $\boldsymbol{C}^{(k)}$.*

   c) *Stop if the maximal component of $|\boldsymbol{C}^{(k)} - \boldsymbol{C}^{(k-1)}|$ is smaller than $\mathrm{tol}_{\mathrm{nls}}$ or the number of iterations equals M.*

3. $\boldsymbol{C}_A := \boldsymbol{C}^{(k)}$

Using Matlab we realized Algorithm 4.2.1 in a function called *Selfconsistent*. This function returns the apparent stiffness $\boldsymbol{C}_A$, which we also denote by $\boldsymbol{C}_{\mathrm{SC}}$, in Voigt notation. It has the input quantities

$$\mathrm{vf}_1, \quad \mathrm{ar}_1, \quad \mathrm{ar}_2, \quad \boldsymbol{C}_1, \quad \boldsymbol{C}_2, \quad \mathrm{tol}_{\mathrm{nls}}, \quad \mathrm{tol}_{\mathrm{int}} \quad \text{and} \quad \boldsymbol{C}^{(0)}. \tag{4.13}$$

Note that employing Algorithm 4.2.1 to solve the nonlinear system $\boldsymbol{G} = 0$, the computation of $\boldsymbol{C}_A$ is cheaper than using the Newton algorithm for the nonlinear system $\boldsymbol{F} = 0$. This is because, firstly, the evaluation of the Jacobian matrix of $\boldsymbol{G}$ costs less than the evaluation of $\boldsymbol{F}'$. Note therefore, that, since the Hill tensors, $\boldsymbol{P}_1^{\mathrm{SC}}(\boldsymbol{C}^{(k)})$ and $\boldsymbol{P}_2^{\mathrm{SC}}(\boldsymbol{C}^{(k)})$, only appear as a constant (independent of the unknown) in $\boldsymbol{G}$, we need to evaluate only two Hill tensors during each step of Algorithm 4.2.1. Secondly, the total number of Hill tensor evaluations is smaller for Algorithm 4.2.1 than for the Newton-type algorithm employed for the nonlinear system (4.11). Denoting by N and K, the number of iterations required for Algorithm 4.2.1 and the Newton-type algorithm, respectively, the total number of Hill tensor evaluations for the former is only $2 \cdot N$, whereas for the latter it is $2 \cdot 22 \cdot K$ with $22 \cdot K > N$ in general.

5 Accuracy and computational efficiency of the self-consistent, the Mori-Tanaka and the AHF method

In Chapters 3 and 4 we introduced the self-consistent, the Mori-Tanaka and the AHF method and described their implementation, respectively. In this chapter we adjust these homogenization methods for their application in Chapter 6. Since in Chapter 6 we employ these homogenization methods in the MTLT model, it appears appropriate to perform our numerical tests for MTLT tissue. As test material we choose the building unit of the MTLT, i.e. the MCF. We model the MCF as a two-phase composite of the phases collagen (col) and mineral, more precisely hydroxyapatite (ha).

All employed homogenization methods predict the apparent stiffness tensor of the MCF, $\boldsymbol{C}_{\text{MCF}}$. By construction, this tensor is transverse isotropic and is a function such that

$$\begin{aligned}
\text{Self-consistent method:} \quad & \boldsymbol{C}_{\text{MCF}} = \boldsymbol{C}_{\text{MCF}}(\text{vf}_{\text{ha}}, \text{ar}_{\text{ha}}, \text{ar}_{\text{col}}, \boldsymbol{C}_{\text{col}}, \boldsymbol{C}_{\text{ha}}, \text{tol}_{\text{int}}, \text{tol}_{\text{nls}}, \boldsymbol{C}^{(0)}), \\
\text{Mori-Tanaka method:} \quad & \boldsymbol{C}_{\text{MCF}} = \boldsymbol{C}_{\text{MCF}}(\text{vf}_{\text{ha}}, \text{ar}_{\text{ha}}, \boldsymbol{C}_{\text{col}}, \boldsymbol{C}_{\text{ha}}, \text{tol}_{\text{int}}), \\
\text{AHF method:} \quad & \boldsymbol{C}_{\text{MCF}} = \boldsymbol{C}_{\text{MCF}}(\text{vf}_{\text{ha}}, \boldsymbol{C}_{\text{col}}, \boldsymbol{C}_{\text{ha}}, n_{\text{terms}}),
\end{aligned}$$

where vf_{ha} is the volume fraction of hydroxyapatite, ar_{ha} the aspect ratio of the hydroxyapatite inclusion, ar_{col} the aspect ratio of the collagen inclusion, $\boldsymbol{C}_{\text{col}}$ the stiffness tensor of the collagen phase, $\boldsymbol{C}_{\text{ha}}$ the stiffness tensor of the ha phase and tol_{int}, tol_{nls}, n_{terms} and $\boldsymbol{C}^{(0)}$, are tool parameters as explained in Chapter 4. For the self-consistent and the Mori-Tanaka method the accurate computation of $\boldsymbol{C}_{\text{MCF}}$ hinges also on the computation of the Hill tensor $\boldsymbol{P}$. Recall, that this tensor is a function of the aspect ratio and the integration tolerance tol_{int}.

In Sections 5.1 to 5.4 we study how the accuracy and the computation time of the tensors $\boldsymbol{P} = \boldsymbol{P}(\text{ar}_{\text{ha}}, \text{tol}_{\text{int}})$ and $\boldsymbol{C}_{\text{MCF}} = \boldsymbol{C}_{\text{MCF}}(\text{vf}_{\text{ha}}, p)$, where p is some input quantity introduced above, depend on their input arguments. Thereby, we consider vf_{ha} to be a variable of $\boldsymbol{C}_{\text{MCF}}$. This special role of vf_{ha} is justified, since increasing values of vf_{ha} correspond to an increasing tissue mineralization, a process which takes place in the MCF over time. Furthermore, we consider p to be one of the three quantities, the aspect ratio ar_{ha}, the tool parameter (tol_{int}, tol_{nls} and n_{terms}), and the starting value $\boldsymbol{C}^{(0)}$. Quantities not investigated in this chapter are: ar_{col}, $\boldsymbol{C}_{\text{col}}$ and $\boldsymbol{C}_{\text{ha}}$. These quantities were not considered because either we perform a similar study (instead of at ar_{col} we look at ar_{ha}) or the quantities are of minor interest in Chapter 6 ($\boldsymbol{C}_{\text{col}}$ and $\boldsymbol{C}_{\text{ha}}$).

Unless not mentioned otherwise, we let the mineral volume fraction vf_{ha} take its values in the set $[0, 1]$. As default values for the aspect ratios we choose $\text{ar}_{\text{ha}} = 15$ and $\text{ar}_{\text{col}} = 100$. Thereby, our value for ar_{col} corresponds to the lower limit of values given for ar_{col} in the literature (Akkus, 2005; Weiner and Wagner, 1998). However, more elaborated values are employed in Section 6.2.1. Default values for the tool parameters, tol_{int}, tol_{nls} and n_{terms}, are determined in particular in Section 5.2. The stiffness tensors $\boldsymbol{C}_{\text{col}}$ and $\boldsymbol{C}_{\text{ha}}$ we specify, assuming that both, the collagen and the mineral phase, are isotropic with bulk and shear moduli (Hellmich et al., 2004; Reisinger et al., 2010)

$$K_{\text{col}} = 4.17 \text{ [GPa]}, \; G_{\text{col}} = 1.92 \text{ [GPa]} \quad \text{and} \quad K_{\text{ha}} = 82.6 \text{ [GPa]}, \; G_{\text{ha}} = 44.9 \text{ [GPa]}.$$

Finally, as starting value $\boldsymbol{C}^{(0)}$ for the self-consistent method we choose the volume average of $\boldsymbol{C}_{\text{col}}$ and $\boldsymbol{C}_{\text{ha}}$, i.e. we set $\boldsymbol{C}^{(0)} = \boldsymbol{C}_{\text{Voigt}}$, where $\boldsymbol{C}_{\text{Voigt}}$ is defined by Eq. (3.43) with $\text{vf}_1 = \text{vf}_{\text{ha}}$, $\text{vf}_2 = 1 - \text{vf}_{\text{ha}}$, $\boldsymbol{C}_1 = \boldsymbol{C}_{\text{ha}}$ and $\boldsymbol{C}_2 = \boldsymbol{C}_{\text{col}}$.

Analyzing the results of our numerical tests, we employ different error measures. To this end, let $\boldsymbol{T} = \boldsymbol{T}(\text{vf}_{\text{ha}}, p)$ denote an approximation of the fourth-order tensor $\boldsymbol{T}^{\text{ref}} = \boldsymbol{T}^{\text{ref}}(\text{vf}_{\text{ha}}, p)$, where $p \in \{\text{ar}_{\text{ha}}, \text{tol}_{\text{int}}, \text{tol}_{\text{nls}}, n_{\text{terms}}\}$ and both, $\boldsymbol{T}$ and $\boldsymbol{T}^{\text{ref}}$, are given in Kelvin notation. Likewise, let

$t = t(\mathrm{vf_{ha}}, p)$ and $t^{\mathrm{ref}} = t^{\mathrm{ref}}(\mathrm{vf_{ha}}, p)$ denote a scalar quantity and its reference value, respectively. As error measures we use

$$\mathrm{rE}(\boldsymbol{T}) = \frac{\left\|\boldsymbol{T} - \boldsymbol{T}^{\mathrm{ref}}\right\|}{\left\|\boldsymbol{T}^{\mathrm{ref}}\right\|}, \qquad \mathrm{mrE}(\boldsymbol{T}) = \max_{\mathrm{vf_{ha}} \in I} \left\{ \mathrm{rE}\left(\boldsymbol{T}\right) \right\}, \qquad \mathrm{raE}(t) = \left| \frac{t - t^{\mathrm{ref}}}{1 + \max\{|t|, |t^{\mathrm{ref}}|\}} \right|, \tag{5.1}$$

where $\|\cdot\|$ refers to the Frobenius norm and $I \subseteq [0,1]$. The fourth-order tensor $\boldsymbol{T}$ in (5.1) will be either the Hill tensor $\boldsymbol{P}$ or the apparent stiffness tensor $\boldsymbol{C}_{\mathrm{MCF}}$. In case of $\boldsymbol{T} = \boldsymbol{P}$, we use the standard relative error and, thus, employ rE. In case of $\boldsymbol{T} = \boldsymbol{C}_{\mathrm{MCF}}$, the error measure $\mathrm{rE}(\boldsymbol{C}_{\mathrm{MCF}}) = \mathrm{rE}(\boldsymbol{C}_{\mathrm{MCF}}(\mathrm{vf_{ha}}))$ would give an error for each mineral volume fraction value $\mathrm{vf_{ha}} \in I$. However, being interested in an error over all values $\mathrm{vf_{ha}} \in I$, we consider the maximum of rE over $\mathrm{vf_{ha}}$. To this end, we employ mrE as defined in (5.1). The scalar quantity t in (5.1) will be either a single elastic constant of $\boldsymbol{C}_{\mathrm{MCF}}$ or a component of $\boldsymbol{C}_{\mathrm{MCF}}$. Here, it is worth to mention the transverse and the axial stiffness component, denoted C_{trv} and C_{axi}, respectively. These components represent the elastic properties of the MCF perpendicular and parallel to its long axis, respectively. Since the elastic constants, C_{trv} or C_{axi} might become zero, the standard relative error is not well defined. Therefore, we consider the mixed absolute-relative error measure raE, whose denominator cannot become zero.

Finally, we introduce the target accuracy ERR and the target integration tolerance $\mathrm{TOL_{int}}$. These quantities are useful in Section 5.1 and Section 5.2, where we, in particular, ask, which integration tool parameter $\mathrm{tol_{int}}$ is necessary to achieve ERR. To this end we define $\mathrm{TOL_{int}}$ as the largest integration tolerance for which holds that

$$\mathrm{rE}\left(\boldsymbol{T}(\mathrm{tol_{int}}, \mathrm{ar_{ha}})\right) \leq \mathrm{ERR}, \tag{5.2}$$

with logarithmically spaced $\mathrm{tol_{int}} \in [10^{-10}, 10^{-1}]$ and $\mathrm{ERR} = 10^{-4}$.

5.1 Hill tensor

In this section we consider the Hill tensor $\boldsymbol{P}$ as function of the mineral aspect ratio $\mathrm{ar_{ha}}$ and the integration tolerance $\mathrm{tol_{int}}$, i.e. $\boldsymbol{P} = \boldsymbol{P}(\mathrm{ar_{ha}}, \mathrm{tol_{int}})$, see Eq. (3.54a) and Section 4.2 for details. We address the following research questions:

1. Can we choose a value for $\mathrm{tol_{int}}$ such that $\mathrm{rE}(\boldsymbol{P}(\mathrm{ar_{ha}}, \mathrm{tol_{int}})) \leq \mathrm{ERR}$ holds for all values of $\mathrm{ar_{ha}} \in [1, 200]$? This is desirable for Chapter 6, where we compute the Hill tensor $\boldsymbol{P}(\mathrm{ar_{ha}}, \mathrm{tol_{int}})$ for a large range of values of $\mathrm{ar_{ha}} \in [1, 200]$. Note that the given interval for $\mathrm{ar_{ha}}$ covers the whole spectrum of aspect ratio values of all phases in Chapter 6 (mineral, collagen, ...).

2. Given some integration tolerance $\mathrm{tol_{int}}$, how well is the Hill tensor of a cylindrical inclusion, $\boldsymbol{P}(\infty, \mathrm{tol_{int}})$, approximated by the Hill tensor $\boldsymbol{P}(\mathrm{ar_{ha}}, \mathrm{tol_{int}})$ with $\mathrm{ar_{ha}} \in [100, 200]$? This question arises in Sections 6.2.1 and 6.2.3, where we idealize cylindrically shaped constituents, such as collagen molecules or MCFs, as highly prolated ellipsoidal inclusions with aspect ratios between 100 and 200. The corresponding question for the apparent stiffness tensor $\boldsymbol{C}_{\mathrm{MCF}}$, instead of $\boldsymbol{P}$, is considered in Section 5.3.

3. How does the computation time of the Hill tensor $\boldsymbol{P}$ depend on $\mathrm{tol_{int}}$ and $\mathrm{ar_{ha}}$? Which computation times do we obtain for the values of $\mathrm{ar_{ha}}$ and $\mathrm{tol_{int}}$ usually employed in Chapter 6?

In order to answer the first question we determine the target integration tolerance $\mathrm{TOL_{int}}$ based on Eq. (5.2) and Eq. (5.1). Thereby, we employ the error measure $\mathrm{rE}(\boldsymbol{P})$, set $\mathrm{ar_{ha}} = \{1, 20, 40, \ldots, 200\}$ and $\mathrm{tol_{int}} \in [10^{-10}, 10^{-1}]$, and use $\boldsymbol{P}^{\mathrm{ref}} = \boldsymbol{P}(\mathrm{ar_{ha}}, 10^{-11})$. In the lower plot of Fig. 5.1 we display $\mathrm{TOL_{int}}$ versus $\mathrm{ar_{ha}}$, in the upper plot of Fig. 5.1 we show the resulting error $\mathrm{rE}(\boldsymbol{P})$ versus $\mathrm{ar_{ha}}$.

Table 5.1.: The relative error $\mathrm{rE}(\boldsymbol{P}) = \mathrm{rE}(\boldsymbol{P}(\mathrm{ar_{ha}}, \mathrm{tol_{int}}))$ for various values of aspect ratio $\mathrm{ar_{ha}}$ and integration tolerance $\mathrm{tol_{int}}$. As reference value $\boldsymbol{P}^{\mathrm{ref}}$ we use the Hill tensor for a cylindrical inclusion (Eq. (C.1)).

$\mathrm{ar_{ha}}$ \ $\mathrm{tol_{int}}$	10^{-2}	10^{-4}	10^{-6}	10^{-8}	10^{-10}	10^{-12}
1	$4.1249 \cdot 10^{-1}$	$4.1249 \cdot 10^{-1}$	$4.1199 \cdot 10^{-1}$	$4.1199 \cdot 10^{-1}$	$4.1199 \cdot 10^{-1}$	$4.1199 \cdot 10^{-1}$
10	$3.6242 \cdot 10^{-2}$	$3.7270 \cdot 10^{-2}$	$3.7053 \cdot 10^{-2}$	$3.7047 \cdot 10^{-2}$	$3.7046 \cdot 10^{-2}$	$3.7046 \cdot 10^{-2}$
10^2	$1.1355 \cdot 10^{-3}$	$4.2598 \cdot 10^{-4}$	$8.8756 \cdot 10^{-4}$	$8.8493 \cdot 10^{-4}$	$8.8466 \cdot 10^{-4}$	$8.8466 \cdot 10^{-4}$
10^3	$1.0534 \cdot 10^{-3}$	$4.2719 \cdot 10^{-6}$	$4.2712 \cdot 10^{-6}$	$1.3206 \cdot 10^{-5}$	$1.3877 \cdot 10^{-5}$	$1.4130 \cdot 10^{-5}$
10^4	$1.0533 \cdot 10^{-3}$	$1.3476 \cdot 10^{-7}$	$4.7768 \cdot 10^{-8}$	$4.7768 \cdot 10^{-8}$	$1.7447 \cdot 10^{-7}$	$1.7656 \cdot 10^{-7}$
10^5	$1.0533 \cdot 10^{-3}$	$1.2692 \cdot 10^{-7}$	$1.1420 \cdot 10^{-8}$	$1.1420 \cdot 10^{-8}$	$9.1105 \cdot 10^{-10}$	$2.1840 \cdot 10^{-9}$
10^6	$1.0533 \cdot 10^{-3}$	$1.2691 \cdot 10^{-7}$	$1.1266 \cdot 10^{-8}$	$1.1266 \cdot 10^{-8}$	$3.1771 \cdot 10^{-10}$	$6.3288 \cdot 10^{-12}$

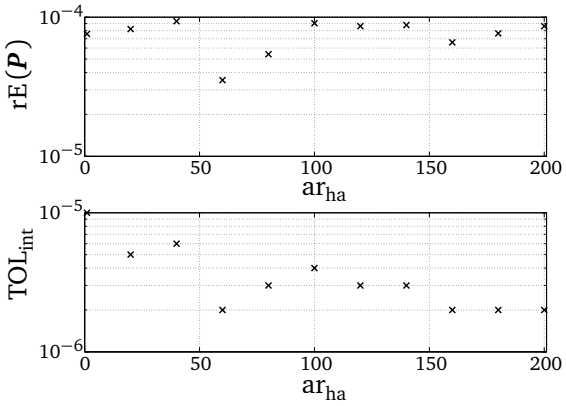

Figure 5.1.: Relative error $\mathrm{rE}(\boldsymbol{P}) = \mathrm{rE}(\boldsymbol{P}(\mathrm{ar_{ha}}, \mathrm{TOL_{int}}))$ and target integration tolerance $\mathrm{TOL_{int}}$, both versus the aspect ratio $\mathrm{ar_{ha}}$. Target error is $\mathrm{ERR} = 10^{-4}$. Reference value is $\boldsymbol{P}^{\mathrm{ref}} = \boldsymbol{P}(\mathrm{ar_{ha}}, 10^{-11})$.

Table 5.2.: Computation time of the Hill tensor in seconds for various values of aspect ratio $\mathrm{ar_{ha}}$ and integration tolerance $\mathrm{tol_{int}}$.

$\mathrm{ar_{ha}}$ \ $\mathrm{tol_{int}}$	10^{-2}	10^{-4}	10^{-6}	10^{-8}	10^{-10}	10^{-12}
1	1.33	1.33	6.00	8.92	57.84	145.52
10	1.36	2.60	8.25	24.57	133.47	388.47
10^2	1.37	2.04	8.07	23.35	134.36	326.65
10^3	1.37	2.01	2.87	9.72	30.46	216.10
10^4	1.35	2.01	2.82	3.66	22.28	41.94
10^5	1.35	2.01	2.83	3.67	21.31	40.99
10^6	1.35	2.01	2.84	3.65	21.35	37.03

Fig. 5.1 shows the trend that the larger $\mathrm{ar_{ha}}$, the smaller $\mathrm{TOL_{int}}$. However, $\mathrm{TOL_{int}}$ values differ by less than 10^{-5} among the aspect ratios $\mathrm{ar_{ha}} \in [1, 200]$. Therefore, we neglect the observed dependence between $\mathrm{TOL_{int}}$ and $\mathrm{ar_{ha}}$, and select for all aspect ratios $\mathrm{ar_{ha}}$ the same integration tolerance $\mathrm{tol_{int}}$. An appropriate value for the integration tolerance is, for instance, $\mathrm{tol_{int}} = 10^{-6}$; with $\mathrm{tol_{int}} = 10^{-6}$ Eq. (5.2) holds for all aspect ratios $\mathrm{ar_{ha}}$ displayed in Fig. 5.1.

In order to answer the second question, we compute the Hill tensor $\boldsymbol{P}(\mathrm{ar_{ha}}, \mathrm{tol_{int}})$ for various values of $\mathrm{ar_{ha}} \in \{10^1, 10^2, \cdots, 10^6\}$ and $\mathrm{tol_{int}} \in \{10^{-2}, 10^{-4}, \ldots, 10^{-12}\}$. For these Hill tensors we determine the errors $\mathrm{rE}(\boldsymbol{P})$, where $\boldsymbol{P}^{\mathrm{ref}}$ is the Hill tensor for a cylindrical inclusion, given analytically in Eq. (C.1). Corresponding results we list in Table 5.1. We approximate the modeling error of the Hill tensor for aspect ratio $\mathrm{ar_{ha}}$, by $\mathrm{rE}(\boldsymbol{P}(\mathrm{ar_{ha}}, 10^{-12}))$.

Table 5.1 demonstrates that the modeling error decreases as $\mathrm{ar_{ha}} \to 10^6$. In particular, we observe a modeling error of order of magnitude of 10^{-3}–10^{-5} for $\mathrm{ar_{ha}} \in [100, 200]$. We regard this a satisfactory accuracy. Therefore, we conclude that, yes, we can well approximate the Hill tensor of a cylindrical inclusion, $\boldsymbol{P}(\infty, \mathrm{tol_{int}})$, by the Hill tensor $\boldsymbol{P}(\mathrm{ar_{ha}}, \mathrm{tol_{int}})$ with $\mathrm{ar_{ha}} \in [100, 200]$ and $\mathrm{tol_{int}}$ selected appropriately strict. Finally, it is worth to note that in case of $\mathrm{ar_{ha}} = 100$ and for $\mathrm{tol_{int}} \leq 10^{-6}$ the error $\mathrm{rE}(\boldsymbol{P}(\mathrm{ar_{ha}}, \mathrm{tol_{int}}))$, compare Table 5.1, is of the order of magnitude of the modeling error. Thus, once again (see the results on our first research question), there is an indication for that $\mathrm{tol_{int}} = 10^{-6}$ is an appropriate value for the integration tolerance when computing the Hill tensor.

Finally, we address the third question by listing the computation time of the Hill tensor for various values of $\mathrm{ar_{ha}} \in \{10^0, 10^1, 10^2, \cdots, 10^6\}$ and integration tolerance $\mathrm{tol_{int}} \in \{10^{-2}, 10^{-4}, \ldots, 10^{-12}\}$ in Table 5.2.

Table 5.2 shows that the computation time is determined by both, the aspect ratio $\mathrm{ar}_{\mathrm{ha}}$ and the integration tolerance $\mathrm{tol}_{\mathrm{int}}$. We observe different trends: (1) if we keep $\mathrm{ar}_{\mathrm{ha}}$ fix and decrease $\mathrm{tol}_{\mathrm{int}}$, the computation time increases, (2) if we keep $\mathrm{tol}_{\mathrm{int}}$ fix and increase $\mathrm{ar}_{\mathrm{ha}} \geq 10$, the computation time generally decreases (not significant exceptions are the cases $\mathrm{ar}_{\mathrm{ha}} = 1, 10$). The reason for the first trend lies in that we employ an adaptive numerical integration scheme. Decreasing values of $\mathrm{tol}_{\mathrm{int}}$ require more subdivision steps of the scheme and, thus, a larger computation time. The second trend may be due to our employed integration scheme controls the absolute error. For $\mathrm{ar}_{\mathrm{ha}} \to 10^6$ the number of Hill tensor components, whose integrands $|N_{ijkl}|$ converge to zero, increases; compare Table D.1 in Appendix D, which shows $\max_{\theta,\eta}(|N_{ijkl}(\theta,\eta)|)$ versus the aspect ratio $\mathrm{ar}_{\mathrm{ha}} \geq 10$. Together with the maximum of $|N_{ijkl}|$, the absolute error of the numerical integration scheme may decrease for $\mathrm{ar}_{\mathrm{ha}} \to 10^6$. Then, for a sufficient small and fix absolute tolerance, Hill tensor components, for which $\max_{\theta,\eta}(|N_{ijkl}(\theta,\eta)|)$ is close to zero, can be computed faster (they require less subdivision steps of the scheme) than those Hill tensor components, for which $\max_{\theta,\eta}(|N_{ijkl}(\theta,\eta)|)$ is not so close to zero.

Finally, we read off the computation time of the Hill tensor for the aspect ratios $\mathrm{ar}_{\mathrm{ha}}$ and the integration tolerances $\mathrm{tol}_{\mathrm{int}}$ usually employed in this thesis from Table 5.2. For $\mathrm{ar}_{\mathrm{ha}} \in [1, 200]$ and $\mathrm{tol}_{\mathrm{int}} \geq 10^{-6}$ the computation time of the Hill tensor is less than 9 seconds.

5.2 Tool parameters

In this section we consider $\boldsymbol{C}_{\mathrm{MCF}}$ as function of the mineral volume fraction $\mathrm{vf}_{\mathrm{ha}}$ and some tool parameter ($\mathrm{tol}_{\mathrm{int}}$, $\mathrm{tol}_{\mathrm{nls}}$, n_{terms}), i.e. $\boldsymbol{C}_{\mathrm{MCF}} = \boldsymbol{C}_{\mathrm{MCF}}(\mathrm{vf}_{\mathrm{ha}}, \text{tool parameter})$. Recall that the self-consistent method has the tool parameters $\mathrm{tol}_{\mathrm{int}}$ and $\mathrm{tol}_{\mathrm{nls}}$, while the Mori-Tanaka and the AHF method have the tool parameters, $\mathrm{tol}_{\mathrm{int}}$ and n_{terms}, respectively. We concentrate on the following research questions:

1. Can we improve the accuracy of $\boldsymbol{C}_{\mathrm{MCF}}$ by one or more orders of magnitude when decreasing the tool parameters $\mathrm{tol}_{\mathrm{int}}$ and $\mathrm{tol}_{\mathrm{nls}}$ about one order of magnitude or increasing n_{terms} about two?

2. In order to obtain a target error $\mathrm{ERR} = 10^{-4}$ for $\boldsymbol{C}_{\mathrm{MCF}}$, which value for the tool parameters should we select? Recall that we pursued a similar question for the Hill tensor in Section 5.1. Based on the results we will select default values for the tool parameters.

3. How does the computation time of $\boldsymbol{C}_{\mathrm{MCF}}$ depend on the tool parameter? Which computation times can we expect in general, and, in particular, for the default tool parameters?

We organize this section such that we answer first all research questions for the self-consistent method, proceed then to the Mori-Tanaka method and, finally, consider the AHF method.

Self-consistent method: We address the first research question, computing $\boldsymbol{C}_{\mathrm{MCF}}$ for various values of mineral volume fractions $\mathrm{vf}_{\mathrm{ha}} \in [0, 1]$ and tool parameters $(\mathrm{tol}_{\mathrm{int}}, \mathrm{tol}_{\mathrm{nls}})$, and comparing these tensors with some reference tensor $\boldsymbol{C}^{\mathrm{ref}}_{\mathrm{MCF}}$; see Table 5.3 for the actual values of the tool parameters and the reference tool parameter. We quantify the relative error of $\boldsymbol{C}_{\mathrm{MCF}}$ using the measure $\mathrm{mrE}(\boldsymbol{C}_{\mathrm{MCF}})$ as defined in Eq. (5.1). Corresponding results are shown in Fig. 5.2.

We observe that the accuracy of $\boldsymbol{C}_{\mathrm{MCF}}$, predicted by the self-consistent method, improves about one order of magnitude with $\mathrm{tol}_{\mathrm{int}}$ or $\mathrm{tol}_{\mathrm{nls}}$ if

(1) $\mathrm{tol}_{\mathrm{nls}} = \{10^{-3}, 10^{-4}, 10^{-5}\}$ is fix and $\mathrm{mrE}(\boldsymbol{C}_{\mathrm{MCF}})$ is considered a function of $\mathrm{tol}_{\mathrm{int}}$,

(2) $\mathrm{tol}_{\mathrm{int}} = \{10^{-4}, 10^{-5}, 10^{-6}\}$ is fix and $\mathrm{mrE}(\boldsymbol{C}_{\mathrm{MCF}})$ is considered a function of $\mathrm{tol}_{\mathrm{nls}} \geq \mathrm{tol}_{\mathrm{int}}$.

For other cases no improvement of the accuracy of $\boldsymbol{C}_{\mathrm{MCF}}$ can be observed in Fig. 5.2. This also applies for the case that $\mathrm{tol}_{\mathrm{int}} = \{10^{-4}, 10^{-5}, 10^{-6}\}$ is fix and $\mathrm{mrE}(\boldsymbol{C}_{\mathrm{MCF}})$ is considered a function of $\mathrm{tol}_{\mathrm{nls}} < \mathrm{tol}_{\mathrm{int}}$ (this case is similar to case (2), however, has another assumption on $\mathrm{tol}_{\mathrm{nls}}$). Here, the relative error $\mathrm{mrE}(\boldsymbol{P})$ stagnates with decreasing values of $\mathrm{tol}_{\mathrm{nls}}$; compare therefore, for instance, the line

for $\mathrm{tol}_{\mathrm{int}} = 10^{-4}$ with $\mathrm{tol}_{\mathrm{nls}} < 10^{-4}$ in Fig. 5.2. Such a behavior is due to the integration tolerance $\mathrm{tol}_{\mathrm{int}}$ restricts the accuracy of the Hill tensor $\boldsymbol{P}$ and thus of the apparent stiffness $\boldsymbol{C}_{\mathrm{MCF}}$.

The second question regarding the target error of 10^{-4} and corresponding tool parameters, can be answered reading off these tool parameters from Fig. 5.2. It shows that we have an error smaller or equal to 10^{-4}, if we choose the tool parameters $\mathrm{tol}_{\mathrm{int}} = 10^{-6}$ and $\mathrm{tol}_{\mathrm{nls}} = 10^{-5}$. In the following we will use these values as default values for $\mathrm{tol}_{\mathrm{int}}$ and $\mathrm{tol}_{\mathrm{nls}}$.

Moving to our third question, we firstly determine the computation time of $\boldsymbol{C}_{\mathrm{MCF}}(\mathrm{vf}_{\mathrm{ha}}, \mathrm{tol})$ for values of $\mathrm{vf}_{\mathrm{ha}}$ and $\mathrm{tol} \in \{\mathrm{tol}_{\mathrm{int}}, \mathrm{tol}_{\mathrm{nls}}\}$ as given in Table 5.3, and secondly, take the mean of the computation time over $\mathrm{vf}_{\mathrm{ha}} \in I$. In Table 5.4 we list the corresponding results. This data shows that the computation time of $\boldsymbol{C}_{\mathrm{MCF}}$ vary between 9 and 510 seconds. Furthermore, it shows that the computation time for the self-consistent method increases with decreasing values of the tool parameters, $\mathrm{tol}_{\mathrm{nls}}$ and $\mathrm{tol}_{\mathrm{int}}$. This is because a smaller value of $\mathrm{tol}_{\mathrm{nls}}$ or $\mathrm{tol}_{\mathrm{int}}$ entails more effort for the self-consistent method. Decreasing $\mathrm{tol}_{\mathrm{nls}}$ we have to perform more iterations for Algorithm 4.2.1, while decreasing $\mathrm{tol}_{\mathrm{int}}$ more subdivision steps for the employed numerical integration scheme are required. Finally, the computation time of $\boldsymbol{C}_{\mathrm{MCF}}$ with the self-consistent method using the default tool parameters $\mathrm{tol}_{\mathrm{int}} = 10^{-6}$ and $\mathrm{tol}_{\mathrm{nls}} = 10^{-5}$ is 252 seconds.

Mori-Tanaka method: We answer the first question displaying $\mathrm{mrE}(\boldsymbol{C}_{\mathrm{MCF}})$ versus $\mathrm{tol}_{\mathrm{int}}$ in Fig. 5.3. Thereby, we proceed similarly as for the self-consistent method, see the corresponding paragraph above and Table 5.3 for the employed tool parameters. Similar to the self-consistent method, the accuracy of $\boldsymbol{C}_{\mathrm{MCF}}$ according to the Mori-Tanaka method increases about one order of magnitude, if the integration tool parameter $\mathrm{tol}_{\mathrm{int}}$ decreases about the same order of magnitude.

We address the second question, reading off $\mathrm{tol}_{\mathrm{int}}$ for a target error of 10^{-4} from Fig. 5.3. It shows that we have an error smaller or equal to 10^{-4}, if we choose the tool parameter $\mathrm{tol}_{\mathrm{int}} = 10^{-4}$. We employ this value as default tool parameter for the Mori-Tanaka method throughout this thesis.

Finally, to answer the third question, we display in Table 5.4 the computation time of $\boldsymbol{C}_{\mathrm{MCF}}(\mathrm{vf}_{\mathrm{ha}}, \mathrm{tol})$ for values of $\mathrm{vf}_{\mathrm{ha}}$ and $\mathrm{tol}_{\mathrm{int}}$ as given in Table 5.3. Similarly to the self-consistent method, it shows that the computation time for the Mori-Tanaka method increases with decreasing values of $\mathrm{tol}_{\mathrm{int}}$. This is because a smaller value of $\mathrm{tol}_{\mathrm{int}}$ entails more effort for the Hill tensor computation and thus for the Mori-Tanaka method. Finally, we read off from Table 5.4 computation times of 1–26 for the Mori-Tanaka method. Moreover, we observe a computation time of 5 seconds for the default tool parameter $\mathrm{tol}_{\mathrm{int}} = 10^{-4}$.

AHF method: In order to address the first question it is necessary to provide a bit of extra information. It is not clear, whether the tensor $\boldsymbol{C}_{\mathrm{MCF}}$ gets more accurate as the number n_{terms} of terms in the multipole expansion increases. Nevertheless, Parnell (2004) has shown that the shear modulus G of the AHF method converges to the shear modulus G^* predicted by the homogenization method of Waterman and Truell (1961). To this end, we focus now on the shear modulus G of $\boldsymbol{C}_{\mathrm{MCF}}$. Using the AHF method we compute $G(\mathrm{vf}_{\mathrm{ha}}, n_{\mathrm{terms}})$ for different values of $\mathrm{vf}_{\mathrm{ha}}$ and $n_{\mathrm{terms}} = \{3, 5, 7, 9\}$. We employ the error $\mathrm{raE}(G)$, see Eq. (5.1), and set $G^{\mathrm{ref}}(\mathrm{vf}_{\mathrm{ha}}) = G(\mathrm{vf}_{\mathrm{ha}}, 11)$. In Fig. 5.4 we display $\mathrm{raE}(G(\mathrm{vf}_{\mathrm{ha}}, n_{\mathrm{terms}}))$ versus n_{terms} for different values of mineral volume fraction $\mathrm{vf}_{\mathrm{ha}}$. Since Parnell (2004) found that convergence can be observed only for inclusion volume fractions which are smaller or equal to 0.4, we restrict us here to $\mathrm{vf}_{\mathrm{ha}} \in \{0.1, 0.2, 0.3, 0.4\}$.

Fig. 5.4 shows that for $\mathrm{vf}_{\mathrm{ha}}$ fix and a step of n_{terms} from 3 to 5, the error $\mathrm{raE}(G)$ decreases about four order of magnitudes. For $n_{\mathrm{terms}} > 5$, however, the error $\mathrm{raE}(G)$ decreases only about two order of magnitudes.

We answer the second question, reading off the tool parameter n_{terms} for the target error $\mathrm{ERR} = 10^{-4}$ from Fig. 5.4. It shows that we have an error smaller or equal to 10^{-4}, if we choose the tool parameter $n_{\mathrm{terms}} = 3$. In order to compensate for the fact that we considered only the error $\mathrm{raE}(G)$ and not $\mathrm{mrE}(\boldsymbol{C}_{\mathrm{MCF}})$, we increase n_{terms} about two. To this end, we use as default tool parameter for the AHF method $n_{\mathrm{terms}} = 5$ throughout this thesis.

Table 5.3.: Variation ranges of tool parameters, reference tool parameters and mineral volume fractions employed for the self-consistent (SC), the Mori-Tanaka (MT) and the AHF method.

Method	Test tool parameters			Reference tool parameters			$vf_{ha} \in I$
	tol_{int}	tol_{nls}	n_{terms}	tol_{int}	tol_{nls}	n_{terms}	
SC	$[10^{-6}, 10^{-1}]$	$[10^{-5}, 10^{-1}]$	–	10^{-7}	10^{-6}	–	$[0, 1]$
MT	$[10^{-6}, 10^{-1}]$	–	–	10^{-7}	–	–	$[0, 1]$
AHF	–	–	$3, 5, 7, 9$	–	–	11	$[0, 0.4]$

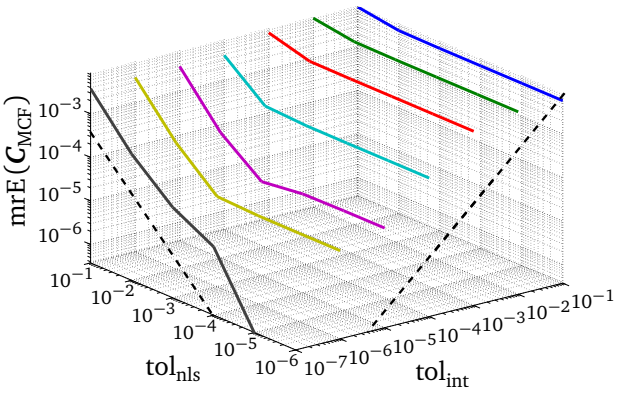

Figure 5.2.: Relative error $\mathrm{mrE}(\boldsymbol{C}_{\mathrm{MCF}})$ of the self-consistent method versus $\mathrm{tol}_{\mathrm{int}}$ and $\mathrm{tol}_{\mathrm{nls}}$. The dashed lines denote the lines $\mathrm{mrE}(\boldsymbol{C}_{\mathrm{MCF}}(\mathrm{tol})) = c\,\mathrm{tol}$, where c is a constant and $\mathrm{tol} = \mathrm{tol}_{\mathrm{int}}$ or $\mathrm{tol} = \mathrm{tol}_{\mathrm{nls}}$.

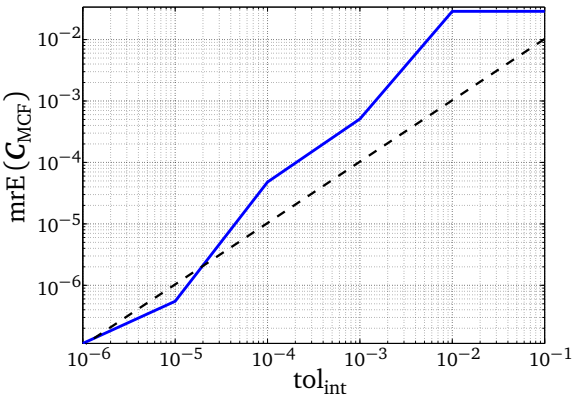

Figure 5.3.: Relative error $\mathrm{mrE}(\boldsymbol{C}_{\mathrm{MCF}})$ of the Mori-Tanaka method versus $\mathrm{tol}_{\mathrm{int}}$. The dashed line denotes the line $\mathrm{mrE}(\boldsymbol{C}_{\mathrm{MCF}}(\mathrm{tol}_{\mathrm{int}})) = c\,\mathrm{tol}_{\mathrm{int}}$, compare Fig. 5.2.

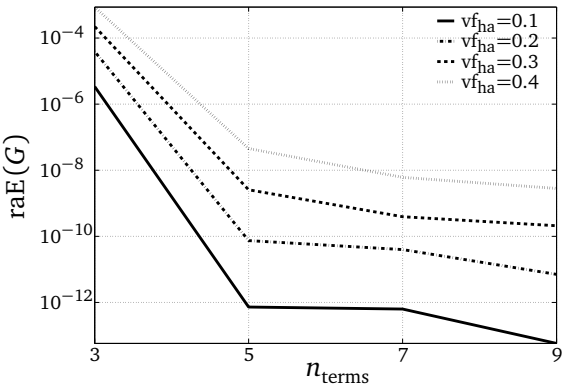

Figure 5.4.: Relative error $\mathrm{raE}(G)$ of the AHF method versus n_{terms}. The mineral volume fraction was set to $\mathrm{vf}_{\mathrm{ha}} = 0.1, 0.2, 0.3, 0.4$.

Table 5.4.: Mean computation time (seconds) of $\boldsymbol{C}_{\mathrm{MCF}}$ for the self-consistent, the Mori-Tanaka and the AHF method for various values of tool parameters $\mathrm{tol}_{\mathrm{int}}$, $\mathrm{tol}_{\mathrm{nls}}$ and n_{terms}.

Self-consistent method							**Mori-Tanaka method**		**AHF method**	
$\mathrm{tol}_{\mathrm{int}}$ \ $\mathrm{tol}_{\mathrm{nls}}$	10^{-1}	10^{-2}	10^{-3}	10^{-4}	10^{-5}	10^{-6}	$\mathrm{tol}_{\mathrm{int}}$	time	n_{terms}	time
10^{-1}	8.91	11.96	15.05	18.65	21.56	25.35	10^{-1}	0.93	3	$1.87 \cdot 10^{-2}$
10^{-2}	9.12	12.20	15.13	18.04	20.59	23.69	10^{-2}	0.93	5	$1.66 \cdot 10^{-2}$
10^{-3}	14.52	19.90	24.89	30.05	34.72	39.77	10^{-3}	2.43	7	$2.81 \cdot 10^{-2}$
10^{-4}	26.36	35.20	43.79	52.60	61.64	69.77	10^{-4}	5.38	9	$3.71 \cdot 10^{-2}$
10^{-5}	56.86	77.26	96.34	115.68	134.64	153.63	10^{-5}	8.77	11	$6.40 \cdot 10^{-2}$
10^{-6}	106.76	144.61	180.25	216.58	251.99	287.70	10^{-6}	13.10		
10^{-7}	183.11	250.09	313.17	377.70	447.95	510.41	10^{-7}	26.60		

Moving to the third question, we determine the computation time of G, that is $\boldsymbol{C}_{\mathrm{MCF}}$, versus n_{terms}, see Table 5.4. It shows that the computation time for the AHF method is very small (less than 0.6 seconds) for all the investigated values of n_{terms}. This is because, we have to solve a linear system whose dimension n_{terms} is small and similar for all values of $n_{\mathrm{terms}} \in \{3, 5, 7, 9\}$. Finally, we read off the regions of the computation time from Table 5.4. The computation time of G is about 0.02–0.06 seconds for the AHF method. Using the default tool parameter $n_{\mathrm{terms}} = 5$, we have a computation time of 0.02 seconds.

5.3 Aspect ratio of the inclusion

In this section we consider $\boldsymbol{C}_{\mathrm{MCF}}$ as a function of the mineral volume fraction $\mathrm{vf}_{\mathrm{ha}}$ and the mineral aspect ratio $\mathrm{ar}_{\mathrm{ha}}$, i.e. $\boldsymbol{C}_{\mathrm{MCF}} = \boldsymbol{C}_{\mathrm{MCF}}(\mathrm{vf}_{\mathrm{ha}}, \mathrm{ar}_{\mathrm{ha}})$. We employ the self-consistent and the Mori-Tanaka method, however, omit the AHF method. The latter is because the aspect ratio $\mathrm{ar}_{\mathrm{ha}}$ is a fix parameter of the AHF method, which by construction is $\mathrm{ar}_{\mathrm{ha}} = \infty$.

Similar as for the Hill tensor in Section 5.1, we verify in this section that it is justified to consider the stiffness tensor $\boldsymbol{C}_{\mathrm{MCF}}(\mathrm{vf}_{\mathrm{ha}}, \mathrm{ar}_{\mathrm{ha}})$ with $\mathrm{ar}_{\mathrm{ha}} \in [100, 200]$ as a good approximation of $\boldsymbol{C}_{\mathrm{MCF}}(\mathrm{vf}_{\mathrm{ha}}, \infty)$. More precisely, we ask the research questions

1. Employing the Mori-Tanaka or the self-consistent method, which error in $\boldsymbol{C}_{\mathrm{MCF}}$ do we obtain when approximating cylindrical inclusions by prolated ellipsoidal inclusions with $\mathrm{ar}_{\mathrm{ha}} \in [100, 200]$, or more generally for $\mathrm{ar}_{\mathrm{ha}} \in [1, \infty)$?

2. Performing the above approximations, what is the error of specific components of the stiffness tensor $\boldsymbol{C}_{\mathrm{MCF}}$ for $\mathrm{ar}_{\mathrm{ha}} \in [1, 200]$ or $\mathrm{ar}_{\mathrm{ha}} \in [1, \infty)$? Since in Chapter 6 we generally consider only the components, C_{axi} and C_{trv}, of $\boldsymbol{C}_{\mathrm{MCF}}$, we are interested in the errors of these components.

Note that we consider our approximations to be justified, if the errors of $\boldsymbol{C}_{\mathrm{MCF}}$, C_{axi} and C_{trv} are less than 10^{-2}.

In order to answer the first question, we compute $\boldsymbol{C}_{\mathrm{MCF}}$ for the aspect ratios $\mathrm{ar}_{\mathrm{ha}} \in [1, 10^5]$, the mineral volume fractions $\mathrm{vf}_{\mathrm{ha}} \in [0, 1]$ and the tool parameters, $\mathrm{tol}_{\mathrm{int}} = 10^{-6}$ and $\mathrm{tol}_{\mathrm{nls}} = 10^{-5}$. These tensors are compared to a reference apparent stiffness tensor, $\boldsymbol{C}^{\mathrm{ref}}_{\mathrm{MCF}}$, which was computed for the same values of $\mathrm{vf}_{\mathrm{ha}}$, however, for $\mathrm{ar}_{\mathrm{ha}} = 10^6$, $\mathrm{tol}_{\mathrm{int}} = 10^{-11}$ and $\mathrm{tol}_{\mathrm{nls}} = 10^{-10}$. We consider $\boldsymbol{C}^{\mathrm{ref}}_{\mathrm{MCF}}$ a good approximation of the stiffness tensor $\boldsymbol{C}_{\mathrm{MCF}}$ for $\mathrm{ar}_{\mathrm{ha}} = \infty$, and quantify the difference between $\boldsymbol{C}_{\mathrm{MCF}}$ and $\boldsymbol{C}^{\mathrm{ref}}_{\mathrm{MCF}}$ using the measure $\mathrm{mrE}(\boldsymbol{C}_{\mathrm{MCF}})$, as given in Eq. (5.1) with $I = [0, 1]$. We display corresponding results in Fig. 5.5a. This data shows that, by approximating cylindrical phases by prolated ellipsoidal inclusions with an aspect ratio $\mathrm{ar}_{\mathrm{ha}} \geq 100$, we make an error $\mathrm{mrE}(\boldsymbol{C}_{\mathrm{MCF}})$ of less than 10^{-2}. This holds for the self-consistent as well as for the Mori-Tanaka method. The error $\mathrm{mrE}(\boldsymbol{C}_{\mathrm{MCF}})$ decreases further for both homogenization methods as the aspect ratio $\mathrm{ar}_{\mathrm{ha}}$ increases. For instance, for $\mathrm{ar}_{\mathrm{ha}} = 10^3$ and $\mathrm{ar}_{\mathrm{ha}} = 10^4$ we have an error of order of magnitude 10^{-4} and 10^{-6} only.

Finally, to answer the second question, we compute the error measures, $\mathrm{raE}(C_{\mathrm{trv}})$ and $\mathrm{raE}(C_{\mathrm{axi}})$, as given in Eq. (5.1), for various values of aspect ratio $\mathrm{ar}_{\mathrm{ha}} \in [1, 10^5]$. Thereby, the tool parameters and the aspect ratio $\mathrm{ar}_{\mathrm{ha}}$ for the reference quantities are the same as for the first research question. In Fig. 5.5b we display the corresponding results. This data shows that for $\mathrm{ar}_{\mathrm{ha}} \in [100, 200]$ and for both homogenization methods an error of $\mathrm{raE}(C_{\mathrm{trv}}) = 10^{-4}$–$10^{-5}$ and $\mathrm{raE}(C_{\mathrm{axi}}) = 10^{-2}$–$10^{-3}$ occurs. Similar to $\mathrm{mrE}(\boldsymbol{C}_{\mathrm{MCF}})$, the errors, $\mathrm{raE}(C_{\mathrm{trv}})$ and $\mathrm{raE}(C_{\mathrm{axi}})$, decrease with increasing aspect ratio $\mathrm{ar}_{\mathrm{ha}}$. In general, the errors $\mathrm{raE}(C_{\mathrm{axi}})$ are larger than the errors $\mathrm{raE}(C_{\mathrm{trv}})$; they differ about two orders of magnitude for $10 \leq \mathrm{ar}_{\mathrm{ha}} < 10^4$, while less for other aspect ratios $\mathrm{ar}_{\mathrm{ha}}$.

As a conclusion of this section, it may be stated, that when approximating cylindrical inclusions using prolated spheroidal inclusions with aspect ratios $\mathrm{ar}_{\mathrm{ha}} \in [100, 200]$, the resulting errors $\mathrm{mrE}(\boldsymbol{C}_{\mathrm{MCF}})$, $\mathrm{raE}(C_{\mathrm{axi}})$ and $\mathrm{raE}(C_{\mathrm{trv}})$ are sufficiently small, i.e. less than 10^{-2}. That is why, it is justified to consider these approximations in Chapter 6.

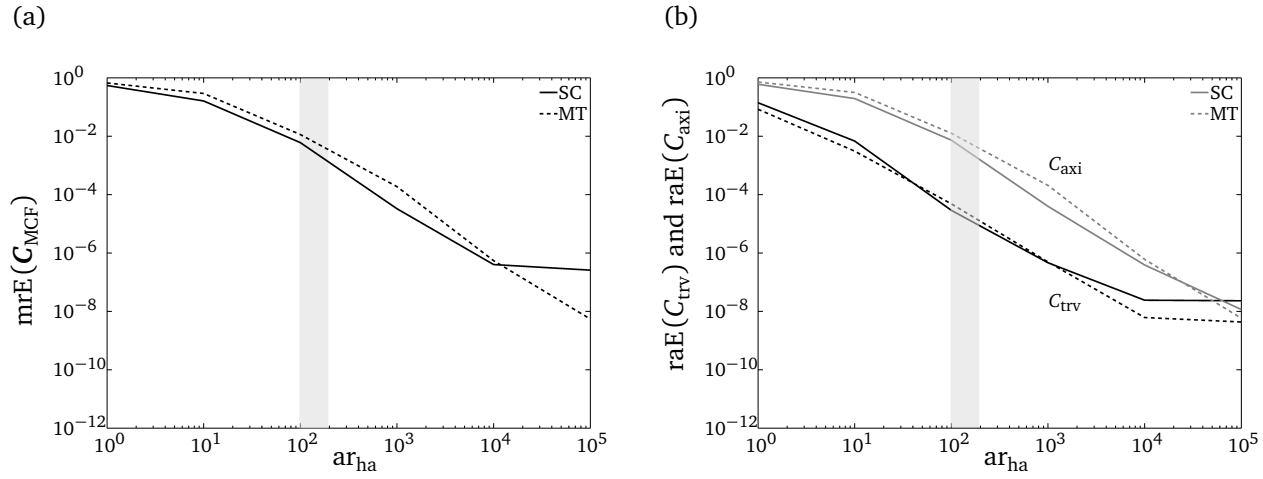

Figure 5.5.: (a) Relative error $\mathrm{mrE}(\boldsymbol{C}_{\mathrm{MCF}})$ versus the aspect ratio $\mathrm{ar}_{\mathrm{ha}}$. (b) Error of transverse and axial stiffness of $\boldsymbol{C}_{\mathrm{MCF}}$, i.e. $\mathrm{raE}(C_{\mathrm{trv}})$ (black lines) and $\mathrm{raE}(C_{\mathrm{axi}})$ (gray lines), versus the aspect ratio $\mathrm{ar}_{\mathrm{ha}}$.
Notes: We plot the errors $\mathrm{mrE}(\boldsymbol{C}_{\mathrm{MCF}})$, $\mathrm{raE}(C_{\mathrm{trv}})$ and $\mathrm{raE}(C_{\mathrm{axi}})$ respectively for the self-consistent (solid lines) and the Mori-Tanaka method (dashed lines). We consider a highly prolated ellipsoidal inclusion with an aspect ratio $\mathrm{ar}_{\mathrm{ha}} \in [100, 200]$ (area is grayed out) a good approximation of a cylindrical inclusion.

5.4 Starting value for the nonlinear system of the self-consistent method

In this section we concentrate on the self-consistent method; see Section 4.2 for details on its implementation. We consider the method's output, $\boldsymbol{C}_{\mathrm{MCF}}$, as function of the mineral volume fraction $\mathrm{vf}_{\mathrm{ha}}$ and the starting value $\boldsymbol{C}^{(0)}$, i.e. $\boldsymbol{C}_{\mathrm{MCF}} = \boldsymbol{C}_{\mathrm{MCF}}(\mathrm{vf}_{\mathrm{ha}}, \boldsymbol{C}^{(0)})$. We focus on the following research questions:

1. Which convergence order has the algorithm of the self-consistent method (Algorithm 4.2.1) developed in Section 4.2?

2. How does the convergence depend on the starting value $\boldsymbol{C}^{(0)}$? What is a good starting value if we compute $\boldsymbol{C}_{\mathrm{MCF}}$ for a single value of $\mathrm{vf}_{\mathrm{ha}}$ only or for various values of $\mathrm{vf}_{\mathrm{ha}}$? In particular, the latter question is of importance in Chapter 6. Here, we have to compute the apparent stiffness tensor of the MTLT for a large range of $\mathrm{vf}_{\mathrm{ha}}$ values. Thereby, we aim for starting values which entail a small number of iterations of Algorithm 4.2.1.

We compute a starting value based on the Voigt technique, see Section 3.6.1. More precisely, we use as starting value some weighted combination of the collagen and the mineral stiffness tensor, given by

$$\boldsymbol{C}^{(0,i)} = i \cdot 0.1\, \boldsymbol{C}_{\mathrm{ha}} + (1 - i \cdot 0.1)\, \boldsymbol{C}_{\mathrm{col}}, \quad \text{for} \quad i = 0, 1, \ldots, 10. \tag{5.3}$$

Note that it holds that $\boldsymbol{C}_{\mathrm{MCF}}(i \cdot 0.1, \boldsymbol{C}^{(0,i)}) \leq \boldsymbol{C}^{(0,i)}$, see Section 3.7 for details.

In order to answer the research questions, we estimate the convergence order as well as the asymptotic error constant of the self-consistent method. Let denote $\mathrm{err}_k := \|\boldsymbol{C}^{(k)} - \boldsymbol{C}_{\mathrm{MCF}}\|$ the error of $\boldsymbol{C}^{(k)}$, which is an estimate of the apparent stiffness tensor $\boldsymbol{C}_{\mathrm{MCF}}$ obtained by Algorithm 4.2.1 in step $k = 1, 2, \ldots, N$. We approximate

$$\mathrm{err}_k \approx \left\| \boldsymbol{C}^{(k)} - \boldsymbol{C}^{(N)} \right\| \tag{5.4}$$

and assume that there exist numbers p and Q such that

$$\mathrm{err}_k \approx Q\, (\mathrm{err}_{k-1})^p, \tag{5.5}$$

where p is the convergence order and Q is the asymptotic error constant. We estimate p and Q as given in Appendix E. In case of $p = 1$ we say that we have linear convergence and call the asymptotic

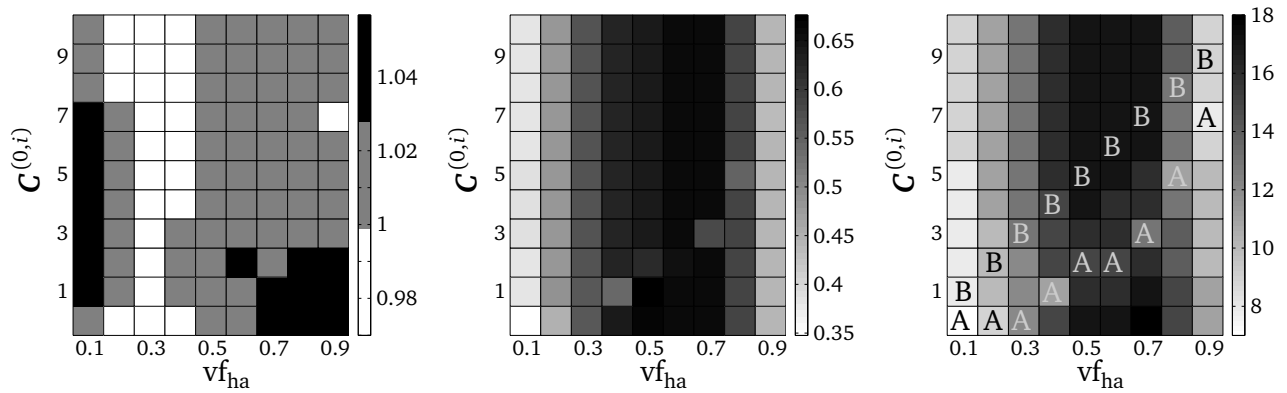

Figure 5.6.: Convergence order p, convergence rate Q and number of iterations of Algorithm 4.2.1 versus the mineral volume fraction $\mathrm{vf}_{\mathrm{ha}}$ and the starting value $\boldsymbol{C}^{(0,i)}$ (see Eq. (5.3) where $i = 0, 1, \ldots, 10$). In subfigure (c) we indicate patches which correspond to strategies A or B with the letters A and B, respectively.

error constant also convergence rate. In Figures 5.6a and 5.6b we plot p and Q, respectively, versus the starting value (5.3) and the mineral volume fraction $\mathrm{vf}_{\mathrm{ha}} \in [0.1, 0.9]$.

It shows that Algorithm 4.2.1 has linear convergence ($p \approx 1$), see Fig. 5.6a. This is in line with the convergence order for the Newton method, which is $p = 2$ if the starting value is sufficiently close to the root, while $p = 1$ otherwise.

The convergence rate Q, displayed in Fig. 5.6b, takes its values in the set $[0.35, 0.68]$. Varying $\mathrm{vf}_{\mathrm{ha}}$ and keeping the starting value $\boldsymbol{C}^{(0,i)}$ fix, we observe fast convergence for values of $\mathrm{vf}_{\mathrm{ha}}$ near to zero or one, and slower convergence for $\mathrm{vf}_{\mathrm{ha}}$ in between. Whereas, varying the starting value and keeping $\mathrm{vf}_{\mathrm{ha}}$ fix, we discover that the convergence rate Q alters only about the small amount of 0.11. One reason for this behavior may be that the function $\boldsymbol{g}$ of the approximated nonlinear system (4.12) is the sum of two terms. These are weighted with either $\mathrm{vf}_{\mathrm{ha}}$ or $1 - \mathrm{vf}_{\mathrm{ha}}$. For $\mathrm{vf}_{\mathrm{ha}}$ near to zero or one, one of the two terms is dominant, which makes possibly solving of the nonlinear system $\boldsymbol{g} = 0$ easier. For values of $\mathrm{vf}_{\mathrm{ha}}$ in between zero and one, both terms are apparent. As a result we obtain a possibly more complex nonlinear system than for $\mathrm{vf}_{\mathrm{ha}} \approx 0, 1$.

Finally, we move to our last questions regarding the proper choice of starting values. To this end we introduce three strategies:

- Strategy A selects for each $\mathrm{vf}_{\mathrm{ha}} = j \cdot 0.1$ with $j = 1, \ldots, 9$ that starting value $\boldsymbol{C}^{(0,i)}$ of (5.3) which entails the smallest number of iterations. Note that this strategy is of more theoretical nature since, in general, it is much too expensive to determine for all starting values the number of iterations required until convergence.

- Strategy B selects a starting value based on the Voigt technique and takes for $\mathrm{vf}_{\mathrm{ha}} = i \cdot 0.1$ for $i = 1, 2, \ldots, 9$ the starting value $\boldsymbol{C}^{(0,i)}$ from (5.3). This strategy is of more practical use and requires no preprocessing.

- Strategy C makes use of previously derived results. This is in contrast to strategies A and B. Given some apparent stiffness tensor $\boldsymbol{C}_{\mathrm{MCF}}(\mathrm{vf}'_{\mathrm{ha}})$ where $\mathrm{vf}'_{\mathrm{ha}} \approx \mathrm{vf}_{\mathrm{ha}}$, strategy C selects the starting value $\boldsymbol{C}^{(0)} = \boldsymbol{C}_{\mathrm{MCF}}(\mathrm{vf}'_{\mathrm{ha}})$ to compute $\boldsymbol{C}_{\mathrm{MCF}}(\mathrm{vf}_{\mathrm{ha}})$.

We, firstly, consider the case that we compute $\boldsymbol{C}_{\mathrm{MCF}}$ for one value of $\mathrm{vf}_{\mathrm{ha}} \in (0, 1)$ only. For each value of $\mathrm{vf}_{\mathrm{ha}}$ we compare the number of iterations obtained when using the starting values proposed by strategies A and B. In the patch plot Fig. 5.6c we display the number of iterations versus the starting value (5.3) and the mineral volume fraction $\mathrm{vf}_{\mathrm{ha}}$.

Table 5.5.: Number of iterations obtained by strategies A, B and C. Strategies A, B and C, respectively, determine a starting value based on the minimal number of iterations, the Voigt technique and previously-derived results.

vf_{ha}	0.1	0.15	0.2	0.25	0.3	0.35	0.4	0.5	0.6	0.7	0.8	0.9
Strategy A	7	7	8	9	10	9	11	15	15	13	11	8
Strategy B	8	9	10	11	13	14	15	17	17	17	13	9
Strategy C	7	7	8	9	10	12	14	16	16	16	14	10

Fig. 5.6c shows that for each value of vf_{ha} the starting values proposed by strategy B result in a significantly higher number of iterations than those proposed by strategy A. That is why we decided against using strategy B. However, since it is usually too expensive to employ strategy A for any tissue in Chapter 6, we strike a middle way. To this end note that it is also seen in Fig. 5.6c that the patches of strategy A in most cases lie slightly below those of strategy B. We transfer this observation to Chapter 6 as follows: to compute the apparent stiffness tensor of some tissue for $vf_{ha} = i \cdot 0.1$, we use as starting value the Voigt result for $vf_{ha} = (i-1) \cdot 0.1$ for $i = 1, \ldots, 10$.

Secondly, we consider the more important case that we need to compute $\boldsymbol{C}_{\mathrm{MCF}}$ for several values of vf_{ha}. We compare strategy C with strategies A and B. In Table 5.5 we list for various values of $vf_{ha} \in (0,1)$ (in 0.05 or 0.1 steps) the number of iterations required in the three strategies A, B and C.

Table 5.5 shows that the number of iterations obtained for strategies A, B and C increases to a maximum in the region $vf_{ha} = 0.5$–0.7. This behavior is in accordance with the behavior of the convergence rates, see Fig. 5.6b. For $vf_{ha} = 0.1$–0.3 the results of strategies C and are as good as those of strategy A. For $0.4 \leq vf_{ha} < 0.8$ or $vf_{ha} \geq 0.8$ the number of iterations for strategy C is in between that of strategy A and B, or is slightly worse than that of strategy B. Nevertheless, since it holds in Chapter 6 that $vf_{ha} \in [0, 0.4]$, we prefer strategy C over strategy B. In consequence, we will employ strategy C for any computation with the self-consistent method in Chapter 6.

5.5 Conclusions

We adjusted the self-consistent, the Mori-Tanaka and the AHF method for their application in the MTLT model in Chapter 6. To this end, we predicted the apparent stiffness tensor $\boldsymbol{C}_{\mathrm{MCF}}$ of the building unit of the MTLT, the MCF, and compared the results of the different homogenization methods under different view points. Our most important findings are summarized below.

The integration tolerance $\mathrm{tol}_{\mathrm{int}}$, determining the accuracy of the Hill tensor $\boldsymbol{P}$, can be chosen independently of the aspect ratio ar. This means, that whenever we perform a parametric study over the aspect ratio in Chapter 6, we can select the same value for $\mathrm{tol}_{\mathrm{int}}$.

Among the investigated homogenization methods, the error in the predictions of the AHF method, decreases the fastest with stricter tool parameters. Furthermore, we observed first-order convergence for both, the Mori-Tanaka and the self-consistent method.

The computation time for the apparent stiffness tensor differs strongly among the homogenization methods. The AHF and the self-consistent method are, in general, the fastest and the slowest homogenization method, respectively. Moreover, we notice that, except for the AHF method, the computation time depends on the tool parameters. In general the computational effort is the larger the stricter the value of the tool parameter.

Cylindrical inclusions in Chapter 6 can be considered as highly prolated ellipsoidal inclusions with an aspect ratio between 100 and 200. We found that both, the Hill tensor and the apparent stiffness tensor of the MCF, are given with a satisfactory accuracy.

The convergence order of our developed algorithm for the self-consistent method, i.e. Algorithm 4.2.1, do neither depend on the starting value nor on the mineral volume fraction vf_{ha}. We observe a convergence order of one. For mineral volume fractions close to zero or one, we can expect fast convergence,

i.e. a small number of iterations. For mineral volume fractions in between zero and one the convergence is slower.

In the context of a parametric study, the smallest number of iterations for Algorithm 4.2.1 is obtained, when selecting the starting value according to strategy C. That is, when computing the apparent stiffness tensor $\boldsymbol{C}_{\mathrm{MCF}}(p_i)$ we choose as starting value $\boldsymbol{C}_{\mathrm{MCF}}(p_i')$, where $p_i' < p_i$. This strategy will find multiple use in Chapter 6, where we perform a parametric study of the MTLT model.

6 Modeling and simulation of the MTLT

In this chapter we develop a structure-driven multiscale model of the elastic properties of MTLT tissue, in particular, of circumferential (CIR) and interstitial (INT) tissue.

Before we start, let us note firstly, that if not mentioned otherwise, all models of MTLT tissue presented in this chapter, ours as well as those of other authors, yield a transverse isotropic stiffness tensor $\boldsymbol{C}$. A parameter of great importance for these models is the anisotropy ratio AR. To this end, recall that this parameter quantifies the rate of anisotropy of a transverse isotropic material, and is defined as the ratio of the stiffness components, C_{33} and C_{11}, where we assume that the stiffness tensor is given in Voigt notation; see Section 2.2.4 for details.

Recently, Spiesz et al. (2012a) have shown that MTLTs have regions of two structurally different tissue types at the tissue scale: CIR and INT tissue. The two subimages in Fig. 6.1a illustrate the structural organization of MTLT tissue in a cross section perpendicular to the tendon's long axis. We refer to such a cross section as a "transverse cross section", while we refer to a cross section parallel to the tendon's long axis as a "longitudinal cross section". Fig. 6.1a, together with further findings of our project partners (Tiburtius et al., 2014), demonstrates that CIR tissue appears predominantly around large canals, while INT tissue fills up the remaining space. Both CIR and INT tissue consist of water-filled pores (micropores) and unidirectionally aligned MCFBs. Note that the micropores are visible as gray background in the right subimage of Fig. 6.1a. We emphasize here, that we do not regard the large black canals, also visible in Fig. 6.1a, as micropores. The volume fraction of the micropores in CIR and INT tissue is what we call microporosity of these tissues. In CIR tissue the MCFBs have a small diameter and the microporosity is small, while INT tissue is characterized by MCFBs with a larger diameter and a higher microporosity. At the micrometer scale the MCFB is made up of the phases MCF and extrafibrillar space (ES), and at the nanometer scale the basic constituents of MTLT tissue are visible: the ES consists of nanopores and minerals, in particular hydroxyapatite, and the MCF comprises minerals and organic material, in particular collagen.

Our project partners experimentally derived elastic properties of CIR and INT tissue, together with site-matched values of the mineralization employing scanning acoustic microscopy and synchrotron radiation micro-computed tomography, see Section 6.1. For simplicity, we refer to their dataset as "our experimental dataset" in what follows.

In order to explain our experimental dataset we developed a multiscale model of CIR and INT tissue. In the past ten years, there have been several modeling and simulation studies on the elastic properties of such tissues. In this context, we emphasize the three models of Hellmich et al. (2004), Reisinger et al. (2010) and Spiesz et al. (2012a), to whom we refer to as the Hellmich, the Reisinger, and the Spiesz model, respectively, in the following.

Both, the Hellmich and the Reisinger model represented tissue of unidirectionally-aligned MCFBs. Hellmich et al. (2004) studied the mineral-collagen interactions of MCFB tissue using Eshelby-based homogenization method. Comparing different concepts, they found that a three-step homogenization procedure (ES, MCF: Self-consistent method, MCFB: Mori-Tanaka method) predicts elastic properties that compare best to experimental data taken from the literature. Reisinger et al. (2010) developed a three-step homogenization procedure employing the Mori-Tanaka method throughout the three scales of the ES, the MCF and the MCFB. This model, in particular, includes the assumption that the MCF can be represented as a two-phase composite of a mineral matrix in which collagen inclusions are embedded. Furthermore, Reisinger et al. (2010) performed a parametric study and identified the most influencing model parameters using a local sensitivity analysis. Spiesz et al. (2012a) extended the MCFB model of Reisinger by the feature of microporosity. To this end, they predicted the elastic properties of MCFB tissue with microporosity using the Mori-Tanaka method. The focus of Spiesz et al. (2012a) lied in explaining their experimental nanoindentaion data.

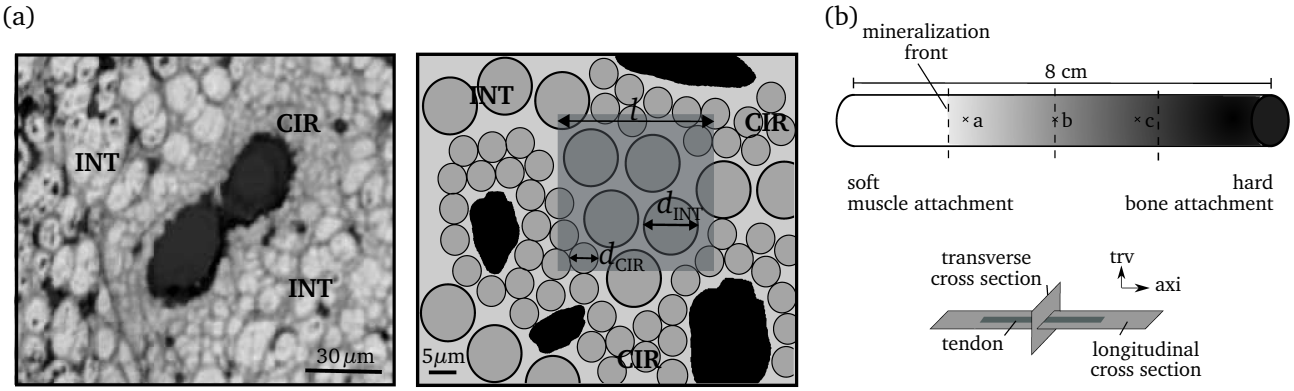

Figure 6.1.: (a) Structure of CIR and INT tissue within a transverse cross section at the tissue scale. Left: 900-MHz scanning acoustic microscopy image. Right: sketch of MTLT tissue. In the sketch the circles and the large black areas represent MCFBs and pmma-filled canals, respectively. The micropores are shown as light gray background. Also, the size l of the interaction volume for the 50-MHz scanning acoustic microscopy and the diameter of the MCFBs for CIR tissue, $d_{\text{CIR}} = 2$–$4\,\mu$m, and for INT tissue, $d_{\text{INT}} = 3.2$–$8.9\,\mu$m, are indicated. (b) Sketch of a domestic turkey leg tendon; cross sections, axial/transverse direction and samples a, b and c are indicated.

Comparing the results of the Hellmich, the Reisinger, and the Spiesz model with our experimental data, we conclude that:

- Neither the MCFB model of Hellmich nor that of Reisinger could explain our experimental data of CIR and INT tissue. There is an important feature of CIR and INT tissue missing in these MCFB models. This is the microporosity. We include this feature in our developed model of CIR and INT tissue.

- Our multiscale model of CIR and INT tissue should employ at the MCF and the ES scale the self-consistent method rather than the Mori-Tanaka method.

We support our first conclusion, noting that both, the Hellmich and the Resinger model, predict anisotropy ratios AR which were significantly smaller than our experimental ones (Hellmich model: 1.3–1.4, Reisinger model: 1.4–1.8, our experiments: $\approx 2, 1.8$ (CIR, INT), see Table 6.4 in Section 6.5.2). We particularly note that the Reisinger model predicts high anisotropy ratios of AR $= 1.8$ only if the tissue mineralization is unrealistically high for MTLT tissue. Moreover, we found that even a change of the base values of the Reisinger model, would yield no predictions closer to our experimentally observed anisotropy ratios AR. The parametric study of the Reisinger model in Reisinger et al. (2010) shows that the values of the anisotropy ratio AR cannot be significantly increased when changing the parameter's base values.

We support our second conclusion noting that the MCF is described in the literature (Alexander et al., 2012; Akkus, 2005; Weiner and Wagner, 1998) as a mixture of interwoven cylindrical collagen molecules and ha platelets. For these constituents it is not clear which one plays the role of a matrix. Therefore, to explicitly specify a matrix phase for the MCF, as necessary when employing the Mori-Tanaka method in the Reisinger or the Spiesz model at the MCF scale, is in our opinion an inappropriate way to model the MCF. Moreover, Hellmich et al. (2004) showed that the stiffness estimates of MCFB tissue are better when considering the MCF as an "interpenetrating network of collagen and mineral" (self-consistent method) rather than as a "mineral matrix with collagen inclusions" (Mori-Tanaka method).

The studies and considerations on the modeling and simulation of the elastic properties of MTLT tissue, discussed above, pursued two different aims. Those of Hellmich et al. (2004) and Spiesz et al. (2012a) considered their model with a given fixed set of parameters and focus mainly on explaining (their) experimental data. In contrast, the study of Reisinger et al. (2010) analyzed the influence of the

input parameters on the model output performing a parametric study and a local sensitivity analysis. Both of these aims are equally important and will be addressed in the development of our MTLT model.

This chapter aims to elucidate

1. Which parameters essentially determine the elastic properties of MTLT at the tissue scale? How do these parameters influence the tissue scale elastic properties of the MTLT?
2. How accurate and efficient does our model predict the elastic properties of MTLT tissue?

In order to achieve this, we address the following tasks:

- Obtain site-matched experimental elastic and compositional properties of MTLT tissue, in particular of CIR and INT tissue, at different scales. This was done by our project partners at the Charité. We briefly describe the experimental dataset and summarize the experimental findings in Section 6.1.
- Develop a multiscale model to predict apparent elastic properties of MTLT tissue. Experimental data of our project partners was used as model input. The model, its parameters and its variables are presented in Section 6.2.
- Perform a global sensitivity analysis to identify sensitive model output and the most crucial parameters influencing these. A parametric study of those parameters complements the global sensitivity analysis. All this is presented in Section 6.3.
- Compare the model predictions with the experimentally assessed coarse-scale elastic properties (validation), see Section 6.4.
- Discuss our findings with respect to all our research questions and present future tasks, see Section 6.5. Finally, in Section 6.6 we draw conclusions.

6.1 Experimental dataset and experimental findings

We give a brief description of the experimental dataset and the experimental findings used throughout this chapter. The experimental data was derived by our project partners, see the Acknowledgements and Section 1.3 for more information on their contributions. For details on the findings, the sample preparation and the measurement procedure, we refer the interested reader to Tiburtius et al. (2014). The measurement techniques, scanning acoustic microscopy (SAM) and synchrotron radiation micro-computed tomography (SR-μCT), employed by our project partner, are described, for instance, in Raum (2011) or Nuzzo et al. (2002).

Our project partners investigated different samples taken from a domestic turkey leg tendon. For their investigations the samples were embedded in polymethylmethacrylate (pmma) and so the micro- and the nanopores, naturally filled with water and non-collageneous proteins, contain now the embedding material pmma. Using SAM (50-MHz, 200-MHz), SR-μCT and light-microscopy they measured

- the direction-dependent *acoustic impedance* $\widetilde{Z}$ in MRayl (1 Rayl = 1 kg/(s m^2)),
- the *tissue degree of mineralization*[1] DMB in g/cm^3, and
- the *microporosity* $\widetilde{\mathrm{vf}}_{\mathrm{mp}}$,

of MTLT tissue at the tissue scale.

The acoustic impedance is a measure of the fine and coarse-scale elastic properties of a tissue and is related to the tissue's local stiffness, see Eq. (6.1) on page 82. The SAM measurements were performed

[1] The acronym DMB stands for *Degree of Mineralization of Bone* and has been established for bone tissue. Nevertheless, we use this term hereinafter also for MTLT tissue.

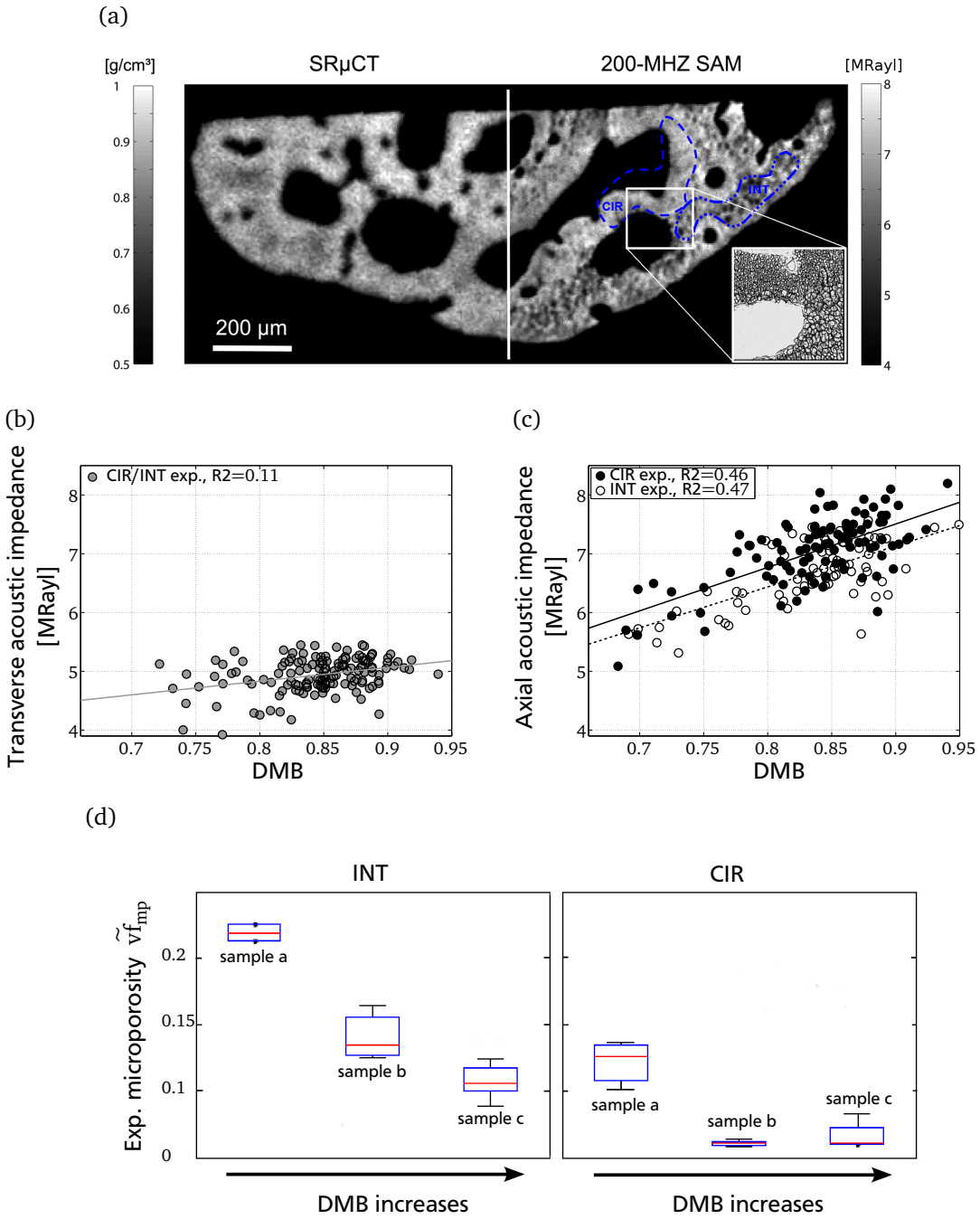

Figure 6.2.: Experimental dataset used for comparison in this thesis (Tiburtius et al., 2014). (a) Site-matched DMB (left) and acoustic impedance (right) images of a transverse MTLT cross section. Typical regions of CIR and INT tissue are identified in the acoustic impedance image. The inlay is a site-matched light microscopy image of MTLT tissue showing INT (lower half) and CIR (upper half) tissue that both are adjacent to a large canal. (b), (c) Plots of the experimental acoustic impedance $\widetilde{Z}^{T_i}_{(i,\nu_i)}$ in transverse (ROIs i with $\nu_i = \text{trv}$) and axial (ROIs i with $\nu_i = \text{axi}$) direction, respectively, versus the site-matched experimental DMB_i values; in the axial case the ROIs are further distinguished according to their tissue type T_i. The solid gray, the solid black and the dashed black lines are the linear regression lines through the experimental data for $(T_i = \text{CIR/INT}, \nu_i = \text{trv})$, $(T_i = \text{CIR}, \nu_i = \text{axi})$ and $(T_i = \text{INT}, \nu_i = \text{axi})$, respectively, see also Section 6.4; their coefficients of determination, $R2$, are given in the legend. (d) Experimental microporosity $\widetilde{\text{vf}}_{\text{mp}}$ in CIR and INT tissue of samples a, b and c. The location of these samples are indicated in Fig. 6.1b. The lines in the boxes mark the median. The bottom and the top of the box identify the 25% and 75% percentile, respectively.

on the transverse as well as on the longitudinal cross section of each sample, yielding the axial (axi) acoustic impedance and the transverse (trv) acoustic impedance, respectively; see Fig. 6.1b for a visualization of the different cross sections and directions. Finally, the acoustic impedance $\widetilde{Z}$ obtained by the 50-MHz SAM, was averaged for regions of interests (ROIs) which consists of either CIR or INT tissue. This worked well on transverse, however, not so well on longitudinal cross sections; see Section 6.5.2. In the latter case, we introduced the tissue type "CIR/INT" which stands for an unknown mixture of CIR and INT tissue. In summary, we obtained for each ROI i an acoustic impedance value $\widetilde{Z}^{T_i}_{(i,\nu_i)}$, where for direction $\nu_i = \text{axi}$ the tissue type is $T_i = \text{CIR}$ or $T_i = \text{INT}$, and for direction $\nu_i = \text{trv}$ the tissue type is $T_i = \text{CIR/INT}$. We refer the interested reader to Appendix F or Tiburtius et al. (2014) for a detailed description on how the acoustic impedance of CIR and INT tissue was derived.

Site-matched values of the acoustic impedance and the DMB for CIR and INT tissue are shown in Figures 6.2a, 6.2b and 6.2c. The microporosity was measured only for three out of all samples, i.e. for samples a, b and c, as indicated in Fig. 6.1b. Corresponding results are displayed in Fig. 6.2d.

In summary, the experimental findings of our project partners are

- in CIR tissue the MCFBs have a diameter of $2.9 - 4.0\,\mu$m and the average microporosity is near to 0; in INT tissue the MCFBs have a diameter of $3.2 - 8.9\,\mu$m and the average microporosity is 0.1,
- the experimental microporosity values decrease with increasing DMB; they range from 0.03 up to 0.2,
- the acoustic impedance values of both CIR and INT tissue increase with increasing DMB,
- all axial acoustic impedance values, for both, CIR and INT tissue, were larger than all (CIR and INT tissue) transverse acoustic impedance values, and,
- the axial acoustic impedance values of CIR tissue tend to be higher than those of INT tissue for the same DMB.

The relation between acoustic impedance and stiffness

In Section 6.4 we compare the elastic properties predicted by our model with our experimental elastic properties. This comparison will be done in terms of the acoustic impedance. Since our model predicts stiffness values, we first have to convert these to acoustic impedance values. Note, therefore, that the acoustic impedance Z_ν in any direction ν is related to the local apparent stiffness in the same direction, denoted C_ν, by

$$Z_\nu = \sqrt{\rho\, C_\nu}\,, \tag{6.1}$$

where ρ is the mass density of the material under investigation, see e.g. Raum et al. (2006a) and Raum (2011). For a two-phase composite with mass densities ρ_1 and ρ_2 and volume fractions vf_1 and vf_2 of the phases, the mass density of the composite is given by

$$\rho = \text{vf}_1\,\rho_1 + \text{vf}_2\,\rho_2. \tag{6.2}$$

Note that if we compare the model and the experimental elastic properties in terms of the stiffness, the density ρ in Eq. (6.1) has to be determined experimentally. This is typically more difficult (error prone) than evaluating the density in the model because vf_1, vf_2, ρ_1 and ρ_2 are known there. Therefore, we prefer to convert models stiffness to model impedance and compare with experimental acoustic impedance.

6.2 Multiscale model of the MTLT

In this section we set up a multiscale model for MTLT tissue. Our multiscale model comprises CIR as well as INT tissue. It is a nested sequence of models $\mathcal{S}_A$ of the composites $A \in \{\text{MCF}, \text{ES}, \text{MCFB}, \text{MTLT}\}$. In Sections 6.2.1 to 6.2.4 we present for each model $\mathcal{S}_A$ the structural organization of A, explain which homogenization methods were used to obtain the apparent stiffness of A, denoted $\boldsymbol{C}_A$, and specify the parameters of the model. For a visualization of the multiscale model of MTLT tissue and the corresponding hierarchy of homogenization methods, see Fig. 6.3. Finally, in Section 6.2.5 we then discuss how to derive all model parameters from experimental or literature data.

Each model $\mathcal{S}_A$ represents the fine-scale structure of the composite A as a material comprised of two phases, denoted A_1 and A_2, which can be composites from a finer scale or basic constituents. The input quantities of $\mathcal{S}_A$ are the volume fractions and the stiffness tensors of the two phases, as well as the aspect ratios of the inclusion phases. The output of each model is the apparent stiffness tensor of A.

The whole model sequence predicts in one simulation the apparent stiffness of MTLT tissue. In such a simulation we consider the volume fraction of hydroxyapatite in the MCFB, $\text{vf}_{\text{ha}}^{\text{MCFB}}$, as a variable of the model; increasing values of it correspond to an increasing tissue mineralization, a process which takes place in MTLT tissue over time. This justifies the special role of $\text{vf}_{\text{ha}}^{\text{MCFB}}$. Another important variable of the model is the microporosity $\text{vf}_{\text{mp}}^{\text{MTLT}}$. Depending on its value we characterize MTLT tissue as CIR or INT tissue. The remaining input quantities are considered as parameters having a fixed base value. Those parameters, for which we explore in the parametric study their influence on the apparent elastic properties, see Section 6.3.2, we refer to as free parameters.

Recall that the basic constituents of the MTLT are collagen, mineral, and the material filling the micro- and nanopores. They are denoted as materials col, ha, mp and np, respectively. In native MTLT tissue (native samples) micro- and nanopores are filled with water and non-collageneous proteins. However, due to the sample preparation they might also be filled with air (dried samples) or with an embedding material (embedded samples). For this study the samples were embedded in pmma and so the pore space materials mp and np refer to pmma. All basic constituents were assumed to have isotropic behavior, their elastic constants were taken from the literature and are fixed throughout this work, see Table 6.1.

The shape of the inclusions has a strong influence on the computed apparent stiffness tensor. The inclusions considered in our models are either spheres or prolate spheroids. In the latter case, the inclusions are elongated in the direction parallel to the MTLT long axis (axial direction) and have a circular cross section in the perpendicular plane (transverse directions). Both inclusion types are completely characterized by their aspect ratio, denoted $\text{ar}_i \geq 1$ for an inclusion made of material A_i. We remark that the composites which we encounter in MTLT tissue do not necessarily have ellipsoidal inclusions. For instance, hydroxyapatite minerals are platelet shaped (Weiner and Wagner, 1998). Hence, the first approximation step when modeling the MTLT is to simplify the given heterogeneous fine-scale structure to a composite material A with perfectly bonded ellipsoidal inclusion phases in a homogeneous matrix phase. Then, to this material A, homogenization techniques such as the Mori-Tanaka or the self-consistent method are applied, see Chapter 3.

The three submodels $\mathcal{S}_{\text{ES}}$, $\mathcal{S}_{\text{MCF}}$ and $\mathcal{S}_{\text{MCFB}}$ are based on the Reisinger model (bone fibril-array model), for which we adapt the homogenization methods and other model features according to our needs. Recall that the Reisinger model represents a single MCFB as matrix of ES material with embedded unidirectionally aligned MCFs as inclusions, see page 78. Details of our submodels are described below.

6.2.1 Model of the mineralized collagen fibril ($\mathcal{S}_{\text{MCF}}$)

The model $\mathcal{S}_{\text{MCF}}$ represents the MCF as a composite of the two phases, collagen and mineral. It predicts the apparent stiffness of the MCF, $\boldsymbol{C}_{\text{MCF}}$, using the self-consistent method (Eq. (3.73)) where $A = \text{MCF}$ and $A_1 = \text{col}$ and $A_2 = \text{ha}$. Thereby we followed the recommendation of Hellmich et al. (2004), who state that modeling the MCF as an "interpenetrating network of collagen and mineral" (self-consistent

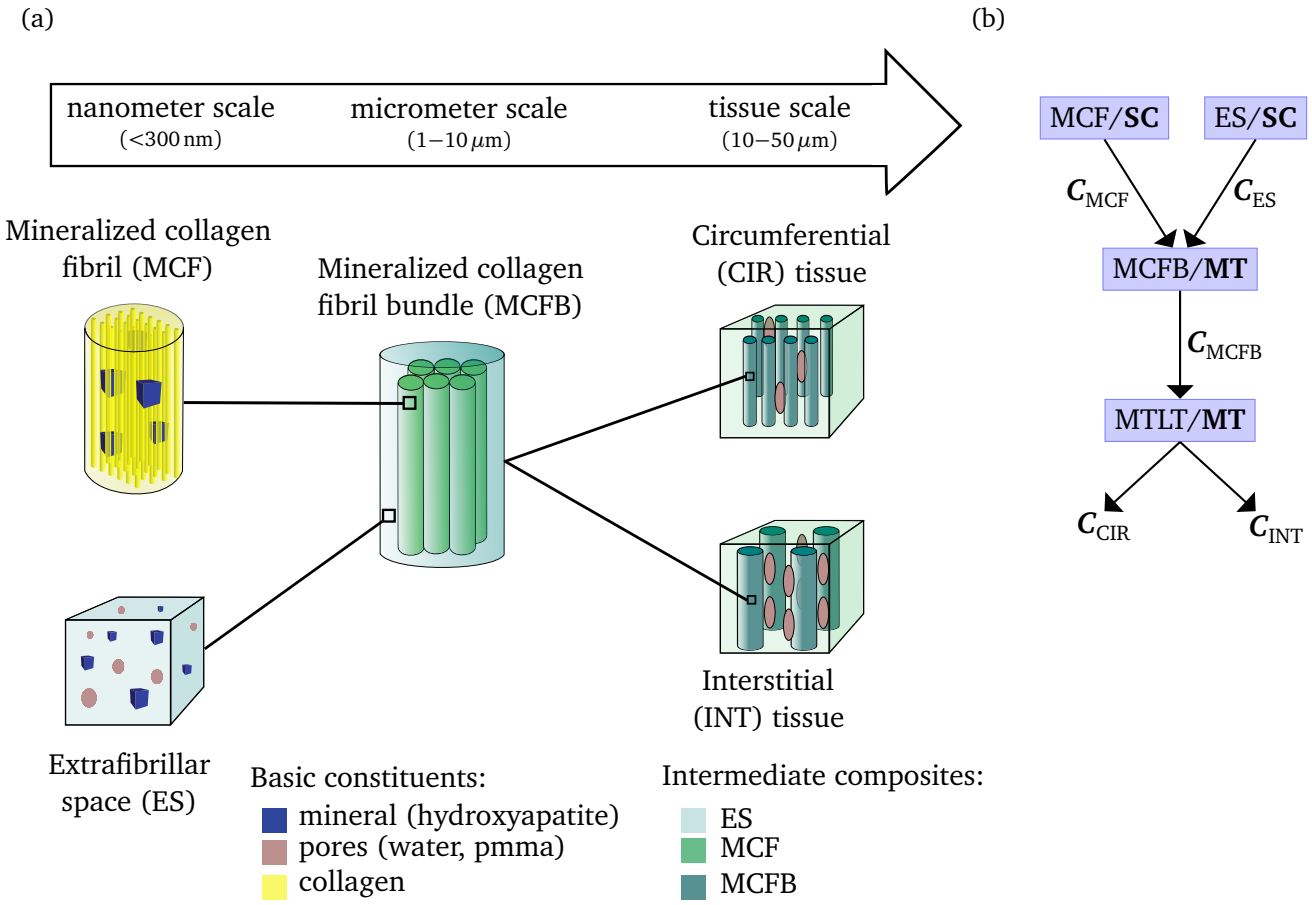

Figure 6.3.: (a) Multiscale model of MTLT (CIR and INT) tissues. (b) Homogenization procedure for the multiscale model of MTLT tissue; SC and MT are the abbreviations for the self-consistent and the Mori-Tanaka method.

method) rather than as a "mineral matrix with collagen inclusions" (Mori–Tanaka method), improves the stiffness estimates.

Collagen molecules are approximately 1.5–2 nm in diameter and 300 nm long (Akkus, 2005; Weiner and Wagner, 1998), that is they have aspect ratios $\mathrm{ar}_{\mathrm{col}}$ between 150 and 200. We therefore model the collagen phase in MCF tissue as highly prolated spheroidal inclusions and set the base value $\mathrm{ar}_{\mathrm{col}} = 175$. To explore the influence of $\mathrm{ar}_{\mathrm{col}}$ on the apparent stiffness $\boldsymbol{C}_{\mathrm{MTLT}}$, we consider it as free parameter of the model and vary it between 100 and 200.

We represent the mineral phase in MCF tissue as prolate spheroidal inclusions with moderate aspect ratio, $\mathrm{ar}_{\mathrm{ha}}$, to reflect its range of 10–30 as reported in (Vaughan et al., 2012; Akkus, 2005; Weiner and Wagner, 1998; Lees et al., 1994; Landis et al., 1993). We set the base value of $\mathrm{ar}_{\mathrm{ha}}$ to 15, which roughly matches the ratio reported by Akkus (2005). To account for the variation in the reported range of $\mathrm{ar}_{\mathrm{ha}}$ values, we regard $\mathrm{ar}_{\mathrm{ha}}$ as free parameter of the model $\mathcal{S}_{\mathrm{MCF}}$ and vary it, even slightly beyond the reported range, in $[1, 50]$.

The respective range of values used for the collagen and mineral aspect ratios goes beyond the corresponding reported ranges of these MCF structural parameters. However, this extended range allows to properly investigate the extreme scenarios and to extend the model to other tissues and artificial compounds.

6.2.2 Model of the extrafibrillar space ($\mathcal{S}_{\mathrm{ES}}$)

The space between the MCFs, the extrafibrillar space ES, is commonly described as a material of minerals and nanopores filled with non-collageneous proteins in water (Fantner et al., 2005; Hellmich et al., 2004). However, since we consider here MTLT samples embedded in pmma, the water and the nanopores were replaced by pmma. Therefore, the model $\mathcal{S}_{\mathrm{ES}}$ represents the ES as a two-phase composite with a mineral and a pmma phase. Since there is no general experimental evidence which of the two phases acts as matrix, we consider both phases as inclusions and predict the apparent stiffness of the ES, $\boldsymbol{C}_{\mathrm{ES}}$, using the self-consistent method (Eq. (3.73)) where $A = \mathrm{ES}$, $A_1 = \mathrm{ha}$, and $A_2 = \mathrm{np}$.

We represent the mineral phase as inclusions of prolate spheroidal shape with moderate aspect ratio, to reflect the reported platelet-shape of the minerals (Lees et al., 1994). Since we found no indication in the literature, whether the aspect ratio or elastic properties of the mineral platelets in the ES and the MCF differ or not, we simply model the minerals in both the same.

The shape of the nanopores, to the knowledge of the authors, has not been revealed yet. We therefore describe nanopores as prolate spheroids and regard their aspect ratio, $\mathrm{ar}_{\mathrm{np}}$, on account of the high uncertainty, as free parameter. We vary the value of $\mathrm{ar}_{\mathrm{np}}$ between 1 and a rather arbitrarily chosen high value of 200 to cover the full range of possible predicted elastic properties.

6.2.3 Model of the mineralized collagen fibril bundle ($\mathcal{S}_{\mathrm{MCFB}}$)

The MCFB is commonly described as a bundle of closely packed MCFs with ES material in between, see for instance Nikolov and Raabe (2008) and Hamed et al. (2010). The clear role of the ES acting as matrix, motivates us to model the MCFB as ES matrix with embedded MCF inclusions, and to predict the apparent stiffness of the MCFB, $\boldsymbol{C}_{\mathrm{MCFB}}$, using the Mori–Tanaka method (Eq. (3.72)) where $A = \mathrm{MCFB}$, $A_1 = \mathrm{MCF}$ (inclusion phase) and $A_2 = \mathrm{ES}$ (matrix phase). The unknown stiffness tensors of the ES and the MCF were approximated by the apparent stiffness tensors obtained by the models $\mathcal{S}_{\mathrm{ES}}$ and $\mathcal{S}_{\mathrm{MCF}}$, respectively.

In general, single MCFs are described as cylinders which are substantially longer than their diameter of about 50–100 nm (Weiner and Wagner, 1998). This makes it difficult to fix the aspect ratio of the MCF, $\mathrm{ar}_{\mathrm{MCF}}$, to a realistic value, and hence, we regard $\mathrm{ar}_{\mathrm{MCF}}$ as a free parameter. We investigate its influence on the predicted elastic properties of MTLT tissue within a large range, $\mathrm{ar}_{\mathrm{MCF}} \in [30, 200]$, and set its base value to 100. Thereby we cover a realistic range of possible predicted elastic properties.

6.2.4 Model of MTLT tissue ($\mathcal{S}_{\mathrm{MTLT}}$)

Recall that we characterize MTLT tissue as a composite consisting of unidirectionally aligned MCFB and micropores. Two characteristic tissue types appear in the MTLT: CIR and INT tissue. They differ in their microporosity $\mathrm{vf}_{\mathrm{mp}}^{\mathrm{MTLT}}$ and their average MCFB diameter. In addition, light microscopy of the MTLT performed by Spiesz et al. (2012a) indicates that the micropores are elongated parallel to the tendon axis and are distributed irregularly. Neither the irregular distribution of the micropores nor the particular MCFB diameters can be represented using the employed homogenization methods, which only account for the volume fraction and the aspect ratio (Section 6.5). Hence, we model CIR and INT tissue as composites which differ only in $\mathrm{vf}_{\mathrm{mp}}^{\mathrm{MTLT}}$; the constituents of these tissues, MCFBs and micropores, as well as the aspect ratio of the micropores, $\mathrm{ar}_{\mathrm{mp}}$, agree for both, CIR and INT tissue. Based on our experimental observations that $\mathrm{vf}_{\mathrm{mp}}^{\mathrm{MTLT}}$ within CIR and INT tissue is smaller than 0.5, see Section 6.1, we consider the MCFB as the matrix phase and the micropores as the inclusion phase of the composite MTLT. The apparent stiffness tensors of MTLT tissue, $\boldsymbol{C}_{\mathrm{MTLT}}$, was then predicted using the Mori–Tanaka method, cf. Eq. (3.72), where $A = \mathrm{MTLT}$, as well as $A_1 = \mathrm{mp}$ (inclusion phase) and $A_2 = \mathrm{MCFB}$ (matrix phase). Depending on the value of $\mathrm{vf}_{\mathrm{mp}}^{\mathrm{MTLT}}$, the apparent stiffness tensor $\boldsymbol{C}_{\mathrm{MTLT}}$ characterizes the elastic properties of CIR or INT tissue. The corresponding stiffness tensors are denoted by $\boldsymbol{C}_{\mathrm{CIR}}$ and $\boldsymbol{C}_{\mathrm{INT}}$, respectively.

Table 6.1.: List of input quantities of the multiscale model of MTLT tissue (CIR, INT).

Model input	Symbol	Unit	Type	Base value	Variation range	References
Collagen aspect ratio	$\mathrm{ar}_{\mathrm{col}}$	1	fp.	175	$100-200$	Akkus (2005); Weiner and Wagner (1998)
Collagen Poisson's ratio	ν_{col}	1	p.	0.3	—	www.efunda.com
Collagen Young's modulus	E_{col}	GPa	p.	5	—	Reisinger et al. (2010)
MCF aspect ratio	$\mathrm{ar}_{\mathrm{MCF}}$	1	fp.	100	$30-200$	Weiner and Wagner (1998)
Hydroxyapatite aspect ratio in MCF and ES	$\mathrm{ar}_{\mathrm{ha}}$	1	fp.	15	$1-50$	Vaughan et al. (2012); Akkus (2005); Weiner and Wagner (1998); Lees et al. (1994); Landis et al. (1993)
Hydroxyapatite Poisson's ratio	ν_{ha}	1	p.	0.28	—	Hellmich et al. (2004)
Hydroxyapatite Young's modulus	E_{ha}	GPa	p.	110	—	Hellmich et al. (2004)
Ratio of MCF mineral to total mineral	α_{MCF}	1	fp.	0.25	$0-1$	Sasaki et al. (2002); Lees et al. (1994)
Nanopores aspect ratio	$\mathrm{ar}_{\mathrm{np}}$	1	fp.	1	$1-200$	—
Micropores aspect ratio	$\mathrm{ar}_{\mathrm{mp}}$	1	fp.	100	$30-200$	Spiesz et al. (2012a)
Nano and micropores Poisson's ratio (pmma)	ν_{np}, ν_{mp}	1	p.	0.37	—	assumption
Nano and micropores Young's modulus (pmma)	E_{np}, E_{mp}	GPa	p.	4.96	—	SAM measurements on pmma
Microporosity in INT tissue	$\mathrm{vf}_{\mathrm{mp}}^{\mathrm{INT}}$	1	var.	0.1	$0-0.2$	staining experiments
Microporosity in CIR tissue	$\mathrm{vf}_{\mathrm{mp}}^{\mathrm{CIR}}$	1	var.	0	—	staining experiments
Volume fraction of hydroxyapatite in MCFB	$\mathrm{vf}_{\mathrm{ha}}^{\mathrm{MCFB}}$	1	var.	—	0.25−0.35	SR-μCT measurements, Eq. (6.4), Eq. (6.5)

For each input quantity we display its symbol, unit, input type (free parameter (fp.), parameter (p.) and variable (var.)), base value, variation range and the corresponding references.

The micropores within our model were represented as highly prolate spheroids. To account for the limited information on the average dimensions of micropores within MTLT tissue in the literature, we regard the aspect ratio of the micropores, $\mathrm{ar}_{\mathrm{mp}}$, as free parameter. Once again, we investigate the effect of the aspect ratio for a large parameter range, i.e., $\mathrm{ar}_{\mathrm{mp}} \in [30, 200]$, and set the parameter's base value to 100.

6.2.5 Phase volume fractions

In order to predict the apparent stiffness tensors of MTLT tissue, it remains to specify for each composite $A \in \{\mathrm{MTLT}, \mathrm{MCFB}, \mathrm{MCF}, \mathrm{ES}\}$ the two volume fractions vf_i^A $(i = 1, 2)$ of its constituents. Because of $\mathrm{vf}_1^A + \mathrm{vf}_2^A = 1$, we already have

$$\mathrm{vf}_{\mathrm{col}}^{\mathrm{MCF}} = 1 - \mathrm{vf}_{\mathrm{ha}}^{\mathrm{MCF}}, \qquad \mathrm{vf}_{\mathrm{ha}}^{\mathrm{ES}} = 1 - \mathrm{vf}_{\mathrm{np}}^{\mathrm{ES}},$$
$$\mathrm{vf}_{\mathrm{ES}}^{\mathrm{MCFB}} = 1 - \mathrm{vf}_{\mathrm{MCF}}^{\mathrm{MCFB}}, \qquad \mathrm{vf}_{\mathrm{MCFB}}^{\mathrm{MTLT}} = 1 - \mathrm{vf}_{\mathrm{mp}}^{\mathrm{MTLT}}.$$

Hence, four volume fractions remain to be specified. These were estimated using quantities available from measurements or literature data:

- the microporosity, $\mathrm{vf}_{\mathrm{mp}}^{\mathrm{MTLT}}$,
- the mineral distribution parameter, α_{MCF}, and
- the volume fraction of mineral in the MCFB, $\mathrm{vf}_{\mathrm{ha}}^{\mathrm{MCFB}}$,

together with an empirical relation $\mathrm{vf}_{\mathrm{col}}^{\mathrm{MCFB}} = h(\mathrm{vf}_{\mathrm{ha}}^{\mathrm{MCFB}})$, cf. Raum et al. (2006a) and see Appendix G.

Mineral distribution parameter α_{MCF} and volume fractions $\mathrm{vf}_{\mathrm{MCF}}^{\mathrm{MCFB}}$ and $\mathrm{vf}_{\mathrm{ha}}^{\mathrm{MCFB}}$

The mineral distribution parameter α_{MCF} is defined as the ratio of the mineral volume in the MCF to the total mineral volume in the MCFB. This parameter is also called the fraction of interfibrillar mineral in the terminology of some authors. Using transmission electron microscopy, Lees et al. (1994) estimated that α_{MCF} is about $0.25 - 0.3$ in MTLT tissue. Sasaki et al. (2002) proposed $\alpha_{\mathrm{MCF}} \approx 0.23$ in bovine cortical bone. More recently, Alexander et al. (2012) estimated, based on transmission electron microscopy on murine bone samples, that $\alpha_{\mathrm{MCF}} \leq 0.7$. This is in agreement with the previous findings. Combining the results from Lees et al. (1994) and Sasaki et al. (2002), we set the base value of α_{MCF} to 0.25. In order to account for the large range of possible values, cf. Alexander et al. (2012), we consider α_{MCF} as a free parameter of our model and vary it between 0 and 1. This meets the extreme cases, in which none, respectively, all mineral particles are located in the MCF.

The parameter α_{MCF} at hand, we can write

$$\begin{aligned} \mathrm{vf}_{\mathrm{MCF}}^{\mathrm{MCFB}} &= \alpha_{\mathrm{MCF}} \cdot \mathrm{vf}_{\mathrm{ha}}^{\mathrm{MCFB}} + \mathrm{vf}_{\mathrm{col}}^{\mathrm{MCFB}} \\ &= \alpha_{\mathrm{MCF}} \cdot \mathrm{vf}_{\mathrm{ha}}^{\mathrm{MCFB}} + h\left(\mathrm{vf}_{\mathrm{ha}}^{\mathrm{MCFB}}\right). \end{aligned} \tag{6.3}$$

For details on the experimental relationship h see Appendix G.

Next, we derive $\mathrm{vf}_{\mathrm{ha}}^{\mathrm{MCFB}}$ values from the experimental DMB values as obtained from the SR-μCT measurements of our samples. Consider the experimental DMB value in a particular voxel V. If V is made up of a specific tissue, then in this voxel the DMB and the volume fraction of mineral $\mathrm{vf}_{\mathrm{ha}}$ of that tissue are related by

$$\mathrm{DMB} = \rho_{\mathrm{ha}} \cdot \mathrm{vf}_{\mathrm{ha}}, \tag{6.4}$$

where $\rho_{\mathrm{ha}} = 3.0\,\mathrm{g\ cm^{-3}}$ is the mass density of ha. We are in particular interested in the DMB of MCFB tissue, $\mathrm{DMB}^{\mathrm{MCFB}}$, because it can be converted to $\mathrm{vf}_{\mathrm{ha}}^{\mathrm{MCFB}}$ using Eq. (6.4). However, our SR-μCT-derived experimental DMB values do not represent the DMB of MCFB tissue because the voxels contain an unknown fraction of the microporosity of the MTLT tissue. Thus, we have to convert the experimental DMB values into $\mathrm{DMB}^{\mathrm{MCFB}}$.

To this end, assume that a voxel V has the fraction $\alpha\,\widetilde{\mathrm{vf}}_{\mathrm{mp}}$ of micropore space and the remaining fraction $(1 - \alpha\,\widetilde{\mathrm{vf}}_{\mathrm{mp}})$ of MCFB space. Here, $\widetilde{\mathrm{vf}}_{\mathrm{mp}}$ is some experimentally measured microporosity and $\alpha \in [0, 1]$. Let V^{MCFB} be the subregion of V which only contains MCFBs. V and V^{MCFB} have the volume $|V|$ and $\left|V^{\mathrm{MCFB}}\right| = (1 - \alpha\,\widetilde{\mathrm{vf}}_{\mathrm{mp}})\,|V|$, respectively. Since the micropore space does not contain ha, the mass m of ha in V^{MCFB} is the same as the mass of ha in V. Then

$$\mathrm{DMB}^{\mathrm{MCFB}} = \frac{m}{\left|V^{\mathrm{MCFB}}\right|} = \frac{m}{(1 - \alpha\,\widetilde{\mathrm{vf}}_{\mathrm{mp}})\,|V|} = \frac{\mathrm{DMB}}{1 - \alpha\,\widetilde{\mathrm{vf}}_{\mathrm{mp}}}. \tag{6.5}$$

In this work we assume, according to the SR-μCT setup for our experimental dataset (Tiburtius et al., 2014), that $\alpha = 1$, i.e. that the full microporosity influenced the DMB measurements. Furthermore, we set $\widetilde{\mathrm{vf}}_{\mathrm{mp}} = 0.1$, the average experimental microporosity of MTLT tissue.

Now, with the formulas Eqs. (6.4) and (6.5), we can convert the experimental DMB values, in particular the DMB_i values in the ROIs, into corresponding values of $\mathrm{vf}_{\mathrm{ha}}^{\mathrm{MCFB}}$. These values cover the range $\mathrm{vf}_{\mathrm{ha}}^{\mathrm{MCFB}} \in [0.25, 0.35]$, for both, INT and CIR tissue. As stated earlier, we consider $\mathrm{vf}_{\mathrm{ha}}^{\mathrm{MCFB}}$ a variable of the model and, over the given range, we study its influence on the apparent elastic properties of MTLT tissue.

Microporosity $\mathrm{vf}_{\mathrm{mp}}^{\mathrm{MTLT}}$

The experimental microporosities observed for CIR and INT tissue ranged from small positive values of about 0.03 up to almost 0.2 (Tiburtius et al., 2014). We found that the microporosity decreases with increasing distance from the mineralization front. Since the mineralization of the MTLT increases with increasing distance from the mineralization front, it is reasonable to hypothesize a dependence of $\mathrm{vf}_{\mathrm{mp}}^{\mathrm{MTLT}}$ from $\mathrm{vf}_{\mathrm{ha}}^{\mathrm{MCFB}}$ and we assume a linear relation as the simplest possible dependence. Therefore, we consider two scenarios for $\mathrm{vf}_{\mathrm{mp}}^{\mathrm{MTLT}}$:

(C) $\mathrm{vf}_{\mathrm{mp}}^{\mathrm{MTLT}}$ is constant, i.e., is independent of $\mathrm{vf}_{\mathrm{ha}}^{\mathrm{MCFB}}$,

(MD) $\mathrm{vf}_{\mathrm{mp}}^{\mathrm{MTLT}}$ is mineralization-dependent, i.e., depends linearly on $\mathrm{vf}_{\mathrm{ha}}^{\mathrm{MCFB}}$.

Since the microporosity of MTLT tissue discriminates between CIR and INT tissue in our model, we will use the specific additional notations $\mathrm{vf}_{\mathrm{mp}}^{\mathrm{CIR}}$ and $\mathrm{vf}_{\mathrm{mp}}^{\mathrm{INT}}$ for $\mathrm{vf}_{\mathrm{mp}}^{\mathrm{MTLT}}$ in the following.

In scenario (C) we regard the microporosity $\mathrm{vf}_{\mathrm{mp}}^{\mathrm{MTLT}}$ as free parameter of our model $\mathcal{S}_{\mathrm{MTLT}}$ and investigate its influence on the apparent stiffness tensor of MTLT tissue for a wide range of values between 0 and 0.2. The base value of the microporosity was fixed to $\mathrm{vf}_{\mathrm{mp}}^{\mathrm{CIR}} = 0$ and $\mathrm{vf}_{\mathrm{mp}}^{\mathrm{INT}} = 0.1$ for CIR and INT tissues, respectively; this corresponds to the mean (rounded) of our experimentally derived microporosities.

In scenario (MD) we consider a linear relation between $\mathrm{vf}_{\mathrm{mp}}^{\mathrm{MTLT}}$ and $\mathrm{vf}_{\mathrm{ha}}^{\mathrm{MCFB}}$. As stated above, we have $\mathrm{vf}_{\mathrm{ha}}^{\mathrm{MCFB}} \in [0.25, 0.35]$ for both, CIR and INT tissue. At the lower end of that range we expect the largest experimental micro porosities (INT 0.15, CIR 0.07) and at the upper end the smallest ones (INT 0.05, CIR 0). Linear interpolation of these data points in the form $\mathrm{vf}_{\mathrm{mp}}^{\mathrm{MTLT}} = a \cdot \mathrm{vf}_{\mathrm{ha}}^{\mathrm{MCFB}} + b$ with coefficients $a < 0$ and b, results in the following $\mathrm{vf}_{\mathrm{ha}}^{\mathrm{MCFB}}$-dependent expressions for the microporosity in CIR and INT tissue

$$\mathrm{vf}_{\mathrm{mp}}^{\mathrm{CIR}} = -0.7\mathrm{vf}_{\mathrm{ha}}^{\mathrm{MCFB}} + 0.245 \qquad \mathrm{vf}_{\mathrm{ha}}^{\mathrm{MCFB}} \in [0.25, 0.35]\,, \tag{6.6}$$

$$\mathrm{vf}_{\mathrm{mp}}^{\mathrm{INT}} = -\mathrm{vf}_{\mathrm{ha}}^{\mathrm{MCFB}} + 0.4 \qquad \mathrm{vf}_{\mathrm{ha}}^{\mathrm{MCFB}} \in [0.25, 0.35]\,. \tag{6.7}$$

We refer to Section 6.4.2 for a discussion of these and other scenarios in MTLT tissue.

The volume fractions $\mathrm{vf}_{\mathrm{ha}}^{\mathrm{MCF}}$ and $\mathrm{vf}_{\mathrm{np}}^{\mathrm{ES}}$

These fractions can be expressed as:

$$\mathrm{vf}_{\mathrm{ha}}^{\mathrm{MCF}} = \alpha_{\mathrm{MCF}} \cdot \frac{\mathrm{vf}_{\mathrm{ha}}^{\mathrm{MCFB}}}{\mathrm{vf}_{\mathrm{MCF}}^{\mathrm{MCFB}}}, \tag{6.8}$$

$$\mathrm{vf}_{\mathrm{np}}^{\mathrm{ES}} = 1 - (1 - \alpha_{\mathrm{MCF}}) \cdot \frac{\mathrm{vf}_{\mathrm{ha}}^{\mathrm{MCFB}}}{1 - \mathrm{vf}_{\mathrm{MCF}}^{\mathrm{MCFB}}}. \tag{6.9}$$

6.3 Global sensitivity analysis and parametric study

In Section 6.3.1 we investigate our multiscale model of MTLT tissue using a global sensitivity analysis. We ask three research questions:

1. Which are the most sensitive components of the model output $\boldsymbol{C}_{\mathrm{MTLT}}$ with respect to variations in the model's variables and free parameters?

2. Which variables and free parameters influence the most sensitive components of $\boldsymbol{C}_{\mathrm{MTLT}}$?

3. How does the sensitivity of the stiffness components depends on $\mathrm{vf}_{\mathrm{ha}}^{\mathrm{MCFB}}$? Note that among all variables and parameters, the variable $\mathrm{vf}_{\mathrm{ha}}^{\mathrm{MCFB}}$ is of particular significance for the MTLT model as it determines the tissue's mineralization.

In contrast to a local analysis, which looks at a particular point in the parameter space (base values), a global analysis considers the full parameter space at once. As such a global analysis is independent from the often difficult selection of parameter base values.

For those model parameters p_i which have a large influence on the model output $\boldsymbol{C}_{\mathrm{MTLT}}$, we perform a parametric study in Section 6.3.2. This study is local in nature since we consider the apparent stiffnesses C_{axi} and C_{trv} as functions $C_{\mathrm{axi}} = C_{\mathrm{axi}}\left(\mathrm{vf}_{\mathrm{ha}}^{\mathrm{MCFB}}, p_i\right)$ and $C_{\mathrm{trv}} = C_{\mathrm{trv}}\left(\mathrm{vf}_{\mathrm{ha}}^{\mathrm{MCFB}}, p_i\right)$, respectively, for $\mathrm{vf}_{\mathrm{ha}}^{\mathrm{MCFB}} \in [0.25, 0.35]$ and a parameter p_i taking its values from its respective range, see Table 6.1.

6.3.1 Global sensitivity analysis

We perform a global sensitivity analysis employing the Elementary Effects method (Saltelli et al., 2008; Morris, 1991). Thereby we assessed for each free parameter (or variable) p_i of the model and for each component C_j of the model output $\boldsymbol{C}_{\mathrm{MTLT}}$ two global sensitivity measures:

1. $\mu^*_{(i,j)}$ describing the overall influence of p_i on C_j, and

2. $\sigma_{(i,j)}$ characterizing linear versus nonlinear effects of p_i on C_j.

The Elementary Effects method computes finite difference approximations to the partial derivative $\partial C_j / \partial p_i$ at a finite set of points of the parameter space. These points are selected in a randomized manner from an equidistant mesh of the parameter space following a suitable strategy for computational efficiency, see Saltelli et al. (2008). The measure $\mu^*_{(i,j)}$ is the sample mean of the approximations of $|\partial C_j / \partial p_i|$, while $\sigma_{(i,j)}$ is the sample standard deviation of the approximations of $\partial C_j / \partial p_i$. The sensitivity measures can be interpreted as follows: the higher the value of $\mu^*_{(i,j)}$ the stronger the influence of p_i on C_j. Moreover, a large value of $\sigma_{(i,j)}$ means that $\partial C_j / \partial p_i$ differs strongly from its mean throughout the parameter space, thus indicating that C_j is a nonlinear function of p_i. Using both sensitivity measures, we can heuristically classify the influence of parameter p_i on C_j as either: (a) negligible ($\mu^*_{(i,j)} \approx \sigma_{(i,j)} \approx 0$) or (b) linear ($\mu^*_{(i,j)} > \sigma_{(i,j)}$) or (c) nonlinear ($\mu^*_{(i,j)} \leq \sigma_{(i,j)}$).

Our global sensitivity analysis of the MTLT model covers a large number of parameters: the volume fraction of mineral in the MCFB, $\mathrm{vf}_{\mathrm{ha}}^{\mathrm{MCFB}}$, the microporosity, $\mathrm{vf}_{\mathrm{mp}}^{\mathrm{MTLT}}$, the mineral distribution parameter, α_{MCF}, and all the inclusion aspect ratios. Note that, though we will handle $\mathrm{vf}_{\mathrm{ha}}^{\mathrm{MCFB}}$ and $\mathrm{vf}_{\mathrm{mp}}^{\mathrm{MTLT}}$ in the course of our global sensitivity analysis as parameters, they are considered variables of our model.

We answer the first research question, comparing the values of the sensitivity measures, $\mu^*_{(i,j)}$ and $\sigma_{(i,j)}$, for all stiffness components. By construction, the apparent stiffness tensor $\boldsymbol{C} = \boldsymbol{C}_{\mathrm{MTLT}}$ of our model is transverse isotropic. Therefore, we obtained the two sensitivity measures for each of six different nonzero stiffness tensor components only: C_{11}, C_{12}, C_{13}, C_{33}, C_{44}, and C_{66}.

The components C_{12}, C_{13}, C_{44}, and C_{66} were not influenced significantly by any of the parameters p_i investigated in the global sensitivity analysis, here $\sigma_{(i,j)} \leq 1.1$, $\mu^*_{(i,j)} \leq 1.6$ for all p_i. The two components $C_{11} = C_{\mathrm{trv}}$ and $C_{33} = C_{\mathrm{axi}}$ were the most sensitive, compare Figures 6.4a and 6.4b for values of $\sigma_{(i,j)}$ and $\mu^*_{(i,j)}$.

We answer the second research question comparing the sensitivity measures, $\mu^*_{(i,j)}$ and $\sigma_{(i,j)}$, for $C_j = C_{\mathrm{trv}}$ and $C_j = C_{\mathrm{axi}}$ and each free parameter p_i. In Fig. 6.4a and Fig. 6.4b we display the tuple $(\mu^*_{(i,j)}, \sigma_{(i,j)})$ for each combination of $C_j \in \{C_{\mathrm{trv}}, C_{\mathrm{axi}}\}$ and p_i. A parameter p_i is said to be important if its corresponding sensitivity measure $\mu^*_{(i,j)}$ is relatively large compared with the $\mu^*_{(k,j)}$ value of other

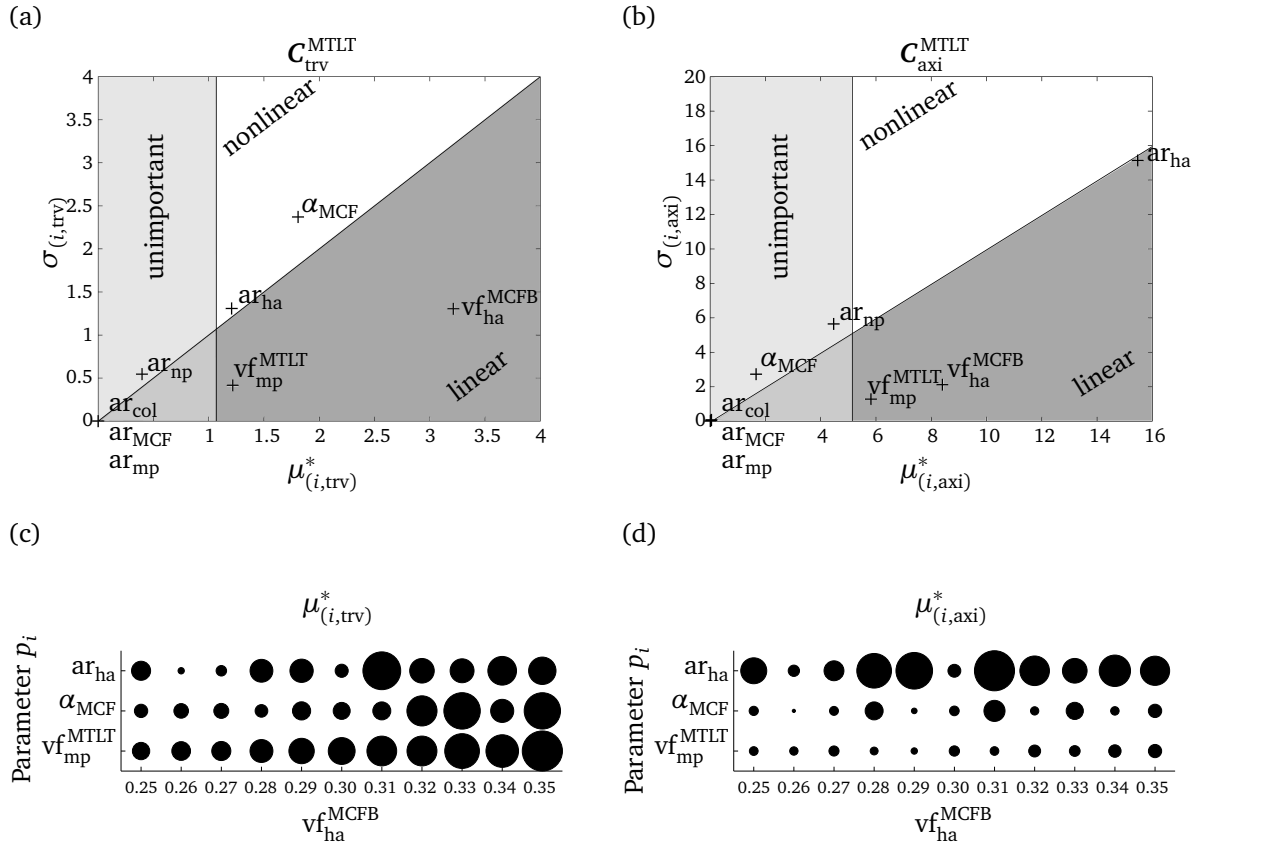

Figure 6.4.: Results of the global sensitivity analysis using the Elementary Effects method. (a),(b): Sensitivity measure $\sigma_{(i,j)}$ versus $\mu^*_{(i,j)}$ for free parameter p_i in transverse ($j = \mathrm{trv}$) and axial ($j = \mathrm{axi}$) direction. The dark gray area in each plot, where $\sigma_{(i,j)} \leq \mu^*_{(i,j)}$, characterizes sensitivity measures $(\mu^*_{(i,j)}, \sigma_{(i,j)})$ corresponding to parameters p_i with linear influence on the model apparent stiffness, whereas outside this area a nonlinear influence can be expected. The light gray area characterizes the unimportant parameters according to condition (6.10). (c),(d): Sensitivity measure $\mu^*_{(i,j)}(\mathrm{vf}^{\mathrm{MCFB}}_{\mathrm{ha}})$ for different values of $\mathrm{vf}^{\mathrm{MCFB}}_{\mathrm{ha}}$ and free parameters p_i in transverse ($j = \mathrm{trv}$) and axial ($j = \mathrm{axi}$) direction. The size of the circles represents $\mu^*_{(i,j)}(\mathrm{vf}^{\mathrm{MCFB}}_{\mathrm{ha}})/\mu^*_{\mathrm{max},j}$, see (6.11). The circles for the parameters $\mathrm{ar}_{\mathrm{np}}$, $\mathrm{ar}_{\mathrm{MCF}}$, $\mathrm{ar}_{\mathrm{col}}$ and $\mathrm{ar}_{\mathrm{mp}}$ were omitted; they are not visible over the whole $\mathrm{vf}^{\mathrm{MCFB}}_{\mathrm{ha}}$ value range in both axial and transverse direction.

parameters p_k. We make this quantitatively precise in the following way: we refer to a parameter p_i as important if

$$\mu^*_{(i,j)} \geq 0.3 \max_k \mu^*_{(k,j)} \quad \text{for } j = \mathrm{axi} \text{ or } j = \mathrm{trv}. \tag{6.10}$$

The $(\mu^*_{(i,j)}, \sigma_{(i,j)})$ area corresponding to unimportant parameters is indicated (light gray) in Fig. 6.4a and Fig. 6.4b.

It is then seen that the important parameters of the model are

- the mineral volume fraction of the MCFB, $\mathrm{vf}^{\mathrm{MCFB}}_{\mathrm{ha}}$,
- the aspect ratio of the mineral inclusion, $\mathrm{ar}_{\mathrm{ha}}$,
- the mineral distribution parameter, α_{MCF} (only from transverse direction), and
- the microporosity, $\mathrm{vf}^{\mathrm{MTLT}}_{\mathrm{mp}}$.

All other free parameters, such as the inclusion aspect ratios of col, mp, np, and MCF only have small or no influence on the axial and transverse apparent stiffness. Furthermore, we observed that the parameters have a stronger (absolute) influence on the axial than on the transverse stiffness ($\mu^*_{(i,\mathrm{axi})} \approx \alpha_i \cdot \mu^*_{(i,\mathrm{trv})}$ with $2 \lesssim \alpha_i \lesssim 12$). By means of both sensitivity measures, $\mu^*_{(i,j)}$ and $\sigma_{(i,j)}$, we classified the type of influence of the important parameters on the apparent stiffness of MTLT tissue. The influence of $\mathrm{vf}_{\mathrm{ha}}^{\mathrm{MCFB}}$ and $\mathrm{vf}_{\mathrm{mp}}^{\mathrm{MTLT}}$ is linear. Parameter α_{MCF} has a clear nonlinear influence on the transverse stiffness. Finally, for $\mathrm{ar}_{\mathrm{ha}}$ we have $\mu^*_{(i,j)} \approx \sigma_{(i,j)}$. Therefore, a clear distinction between linear and nonlinear influence is here not possible. A parametric study will show that the apparent stiffness tensor of the MTLT is (at least locally) a nonlinear function of $\mathrm{ar}_{\mathrm{ha}}$ (and also of α_{MCF}), see Section 6.3.2.

Finally, we move to the third research question. Our global sensitivity analysis, performed for the second research question, confirms that indeed $\mathrm{vf}_{\mathrm{ha}}^{\mathrm{MCFB}}$ is an important parameter determining $\boldsymbol{C}_{\mathrm{MTLT}}$. Accordingly, we observe high sensitivity measures for $\mathrm{vf}_{\mathrm{ha}}^{\mathrm{MCFB}}$ in Fig. 6.4a and Fig. 6.4b. We now consider $\mathrm{vf}_{\mathrm{ha}}^{\mathrm{MCFB}}$ as a variable of our model and investigate the sensitivity measure $\mu^*_{(i,j)}$ as a function of $\mathrm{vf}_{\mathrm{ha}}^{\mathrm{MCFB}}$. To this end we perform a series of global sensitivity analyses of our MTLT model where in each instance $\mathrm{vf}_{\mathrm{ha}}^{\mathrm{MCFB}}$ is kept at a constant value and we determine $\mu^*_{(i,j)}(\mathrm{vf}_{\mathrm{ha}}^{\mathrm{MCFB}})$ for parameters p_i and stiffness component C_j with $j \in \{\mathrm{trv}, \mathrm{axi}\}$ for $\mathrm{vf}_{\mathrm{ha}}^{\mathrm{MCFB}}$ values between 0.25 and 0.35 in 0.01 steps. The scaled values

$$\frac{\mu^*_{(i,j)}(\mathrm{vf}_{\mathrm{ha}}^{\mathrm{MCFB}})}{\mu^*_{\mathrm{max},j}}, \quad \text{where } \mu^*_{\mathrm{max},j} := \max_{i,\,\mathrm{vf}_{\mathrm{ha}}^{\mathrm{MCFB}}} \mu^*_{(i,j)}(\mathrm{vf}_{\mathrm{ha}}^{\mathrm{MCFB}}), \tag{6.11}$$

are shown in Fig. 6.4c and Fig. 6.4d.

The following conclusions can be drawn from Fig. 6.4c and Fig. 6.4d:

- The microporosity $\mathrm{vf}_{\mathrm{mp}}^{\mathrm{MTLT}}$ is an important parameter over the full range of values of $\mathrm{vf}_{\mathrm{ha}}^{\mathrm{MCFB}}$. Its importance increases with increasing $\mathrm{vf}_{\mathrm{ha}}^{\mathrm{MCFB}}$ for the transverse stiffness, while it is rather constant for the axial stiffness.
- The parameter α_{MCF} influences the axial stiffness C_{axi} locally for values of $\mathrm{vf}_{\mathrm{ha}}^{\mathrm{MCFB}} = 0.28, 0.31, 0.33$, however, no clear trend is visible. For C_{trv}, the importance of α_{MCF} is rather constant for $\mathrm{vf}_{\mathrm{ha}}^{\mathrm{MCFB}} < 0.32$ and increases to a significantly larger value for $\mathrm{vf}_{\mathrm{ha}}^{\mathrm{MCFB}} \geq 0.32$.
- The parameter $\mathrm{ar}_{\mathrm{ha}}$ has quite some influence on C_{axi} and C_{trv} but no clear trend with increasing $\mathrm{vf}_{\mathrm{ha}}^{\mathrm{MCFB}}$ values is evident.
- The aspect ratios $\mathrm{ar}_{\mathrm{np}}$, $\mathrm{ar}_{\mathrm{col}}$, $\mathrm{ar}_{\mathrm{MCF}}$, and $\mathrm{ar}_{\mathrm{mp}}$ have essentially no influence on C_{axi} and C_{trv} and are thus not shown in Fig. 6.4c and Fig. 6.4d.

6.3.2 Parametric study

We perform a parametric study for the crucial parameters, α_{MCF}, $\mathrm{ar}_{\mathrm{ha}}$, $\mathrm{vf}_{\mathrm{mp}}^{\mathrm{MTLT}}$, and $\mathrm{vf}_{\mathrm{ha}}^{\mathrm{MCFB}}$ (cf. Section 6.3.1), influencing $\boldsymbol{C}_{\mathrm{MTLT}}$. The results of this study, as discussed below, are mainly in line with the predictions of our sensitivity analysis.

The influence of α_{MCF} on the axial and transverse stiffness of INT tissue ($\mathrm{vf}_{\mathrm{mp}}^{\mathrm{INT}} = 0.1$) is shown in Fig. 6.5; corresponding results are obtained for CIR tissue ($\mathrm{vf}_{\mathrm{mp}}^{\mathrm{CIR}} = 0$) but are not shown here.

For different fixed values of α_{MCF} and increasing mineral volume fraction $\mathrm{vf}_{\mathrm{ha}}^{\mathrm{MCFB}}$ values, the MTLT tissue get stiffer in both, transverse and axial directions. In contrast, increasing α_{MCF} for fixed values of $\mathrm{vf}_{\mathrm{ha}}^{\mathrm{MCFB}}$, MTLT tissue undergoes a stiffening in axial direction, while a softening for $\alpha_{\mathrm{MCF}} < 0.7$ and a stiffening for $\alpha_{\mathrm{MCF}} \geq 0.7$ in transverse direction was observed. We remark that $\alpha_{\mathrm{MCF}} \geq 0.7$ corresponds to a mineral distribution which should not be present in biological tissue, cf. Alexander et al. (2012).

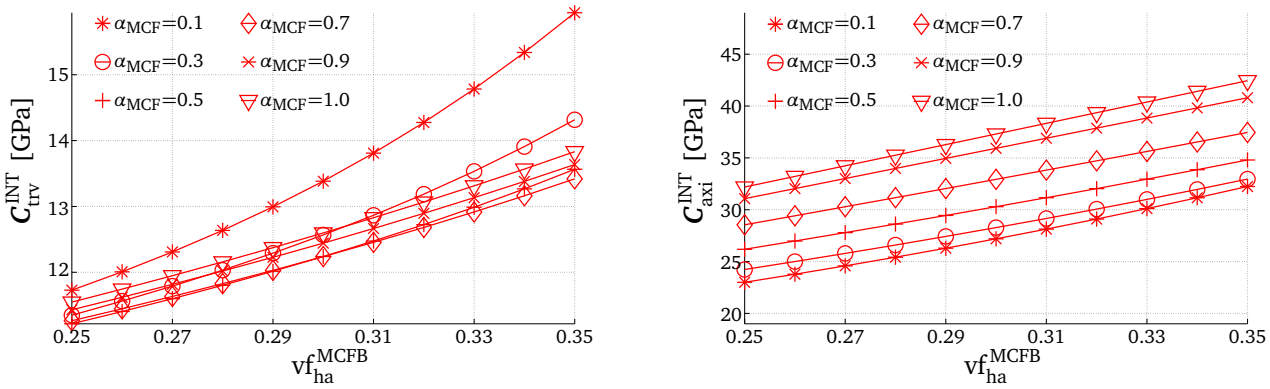

Figure 6.5.: Results of the parametric study. Influence of the parameter α_{MCF} on the apparent stiffness of INT tissue. The left/right image depicts the transverse/axial stiffness. Model parameters other than α_{MCF} were fixed to their base values.

The trend observed for α_{MCF} is similar to that described by Reisinger et al. (2010) for MCFB tissue. They reported that there are two opposing trends when increasing α_{MCF} for fixed values of vf_{ha}^{MCFB}. On the one hand, the transverse and the axial apparent stiffness of the MCF gets larger. On the other hand, those stiffnesses of the ES get smaller, due to the decreasing amount of mineral in the ES. These two processes compete with each other at the next hierarchical level of the MTLT model, i.e. the MCFB (Fig. 6.3). In transverse direction, for $\alpha_{MCF} \leq 0.7$, the softening effect of the ES is predominant; hence, the transverse apparent stiffness values of the MCFB decreases for increasing α_{MCF}. For higher α_{MCF} values the stiffening of the MCF predominates, resulting in increasing apparent stiffnesses of the MCFB. In axial direction, the stiffening of the MCF is the major process regardless of the value of α_{MCF}. Hence, the axial apparent stiffness values of the MCFB gets larger for increasing α_{MCF} values.

An increase in the mineral aspect ratio ar_{ha} for fix mineral volume fractions vf_{ha}^{MCFB} results in increasing axial and decreasing transverse stiffnesses (or acoustic impedances). For example, in Fig. 6.6 we depict the transverse and the axial impedances for $ar_{ha} = 15$ (legend reads *INT model, base values*) and $ar_{ha} = 7$ (legend reads *INT model, $ar_{ha} = 7$*). Obviously, the axial stiffnesses increases from $ar_{ha} = 7$ to $ar_{ha} = 15$. However, there is no apparent decrease for the transverse stiffness visible in Fig. 6.6. This can be explained by the nonlinear effect of the mineral aspect ratio, through which the main decrease in the transverse stiffness is observed if we change ar_{ha} from one to seven. This influence of ar_{ha} is well known and is described, e.g., for MCFB tissue in Reisinger et al. (2010).

The situation is different for the microporosity. A higher amount of micropores decreases the stiffness both in axial and transverse direction. This is seen in Fig. 6.6, where we depict the acoustic impedance for MTLT tissue with a microporosity $vf_{mp}^{INT} = 0.1$ (legend reads *INT model, base values*) and for $vf_{mp}^{CIR} = 0$ (legend reads *CIR model, base values*).

Summarizing the results of Sections 6.3.1 and 6.3.2, we have seen that the parameters α_{MCF}, vf_{ha}^{MCFB}, ar_{ha} and vf_{mp}^{MTLT} have the strongest influence on the stiffness of MTLT tissue in our model. Hence, special attention has to be paid on the accurate derivation of their values from experiments. For example, we discuss the influence of different assumptions for the microporosity on the apparent stiffness tensor in Section 6.4.2. Additionally, we learned that the stiffness components, C_{axi} and C_{trv}, are influenced mostly by the parameters. These two components are now compared to corresponding experimental data in the next section.

6.4 Comparison of model and experimental elastic properties

We convert the model apparent stiffnesses to model acoustic impedances, Z_ν^T, where $T \in \{\text{CIR, INT}\}$ and $\nu \in \{\text{axi, trv}\}$, and consider them as functions of vf_{ha}^{MCFB}, i.e., $Z_\nu^T = Z_\nu^T(vf_{ha}^{MCFB})$. From our experimental

investigations we have, for each ROI i, the values DMB_i, $\widetilde{Z}_i$, ν_i, and T_i. Using Eqs. (6.4) and (6.5), we convert DMB_i to $\mathrm{vf}_{\mathrm{ha},i}^{\mathrm{MCFB}}$. This allows to compare the experimental acoustic impedance $\widetilde{Z}_i$ with the model acoustic impedance $Z_{\nu_i}^{T_i}(\mathrm{vf}_{\mathrm{ha},i}^{\mathrm{MCFB}})$ for model validation. To this end we use the *relative root mean square error* (rRMSE), defined for two vectors a and b of length n by

$$\mathrm{rRMSE}(a,b) = \sqrt{\frac{1}{n}\sum_{j=1}^{n}\left(\frac{a_j - b_j}{\max\{|a_j|,|b_j|\}}\right)^2}. \tag{6.12}$$

We compute four error values rRMSE_ν^T, where $T \in \{\mathrm{CIR}, \mathrm{INT}\}$ and $\nu \in \{\mathrm{axi}, \mathrm{trv}\}$. The vectors a and b contain the values $\widetilde{Z}_i$ and $Z_{\nu_i}^{T_i}(\mathrm{vf}_{\mathrm{ha},i}^{\mathrm{MCFB}})$, respectively, for a subset of ROIs. For $\mathrm{rRMSE}_{\mathrm{axi}}^{\mathrm{CIR}}$ and $\mathrm{rRMSE}_{\mathrm{axi}}^{\mathrm{INT}}$ these are all ROIs i with $(\nu_i, T_i) = (\mathrm{axi}, \mathrm{CIR})$ and $(\nu_i, T_i) = (\mathrm{axi}, \mathrm{INT})$, respectively. Since in the transverse direction we cannot distinguish experimentally between CIR and INT tissue, we use for $\mathrm{rRMSE}_{\mathrm{trv}}^{\mathrm{CIR}}$ and $\mathrm{rRMSE}_{\mathrm{trv}}^{\mathrm{INT}}$ the same subset of ROIs i, namely those with $(\nu_i, T_i) = (\mathrm{trv}, \mathrm{CIR/INT})$, but different model values $\widetilde{Z}_{\mathrm{trv}}^{\mathrm{CIR}}(\mathrm{vf}_{\mathrm{ha},i}^{\mathrm{MCFB}})$ and $\widetilde{Z}_{\mathrm{trv}}^{\mathrm{INT}}(\mathrm{vf}_{\mathrm{ha},i}^{\mathrm{MCFB}})$.

For each of the above three subsets of ROIs we obtain, from the experimental data, a regression line

$$\widetilde{Z}^{reg}(\mathrm{vf}_{\mathrm{ha}}^{\mathrm{MCFB}}) = m\,\mathrm{vf}_{\mathrm{ha}}^{\mathrm{MCFB}} + n\,, \tag{6.13}$$

where $m = m(T,\nu)$ and $n = n(T,\nu)$ were computed using least-squares minimization. These regression lines are shown together with the experimental data points in subsequent figures and will provide an additional criterion to discriminate between models with different parameter values. To this end we define a second error indicator, D_ν^T, for a vector a of mineral volume fraction values $\mathrm{vf}_{\mathrm{ha}}^{\mathrm{MCFB}}$ by

$$\mathrm{D}_\nu^T = \max_j\left\{\frac{|Z_\nu^T(a_j) - \widetilde{Z}^{reg}(a_j)|}{\max\{|Z_\nu^T(a_j)|, |\widetilde{Z}^{reg}(a_j)|\}}\right\}. \tag{6.14}$$

We use $a = [0.25, 0.26, \ldots, 0.35]^T$ in this study.

6.4.1 Model calibration

The model parameters were fixed to their base values, cf. Table 6.1. In particular, we use a constant microporosity $\mathrm{vf}_{\mathrm{mp}}^{\mathrm{CIR}} = 0$ for CIR and $\mathrm{vf}_{\mathrm{mp}}^{\mathrm{INT}} = 0.1$ for INT tissue. Fig. 6.6 depicts, for both tissue types, the model and experimental acoustic impedance values in the transverse and axial directions as functions of the mineral volume fraction $\mathrm{vf}_{\mathrm{ha}}^{\mathrm{MCFB}}$.

It is seen that the model and the experimental values compare well in both directions and for both tissue types. However, there is a larger offset between model and experimental impedance in the axial than in the transverse direction. The observations from the global sensitivity analysis and from the parametric study helped us to adjust the model parameters to obtain a better agreement between experimental and model data. From the values of $\mathrm{ar}_{\mathrm{ha}}$ considered in our parametric study, the choice $\mathrm{ar}_{\mathrm{ha}} = 7$ resulted in the smallest rRMSE_ν^T errors, all ≈ 0.06, cf. Table 6.2. The axial and transverse acoustic impedances of CIR and INT tissue for $\mathrm{ar}_{\mathrm{ha}} = 7$ are also displayed in Fig. 6.6.

6.4.2 Impact of the dependence of microporosity on mineral volume fraction

In a next step, we investigated the impact of different microporosity scenarios on rRMSE_ν^T and D_ν^T, while sticking to the adapted value $\mathrm{ar}_{\mathrm{ha}} = 7$. Fig. 6.6 shows that the slopes of the model curves for a constant

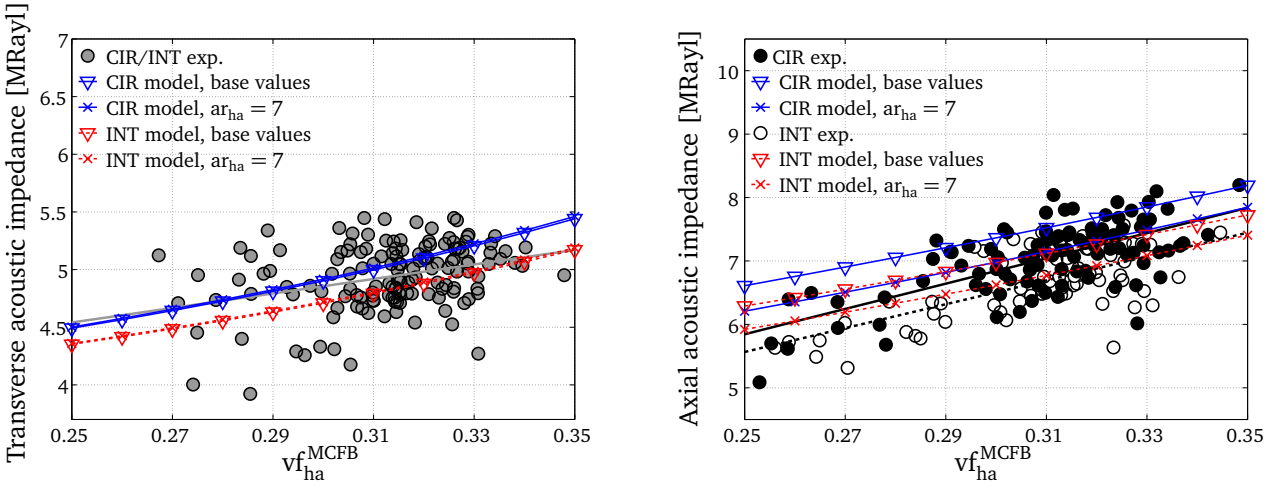

Figure 6.6.: Experimental and model acoustic impedance of CIR and INT tissue in transverse (left image) and axial (right image) direction as functions of $\mathrm{vf}_{\mathrm{ha}}^{\mathrm{MCFB}}$. The mineral aspect ratio is either the base value $\mathrm{ar}_{\mathrm{ha}} = 15$, or reduced to $\mathrm{ar}_{\mathrm{ha}} = 7$. All other parameters were fixed to their base values, see Table 6.1. In particular, the microporosity for the CIR model or the INT model is always $\mathrm{vf}_{\mathrm{mp}}^{\mathrm{CIR}} = 0$ or $\mathrm{vf}_{\mathrm{mp}}^{\mathrm{INT}} = 0.1$, respectively. The solid gray, the solid black and the dashed black lines are the regression lines through the experimental data for ($T = \mathrm{CIR/INT}, \nu = \mathrm{trv}$), ($T = \mathrm{CIR}, \nu = \mathrm{axi}$) and ($T = \mathrm{INT}, \nu = \mathrm{axi}$), respectively.

microporosity and that of the corresponding regression lines are considerably different. The experimental investigations performed by our project partners (Section 6.1) suggest a relationship between the mineralization ($\mathrm{vf}_{\mathrm{ha}}^{\mathrm{MCFB}}$) and the microporosity ($\mathrm{vf}_{\mathrm{mp}}^{\mathrm{MTLT}}$), see Fig. 6.2d, which is not yet included in our model. Here, we now investigate two different types of microporosity scenarios, i.e., constant versus mineral-dependent, cf. Section 6.2.5, with the aim to further improve the agreement between model and experimental data. For CIR tissue we used

(C1) $\mathrm{vf}_{\mathrm{mp}}^{\mathrm{CIR}} = 0,$

(MD1) $\mathrm{vf}_{\mathrm{mp}}^{\mathrm{CIR}} = -0.7\,\mathrm{vf}_{\mathrm{ha}}^{\mathrm{MCFB}} + 0.245 \Rightarrow \mathrm{vf}_{\mathrm{mp}}^{\mathrm{CIR}} \in [0, 0.07],$

and for INT tissue

(C2) $\mathrm{vf}_{\mathrm{mp}}^{\mathrm{INT}} = 0.1,$

(C3) $\mathrm{vf}_{\mathrm{mp}}^{\mathrm{INT}} = 0.2,$

(MD2) $\mathrm{vf}_{\mathrm{mp}}^{\mathrm{INT}} = -\mathrm{vf}_{\mathrm{ha}}^{\mathrm{MCFB}} + 0.4 \quad \Rightarrow \mathrm{vf}_{\mathrm{mp}}^{\mathrm{INT}} \in [0.05, 0.15],$

(MD3) $\mathrm{vf}_{\mathrm{mp}}^{\mathrm{INT}} = -2\,\mathrm{vf}_{\mathrm{ha}}^{\mathrm{MCFB}} + 0.75 \Rightarrow \mathrm{vf}_{\mathrm{mp}}^{\mathrm{INT}} \in [0.05, 0.25],$

(MD4) $\mathrm{vf}_{\mathrm{mp}}^{\mathrm{INT}} = -2\,\mathrm{vf}_{\mathrm{ha}}^{\mathrm{MCFB}} + 0.8 \quad \Rightarrow \mathrm{vf}_{\mathrm{mp}}^{\mathrm{INT}} \in [0.1, 0.3].$

The microporosity ranges above follow with mineral volume fractions $\mathrm{vf}_{\mathrm{ha}}^{\mathrm{MCFB}} \in [0.25, 0.35]$. The scenarios (MD1) and (MD2) correspond to Eqs. (6.6) and (6.7), derived according to the experimental data in Tiburtius et al. (2014), (MD3) widens the range of microporosity values and (MD4) moves them to larger values. Note that Spiesz et al. (2012a) report even larger microporosities than those in (MD4); these are not included here because they resulted in even larger errors rRMSE_{ν}^{T} and D_{ν}^{T}. In Table 6.2 we give the values of rRMSE_{ν}^{T} and D_{ν}^{T} for each microporosity scenario.

The values of rRMSE_{ν}^{T} are small and comparable for all microporosity scenarios, tissue types T and directions ν ($\mathrm{rRMSE}_{\nu}^{T} \in [0.06, 0.08]$). This means, with respect to this error indicator, that model and experimental acoustic impedance values compare very well independent of the microporosity scenario.

The error indicator D_{ν}^{T} allows for an additional quantitative evaluation, how well these scenarios predicted the experimental observations. We observed that, in the case of the axial acoustic impedance, the values of D_{ν}^{T} are smaller for mineral-dependent than for constant microporosities. The smallest

Table 6.2.: Values of rRMSE_ν^T and D_ν^T for constant and mineral-dependent microporosity for CIR and INT tissue.

CIR tissue				
$\mathrm{vf}_{\mathrm{mp}}^{\mathrm{CIR}}$	$\mathrm{rRMSE}_{\mathrm{trv}}^{\mathrm{CIR}}$	$\mathrm{D}_{\mathrm{trv}}^{\mathrm{CIR}}$	$\mathrm{rRMSE}_{\mathrm{axi}}^{\mathrm{CIR}}$	$\mathrm{D}_{\mathrm{axi}}^{\mathrm{CIR}}$
(C1)	0.06	0.05	0.06	0.08
(MD1)	0.06	0.05	0.06	0.05
INT tissue				
$\mathrm{vf}_{\mathrm{mp}}^{\mathrm{INT}}$	$\mathrm{rRMSE}_{\mathrm{trv}}^{\mathrm{INT}}$	$\mathrm{D}_{\mathrm{trv}}^{\mathrm{INT}}$	$\mathrm{rRMSE}_{\mathrm{axi}}^{\mathrm{INT}}$	$\mathrm{D}_{\mathrm{axi}}^{\mathrm{INT}}$
(C2)	0.06	0.03	0.06	0.08
(C3)	0.08	0.07	0.07	0.08
(MD2)	0.06	0.05	0.06	0.05
(MD3)	0.06	0.08	0.06	0.01
(MD4)	0.07	0.09	0.07	0.04

The mineral aspect ratio is $\mathrm{ar}_{\mathrm{ha}} = 7$, all remaining model parameters are at their base value.

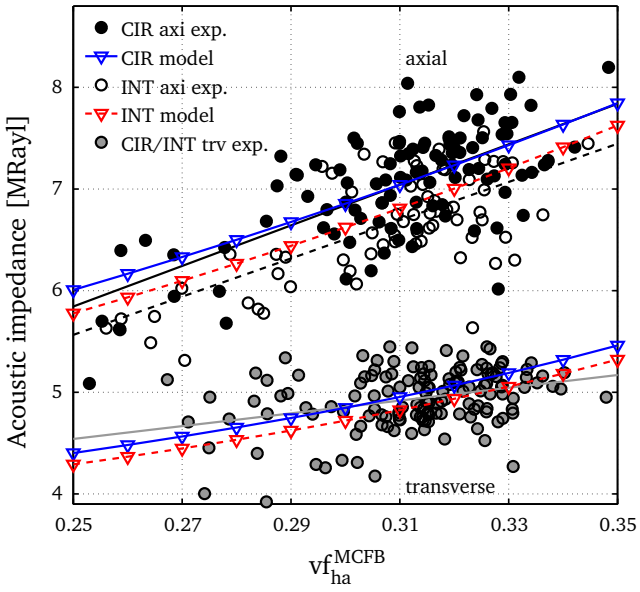

Figure 6.7.: Experimental and best model acoustic impedance values for tissue type T and direction ν. The mineral aspect ratio was set to $\mathrm{ar}_{\mathrm{ha}} = 7$, the mineral-dependent microporosity in CIR and INT tissue is (MD1) and (MD2), respectively. The solid gray, the solid black and the dashed black lines are the regression lines through the experimental data, see Fig. 6.6.

value of $\mathrm{D}_{\mathrm{axi}}^{\mathrm{CIR}}$ is obtained for microporosity scenario (MD1), that of $\mathrm{D}_{\mathrm{axi}}^{\mathrm{INT}}$ for (MD3). In the case of the transverse acoustic impedance, no benefit of the mineral-dependent over the constant microporosity scenarios is seen.

We are interested in a microporosity scenario that provides for a tissue type T small and similar values for $\mathrm{D}_{\mathrm{trv}}^T$ and $\mathrm{D}_{\mathrm{axi}}^T$. Therefore, we consider the scenarios (MD1) and (MD2) the best choice for CIR and INT tissue, respectively. Fig. 6.7 shows the corresponding model acoustic impedance values. Observe that, for the axial impedances, the slopes of the model curves and the corresponding regression lines are now in better agreement. Note that for INT tissue we deliberately chose a microporosity scenario for which the value of $\mathrm{D}_{\mathrm{axi}}^{\mathrm{INT}}$ is not minimal: the minimal value $\mathrm{D}_{\mathrm{axi}}^{\mathrm{INT}} = 0.01$ is reached with the scenario (MD3), however, on cost of a larger discrepancy between $\mathrm{D}_{\mathrm{axi}}^{\mathrm{INT}}$ and $\mathrm{D}_{\mathrm{trv}}^{\mathrm{INT}}$.

6.5 Discussion

In this section we discuss our results with respect to our three research questions. We highlight how our research reflects, differs and extends current knowledge of the elastic properties of MTLTs, in particular, of CIR and INT tissue.

Section 6.5.1 focuses on our first two research questions, i.e. which model parameters are important and how do these parameters influence the elastic properties of CIR and INT tissue. We compare the results of our global sensitivity analysis and our parametric study with the results of other researchers. Additionally, we discuss the relevance of parameters which were not investigated in our study.

Section 6.5.2 concentrates on the third research question. We compare our model predictions with literature data on MTLT tissue and other MMTs. In particular, we consider the anisotropy ratio AR, the values of the axial and the transverse stiffness, and the discrimination between CIR and INT tissue. Furthermore, we clarify limitations of the experimental data used to validate our model. Finally, we discuss the efficiency of our model with respect to computation time, the choice of the homogenization method and the choice of the starting value for the self-consistent method.

6.5.1 Parameters and their influence on the elastic properties of CIR and INT tissue

Global sensitivity analysis and parametric study: In Section 6.3 we derived the global sensitivity measures for all stiffness components of MTLT tissue, in particular for C_{axi} and C_{trv}. We found that the axial and the transverse components of the apparent stiffness tensor of MTLT tissue were influenced mostly by the model parameters. Other stiffness components were only slightly influenced or not at all. The essential parameters determining the axial and the transverse stiffnesses were the mineral volume fraction of the MCFB ($\text{vf}_{\text{ha}}^{\text{MCFB}}$), the microporosity ($\text{vf}_{\text{mp}}^{\text{MTLT}}$), the mineral distribution parameter (α_{MCF}), and the aspect ratio of the mineral inclusion (ar_{ha}).

We compare the results of our sensitivity analysis for MTLT tissue with those of the local sensitivity analysis performed by Reisinger et al. (2010) for MCFB tissue. Note therefore that Reisinger et al. (2010) approximate the local sensitivity of the Young's modulus E_{axi} in axial direction with respect to some parameter p based on the difference quotient. Thereby, p was changed about a small amount around its base value and all other model parameters were kept to their base value. In order to compare the sensitivity estimates for E_{axi} and C_{axi} with each other, we normalized all sensitivity estimates to their respective maximal values. Corresponding results are displayed in Table 6.3.

It can be said that, except for the microporosity, which is no parameter of the Reisinger model at all, similar parameters are important for the axial elastic properties of MCFB and MTLT tissue. Our results differ in the order of importance of the parameters. In particular, we consider ar_{ha} to be most important parameter; its normalized sensitivity measure in Table 6.3 is 1. In contrast, Reisinger et al. (2010) regard $\text{vf}_{\text{ha}}^{\text{MCFB}}$ as the most important parameter and consider ar_{ha} to be of only moderate importance (sensitivity measure 0.002). A reason for the different orders of importance may lie in that we consider global sensitivity measures while Reisinger et al. (2010) determined local ones. Their sensitivity measures were derived for a specific point in the parameter space, in particular, for $\text{vf}_{\text{ha}}^{\text{MCFB}} = 0.3$. Interestingly, if we look at our sensitivity measures for ar_{ha} for fixed values of $\text{vf}_{\text{ha}}^{\text{MCFB}}$, as given in Fig. 6.4d, it is seen that the sensitivity measure for $\text{ar}_{\text{ha}}(\text{vf}_{\text{ha}}^{\text{MCFB}})$ with $\text{vf}_{\text{ha}}^{\text{MCFB}} = 0.3$ is very small compared to those sensitivity measures for other values of $\text{vf}_{\text{ha}}^{\text{MCFB}}$. This holds not only for ar_{ha} but also for other parameters. It shows that locally observed sensitivity measures are not sufficient to derive global statements about the importance of a parameter. This was one of the main reasons why we preferred in this thesis the global over the local sensitivity analysis. The former is independent from the often difficult selection of parameter base values.

The mineral volume fraction $\text{vf}_{\text{ha}}^{\text{MCFB}}$ is an important parameter for various MMTs (Akkus, 2005; Nikolov and Raabe, 2008; Hellmich et al., 2004). Together with the micro porosity $\text{vf}_{\text{mp}}^{\text{MTLT}}$, it has a linear influence on the axial as well as on the transverse apparent stiffness of MTLT tissue, compare Figures 6.4a and 6.4b for values of the sensitivity measures.

The mineral distribution parameter α_{MCF} is globally important for C_{trv}, however, not for C_{axi} or any other stiffness component. This is partly in accordance with what was observed by others. Reisinger et al. (2010) found that α_{MCF} has no influence on E_{axi}, however, made no statement regarding the other stiffness components. Nikolov and Raabe (2008) state that α_{MCF} changes the Young's modulus E_{axi} and some shear modulus, compare their Figures 10 and 11 in Nikolov and Raabe (2008). The differing results regarding which components are influenced, may be due to the different homogenization methods employed.

Obviously, the microporosity is an important parameter determining the elastic properties of MTLT tissue. It has a large sensitivity measure (third important parameter for C_{axi}) and moreover is a discriminate criteria between CIR and INT tissue. To our knowledge, its influence on C_{axi} and C_{trv} was not investigated earlier. In Section 6.4.2 we studied the impact of two microporosity scenarios (constant versus mineral-dependent) on the errors rRMSE_{ν}^{T} and D_{ν}^{T}. We found that our results are in better agreement with the experimental data if the microporosity depends linearly on the mineral volume fraction $\text{vf}_{\text{ha}}^{\text{MCFB}}$

Table 6.3.: Sensitivity measures μ_{axi} and normalized sensitivity measures $\mu_{\text{axi}}/\mu_{\text{max}}$ for the elastic properties of MCFB and MTLT tissue in axial direction (MCFB tissue: Young's modulus E_{axi} (Reisinger et al., 2010), MTLT tissue: stiffness component C_{axi} (Fig. 6.4b)); μ_{max} denotes the maximal sensitivity measure of either E_{axi} or C_{axi}.

Parameters	MCFB tissue		MTLT tissue	
	μ_{axi}	$\mu_{\text{axi}}/\mu_{\text{max}}$	μ_{axi}	$\mu_{\text{axi}}/\mu_{\text{max}}$
ar_{ha}	0.1	0.002	15.5	1.0
$\text{vf}_{\text{ha}}^{\text{MCFB}}$	87.7	1.0	8.4	0.5
$\text{vf}_{\text{mp}}^{\text{MTLT}}$	–	–	5.8	0.4
α_{MCF}	4.8	0.05	1.7	0.1

than if it is constant over $\text{vf}_{\text{ha}}^{\text{MCFB}}$. In order to study this relationship further it needs more experimental data, see the discussion in Section 6.5.2.

Parameters not investigated in this study: Our sensitivity analysis and the parametric study allowed for insight into the influence of compositional and structural model parameters on the apparent stiffness tensor of MTLT tissue. However, model parameters such as the elastic properties of the MTLT's basic constituents were not considered. We discuss their influence below.

All basic constituents were chosen to be isotropic, in order to keep the model as simple as possible. Nevertheless, the structure and composition of collagen (Fratzl, 2008) indicate that it might be more realistic to assume transverse isotropic material properties for this material. However, in order to setup a transverse isotropic stiffness tensor, we need five elastic constants from experimental elastic data at the nanometer scale, data which is neither available nor easily accessible due to the small dimensions. We therefore decided to check first if assuming isotropic collagen results in realistically predicted axial and transverse stiffnesses of MTLT tissue. Having verified this in this study, we can introduce more complexity by assuming collagen to be transverse isotropic in future work. The results of the present study then can serve as reference point when investigating the influence of the collagen's material symmetries on $\boldsymbol{C}_{\text{MTLT}}$.

Collagen Young's moduli reported in the literature differ between one and nine GPa. For this range of values, Reisinger et al. (2010) have shown that the collagen Young's modulus does not significantly influence the apparent stiffness tensor of the MCFB. We can make a similar statement for the apparent stiffness of the MTLT, i.e. MCFB tissue with micropores. Input quantities of the MTLT model are the apparent stiffness tensor $\boldsymbol{C}_{\text{MCFB}}$ of the MCFB, the microporosity $\text{vf}_{\text{mp}}^{\text{MTLT}}$, as well as the aspect ratio ar_{mp} and the apparent stiffness tensor $\boldsymbol{C}_{\text{mp}}$ of the pmma-filled micropores, see Section 6.2. That is, it holds that $\boldsymbol{C}_{\text{MTLT}} = f(\boldsymbol{C}_{\text{MCFB}}, \text{vf}_{\text{mp}}^{\text{MTLT}}, \text{ar}_{\text{mp}}, \boldsymbol{C}_{\text{mp}})$. We assume that none of the three parameters $\text{vf}_{\text{mp}}^{\text{MTLT}}$, ar_{mp} and $\boldsymbol{C}_{\text{mp}}$ is a function of the collagen Young's modulus, because such a dependence appears not to be physically meaningful. Moreover, we assume that f is Lipschitz continuous with respect to $\boldsymbol{C}_{\text{MCFB}}$ with some moderate Lipschitz constant; so that errors in $\boldsymbol{C}_{\text{MCFB}}$ do not increase uncontrollably during evaluation of f. Then, since the collagen Young's modulus has no significant influence on $\boldsymbol{C}_{\text{MCFB}}$, it also has no significant influence on $\boldsymbol{C}_{\text{MTLT}}$. Hence, we can fix the collagen Young's modulus to any arbitrary value between one and nine GPa. The corresponding model predictions will all be very similar.

Young's moduli for pmma reported in the literature do not differ as much as those of collagen. While previous measurements using nanoindentation and SAM reported values of 4.4 and 4.5 GPa, respectively, see Rupin et al. (2009), our SAM measurements on a pmma phantom revealed a slightly larger value of 4.96 GPa, which we used as the base value of the pmma Young's modulus.

Arguing similarly as for the Young's modulus of collagen, we find that the apparent stiffness tensor of MTLT tissue is insensitive to the Young's modulus of mineral and the Poisson's ratios of collagen, pmma

and mineral. Note therefore, that Reisinger et al. (2010) found that the apparent stiffness tensor of MCFB tissue is insensitive to these parameters.

6.5.2 Validation and efficiency of our model

Comparison of our model data with data of other researchers: The anisotropy ratios AR of $\boldsymbol{C}_{\mathrm{MTLT}}$ predicted by our multiscale model of the MTLT compare very well to our experimentally observed anisotropy ratios, see Table 6.4. Note therefore that the values differ about less than 10 %; our model predicts anisotropy ratios of AR $=$ 1.7–1.9 and AR $=$ 1.8–1.9 for CIR and INT tissue, respectively, and our experimental data indicates an anisotropy ratio of AR $=$ 2.0 and AR $=$ 1.8 for CIR and INT tissue, respectively. Not surprisingly, our predicted anisotropy ratios AR do not compare that well to the experimental anisotropy ratios found by Spiesz et al. (2012a) (difference between 11 and 17 %). This can be traced back to the problem already mentioned in the introduction, i.e. that different measurement techniques were employed by Spiesz et al. (2012a) and our project partners. Finally, it is worth to note that we predict, as proposed in the introduction, anisotropy ratios AR for the MTLT which are significantly larger than those of MCFB tissue. Compare therefore our anisotropy ratios AR with those found for MCFB tissue by Hellmich et al. (2004) (AR $=$ 1.3–1.4) and Reisinger et al. (2010) (AR $=$ 1.4–1.8) in Table 6.4. We think two reasons contribute to these higher ratios. Firstly, we have included the microporosity in our model of MTLT tissue. Note therefore that Hellmich et al. (2004) represented the ES, the MCF, and the MCFB employing similar homogenization methods as we have used. However, these authors did not include the microporosity in their model and the resulting anisotropy ratios AR were small. Secondly, we used the self-consistent rather than the Mori-Tanaka method to predict the elastic properties of the MCF and the ES. In order to support the last decision, we compared our MTLT model (self-consistent method for $\mathcal{S}_{\mathrm{MCF}}$) with two other models, denoted (M1) and (M2) in the following. Both models are build up similarly as our MTLT model, however, employ another homogenization method for the submodel $\mathcal{S}_{\mathrm{MCF}}$: model (M1) uses the Mori-Tanaka method and model (M2) uses the AHF method. We observed that the anisotropy ratios AR predicted by our model, in comparison with those of the models (M1) and (M2), agree best with our experimental anisotropy ratios. The anisotropy ratios predicted by models (M1) and (M2) are significantly too small and too large, respectively.

The axial and transverse stiffness values predicted by our MTLT model can be seen as the upper and lower bound, respectively, for the stiffness values of any MMT. In other words, MMTs with a multidirectional fibril orientation, such as lamellar bone or osteonal tissue, should have stiffness values which fall within these bounds. Indeed, this is true for site-matched mineralization and stiffness data from various tissues such as human femur, osteonal tissue from human radius, mice bone (data compiled from Raum et al. (2006a, 2007); Reisinger et al. (2010); Rohrbach et al. (2012); Spiesz et al. (2012b), see Table 6.4 and Fig. 6.8). However, very old osteonal, i.e. interstitial, tissue from human radius samples has stiffness values which are significantly above the predicted upper bound according to our MTLT model. One hypothesis that may explain this observation is that during aging of the tissue more and more mineral crystals fuse and form larger structures. As a consequence the flexibility of the cross-linked collagen matrix is lost and the tissue gets stiffer, but eventually also more brittle. Our MTLT model did not take into account such an agglomeration process. We note that with the homogenization methods employed in this study it is not even possible to model such a process. However, using RVE-based homogenization techniques an improved and more flexible model of the MCF and hence of the MTLT can be developed. This would then allow to test the above hypothesis.

Discriminating criteria between CIR and INT tissue: Here, we discuss the following discriminating criteria between CIR and INT tissue: the microporosity $\mathrm{vf}_{\mathrm{mp}}^{\mathrm{MTLT}}$, the diameter of the MCFB, and the mineral distribution parameter α_{MCF}.

In our model we distinguished between CIR and INT tissue by the microporosity. Thereby we were able to explain our experimental data to a large amount. However, another discriminating criterion of CIR

Table 6.4.: Comparison of experimental (exp.) and model stiffness values as well as of anisotropy ratios $\mathrm{AR} = C_{\mathrm{axi}}/C_{\mathrm{trv}}$ for various tissues from this study and from selected references.

MMT type	Origin	Mineral volume fraction	C_{axi} [GPa]	C_{trv} [GPa]	AR	References
CIR exp.	MTLT	0.3 ± 0.05	26.16 ± 3.97	13.16 ± 1.43	≈ 2.0	This study[a]
INT exp.	MTLT	0.3 ± 0.05	23.39 ± 3.72	13.16 ± 1.43	≈ 1.8	This study[a]
MTLT CIR model	–	$0.2 - 0.5$	$19 - 54$	$11 - 29$	$1.7 - 1.9$	This study, base values, $\mathrm{ar}_{\mathrm{ha}} = 7$
MTLT INT model	–	$0.2 - 0.5$	$18 - 49$	$10 - 26$	$1.8 - 1.9$	This study, base values, $\mathrm{ar}_{\mathrm{ha}} = 7$
MCFB tissue model	–	$0.15 - 0.45$	$12.5 - 40$	$9 - 22.5$	$1.4 - 1.8$	Reisinger et al. (2010)
MCFB tissue model (Concept III)	–	$0.31 - 0.55$	$12 - 52$	$9 - 37$	$1.3 - 1.4$	Hellmich et al. (2004)
CIR tissue	MTLT, dry	0.18	17.42	10.34	1.7	Spiesz et al. (2012b)[b]
CIR tissue	MTLT, wet	0.16	16.16	10	1.6	Spiesz et al. (2012b)[b]
INT tissue	MTLT, dry	0.16	15.42	9.9	1.6	Spiesz et al. (2012b)[b]
INT tissue	MTLT, wet	0.15	14.9	9.7	1.5	Spiesz et al. (2012b)[b]
Osteonal tissue exp.	Human radius	0.355 ± 0.025	28.4 ± 8.3	–	–	Raum et al. (2006a)[c]
Interstitial tissue exp.	Human radius	0.385 ± 0.015	45.6 ± 10.1	–	–	Raum et al. (2006a)[c]
Cortical bone	Human femur	0.37 ± 0.01	33.0 ± 3.0	23.7 ± 1.94	≈ 1.4	Rohrbach et al. (2012)[c]
Cortical bone	B6 mice, femur	0.43 ± 0.01	–	21.7 ± 2.4	–	Raum et al. (2007)[c]
Cortical bone	C3H mice, femur	0.44 ± 0.003	–	30.1 ± 2.6	–	Raum et al. (2007)[c]

For experimental data, we give the mean and the standard deviation of the mineral volume fraction, C_{axi} and C_{trv}. For model data, we give the range of values of the mineral volume fraction, C_{axi} and C_{trv}.
[a] Experimental acoustic impedance is converted to stiffness according to Eq. (6.1) using an approximated density ρ_{MTLT};
[b] the given average indentation modulus, E^{ind}, was converted to stiffness using our model at the base values, i.e., we give in the table the components C_{axi} and C_{trv} of $\boldsymbol{C}(\mathrm{vf}_{\mathrm{ha}})$ where $\mathrm{vf}_{\mathrm{ha}}$ is such that our model returns a Young's modulus $E(\boldsymbol{C}(\mathrm{vf}_{\mathrm{ha}}))$ closest to E^{ind};
[c] DMB converted to mineral volume fraction using Eq. (6.4).

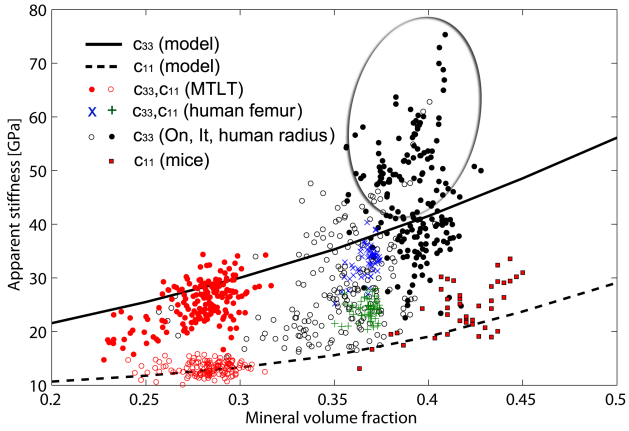

Figure 6.8.: Site-matched mineralization and stiffness data from various tissues and specimen: MTLT data (this study), human femur (Rohrbach et al., 2012), human radius (Raum et al., 2006a) and mice (Raum et al., 2007). The lines show the upper and lower stiffness bounds predicted by our MTLT model. Experimental properties indicated with crosses were measured using 50-MHz SAM. All other elastic values were derived from 200-MHz SAM measurements. The values for osteonal (On) and interstitial (It) are average values.

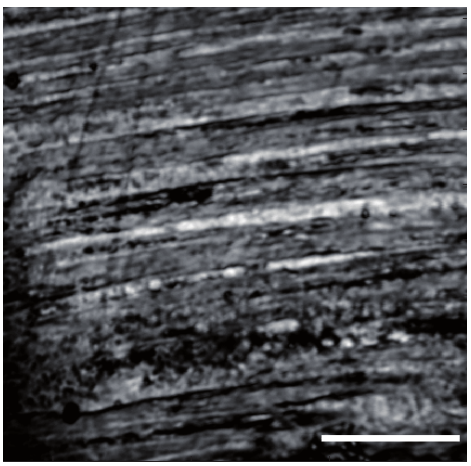

Figure 6.9.: An image of a typical longitudinal cross section of an MTLT sample obtained using 900-MHz SAM. Bar is 50 μm.

and INT tissue was visible in the SAM images, the MCFB diameter. The present model cannot account for the MCFB diameter, since the employed homogenization methods are based on volume fractions. In order to investigate the influence of the MCFB diameter on the elastic properties of the CIR and INT tissue, a promising approach is to develop a finite element model of these tissues and to use RVE-based homogenization to predict their elastic properties (Grimal et al., 2011; Raum et al., 2011).

Experimentally, we distinguished between CIR and INT tissue regions based on the diameter of the MCFBs. The detection of CIR and INT tissue regions worked well in transverse cross sections of the samples, but was hard to perform in longitudinal cross sections, see Fig. 6.9 for a typical image of a longitudinal cross section obtained by 900-MHz SAM. In the latter case, the two main distinctive criteria of CIR and INT tissue, the microporosity and the diameter of the MCFBs, could not be determined reliably. In particular, the MCFB diameter could not be assessed, because longitudinal cross sections of the MTLT tissue do not in general cut through the middle of MCFBs. Hence the depicted thickness of these bundles typically underestimates the actual MCFB diameter. Another problem with longitudinal cross sections was caused by the SAM measurements itself. When examining tissue which is inhomogeneous in the beam direction, the reflections of the ultrasound waves cannot be distinguished appropriately, and hence, the resulting acoustic impedances do not necessarily represent the tissues' elastic properties. This problem particularly arises when assessing MTLT tissue in transverse direction because, due to the change of thickness from center to edge of longitudinal cuts of MCFBs, the tissue is inhomogeneous in the beam direction. As a results the experimentally derived transverse acoustic impedance values are less reliable than the experimentally derived axial acoustic impedance values.

As a consequence of the two problems discussed in the former paragraph, the experimental acoustic impedance values derived from longitudinal cross sections, i.e., the transverse acoustic impedances, were not assigned a particular tissue type, but referred to as CIR/INT tissue. We cannot quantify directly the impact of this shortcoming for the transverse acoustic impedances on the validation of the model. However, this can be done for the axial acoustic impedances. To this end we combine all CIR and INT regions of interest from transverse cross sections and compute for this combined data set the error indicator $\mathrm{rRMSE}^{T}_{\mathrm{axi}}$ for $T = \mathrm{CIR}$ and $T = \mathrm{INT}$. The values increase from 0.06, cf. Table 6.2, scenarios (MD1) and (MD2), to 0.07. From this, we conclude that even if we could distinguish between CIR and INT tissue in longitudinal cross sections, the model would still predict very reasonable acoustic impedance values.

Throughout this thesis we assumed that α_{MCF} is the same for CIR and INT tissue and, hence, considered α_{MCF} a non-discriminating parameter between CIR and INT tissue. However, the observation of Spiesz et al. (2012a), that α_{MCF} differ in CIR ($\alpha_{\mathrm{MCF}} = 0.7$) and INT ($\alpha_{\mathrm{MCF}} = 0.3$) tissue, motivates us to discuss the use of α_{MCF} as a discriminating parameter. Up to now, to the knowledge of the author, no experimental studies on the above topic have been performed. In order to shed more light on this topic, one possibility is to set up, analogously to Spiesz et al. (2012a), an inverse problem based on our MTLT model and our experimental data. To this end, one fixes all free parameters of the model to their base values and search for each tissue type (CIR and INT) for that value of α_{MCF}, for which the model output compares best to our experimental data.

Limitations of the experimental dataset: So far, we compared our model predictions with our experimental results and results of different researchers. Now, we discuss limitations of our experimental data. We describe what an ideal experimental dataset should include to improve model validation. We would like to have

- the acoustic impedance of MTLT (CIR and INT) tissue in all possible directions,
- local values of the microporosity which are site-matched with the DMB,
- an empirical relationship between the volume fractions of the constituents adapted to our tissue type.

MTLTs have most likely transverse isotropic elastic properties and, thus, the material has five independent elastic constants. In Section 6.4 we compared the normal elastic properties, more precisely, the axial elastic properties (parallel to the long axis of the tendon) and the transverse elastic properties (perpendicular to the long axis of the tendon) with experimental data. We found that the elastic properties in these directions agree very well to our experimental data (relative error is about 0.08). Still outstanding, is a validation of the shear acoustic impedances. Experimental data found in the literature, usually describe only the normal elastic properties. Not much is known on the elastic properties in other directions than these. This is because, at present, experimental methods, such as SAM or nanoindentation, cannot determine shear elastic properties. Moreover, experimental methods such as the resonance ultrasound (Li and Gladden, 2010), which in general could determine the overall elastic properties of a sample, cannot be applied, because of the small sample size we look at.

Based on local microporosity data site-matched with the DMB, we can improve the derivation of $\mathrm{vf}_{\mathrm{ha}}^{\mathrm{MCFB}}$ from the experimental DMB data (Eqs. (6.4) and (6.5)). This derivation, in particular, hinges on the experimentally derived microporosity $\widetilde{\mathrm{vf}}_{\mathrm{mp}}$ in Eq. (6.5). We assumed that $\widetilde{\mathrm{vf}}_{\mathrm{mp}}$ is constant throughout the sample, and employed a fixed average value of $\widetilde{\mathrm{vf}}_{\mathrm{mp}} = 0.1$. However, this assumption was a simplification since, usually, $\widetilde{\mathrm{vf}}_{\mathrm{mp}}$ varies spatially.

Furthermore, local microporosity data site-matched with the DMB, could help to improve the relationship between the micro porosity $\mathrm{vf}_{\mathrm{mp}}^{\mathrm{MTLT}}$ and the mineral volume fraction $\mathrm{vf}_{\mathrm{ha}}^{\mathrm{MCFB}}$, see Section 6.2.5. Until now, we assumed that either $\mathrm{vf}_{\mathrm{mp}}^{\mathrm{MTLT}}$ and $\mathrm{vf}_{\mathrm{ha}}^{\mathrm{MCFB}}$ depend linearly on each other or that $\mathrm{vf}_{\mathrm{mp}}^{\mathrm{MTLT}}$ is independent of $\mathrm{vf}_{\mathrm{ha}}^{\mathrm{MCFB}}$. Based on local microporosity data site-matched with the DMB, we can derive an experimental relationship between $\mathrm{vf}_{\mathrm{mp}}^{\mathrm{MTLT}}$ and $\mathrm{vf}_{\mathrm{ha}}^{\mathrm{MCFB}}$. This relationship might be more realistic.

In Section 6.2.5 we derived the phase volume fractions for our model based on an empirical relation $\mathrm{vf}_{\mathrm{col}}^{\mathrm{MCFB}} = h(\mathrm{vf}_{\mathrm{ha}}^{\mathrm{MCFB}})$, cf. Raum et al. (2006a, Eq. (10), p. 750), suitable for human cortical bone. Since the basic constituents of MTLT tissue and cortical bone are similar, and due to a lack of similar relationships for MTLT tissue, we have used this relationship for MTLT tissue. However, it remains to show that this relationship is really suitable for MTLT tissue.

Computational aspects of our model: Finally, we discuss the computation time, our choice of homogenization methods for different submodels and our choice of starting values for the nonlinear system of the self-consistent method.

The computational effort of our MTLT model is larger than that of the MCFB models of Reisinger et al. (2010) and Hellmich et al. (2004), and the MTLT model of Spiesz et al. (2012a). Assuming that we compute the apparent stiffness tensor for each submodel using the default tool tolerances (see Section 5.2), our MTLT model needs, on average, about 514 seconds to derive the apparent stiffness tensor of MTLT tissue. Thereby, our model is about the factor 34, 1.01 and 26 slower than the Reisinger, the Hellmich and the Spiesz model, respectively; see Table 6.5 for the absolute values of the computation time. Despite the higher computation time of our model, our results, discussed in detail above and presented in the Sections 6.3 and 6.4, show that it is worth to invest such an effort.

As mentioned before, we decided against using the RVE-based homogenization method or the AHA method in our MTLT model. This was because the detailed fine-scale structure of several subtissues is unknown or only partly known. For instance, for the MCF and the ES the distribution of the mineral platelets, the collagen molecules or the nanopores is not completely known. Furthermore, for MTLT tissue the shape and the distribution of the micropores is unknown. Nevertheless, there are some researchers which employ the RVE-based homogenization method or the AHA method for different types of MMTs. For instance, Vercher et al. (2014) developed a model of the MCF and lamellar bone based on the AHA method. In order to investigate how much the detailed fine-scale structure of the MCF (local distribution of the minerals or the collagen molecules) influences the apparent stiffness tensor of the MCF, a comparison of our model predictions ($\mathcal{S}_{\mathrm{MCF}}$) with the results of Vercher et al. (2014) would be desirable. Unfortunately, this is not possible because the stiffness tensors of the MCF predicted by

Table 6.5.: Computation time in seconds for our MTLT model, the MCFB models of Reisinger et al. (2010) and Hellmich et al. (2004) and the MTLT model of Spiesz et al. (2012a). All models employ the Mori-Tanaka or the self-consistent method. In column two and three of this table, we note for which tissue type (MCF, ES, MCFB, MTLT (CIR,INT)) these methods were employed.

Model	Self-consistent method	Mori-Tanaka method	Total computation time (seconds)
This study	MCF, ES	MCFB, MTLT (CIR, INT)	514
Reisinger et al. (2010)	–	MCF, ES, MCFB	15
Hellmich et al. (2004)	MCF, ES	MCFB	509
Spiesz et al. (2012a)	–	MCF, ES, MCFB, MTLT (CIR, INT)	20

The total computation time was derived using the default tool parameters, i.e. $\text{tol}_{\text{int}} = 10^{-4}$ for the Mori-Tanaka method and $\text{tol}_{\text{int}} = 10^{-6}$ and $\text{tol}_{\text{nls}} = 10^{-5}$ for the self-consistent method; see Section 5.2. Employing these tool parameters, the computation of the apparent stiffness tensor using the Mori-Tanaka or the self-consistent method, respectively, lasts about 5 or 252 seconds; see Table 5.4.

Vercher et al. (2014) are given in terms of a quantity (the volume fraction of platelet reinforcement), which we cannot convert to our model variable (the mineral volume fraction).

Section 5.4 has shown that the computation time of $\boldsymbol{C}_{\text{MCF}}$ (or the number of iterations of Algorithm 4.2.1) using the self-consistent method depends on the starting value for the nonlinear system. We found that the best strategy, i.e. the strategy which yields the smallest number of iterations, is to choose a starting values based on a previously computed apparent stiffness tensors (strategy C). We adapted this strategy to our multiscale model of the MTLT and, thus, propose starting values using strategy C when computing $\boldsymbol{C}_{\text{ES}}$ and $\boldsymbol{C}_{\text{MCF}}$ (self-consistent method). This decreased our computation time by about 11 %.

6.6 Conclusions

Our model predicts the apparent stiffness tensor of CIR and INT tissue at the tissue scale, taking into account the composition, the elastic properties and the microstructure of the tissue at the micrometer and the nanometer scale. The model's variables and parameters are the volume fraction of the mineral and the microporosity (variables), the shape and the distribution (intra- versus interfibrillar) of the mineral platelets as well as the elastic properties of the basic constituents of CIR and INT tissue (water/pmma, collagen and mineral). Any input data for the submodels in the hierarchy was taken from the output of a finer scale submodel, from experiment or from literature.

We found that the axial and the transverse components of the apparent stiffness tensor of CIR and INT tissue were influenced mostly by the model parameters. Other stiffness components were only slightly influenced or not at all. The essential parameters determining the axial and the transverse stiffnesses were the mineral volume fraction of the MCFB, the microporosity, the ratio of MCF mineral to total mineral, and the aspect ratio of the mineral inclusion.

We have shown that increasing the mineral volume fraction reinforces the apparent stiffness of CIR and INT tissue. Moreover, increasing the microporosity reduces the apparent stiffness. Assuming that the microporosity depends linearly on the mineral volume fraction, we significantly improved our model acoustic impedance values predicted in axial direction. Looking at the influence of the inclusion shape, we have seen that increasing the mineral aspect ratio also reinforces MTLT tissue. Other aspect ratios only influence the MTLT to a small amount or not at all. Their values can be chosen more or less arbitrary in the range considered without consequences. Our observations were derived based on a global sensitivity analysis and thus are valid globally, i.e., over the whole parameter space. This is in contrast to the parametric studies performed, for instance, by Reisinger et al. (2010), where the influence is valid only locally.

The model and the experimental elastic properties agree very well (relative errors of 6-8%) for both tissue types and measurement directions.

In order to further extend our knowledge on the essential features influencing the apparent stiffness of CIR and INT tissue, more experimental data and further investigation of the distribution of the minerals in the MCFB, is needed. In the future, our established model or parts of it can be used to setup more complex MMT models, such as for lamellar bone, primary or secondary osteonal tissue. For model validation, the combination of SAM and SR-μCT can be used to assess experimentally tissue mineralization and elastic properties.

7 Modelling and simulation of the osteon

Osteons are the basic structural unit of cortical bone. They are cylindrically shaped and comprise a central cylinder, the so-called Haversian canal (HC), and approximately circular lamellae surrounding this canal, see Fig. 7.1. The Haversian canal contains the blood vessel of the osteon. Each circular lamella consists of several sublamellae made up of unidirectionally-aligned MCFBs. Usually, the osteon does not appear alone, but is embedded, together with other osteons, in some material. This embedding material may consist of woven/plexi-form bone or osteonal tissue, when considering primary osteonal tissue or secondary osteonal tissue, respectively. For instance, the osteon visible in Fig. 7.1 is embedded in osteonal tissue.

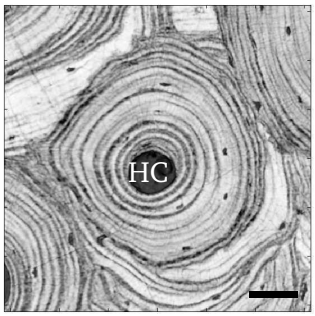

Figure 7.1.: 200-MHz SAM image of an osteon embedded in osteonal tissue. Haversian canal is indicated. Bar is $50\,\mu$m.

The major determinants of the osteon's elastic properties at the tissue scale ($\sim 100\,\mu$m) are still poorly understood. Martin and Ishida (1989) found that the elastic properties of cortical bone are highly influenced by the orientation of the MCFBs, followed by the density, the Haversian porosity (ratio of the volumes of the Haversian canal and the osteon) and the mineralization. Recently, various experimental and modeling studies (Varga et al., 2013; Hamed et al., 2010; Vercher et al., 2014; Reisinger et al., 2011; Raum et al., 2010; Yoon and Cowin, 2008; Vaughan et al., 2012) aimed to clarify the orientation pattern of the MCFBs within a circular lamella. All authors agree that the osteon consists of repeating circular lamellar units (cLUs). One cLU is considered a unit of N circular sublamellae sl_i of different thickness. The orientation of the MCFBs in the sublamella closest to the Haversian canal is referred to as starting angle. The orientation of the MCFBs changes from sublamella sl_{i-1} to sublamella sl_i about the twist angle $\theta_{i-1,i}$ for $i = 2,\ldots,N$. The values of the twist angles $\theta_{i-1,i}$, as well as the thicknesses of the individual sublamellae are still under discussion.

In order to study the influence of the cLU on the tissue-scale elastic properties of the osteon, we develop a model of the osteon. Recently, various cLU types were proposed. Raum et al. (2010) and others (Hamed et al., 2010; Vercher et al., 2014; Reisinger et al., 2011) studied *regular and asymmetric twisted plywood*. In particular, Raum et al. (2010) assumed that each cLU of these cLU types is composed of six sublamellae, where the twist angles are constant and given by $\theta_{i-1,i} = 30^\circ$. They referred to it as regular twisted plywood, if each sublamella has the same thickness, and as asymmetric twisted plywood otherwise. *Orthogonal plywood tissue* was modeled by Raum et al. (2010); Yoon and Cowin (2008); Reisinger et al. (2011). For these cLU types the cLU consists of two equally sized sublamellae with twist angle $\theta_{1,2} = 90^\circ$. *Longitudinal* cLUs , studied by Yoon and Cowin (2008); Vaughan et al. (2012), are composed of a single sublamella, in which all MCFBs are aligned parallel to the osteon's long axis. In contrast to longitudinal cLUs, *transverse* cLUs (Yoon and Cowin, 2008; Vaughan et al., 2012) consist only of MCFBs which are circumferentially aligned perpendicular to the osteon's long axis. Finally, there was introduced the *helicoidal twisted plywood* tissue, which is made up of MCFBs whose orientation changes continuously (Wagermaier et al., 2006).

Usually, studies on the modeling and simulation of the elastic properties of osteons neither call into question their choice of homogenization method nor its tool parameters. Precisely, here we take further action. On one hand, we validate the suitability of our numerical approximation of the apparent stiffness tensor. On the other hand we study how our model predictions depend on the choice of the homogenization methods and corresponding tool parameters. Besides this, we also address the two important

aims, pursued by most of the studies in the literature: we analyze the influence of model parameters on our model output and we compare our result to existing (experimental) and literature data.

We address the following tasks:

- Develop a multiscale model to predict apparent elastic properties of the osteon at the tissue scale. The model, its parameters and its variables are presented in Section 7.1.
- Conduct a numerical convergence analysis of the employed homogenization method. Compare the model predictions when using different homogenization methods. The results are presented in Sections 7.2 and 7.3.
- Perform a parametric study of our model and identify the most crucial parameters influencing the apparent stiffness of the osteon. Compare the apparent stiffness of the osteon for different cLU types with existing data in the literature. These studies together with their results are described in Section 7.4.
- Compare the model predictions with experimental data from other researchers and discuss our findings with respect to all our research questions, see Section 7.5.
- Finally, in Section 7.6 we draw conclusions.

7.1 Model of the osteon

We now set up a model for the osteon. In Section 7.1.1 we present the structural organization of the osteon, and explain which homogenization methods were used to obtain the apparent stiffness of the osteon at the tissue scale, denoted $\boldsymbol{C}_{\mathrm{Os}}$ in the following. For a visualization of our model, see Fig. 7.2. Finally, in Section 7.1.2 we discuss how to derive all model parameters from experimental or literature data.

7.1.1 Description of the model

We consider a three-dimensional Cartesian coordinate system with coordinates denoted x_i, where $i = 1, 2, 3$, and let the coordinate x_3 be aligned with the long axis of the osteon, see Fig. 7.2.

Our model realizes a simplified representation of the real osteon. We represent

- the Haversian canal,
- several cLUs,
- the embedding box (EB) in which the osteon is fully contained.

Each of these parts occupies the disjoint domains Ω_{HC}, Ω_{cLU} and Ω_{EB}, respectively. The total domain, occupied by the osteon and its surrounding, is denoted $\Omega = \Omega_{\mathrm{HC}} \cup \Omega_{\mathrm{cLU}} \cup \Omega_{\mathrm{EB}}$. In our model we do not represent fine-scale structures such as lacunae, canaliculi or the cement line of an osteon. These structures are highly complex and their description is beyond the scope of this thesis.

We assume that the osteon is a circular cylinder of radius r_{Os} and height h_{Os}. Central within the osteon there is the Haversian canal, a circular cylinder of radius r_{HC} and height $h_{\mathrm{HC}} = h_{\mathrm{Os}}$. A number of n_{cLU} cLUs, each of thickness τ_{cLU} and height h_{Os}, surround the Haversian canal. One single cLU consists of N sublamellae sl_i, in each of which the orientation of the MCFBs is constant. Assuming that sublamella sl_i has thickness τ_i, the total thickness of a cLU, i.e τ_{cLU}, reads

$$\tau_{\mathrm{cLU}} = \sum_{i=1}^{N} \tau_i. \tag{7.1}$$

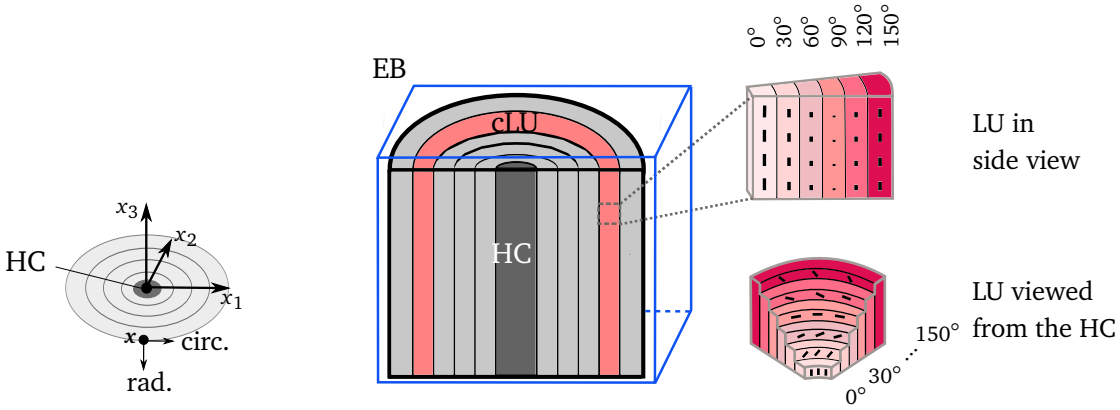

Figure 7.2.: Model of the osteon. We show the Haversian canal (HC), a nearly block-shaped lamellar unit (LU) in side view and viewed from the Haversian canal, the circular lamellar unit (cLU) and the embedding box (EB). Bars in the LU indicate the MCFBs; degree numbers next to the LU indicate the orientation of the MCFBs within the sublamellae (angle γ). Additionally, we display the Cartesian coordinate system with coordinates x_1, x_2 and x_3 and define what we call circumferential (circ.) and radial (rad.) direction.

In summary, the radius of the osteon becomes

$$r_{\mathrm{Os}} = r_{\mathrm{HC}} + n_{\mathrm{cLU}}\,\tau_{\mathrm{cLU}}. \tag{7.2}$$

Locally, each cLU has a nearly block-shaped form because $\tau_{\mathrm{cLU}} < r_{\mathrm{HC}}$. Such a block-shaped cLU is called simply LU in the following. We consider the LU a small rectangular box of size $\widetilde{l}_1 \times \widetilde{l}_2 \times \widetilde{l}_3$, which is aligned with the x_1, the x_2 and the x_3-axis. Except for in x_2 direction, the LU is made up similar as the cLU, i.e. it consists of N sublamellae and has the same total thickness ($\widetilde{l}_1 = \tau_{\mathrm{cLU}}$), the same sublamellae thickness and the same height ($\widetilde{l}_3 = h_{\mathrm{Os}}$) as the cLU.

The orientation of the MCFBs within the cLUs is characterized by two angles, β and γ, where $0 \le \beta \le 360^\circ$ and $0 \le \gamma \le 180^\circ$. Consider some point $\boldsymbol{x} \in \Omega_{\mathrm{cLU}}$ and the plane defined by the radial and the x_3-axis in $\boldsymbol{x}$, see Fig. 7.2 for a visualization of the different axes. Then, an MCFB at $\boldsymbol{x}$ is rotated around radial direction by an angle $\gamma(\boldsymbol{x})$ out of this plane. Since the orientation of the MCFBs within each sublamella sl_i is the same, the angle γ is constant in each sublamella sl_i, i.e. $\gamma = \gamma_i$ with constant $\gamma_i \in [0^\circ, \ldots, 180^\circ]$. The angle $\beta(\boldsymbol{x})$ is defined as the angle between the x_1-axis and the radial direction. Based on the angle γ_i, we define the twist angle $\theta_{i-1,i}$, introduced in the introduction, by $\theta_{i-1,i} := \gamma_i - \gamma_{i-1}$, where $i = 2, \ldots, N$. Finally, we note that we set the starting angle to zero.

The embedding box is assumed to be brick-shaped and to have the size $L_1 \times L_2 \times L_3$. The osteon is fully contained in the box and does not touch the boundary.

Mechanically, the osteon is characterized by its local stiffness tensor $\boldsymbol{C}$. We assume that $\boldsymbol{C}$ is homogeneous in x_3 direction, and consider the three parts of the osteon, i.e. the Haversian canal, several cLUs and the embedding box, to have distinct elastic properties. We define

$$\boldsymbol{C}(\boldsymbol{x}) = \begin{cases} \boldsymbol{C}_{\mathrm{HC}}, & \boldsymbol{x} \in \Omega_{\mathrm{HC}}, \\ \boldsymbol{C}_{\mathrm{cLU}}(\boldsymbol{x}), & \boldsymbol{x} \in \Omega_{\mathrm{cLU}}, \\ \boldsymbol{C}_{\mathrm{EB}}, & \boldsymbol{x} \in \Omega_{\mathrm{EB}}, \end{cases} \tag{7.3}$$

where $\boldsymbol{C}_{\mathrm{HC}}$ is homogeneous and isotropic, $\boldsymbol{C}_{\mathrm{cLU}}(\boldsymbol{x})$ is heterogeneous, and $\boldsymbol{C}_{\mathrm{EB}}$ is homogeneous and anisotropic. We determine the stiffness tensor $\boldsymbol{C}_{\mathrm{cLU}}(\boldsymbol{x})$ based on the angle β and the apparent stiffness tensor of the LU, denoted $\boldsymbol{C}_{\mathrm{LU}}$. The stiffness $\boldsymbol{C}_{\mathrm{cLU}}$ reads

$$\boldsymbol{C}_{\mathrm{cLU}}(\boldsymbol{x}) = \boldsymbol{C}_{\mathrm{LU}}(\beta(\boldsymbol{x})), \quad \text{for} \quad 0 \le \beta(\boldsymbol{x}) \le 360^\circ, \tag{7.4}$$

where $\boldsymbol{C}_{\mathrm{LU}}(\beta(\boldsymbol{x}))$ denotes the rotation of $\boldsymbol{C}_{\mathrm{LU}}$ about the angle β in the x_1x_2-plane. By construction, we obtain a stiffness tensor $\boldsymbol{C}_{\mathrm{cLU}}$, which is homogeneous in the plane defined by the radial and the x_3-axis, while heterogeneous in any other direction. In order to derive an approximation to $\boldsymbol{C}_{\mathrm{LU}}$, we employ the LU model of Raum et al. (2010). For a given set of parameters, the authors computed the effective stiffness tensor of the LU using the RVE-based homogenization method with displacement boundary conditions. We assume that, in the $x_1\,x_3$-plane, the stiffness $\boldsymbol{C}_{\mathrm{cLU}}$ equals the effective stiffness $\boldsymbol{C}_{\mathrm{LU}}$.

For a given set of parameters of the osteon model, we compute the apparent stiffness $\boldsymbol{C}_{\mathrm{Os}}$ of the osteon using the self-consistent RVE-based homogenization method with displacement boundary conditions, i.e. we use Algorithm 4.1.2. Thereby, we decided against employing the AHF method or the Eshelby-based homogenization methods, because these techniques do not allow to realize the complex organization of the MCFBs within the cLU. Note therefore that these methods cannot represent a precise distribution of MCFBs within the cLU. Finally, we remark that, due to our choice of homogenization method, the stiffness $\boldsymbol{C}_{\mathrm{EB}}$ of the embedding box equals the stiffness of the effective material, that is the stiffness tensor of the osteon.

Tool parameters of Algorithm 4.1.2 are the mesh size h, the tolerance TOL and the starting value $\boldsymbol{C}^{(0)}$.

7.1.2 Derivation of model and tool parameters

We specify the model and the tool parameters, necessary to perform a simulation run of our osteon model. Analogously to the study of the MTLT model, we call model parameters which we vary *free parameters*. Other parameters than the free parameters were fixed to a base value. Our choice of parameters describing the fine-scale structure of the cLU and the LU are listed in Table 7.1; stiffness tensors of the various LUs are listed in Table 7.2. Our choice of base values and variation ranges for parameters of our osteon model are summarized in Table 7.3. Below, we briefly discuss how to derive all these values.

Structural parameters: Young and mature osteons have a Haversian canal with radius $r_{\mathrm{HC}} = 27\,\mu$m approximately, an average value reported in Raum et al. (2006b, page 740).

The thickness τ_{cLU} of a mature osteon was taken from Raum et al. (2011). These authors estimated τ_{cLU} from a 1.2-GHz SAM image of an osteon in femoral human cortical bone to be in average $\tau_{\mathrm{cLU}} = 6.9\ \mu$m.

The number of cLUs was set to the base value $n_{\mathrm{cLU}} = 10$, a value which was chosen based on an average value of cLUs visible in images of mature osteons in Raum et al. (2010, 2011). Values for n_{cLU} reported in the literature differ strongly, that is why we consider n_{cLU} a free parameter. It is known that n_{cLU} increases with the age of the osteon from 1 to larger values. Being interested in the elastic properties of the osteon as function of the age, we vary n_{cLU} between the extreme cases of a very young osteon ($n_{\mathrm{cLU}} = 1$) and a mature osteon ($n_{\mathrm{cLU}} = 10$). Note that with age also the mineralization changes, an aspect which we do not consider in our model.

Given r_{HC}, τ_{cLU} and n_{cLU} as specified before, we determine the radius r_{Os} of the osteon based on Eq. (7.2). Since n_{cLU} varies between 1 and 10, we obtain $r_{\mathrm{Os}} = 33.9\,\mu$m for $n_{\mathrm{cLU}} = 1$ to $r_{\mathrm{Os}} = 96\,\mu$m for $n_{\mathrm{cLU}} = 10$.

To the best of our knowledge, osteons (and thus also their Haversian canal because $h_{\mathrm{Os}} = h_{\mathrm{HC}}$) are substantially higher than their diameter of about $2\,r_{\mathrm{Os}} = 192\,\mu$m. However, the precise value of the osteon height h_{Os} is unknown. That is why, we consider h_{Os} a free parameter. Aiming for an osteon height as small as possible for computational reasons (usually the computation time is smaller with smaller h_{Os}), we vary h_{Os} in the large range between 8 and 256 μm. The base value of $h_{\mathrm{Os}} = 96\,\mu$m was chosen based on our parametric study, see Section 7.4.

We assume that the embedding box has the same width and length, i.e. we set $L_1 = L_2$. Since the osteon should be fully contained in the box and should not touch the boundary, we choose L_1 and L_3 slightly larger than the osteon. We set $L_1 = m_1 2\,r_{\mathrm{Os}}$ and $L_3 = m_2\,h_{\mathrm{Os}}$, where $m_1, m_2 > 1$. Note

Table 7.1.: Twist angle $\theta_{i-1,i}$, orientation of the MCFBs within the cLU, and sublamellae thickness τ_i of various cLU types. The stiffness tensors of these cLUs are given in Table 7.2. The starting angle is zero.

cLU type	Twist angle $\theta_{i-1,i}$ [deg.]	Orientation of MCFBs [deg.]	Sublamella thickness τ_i, $i = 1, \ldots, N$ [μm]
Regular twisted plywood	30	–	(1.15, 1.15, 1.15, 1.15, 1.15, 1.15)
Asymmetric twisted plywood	30	–	(2.95, 1.1, 0.35, 0.95, 0.35, 1.15)
Longitudinal	–	0	(6.9)
Transverse	–	90	(6.9)

Table 7.2.: Stiffness tensor $\boldsymbol{C}_{\text{MCFB}}$ of the MCFB (Raum et al., 2010), and stiffness components C_{ij} of $\boldsymbol{C}_{\text{LU}}$ [GPa] for different LU types; $\boldsymbol{C}_{\text{LU}}$ was computed using the LU model of Raum et al. (2010) with the model parameters as given in Table 7.1.

LU type	Symbol	C_{11}	C_{12}	C_{13}	C_{22}	C_{23}	C_{33}	C_{44}	C_{55}	C_{66}
Regular twisted plywood	$\boldsymbol{C}_{\text{LU}}^{\text{reg}}$	15.6	7.0	7.0	22.4	11.2	22.4	4.3	5.6	4.3
Asymmetric twisted plywood	$\boldsymbol{C}_{\text{LU}}^{\text{as}}$	15.6	6.3	7.8	19.4	10.3	26.9	4.6	4.8	3.9
Longitudinal	$\boldsymbol{C}_{\text{LU}}^{\text{axi}}$	15.6	5.2	8.9	15.6	8.9	33.9	3.4	3.4	5.2
Transverse	$\boldsymbol{C}_{\text{LU}}^{\text{trv}}$	15.6	8.9	5.2	33.9	8.9	15.6	3.4	5.2	3.4
Experimental-data derived	$\boldsymbol{C}_{\text{LU}}^{\text{exp}}$	21.6	9.8	10.3	21.6	10.3	29.5	4.6	4.6	5.9
MCFB	$\boldsymbol{C}_{\text{MCFB}}$	15.6	5.2	8.9	15.6	8.9	33.9	3.4	3.4	5.2

that the smaller the values of m_1 and m_2, the more our mesh size in the embedding box is restricted. Varying m_1 and m_2 between 1.1 and 1.5, we search in Section 7.4 for values of m_1 and m_2, which give results of sufficient accuracy with small computational effort. Suitable values found were $m_1 = 1.2$ and $m_2 = 1.25$, these we choose as base values in the following.

Elastic properties: Naturally, the Haversian canal is filled with blood. In view of that we will compare our model outcome with experimental data taken from Raum et al. (2011), who determined the elastic properties of osteonal tissue embedded in pmma, $\boldsymbol{C}_{\text{HC}}$ should match the elastic properties of pmma. Similarly as for the MTLT in Chapter 6, we assume that pmma is homogeneous and isotropic, and has the Young's modulus $E_{\text{HC}} = 4.96$ and the Poisson's ratio $\nu_{\text{HC}} = 0.37$.

The stiffness tensor $\boldsymbol{C}_{\text{cLU}} = \boldsymbol{C}_{\text{LU}}(\beta)$ was determined for various cLU types: (i) regular twisted plywood, (ii) asymmetric twisted plywood, (iii) longitudinal, and (iv) transverse. Parameters characterizing the fine-scale structure of these cLUs and corresponding stiffness tensors $\boldsymbol{C}_{\text{LU}}$, are presented in Tables 7.1 and 7.2. As base value for $\boldsymbol{C}_{\text{LU}}$ we select $\boldsymbol{C}_{\text{LU}}^{\text{exp}}$, a stiffness tensor taken from Raum et al. (2010), which was derived from 200-MHz SAM measurements on osteonal tissue of femoral human cortical bone. Stiffness tensors $\boldsymbol{C}_{\text{LU}}$ for cases (i) and (ii), denoted $\boldsymbol{C}_{\text{LU}}^{\text{reg}}$ and $\boldsymbol{C}_{\text{LU}}^{\text{as}}$, respectively, were determined based on the LU model of Raum et al. (2010). The use of the latter model incurs to specify the stiffness tensor $\boldsymbol{C}_{\text{MCFB}}$ for $\gamma = 0$ (all MCFBs are aligned parallel to the x_3-axis); we choose it as given in Table 7.2. For case (iii) we take $\boldsymbol{C}_{\text{LU}} = \boldsymbol{C}_{\text{MCFB}}$, since for a longitudinal LU all MCFBs are aligned in parallel with the osteon's long axis. Naturally, we select for case (vi) $\boldsymbol{C}_{\text{LU}} = \boldsymbol{C}_{\text{MCFB}}(90°)$, i.e. we rotate $\boldsymbol{C}_{\text{MCFB}}$ about 90 degrees.

Tool parameters: The mesh size h was set to a value found in the numerical convergence analysis in Section 7.2. The tolerance TOL for Algorithm 4.1.2 we fix to 10^{-2}. Finally, we select the starting value $\boldsymbol{C}^{(0)}$ as follows. We assume that $\boldsymbol{C}^{(0)}$ equals the result of the Voigt technique, more precisely, we use

$$\boldsymbol{C}^{(0)} = \text{vf}_{\text{HC}}\, \boldsymbol{C}_{\text{HC}} + (1 - \text{vf}_{\text{HC}})\, \boldsymbol{C}_{\text{LU}}, \tag{7.5}$$

Table 7.3.: List of input quantities of the osteon model. For each input quantity we display its symbol, unit, input type (free parameter (fp.), parameter (p.)), base value and the variation range. The stiffness components of $\boldsymbol{C}_{\mathrm{LU}}$ are given in Table 7.2.

Model input	Symbol	Unit	Type	Base value	Variation range
HC radius	r_{HC}	μm	p.	27	—
LU and cLU thickness	τ_{cLU}	μm	p.	6.9	—
Osteon radius	$r_{\mathrm{Os}} = r_{\mathrm{HC}} + n_{\mathrm{cLU}}\,\tau_{\mathrm{cLU}}$	μm	fp.	96 ($n_{\mathrm{cLU}} = 10$)	$n_{\mathrm{cLU}} = 1 - 10$
Osteon and HC height	$h_{\mathrm{Os}}, h_{\mathrm{HC}};\ (h_{\mathrm{Os}} = h_{\mathrm{HC}})$	μm	fp.	96	$8, 16, 32, \ldots, 256$
EB width, depth	$L_1 = L_2 = m_1\, 2\, r_{\mathrm{Os}}$	μm	fp.	230.4 ($m_1 = 1.2$)	$m_1 = 1.1$ — 1.5
EB height	$L_3 = m_2\, h_{\mathrm{Os}}$	μm	fp.	160 ($m_2 = 1.25$)	$m_2 = 1.1$ — 1.5
Young's modulus HC	E_{HC}	GPa	p.	4.96	—
Poisson's ratio HC	ν_{HC}	1	p.	0.37	—
Stiffness tensor of the LU	$\boldsymbol{C}_{\mathrm{LU}}$	GPa	fp.	$\boldsymbol{C}_{\mathrm{LU}}^{\mathrm{exp}}$	$\boldsymbol{C}_{\mathrm{LU}}^{\mathrm{reg}}, \boldsymbol{C}_{\mathrm{LU}}^{\mathrm{as}}, \boldsymbol{C}_{\mathrm{LU}}^{\mathrm{axi}}, \boldsymbol{C}_{\mathrm{LU}}^{\mathrm{trv}}$

where $\mathrm{vf}_{\mathrm{HC}} = r_{\mathrm{HC}}^2 / r_{\mathrm{Os}}^2$ is the volume fraction of the Haversian canal, see Table 7.3 for base values of r_{HC} and r_{Os}. The starting value (7.5) is cheap to derive and turns out to give small numbers of iterations of Algorithm 4.1.2. Computing $\boldsymbol{C}_{\mathrm{Os}} = \boldsymbol{C}_{\mathrm{Os}}(p_i)$ for some parameter p_i ($i = 1, 2 \ldots$), we decided to not conduct a strategy similar to strategy C performed in Section 5.4; recall that we compute $\boldsymbol{C}_{\mathrm{MCF}}(p_{i+1})$ using $\boldsymbol{C}_{\mathrm{MCF}}(p_i)$ as starting value. This was not an option because the computation of the osteon model lasts several hours and we usually run our osteon model for different parameter values in parallel.

7.2 Numerical convergence analysis

Given that the model parameters are fixed to their respective base values, we study the error in the displacement $\boldsymbol{u}$ and the apparent stiffness tensor $\boldsymbol{C}_{\mathrm{Os}}$ as the mesh size h decreases. Based on our results, we select a suitable value for h.

We use Lagrange elements of order one and two. Furthermore, we consider tetrahedral meshes on Ω, with the mesh size h varying from $22.5\,\mu$m down to $7.5\,\mu$m. For the displacement $\boldsymbol{u}$ we show convergence for the exemplary boundary value problem (3.36a) with displacement boundary conditions $\boldsymbol{u} = (2\boldsymbol{y}, 2\boldsymbol{x}, 0)^T$ on boundary Γ_V. The corresponding displacement $\boldsymbol{u}$, obtained when using the mesh size h, is denoted by $\boldsymbol{u}_h$. The apparent stiffness tensor of the osteon associated to mesh size h, more precisely, the result we obtain when using Algorithm 4.1.2 with the mesh size h and displacement boundary conditions with $\beta = 2$, is denoted by $\boldsymbol{C}_{\mathrm{Os}}^{(h)}$. As reference values to $\boldsymbol{u}_h$ and $\boldsymbol{C}_{\mathrm{Os}}^{(h)}$, we choose the results obtained when using $h_{\mathrm{ref}} = 5\,\mu$m. The latter are denoted $\boldsymbol{u}_{\mathrm{ref}}$ and $\boldsymbol{C}_{\mathrm{Os}}^{(\mathrm{ref})}$, respectively.

We first focus on the displacement $\boldsymbol{u}$. We quantify the error in $\boldsymbol{u}_h$ by the measure $\mathrm{aE}(\boldsymbol{u}_h)$, as defined by Eq. (4.8). This error is expected to converge of order as stated in Theorem 2.4.2. Thus, the convergence order should equal two and three for Lagrange elements of order one and two, respectively.

Figures (7.3a) and (7.3b) show the error $\mathrm{aE}(\boldsymbol{u}_h)$ versus the mesh size h for Lagrange elements of order one and two, respectively. We observe that the convergence order of $\mathrm{aE}(\boldsymbol{u}_h)$ met theoretical values.

We now consider the error in the apparent stiffness tensor $\boldsymbol{C}_{\mathrm{Os}}$ as the mesh size h decreases. Here, we quantify the error in $\boldsymbol{C}_{\mathrm{Os}}^{(h)}$ by the measure raE, defined by

$$\mathrm{raE}(\boldsymbol{C}_{\mathrm{Os}}^{(h)}) = \left\| \frac{\boldsymbol{C}_{\mathrm{Os}}^{(h)} - \boldsymbol{C}_{\mathrm{Os}}^{(\mathrm{ref})}}{1 + \max\{|\boldsymbol{C}_{\mathrm{Os}}^{(h)}|, |\boldsymbol{C}_{\mathrm{Os}}^{(\mathrm{ref})}|\}} \right\|, \tag{7.6}$$

where $\|\cdot\|$ refers to the Frobenius norm.

In Figures (7.3c) and (7.3d) we display $\mathrm{raE}(\boldsymbol{C}_{\mathrm{Os}}^{(h)})$ versus the mesh size h for Lagrange elements of order one and two, respectively. We observe a convergence order of one and two for Lagrange elements of order one and two, respectively.

(a) Displacement, Lagrange elements of order one

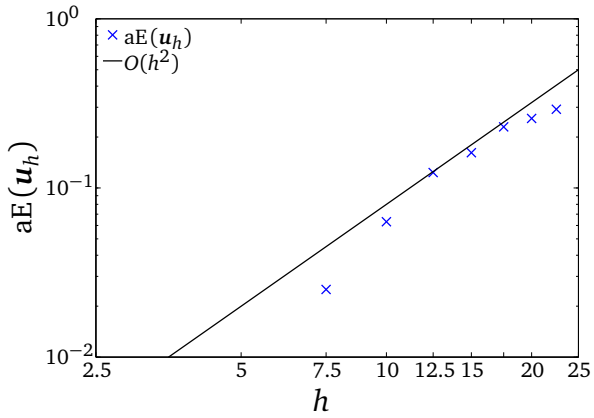

(b) Displacement, Lagrange elements of order two

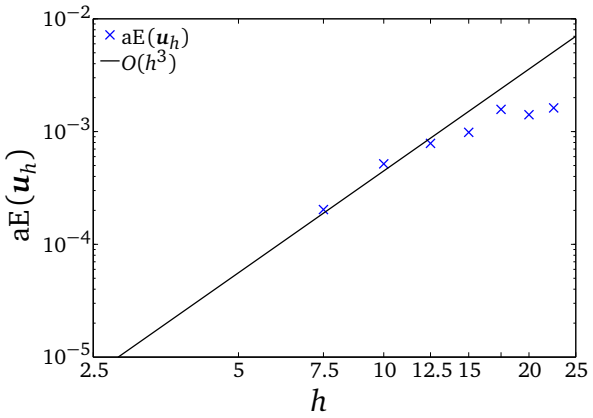

(c) Stiffness $\boldsymbol{C}_{\mathrm{Os}}$, Lagrange elements of order one

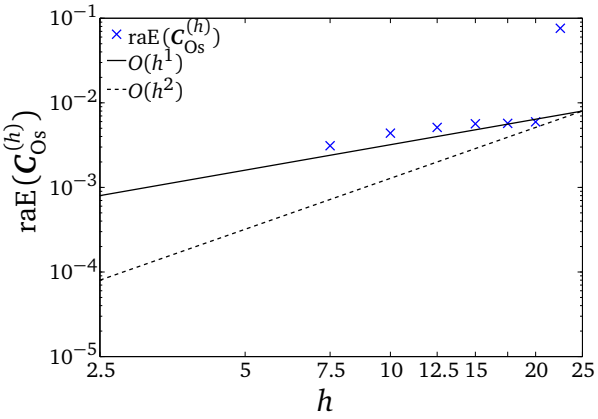

(d) Stiffness $\boldsymbol{C}_{\mathrm{Os}}$, Lagrange elements of order two

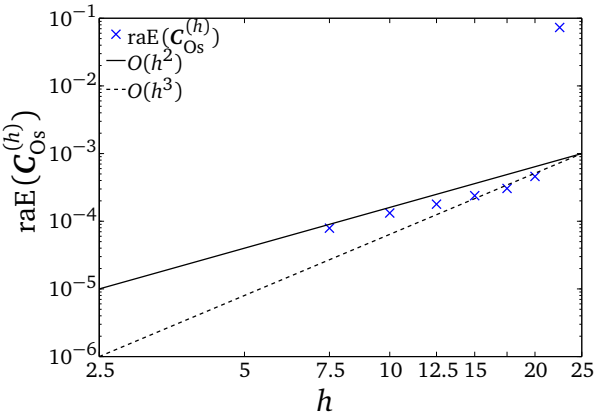

Figure 7.3.: Errors aE$(\boldsymbol{u}_h)$ and raE$(\boldsymbol{C}_{\mathrm{Os}}^{(h)})$ versus the mesh size h, both for Lagrange elements of order one and two. Lines corresponding to convergence order one, two and three are indicated by $O(h^1)$, $O(h^2)$ and $O(h^3)$, respectively.

In the following, we set the mesh size to $h = 10\,\mu$m. This value is a good compromise between accuracy and computational effort (in average the computation time of $\boldsymbol{C}_{\mathrm{Os}}$ is two hours). Furthermore, we will stick to Lagrange elements of order two. Note, therefore, that these Lagrange elements result in errors, aE$(\boldsymbol{u}_h)$ and raE$(\boldsymbol{C}_{\mathrm{Os}}^{(h)})$, which are about one to two orders smaller than the errors for Lagrange elements of order one, compare Figures 7.3a, 7.3b, 7.3c and 7.3d.

In conclusion of this section, we consider our approximate displacement $\boldsymbol{u}$ as well as the approximate apparent stiffness tensor $\boldsymbol{C}_{\mathrm{Os}}$ numerically reasonable.

7.3 Comparison of different homogenization methods

Given that the model parameters are fixed to their respective base values, we study whether the difference in the apparent stiffness $\boldsymbol{C}_{\mathrm{Os}}$ depends on our choice of homogenization method. To this end, we compare the predictions of the self-consistent RVE-based homogenization method with displacement boundary conditions ($\boldsymbol{C}_{\mathrm{Os}}^{(\mathrm{sd})}$), the self-consistent RVE-based homogenization method with traction boundary condition ($\boldsymbol{C}_{\mathrm{Os}}^{(\mathrm{st})}$) and the self-consistent AHA method ($\boldsymbol{C}_{\mathrm{Os}}^{(\mathrm{sAHA})}$) with each other. Tool parameters of the latter two homogenization methods were fixed as for the first homogenization method, see Section 7.1.2 for details.

According to the theory (Section 3.7) we expect

$$\boldsymbol{C}_{\mathrm{Os}}^{(\mathrm{st})} \leq \boldsymbol{C}_{\mathrm{Os}}^{(\mathrm{sAHA})} \leq \boldsymbol{C}_{\mathrm{Os}}^{(\mathrm{sd})}. \tag{7.7}$$

Define the *difference tensors*

$$\boldsymbol{D}(\boldsymbol{C}_{\mathrm{Os}}^{(1)}, \boldsymbol{C}_{\mathrm{Os}}^{(2)}) := \boldsymbol{C}_{\mathrm{Os}}^{(1)} - \boldsymbol{C}_{\mathrm{Os}}^{(2)}, \tag{7.8}$$

where $\boldsymbol{C}_{\mathrm{Os}}^{(1)}, \boldsymbol{C}_{\mathrm{Os}}^{(2)} \in \{\boldsymbol{C}_{\mathrm{Os}}^{(\mathrm{sAHA})}, \boldsymbol{C}_{\mathrm{Os}}^{(\mathrm{st})}, \boldsymbol{C}_{\mathrm{Os}}^{(\mathrm{sd})}\}$. Then, the inequalities in (7.7) express the fact that the three difference tensors $\boldsymbol{D}(\boldsymbol{C}_{\mathrm{Os}}^{(\mathrm{sAHA})}, \boldsymbol{C}_{\mathrm{Os}}^{(\mathrm{st})})$, $\boldsymbol{D}(\boldsymbol{C}_{\mathrm{Os}}^{(\mathrm{sd})}, \boldsymbol{C}_{\mathrm{Os}}^{(\mathrm{st})})$ and $\boldsymbol{D}(\boldsymbol{C}_{\mathrm{Os}}^{(\mathrm{sd})}, \boldsymbol{C}_{\mathrm{Os}}^{(\mathrm{sAHA})})$ have positive eigenvalues. Besides this, we expect these difference tensors to have small measures

$$\mathrm{raE}\left(\boldsymbol{D}(\boldsymbol{C}_{\mathrm{Os}}^{(1)}, \boldsymbol{C}_{\mathrm{Os}}^{(2)})\right) = \left\| \frac{\boldsymbol{D}(\boldsymbol{C}_{\mathrm{Os}}^{(1)}, \boldsymbol{C}_{\mathrm{Os}}^{(2)})}{1 + \max\{|\boldsymbol{C}_{\mathrm{Os}}^{(1)}|, |\boldsymbol{C}_{\mathrm{Os}}^{(2)}|\}} \right\|, \tag{7.9}$$

where $\|\cdot\|$ refers to the Frobenius norm and $\boldsymbol{C}_{\mathrm{Os}}^{(1)}, \boldsymbol{C}_{\mathrm{Os}}^{(2)} \in \{\boldsymbol{C}_{\mathrm{Os}}^{(\mathrm{sAHA})}, \boldsymbol{C}_{\mathrm{Os}}^{(\mathrm{st})}, \boldsymbol{C}_{\mathrm{Os}}^{(\mathrm{sd})}\}$. This would mean that the stiffness components of $\boldsymbol{C}_{\mathrm{Os}}^{(\mathrm{sd})}$, $\boldsymbol{C}_{\mathrm{Os}}^{(\mathrm{st})}$ and $\boldsymbol{C}_{\mathrm{Os}}^{(\mathrm{sAHA})}$ are very similar.

In Table 7.4 we display the eigenvalues and the measure raE for all three difference tensors. In accordance with Eq. (7.7), we observe that the eigenvalues of all three difference tensors are positive. Furthermore, we notice that all eigenvalues are small and in a good agreement. For $\boldsymbol{D}(\boldsymbol{C}_{\mathrm{Os}}^{(\mathrm{sd})}, \boldsymbol{C}_{\mathrm{Os}}^{(\mathrm{sAHA})})$ we obtain the smallest eigenvalues. Finally, we observe that all difference tensors have a small measure raE (raE $\in [0.008, 0.05]$). Hence, the stiffness components of $\boldsymbol{C}_{\mathrm{Os}}^{(\mathrm{sd})}$, $\boldsymbol{C}_{\mathrm{Os}}^{(\mathrm{st})}$ and $\boldsymbol{C}_{\mathrm{Os}}^{(\mathrm{sAHA})}$ are very similar.

As a conclusion of this section, it may be stated, that the apparent stiffness tensor $\boldsymbol{C}_{\mathrm{Os}}$ does not depend on the choice of the employed homogenization method.

Table 7.4.: Eigenvalues and raE of the difference tensors $\boldsymbol{D}(\boldsymbol{C}_{\mathrm{Os}}^{(\mathrm{sAHA})}, \boldsymbol{C}_{\mathrm{Os}}^{(\mathrm{st})})$, $\boldsymbol{D}(\boldsymbol{C}_{\mathrm{Os}}^{(\mathrm{sd})}, \boldsymbol{C}_{\mathrm{Os}}^{(\mathrm{sAHA})})$ and $\boldsymbol{D}(\boldsymbol{C}_{\mathrm{Os}}^{(\mathrm{sd})}, \boldsymbol{C}_{\mathrm{Os}}^{(\mathrm{st})})$.

	$\boldsymbol{D}(\boldsymbol{C}_{\mathrm{Os}}^{(\mathrm{sAHA})}, \boldsymbol{C}_{\mathrm{Os}}^{(\mathrm{st})})$	$\boldsymbol{D}(\boldsymbol{C}_{\mathrm{Os}}^{(\mathrm{sd})}, \boldsymbol{C}_{\mathrm{Os}}^{(\mathrm{sAHA})})$	$\boldsymbol{D}(\boldsymbol{C}_{\mathrm{Os}}^{(\mathrm{sd})}, \boldsymbol{C}_{\mathrm{Os}}^{(\mathrm{st})})$
Eigenvalues	1.2397	0.0018	1.2734
	0.0624	0.0706	0.1330
	0.0034	0.0713	0.0428
	0.0230	0.0373	0.0603
	0.0265	0.0434	0.0699
	0.0265	0.0434	0.0699
raE	0.0445	0.0081	0.0467

7.4 Parametric study

We perform a parametric study for the model parameters, h_{Os}, L_1, L_2, L_3, n_{cLU} and $\boldsymbol{C}_{\mathrm{LU}}$. The results of this study, as discussed below, are presented in Fig. 7.4.

For our parametric study we consider the stiffnesses components C_{ij} of $\boldsymbol{C}_{\mathrm{Os}}$ (Voigt notation) as functions $C_{ij} = C_{ij}\left(p_i\right)$ for a parameter p_i taking its values from its respective range and all other parameters fixed to their base value, see Table 7.3. By construction, the apparent stiffness tensor $\boldsymbol{C}_{\mathrm{Os}}$ is transverse isotropic. Therefore, we focus in the following only on the five independent nonzero stiffness components of $\boldsymbol{C}_{\mathrm{Os}}$, i.e. C_{11}, C_{12}, C_{13}, C_{33}, C_{44}. Note that the stiffness components C_{11} and C_{33} refer to the stiffness in direction perpendicular and parallel to the osteon's long axis, respectively.

Influence of the model parameters h_{Os}, L_1, L_2 and L_3: The influence of the osteon height h_{Os} on $\boldsymbol{C}_{\mathrm{Os}}$

(a) Osteon height

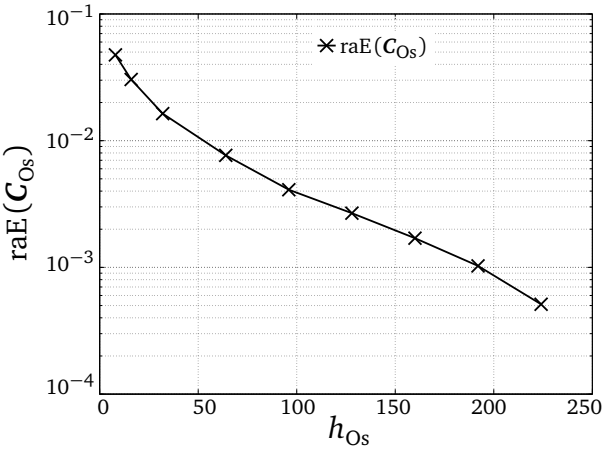

(b) Number of cLUs

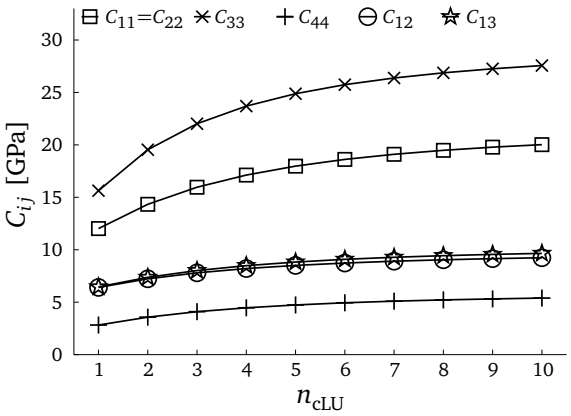

(c) Type of cLU

cLU type	C_{11}	C_{33}	C_{44}	C_{12}	C_{13}	AR
Asymmetric twisted plywood	15.7	25.3	4.3	7.2	8.7	1.6
Regular twisted plywood	17	21.1	4.6	7.8	8.7	1.2
Longitudinal	14.9	31.7	3.2	5.2	8.5	2.1
Transverse	20.1	15.0	3.9	11.2	6.7	0.7
Experimental-data derived	20	27.6	5.4	9.2	9.7	1.4
Experimental data						
Human cortical bone (Franzoso and Zysset, 2009)	14.1	38	15.4	10	12	2.7
Human cortical bone (Raum et al., 2011)	21.6	29.5	4.6	9.8	10.3	1.4

Figure 7.4.: Results of the parametric study. (a) Error raE($\boldsymbol{C}_{\mathrm{Os}}$) versus the osteon height h_{Os} [μm]. (b) Stiffness components C_{ij} of $\boldsymbol{C}_{\mathrm{Os}}$ [GPa] versus the number of cLUs (n_{cLU}). (c) For various cLU types we plot the stiffness components C_{ij} of $\boldsymbol{C}_{\mathrm{Os}}$ [GPa] and the corresponding anisotropy ratio AR. Additionally, we display experimentally-derived stiffness tensors of cortical bone.

is shown in Fig. 7.4a. In this plot we display the measure raE($\boldsymbol{C}_{\mathrm{Os}}$), as defined by Eq. (7.6), where we consider the stiffness tensor $\boldsymbol{C}_{\mathrm{Os}}$ obtained for the maximal height $h_{\mathrm{Os}} = 256$ as our reference value. It shows that within the investigated range, the osteon height h_{Os} has only a very small influence on $\boldsymbol{C}_{\mathrm{Os}}$; note therefore that raE($\boldsymbol{C}_{\mathrm{Os}}$) $\in [4 \cdot 10^{-2}, 4 \cdot 10^{-4}]$. Considering a value of raE($\boldsymbol{C}_{\mathrm{Os}}$) of about $3 \cdot 10^{-3}$ sufficient, we fix the osteon height to $h_{\mathrm{Os}} = 96$ in the following.

We now vary the embedding box size, $L_1 = L_2$ and L_3, that is the quantities m_1 and m_2. As reference value we choose the stiffness tensor $\boldsymbol{C}_{\mathrm{Os}}$, obtained for $(m_1, m_2) = (1.5, 1.5)$ and r_{Os} and h_{Os} fixed to their respective base values. Using the measure raE($\boldsymbol{C}_{\mathrm{Os}}$), we compare the reference value to the stiffness tensors $\boldsymbol{C}_{\mathrm{Os}}$, obtained when changing one of m_1 and m_2 in $[1.1, 1.5]$ and keeping the other fix. It shows (results are not presented) that neither m_1 nor m_2 has an influence on $\boldsymbol{C}_{\mathrm{Os}}$. Note, therefore, that for all values of m_1 and m_2, it holds that raE($\boldsymbol{C}_{\mathrm{Os}}(m_1, m_2)$) $\leq 10^{-2}$. We consider this difference sufficient and fix m_1 and m_2, such that the embedding box size is $L_1 = L_2 = 1.2 \cdot 2\, r_{\mathrm{Os}}$ and $L_3 = 1.25 \cdot h_{\mathrm{Os}}$. These values guarantee that the mesh between the embedding box and the osteon can have a mesh size which equals $h = 10\,\mu$m, i.e. the mesh size found to be suitable by our numerical convergence analysis in Section 7.2.

Influence of the model parameters n_{cLU} and $\boldsymbol{C}_{\mathrm{LU}}$: The influence of the number of cLUs (n_{cLU}) on the stiffness components C_{11}, C_{12}, C_{13}, C_{33} and C_{44} is shown in Fig. 7.4b. It shows that all stiffness components increase with increasing values of n_{cLU}. This is as expected, since with increasing n_{cLU}, the amount of the stiffest part of the osteon, the cLUs, increases, and so does the apparent stiffness tensors $\boldsymbol{C}_{\mathrm{Os}}$. Furthermore, in Fig. 7.4b it is seen that the stiffness components C_{ij} are affected by n_{cLU} to varying degrees. While C_{11} and C_{33} are influenced mostly by n_{cLU}, the other three stiffness components C_{12}, C_{13} and C_{44} are influenced only to a small amount.

In Fig. 7.4c we display the stiffness components of $\boldsymbol{C}_{\mathrm{Os}}$ as well as corresponding anisotropy ratios AR for various cLU types. It shows that all stiffness tensors $\boldsymbol{C}_{\mathrm{Os}}$ are within the range of experimentally-derived data of cortical bone (Franzoso and Zysset, 2009; Raum et al., 2011). Furthermore, we observe that the anisotropy ratios AR vary strongly among the various cLU types. Since the experimental-data derived cLU gives anisotropy ratios AR closest to that of the experimental data of Raum et al. (2011), we henceforth use as base value $\boldsymbol{C}_{\mathrm{LU}} = \boldsymbol{C}_{\mathrm{LU}}^{\mathrm{exp}}$. The cLUs of type regular and asymmetric twisted plywood yield anisotropy ratios AR which are slightly smaller or larger than the experimental ones of Raum et al. (2011), respectively. The anisotropy ratios AR obtained for the longitudinal or the transverse cLU are significantly larger or smaller than the experimental ones of Raum et al. (2011), respectively.

Summary: Locally around the base parameter set, the stiffness $\boldsymbol{C}_{\mathrm{Os}}$ is influenced mostly by the parameters n_{cLU} and $\boldsymbol{C}_{\mathrm{LU}}$. These parameters influence the stiffness components, C_{11} and C_{33} to a large extent, while have a less strong influence on other components. Furthermore, we may state that the experimental-data derived cLU compares best with the experimental data of Raum et al. (2011), and the regular/asymmetric twisted plywood cLU second best with this data. Finally, we fixed parameters with little influence, such as the osteon height and the size of the embedding box, to meaningful base values.

7.5 Discussion and future work

In the following we highlight how our research reflects, differs and extends current knowledge of the elastic properties of osteons. In this context, we list future tasks.

Stiffness components of $\boldsymbol{C}_{\mathrm{Os}}$ as well as corresponding anisotropy ratios AR, predicted by our osteon model, lie within the range of data reported by various authors (Franzoso and Zysset, 2009; Raum et al., 2011; Cowin, 2001; Vercher et al., 2014; Hamed et al., 2010; Yoon and Cowin, 2008), see Table 7.5. This comparison, however, allows for no quantitative statement about the agreement of model and experimental data, since different osteon types were investigated by the authors: the embedding material and the LU types among the model studies differ. Moreover, the experimentally-measured data of Raum et al. (2011) and Franzoso and Zysset (2009) might be inconsistent, due to the different measurement techniques employed (nanoindentation and scanning acoustic microscopy). For a more quantitative validation of our osteon model, as given in Chapter 6 for the MTLT model, we require experimentally-derived tissue-scale elastic properties of the osteon, site-matched with fine-scale structural data of the osteon.

Our numerical convergence analysis demonstrated that our approximate apparent stiffness tensors $\boldsymbol{C}_{\mathrm{Os}}$ can be considered suitable. Using the self-consistent RVE-based homogenization method with displacement boundary conditions, we observed second-order convergence for the error $\mathrm{raE}(\boldsymbol{C}_{\mathrm{Os}})$ as the mesh size decreases. This met the convergence order reported by Raum et al. (2010), who employed the self-consistent RVE-based homogenization method for both, traction and displacement boundary conditions, for LU tissue.

In Section 7.3 we found that our model predictions $\boldsymbol{C}_{\mathrm{Os}}$ do not depend on the choice of considered homogenization methods. A similar observation was made by Raum et al. (2010) for LU tissue. They found that the apparent stiffness tensors of the LU, when predicted by the self-consistent RVE-based homogenization method with displacement or with traction boundary conditions, are in a good agreement.

Table 7.5.: Experimental and model stiffnesses of various tissues from this study and from selected references. For each tissue we display the corresponding study type (experimental (exp.), model, this study), its stiffness components C_{ij} in GPa, its anisotropy ratio AR $= C_{33}/C_{11}$ and corresponding references. The abbreviations NI and SAM stand for nanoindentation and scanning acoustic microscopy, respectively.

Tissue	Study type	C_{11}	C_{12}	C_{13}	C_{22}	C_{23}	C_{33}	C_{44}	C_{55}	C_{66}	AR	References
Human cortical bone	exp. (NI)	14.1	10.0	12.0	26.7	16.5	38	7.7	5.6	4.7	2.7	Franzoso and Zysset (2009)
Human femoral cortical bone	exp. (SAM)	21.6	9.8	10.3	21.6	–	29.5	4.6	4.6	4.6	1.4	Raum et al. (2011)
Cortical bone	model	18.7	10.2	9.6	19.5	10	27.6	5.3	5.8	4.5	1.5	Cowin (2001)
Osteon, twisted plywood	model	12.9	4.6	4.9	15.6	5.8	28.9	5.3	4.6	3.5	2.2	Vercher et al. (2014)
Osteon, helicoidal twisted plywood	model	18.9	3.7	3.7	12.6	4.3	12.6	4.2	5.7	5.7	0.7	Hamed et al. (2010)
Osteon, orthogonal plywood	model	19.9	10.1	10.1	25	10.5	25	7.5	6.3	6.3	1.3	Yoon and Cowin (2008)
Osteon, experimental-data derived cLU	this study	20.0	9.2	9.7	20.0	9.7	27.6	5.4	4.3	4.3	1.4	—
Osteon, asymmetric twisted plywood	this study	15.7	7.2	8.7	15.7	8.7	25.3	4.3	4.4	4.4	1.6	—

Of course, convergence of the displacement and the stiffness tensor $\boldsymbol{C}_{\mathrm{Os}}$ and the comparison of different homogenization methods, does not guarantee the correctness of our model in capturing the physics. To this end, we performed a local parametric study. The crucial parameters found for the osteon (number of cLUs and the cLU type, characterized in our model through $\boldsymbol{C}_{\mathrm{LU}}$) are partly in accordance with those parameters detected by Martin and Ishida (1989) for the tensile strength of bovine cortical bone. Additionally, Martin and Ishida (1989) stated that the orientation of the MCFBs seems to be the most important parameter in influencing the tensile strength of bovine cortical bone. A similar conclusion for the osteon was not possible in this study. This was because our observations were based on a local parametric study, which allows no serious conclusions about the global importance of any parameter. A global sensitivity analysis can remedy this, see the future tasks.

Only a few authors have studied the influence of the cLU/LU type on the elastic properties of the osteon. Reisinger et al. (2011) used periodic homogenization to predict the apparent stiffness tensor of the osteon. They favor the regular twisted plywood cLU. Raum et al. (2010), who compared the stiffness tensor $\boldsymbol{C}_{\mathrm{LU}}$ for different LUs (asymmetric twisted plywood, regular twisted plywood and orthogonal plywood), found that only the asymmetric twisted plywood LU can explain the experimentally observed tissue anisotropy. Our observations for the osteon are similar to those of Raum et al. (2010) and Reisinger et al. (2011). Anyhow, we found that the experimental-data derived cLU with stiffness $\boldsymbol{C}_{\mathrm{LU}}^{\mathrm{exp}}$ compares best with the experimental data of Raum et al. (2011), and the asymmetric and the regular twisted plywood cLU compare second best with this data.
Future tasks are

1. Decrease the large computation time of our osteon model. At the moment our osteon model requires about several hours to compute the whole apparent stiffness tensor $\boldsymbol{C}_{\mathrm{Os}}$. There are several possibilities to achieve a reduction. Firstly, we might want to make use of symmetries of the osteon, compare Fig. 7.2, to shrink thereby our computational domain. For instance, Hogan (1992) represented only one quarter of the osteon, and imposed then symmetry conditions on the inner boundary of the osteon. Secondly, we can adaptively refine our finite-element mesh during the iterations of the self-consistent RVE-based homogenization method. At the moment, we use for all iterations the same mesh. Adaptive refinement of the finite-element mesh may incur less computational effort, since the total number of iterations may decrease and the mesh may be coarser.

2. Perform a global sensitivity analysis to identify the global influence of the model parameters on the apparent stiffness tensor $\boldsymbol{C}_{\mathrm{Os}}$. Unfortunately, employing the Elementary Effects method, as done for the MTLT model in Section 6.3, is no reasonable option at the moment, because using the Elementary Effects method incurs too many runs of our time-consuming self-consistent RVE-based homogenization method. However, using another global sensitivity method will not be cheaper, since among the global sensitivity analysis methods the Elementary Effects method is quite an

effective one (Saltelli et al., 2008). Therefore, we have to reduce the computation time of the self-consistent RVE-based homogenization method.

3. Model a complex and more realistic cLU type, recently observed by Varga et al. (2013). These authors studied the three-dimensional organization of MCFBs in human cortical bone using synchrotron X-ray phase nano-tomography and found that two cLU types, i.e. helicoidal plywood and asymmetric twisted plywood, coexist in a single osteon.

7.6 Conclusions

Our osteon model, developed in Section 7.1, predicts the apparent stiffness tensor $\boldsymbol{C}_{\mathrm{Os}}$ of the osteon at the tissue scale. These predictions compare well with experimental or model data of other researchers. However, this was not the main focus of this chapter. The main points were

- Our convergence analysis has shown that the approximate displacement $\boldsymbol{u}$ and the approximate apparent stiffness $\boldsymbol{C}_{\mathrm{Os}}$ on a given mesh are numerically reasonable. Based on the convergence analysis we selected a default mesh size, such that we have a good balance between accuracy and computational effort.
- All homogenization methods, compared in Section 7.3, predict similar apparent stiffness tensors $\boldsymbol{C}_{\mathrm{Os}}$.
- Parameters influencing $\boldsymbol{C}_{\mathrm{Os}}$ to a large extent are: the number of cLUs (n_{cLU}) and the stiffness tensor of the LU ($\boldsymbol{C}_{\mathrm{LU}}$). Our parametric study has shown that the height of the osteon and the size of the embedding box, when changed in their respective variation ranges, do not influence $\boldsymbol{C}_{\mathrm{Os}}$. Therefore, these parameters were set to meaningful values, see Table 7.3. Ranking all parameters in a quantitative order of importance, as done for the MTLT model in Chapter 6, is not possible based on our local parametric study. Further investigations are necessary here.
- The stiffness $\boldsymbol{C}_{\mathrm{Os}}$ increases with the number of cLUs. Among the investigated cLU types (asymmetric and regular twisted plywood, transverse and longitudinal, experimental-data derived), we found the experimental-data derived cLU to give an apparent stiffness $\boldsymbol{C}_{\mathrm{Os}}$ which compares best with the experimental data of Raum et al. (2011). The asymmetric twisted plywood cLU and the regular twisted plywood cLU yield the second best results.

8 Conclusions of this thesis

Using multiscale models and homogenization methods, the elastic properties of two important MMTs, the MTLT and the osteon, are modeled and simulated at different length scales. In this thesis we studied homogenization methods from Eshelby-based, RVE-based and periodic homogenization. In particular, these were the Mori-Tanaka method and the self-consistent method from Eshelby-based homogenization, the AHF method and the AHA method for periodic homogenization, and the RVE-based homogenization method with displacement and traction boundary conditions in RVE-based homogenization.

We modeled the fine-scale structure of the MTLT and the osteon and simulated their elastic properties. For the MTLT we considered two structurally different tissue types appearing in MTLT tissue: circumferential and interstitial tissue. These differ in their tissue microporosity (volume fraction of micropores in MTLT tissue) and their average diameter of the MCFBs. A multiscale model of MTLT tissue was developed using the Mori-Tanaka and the self-consistent method. Our model gives the tissue-scale apparent stiffness of the MTLT as function of the mineral volume fraction of the MCFB, the microporosity, the shape of the inclusions and the mineral distribution parameter (ratio of the mineral volume in the MCF to total mineral).

Osteons are the basic structural unit of cortical bone. They are cylindrically shaped and comprise a central cylinder, the so-called Haversian canal, and approximately circular lamellar units surrounding this canal. Each circular lamellar unit consists of several sublamellae made up of unidirectionally-aligned MCFBs. A two-scale model of the osteon was developed using the RVE-based homogenization method with displacement boundary conditions. Our model gives the tissue-scale apparent stiffness of the osteon as function of the shape of the osteon, the shape of the Haversian canal, the number of circular lamellar units, and the organization of the MCFBs within the circular lamellar unit, characterized through the stiffness tensor of the circular lamellar unit.

We performed different types of tests to clarify the model accuracy and the numerical accuracy of the employed homogenization method. We found that cylindrical inclusions appearing in the MTLT can be considered as highly prolated ellipsoidal inclusions with an aspect ratio between 100 and 200. Doing so, the predicted stiffness tensor is given with a satisfactory accuracy. Furthermore, we showed that the numerical accuracy of the Mori-Tanaka method improves about one order of magnitude, if we decrease the tool parameter of the Mori-Tanaka method about one order of magnitude. Similar applies to the self-consistent method. A numerical convergence analysis of the RVE-based homogenization method with displacement boundary conditions (when using the finite element method with Lagrange elements of order two) showed that the error in the stiffness tensor decreases about second-order if we decrease the mesh size.

We studied the computational effort of the employed homogenization methods. In general, the computational effort of the Mori-Tanaka method and the self-consistent method is much less than for the RVE-based homogenization method with displacement boundary conditions. While the former two methods need at most several minutes to compute the apparent stiffness tensor, the latter needs several hours. Moreover, we notice that the computation time of the apparent stiffness tensor depends on the tool parameters. In general, the computation time is the larger the stricter the value of the tool parameter. For the self-consistent method we determine a suitable starting value for our algorithm, which results in a smaller number of nonlinear systems to be solved in the iteration.

Our modeling and simulation studies on the apparent elastic properties of MTLT tissue and osteons have given some insights into the original design principles of these tissues. For MTLT tissue, we performed a global sensitivity analysis and a local parametric study. We found that the MTLT's tissue-scale apparent stiffness is influenced mostly by: the mineral volume fraction of the MCFBs, the shape of the mineral inclusion, the mineral distribution parameter and the microporosity. We have shown that increasing the mineral volume fraction of the MCFBs reinforces the apparent stiffness of MTLT tissue, while

increasing the microporosity reduces it. The microporosity and the mineral volume fraction most likely depend linearly on each other, further investigations are necessary here. For the osteon, we performed a local parametric study. We found that the tissue-scale apparent stiffness of the osteon is influenced to a large extent by the number of circular lamellar units and the organization of the MCFBs within the circular lamellar units, i.e. the type of the circular lamellar unit. Employing a global sensitivity analysis of the osteon model, as done for the MTLT model, was not possible, since this is up to now too expensive. The apparent stiffness of the osteon increases with the number of circular lamellar units. Among the investigated circular lamellar unit types (asymmetric twisted plywood, regular twisted plywood, and transverse, longitudinal and experimental-data derived circular lamellar unit) the experimental-data derived circular lamellar unit and the asymmetric twisted plywood give the most reasonable apparent stiffness values.

The predictions of our MTLT model were in a good agreement with experimental data of our project partners (small relative errors of 6-8 %), as well as with experimental and model data in the literature. The experimentally-derived tissue-scale elastic properties of the MTLT were given site-matched with mineralization information on the MTLT. This allowed for a good adaption of our model to the given data. For the osteon no such experimental data was available, and we, therefore, compared our model results with (experimentally-derived and model-derived) data taken from the literature. The agreement was good, however, not as good as for the MTLT model. This is because the data was belonging to different osteon types in different studies: the LU type, the embedding material of the osteon, and the base values of the model parameters differ among the studies. For a more quantitative validation of our osteon model, we require experimentally-derived tissue-scale elastic properties of the osteon, site-matched with fine-scale structural data of the osteon.

In this thesis we have shown that homogenization methods are useful and reliable tools to predict reasonable apparent elastic properties of different MMTs. In the future, our established models or parts of them can be used to setup more complex MMT models, such as for cortical bone tissue. Moreover, the insights gained from our modeling and simulation studies can be transferred to the development of artificial hierarchical structured materials in the field of biomimetic materials research.

A Hooke's law in Voigt, Kelvin or Mandel notation

We fix some orthonormal system of $\mathbb{R}^3$, denoted $\{\boldsymbol{e}_i\}$. As described in Section 2.1.3, we employ the Kelvin, the Mandel or the Voigt notation to represent the stiffness tensor $\boldsymbol{C}$ in $\mathbb{S}\mathrm{ym}(\mathbb{R}^3)$ as a symmetric matrix $\tilde{\boldsymbol{C}}$ in $\mathbb{R}^{6\times 6}$, and the second-order tensors $\boldsymbol{\sigma}$, $\boldsymbol{\varepsilon}$ in $\mathrm{Sym}(\mathbb{R}^3)$ as vectors $\tilde{\boldsymbol{\sigma}}$, $\tilde{\boldsymbol{\varepsilon}}$ in $\mathbb{R}^6$. Recall that the corresponding index maps, Ψ_1 and Ψ_2, were defined in Table 2.1.

Hooke's law in symbolic notation reads

$$\boldsymbol{\sigma} = \boldsymbol{C} : \boldsymbol{\varepsilon}.$$

Using Voigt, Kelvin, or Mandel notation we obtain the matrix-vector relation

$$\tilde{\boldsymbol{\sigma}} = \tilde{\boldsymbol{C}}\,\tilde{\boldsymbol{\varepsilon}},$$

where the components of $\tilde{\boldsymbol{\sigma}}$, $\tilde{\boldsymbol{C}}$ and $\tilde{\boldsymbol{\varepsilon}}$ depend on the employed notation.

In Kelvin notation $\tilde{\boldsymbol{\sigma}}$, $\tilde{\boldsymbol{\varepsilon}}$ and $\tilde{\boldsymbol{C}}$ are given by

$$\tilde{\boldsymbol{\sigma}} = \begin{pmatrix} \boldsymbol{\sigma}_{11} \\ \boldsymbol{\sigma}_{22} \\ \boldsymbol{\sigma}_{33} \\ \sqrt{2}\,\boldsymbol{\sigma}_{23} \\ \sqrt{2}\,\boldsymbol{\sigma}_{13} \\ \sqrt{2}\,\boldsymbol{\sigma}_{12} \end{pmatrix}, \quad \tilde{\boldsymbol{\varepsilon}} = \begin{pmatrix} \boldsymbol{\varepsilon}_{11} \\ \boldsymbol{\varepsilon}_{22} \\ \boldsymbol{\varepsilon}_{33} \\ \sqrt{2}\,\boldsymbol{\varepsilon}_{23} \\ \sqrt{2}\,\boldsymbol{\varepsilon}_{13} \\ \sqrt{2}\,\boldsymbol{\varepsilon}_{12} \end{pmatrix}, \quad \tilde{\boldsymbol{C}} = \begin{bmatrix} C_{1111} & C_{1122} & C_{1133} & \sqrt{2}\,C_{1123} & \sqrt{2}\,C_{1113} & \sqrt{2}\,C_{1112} \\ C_{1122} & C_{2222} & C_{2233} & \sqrt{2}\,C_{2223} & \sqrt{2}\,C_{2213} & \sqrt{2}\,C_{2212} \\ C_{1133} & C_{2233} & C_{3333} & \sqrt{2}\,C_{3323} & \sqrt{2}\,C_{3313} & \sqrt{2}\,C_{3312} \\ \sqrt{2}\,C_{1123} & \sqrt{2}\,C_{2223} & \sqrt{2}\,C_{3323} & 2\,C_{2323} & 2\,C_{2313} & 2\,C_{2312} \\ \sqrt{2}\,C_{1113} & \sqrt{2}\,C_{2213} & \sqrt{2}\,C_{3313} & 2\,C_{2313} & 2\,C_{1313} & 2\,C_{1312} \\ \sqrt{2}\,C_{1112} & \sqrt{2}\,C_{2212} & \sqrt{2}\,C_{3312} & 2\,C_{2312} & 2\,C_{1312} & 2\,C_{1212} \end{bmatrix}.$$

In Mandel notation the components of $\tilde{\boldsymbol{C}}$, $\tilde{\boldsymbol{\sigma}}$ and $\tilde{\boldsymbol{\varepsilon}}$ are similar to those when using the Kelvin notation, however, the rows and columns are permuted. We have

$$\tilde{\boldsymbol{\sigma}} = \begin{pmatrix} \boldsymbol{\sigma}_{11} \\ \boldsymbol{\sigma}_{22} \\ \boldsymbol{\sigma}_{33} \\ \sqrt{2}\,\boldsymbol{\sigma}_{12} \\ \sqrt{2}\,\boldsymbol{\sigma}_{23} \\ \sqrt{2}\,\boldsymbol{\sigma}_{13} \end{pmatrix}, \quad \tilde{\boldsymbol{\varepsilon}} = \begin{pmatrix} \boldsymbol{\varepsilon}_{11} \\ \boldsymbol{\varepsilon}_{22} \\ \boldsymbol{\varepsilon}_{33} \\ \sqrt{2}\,\boldsymbol{\varepsilon}_{12} \\ \sqrt{2}\,\boldsymbol{\varepsilon}_{23} \\ \sqrt{2}\,\boldsymbol{\varepsilon}_{13} \end{pmatrix}, \quad \tilde{\boldsymbol{C}} = \begin{bmatrix} C_{1111} & C_{1122} & C_{1133} & \sqrt{2}\,C_{1112} & \sqrt{2}\,C_{1123} & \sqrt{2}\,C_{1113} \\ C_{1122} & C_{2222} & C_{2233} & \sqrt{2}\,C_{2212} & \sqrt{2}\,C_{2223} & \sqrt{2}\,C_{2213} \\ C_{1133} & C_{2233} & C_{3333} & \sqrt{2}\,C_{3312} & \sqrt{2}\,C_{3323} & \sqrt{2}\,C_{3313} \\ \sqrt{2}\,C_{1112} & \sqrt{2}\,C_{2212} & \sqrt{2}\,C_{3312} & 2\,C_{1212} & 2\,C_{1223} & 2\,C_{1213} \\ \sqrt{2}\,C_{1123} & \sqrt{2}\,C_{2223} & \sqrt{2}\,C_{3323} & 2\,C_{1223} & 2\,C_{2323} & 2\,C_{2313} \\ \sqrt{2}\,C_{1113} & \sqrt{2}\,C_{2213} & \sqrt{2}\,C_{3313} & 2\,C_{1213} & 2\,C_{2313} & 2\,C_{1313} \end{bmatrix}.$$

In Voigt notation we obtain

$$\tilde{\boldsymbol{\sigma}} = \begin{pmatrix} \boldsymbol{\sigma}_{11} \\ \boldsymbol{\sigma}_{22} \\ \boldsymbol{\sigma}_{33} \\ \boldsymbol{\sigma}_{23} \\ \boldsymbol{\sigma}_{13} \\ \boldsymbol{\sigma}_{12} \end{pmatrix}, \quad \tilde{\boldsymbol{\varepsilon}} = \begin{pmatrix} \boldsymbol{\varepsilon}_{11} \\ \boldsymbol{\varepsilon}_{22} \\ \boldsymbol{\varepsilon}_{33} \\ 2\,\boldsymbol{\varepsilon}_{23} \\ 2\,\boldsymbol{\varepsilon}_{13} \\ 2\,\boldsymbol{\varepsilon}_{12} \end{pmatrix}, \quad \tilde{\boldsymbol{C}} = \begin{bmatrix} C_{1111} & C_{1122} & C_{1133} & C_{1123} & C_{1113} & C_{1112} \\ C_{1122} & C_{2222} & C_{2233} & C_{2223} & C_{2213} & C_{2212} \\ C_{1133} & C_{2233} & C_{3333} & C_{3323} & C_{3313} & C_{3312} \\ C_{1123} & C_{2223} & C_{3323} & C_{2323} & C_{2313} & C_{2312} \\ C_{1113} & C_{2213} & C_{3313} & C_{2313} & C_{1313} & C_{1312} \\ C_{1112} & C_{2212} & C_{3312} & C_{2312} & C_{1312} & C_{1212} \end{bmatrix}.$$

Voigt notation is convenient because the components of the matrix $\tilde{\boldsymbol{C}}$ equal those of the tensor $\boldsymbol{C}$, and no annoying prefactors, such as 2 or $\sqrt{2}$, appear, i.e. $\tilde{C}_{\Psi_1(i,j)\Psi_1(k,l)} = C_{ijkl}$. However, one important drawback of the Voigt notation is that $\tilde{\boldsymbol{C}}$ is no longer a Cartesian tensor. Hence, Theorem 2.1.3 does not hold, and, in particular, the norm and the inverse of the tensor $\boldsymbol{C}$, generally do not equal the norm and the inverse of the matrix $\tilde{\boldsymbol{C}}$, respectively.

Both the Kelvin and the Mandel notation of $\boldsymbol{C}$, have none of the former mentioned disadvantages. Employing these notations, the constructed object $\tilde{\boldsymbol{C}}$ is a Cartesian tensor of second order. This brings some clear benefits, see Theorem 2.1.3 for details. In particular, the double contraction, $\boldsymbol{C} : \boldsymbol{\varepsilon}$, can be

translated to the matrix-vector product, $\tilde{\boldsymbol{C}}\,\tilde{\boldsymbol{\varepsilon}}$. Moreover, the norm and the inverse of the fourth-order tensor $\boldsymbol{C}$ can simply be understood as the norm and the inverse of the matrix $\tilde{\boldsymbol{C}}$, respectively.

B Derivation of Eq. (3.29) in periodic homogenization

We now prove Eq. (3.29) from Section 3.4.1.

Theorem B.0.1 *Given $\boldsymbol{C}_A$, $\boldsymbol{w}_i$, $\boldsymbol{\varepsilon}_i = \boldsymbol{\varepsilon}(\boldsymbol{w}_i)$, $\boldsymbol{\sigma}_i = \boldsymbol{\sigma}(\boldsymbol{w}_i)$ as described in Section 3.4.1, and $\boldsymbol{p}_i$ defined by $(\boldsymbol{p}_i(\boldsymbol{y}))_m = y_l\,\delta_{mk}$, with $m,k = 1,2,3$, $i = \Psi_1(k,l) = 1,2,\ldots,6$ and index map Ψ_1, given by Table 2.1. It holds that*

$$\mathcal{M}_V\left(\boldsymbol{\sigma}_i\right) = \boldsymbol{C}_A : \mathcal{M}_V\left(\boldsymbol{\varepsilon}_i\right) \quad \textit{with} \quad \mathcal{M}_V\left((\boldsymbol{\varepsilon}_{\Psi_1(k,l)})_{op}\right) = \frac{1}{2}(\delta_{lp}\delta_{ko} + \delta_{lo}\delta_{kp}), \tag{B.1}$$

where $i = \Psi_1(k,l)$ and $o,p = 1,2,3$.

Proof. We note first that the second equality in Eq. (B.1) follows from

$$0 = \mathcal{M}_V\left((\varepsilon(\boldsymbol{w}_{\Psi_1(k,l)} - \boldsymbol{p}_{\Psi_1(k,l)}))_{op}\right) = \mathcal{M}_V\left((\varepsilon(\boldsymbol{w}_{\Psi_1(k,l)}))_{op}\right) - \mathcal{M}_V\left((\varepsilon(\boldsymbol{p}_{\Psi_1(k,l)}))_{op}\right) \tag{B.2}$$

$$= \mathcal{M}_V\left((\varepsilon(\boldsymbol{w}_{\Psi_1(k,l)}))_{op}\right) - \frac{1}{2}\left(\frac{\partial(y_l\delta_{ok})}{\partial y_p} + \frac{\partial(y_l\delta_{pk})}{\partial y_o}\right) \tag{B.3}$$

$$= \mathcal{M}_V\left((\varepsilon(\boldsymbol{w}_{\Psi_1(k,l)}))_{op}\right) - \frac{1}{2}\left(\delta_{lp}\delta_{ok} + \delta_{lo}\delta_{pk}\right). \tag{B.4}$$

Thereby, the first equality in Eq. (B.2) is satisfied, because $\boldsymbol{w}_{\Psi_1(k,l)} - \boldsymbol{p}_{\Psi_1(k,l)}$ is V-periodic and, thus, by Theorem 2.1.2 the mean of $\nabla(\boldsymbol{w}_{\Psi_1(k,l)} - \boldsymbol{p}_{\Psi_1(k,l)})$ is zero. The second equality in Eq. (B.2) holds because the mean is a linear function. Eq. (B.3) follows by definition of the strain $\boldsymbol{\varepsilon}$, and Eq. (B.4) follows by definition of $\boldsymbol{p}_{\Psi_1(k,l)}$.

In order to prove the first equality in Eq. (B.1) for $k \neq l$, we make use of Eq. (B.4), exploit that $\boldsymbol{C}_A$ satisfies minor symmetries, and employ Eq. (3.28). It follows

$$(\boldsymbol{C}_A)_{mnop}\,\mathcal{M}_V\left((\varepsilon(\boldsymbol{w}_{\Psi_1(k,l)}))_{op}\right) = \frac{1}{2}(\boldsymbol{C}_A)_{mnkl} + \frac{1}{2}(\boldsymbol{C}_A)_{mnlk} = (\boldsymbol{C}_A)_{mnkl} = \mathcal{M}_V\left((\sigma(\boldsymbol{w}_{\Psi_1(k,l)}))_{mn}\right).$$

For $k = l$, Eq. (B.1) is a straightforward application of Eq. (B.4) and Eq. (3.28)

$$(\boldsymbol{C}_A)_{mnop}\,\mathcal{M}_V\left((\varepsilon(\boldsymbol{w}_{\Psi_1(k,l)}))_{op}\right) = (\boldsymbol{C}_A)_{mnkl} = \mathcal{M}_V\left((\sigma(\boldsymbol{w}_{\Psi_1(k,l)}))_{mn}\right).$$

This proves Eq. (B.1). □

C Eshelby and Hill tensor for a cylindrical inclusion embedded into an isotropic material

Let there be a cylindrical inclusion, A_I, which is embedded into some matrix, A_M. The phase A_M may be an isotropic linear elastic material with stiffness tensor $\boldsymbol{C}_M$. We denote the bulk and the shear modulus of the matrix by K_M and G_M, respectively.

Given a three-dimensional Cartesian coordinate system with coordinates x_i where $i = 1,2,3$, we assume that the inclusions are aligned with the x_3-axis. The non-zero components of the Eshelby tensor $\boldsymbol{S}$ read in Voigt notation (Nemat-Nasser and Hori, 1999)

$$\boldsymbol{S}_{11} = \boldsymbol{S}_{22} = \frac{9}{4}\frac{K_M + G_M}{3K_M + 4G_M}, \quad \boldsymbol{S}_{12} = \boldsymbol{S}_{21} = \frac{1}{4}\frac{3K_M - 5G_M}{3K_M + 4G_M}, \quad \boldsymbol{S}_{13} = \boldsymbol{S}_{23} = \frac{1}{2}\frac{3K_M - 2G_M}{3K_M + 4G_M},$$
$$\boldsymbol{S}_{44} = \boldsymbol{S}_{55} = \frac{1}{4}, \qquad \boldsymbol{S}_{66} = \boldsymbol{S}_{23} = \frac{1}{4}\frac{3K_M + 7G_M}{3K_M + 4G_M}.$$

Finally, the Hill tensor $\boldsymbol{P}$ is given by

$$\boldsymbol{P} = \boldsymbol{S} : (\boldsymbol{C}_M)^{-1}. \tag{C.1}$$

D Integrand of Hill tensor as function of the aspect ratio

Let $0 \leq \theta \leq \pi$, $0 \leq \eta \leq 2\pi$. We denote by N_{ijkl} the integrand of the Hill tensor component $\boldsymbol{P}_{ijkl}$, see Eq. (3.54a) for a definition. In Table D.1 we display $\max_{\theta,\eta}(|N_{ijkl}|)$ versus the aspect ratio $\mathrm{ar}_{\mathrm{ha}} = \{10, 10^2, \ldots, 10^6\}$.

Table D.1.: Maximum value of $|N_{ijkl}|$ versus the aspect ratio $\mathrm{ar}_{\mathrm{ha}}$.

$\max_{\theta,\eta}(\lvert N_{ijkl}\rvert)$ \ $\mathrm{ar}_{\mathrm{ha}}$	10	10^2	10^3	10^4	10^5	10^6
N_{1111}	$7.278 \cdot 10^{-1}$	$7.278 \cdot 10^{-1}$	$7.278 \cdot 10^{-1}$	$7.278 \cdot 10^{-1}$	$7.278 \cdot 10^{-1}$	$7.278 \cdot 10^{-1}$
N_{1122}	$2.600 \cdot 10^{-1}$	$2.600 \cdot 10^{-1}$	$2.600 \cdot 10^{-1}$	$2.600 \cdot 10^{-1}$	$2.600 \cdot 10^{-1}$	$2.600 \cdot 10^{-1}$
N_{1133}	$2.600 \cdot 10^{-1}$	$2.600 \cdot 10^{-1}$	$2.600 \cdot 10^{-1}$	$2.600 \cdot 10^{-1}$	$2.600 \cdot 10^{-01}$	$2.600 \cdot 10^{-1}$
N_{1123}	$2.270 \cdot 10^{-2}$	$2.544 \cdot 10^{-3}$	$2.550 \cdot 10^{-4}$	$2.550 \cdot 10^{-5}$	$2.550 \cdot 10^{-6}$	$2.550 \cdot 10^{-7}$
N_{1113}	$2.788 \cdot 10^{-2}$	$3.265 \cdot 10^{-3}$	$3.280 \cdot 10^{-4}$	$3.280 \cdot 10^{-5}$	$3.280 \cdot 10^{-6}$	$3.280 \cdot 10^{-7}$
N_{1112}	$1.959 \cdot 10^{-1}$	$1.959 \cdot 10^{-1}$	$1.959 \cdot 10^{-1}$	$1.959 \cdot 10^{-1}$	$1.959 \cdot 10^{-1}$	$1.959 \cdot 10^{-1}$
N_{2222}	$7.278 \cdot 10^{-1}$	$7.278 \cdot 10^{-1}$	$7.278 \cdot 10^{-1}$	$7.278 \cdot 10^{-1}$	$7.278 \cdot 10^{-1}$	$7.278 \cdot 10^{-1}$
N_{2233}	$2.600 \cdot 10^{-1}$	$2.600 \cdot 10^{-1}$	$2.600 \cdot 10^{-1}$	$2.600 \cdot 10^{-1}$	$2.600 \cdot 10^{-1}$	$2.600 \cdot 10^{-1}$
N_{2223}	$2.788 \cdot 10^{-2}$	$3.265 \cdot 10^{-3}$	$3.280 \cdot 10^{-4}$	$3.280 \cdot 10^{-5}$	$3.280 \cdot 10^{-6}$	$3.280 \cdot 10^{-7}$
N_{2213}	$2.270 \cdot 10^{-2}$	$2.544 \cdot 10^{-3}$	$2.550 \cdot 10^{-4}$	$2.550 \cdot 10^{-5}$	$2.550 \cdot 10^{-6}$	$2.550 \cdot 10^{-7}$
N_{2212}	$1.959 \cdot 10^{-1}$	$1.959 \cdot 10^{-1}$	$1.959 \cdot 10^{-1}$	$1.959 \cdot 10^{-1}$	$1.959 \cdot 10^{-1}$	$1.959 \cdot 10^{-1}$
N_{3333}	$4.857 \cdot 10^{-2}$	$5.128 \cdot 10^{-4}$	$5.128 \cdot 10^{-6}$	$5.128 \cdot 10^{-8}$	$5.128 \cdot 10^{-10}$	$5.128 \cdot 10^{-12}$
N_{3323}	$4.518 \cdot 10^{-2}$	$5.087 \cdot 10^{-3}$	$5.100 \cdot 10^{-4}$	$5.100 \cdot 10^{-5}$	$5.100 \cdot 10^{-6}$	$5.100 \cdot 10^{-7}$
N_{3313}	$4.518 \cdot 10^{-2}$	$5.087 \cdot 10^{-3}$	$5.100 \cdot 10^{-4}$	$5.100 \cdot 10^{-5}$	$5.100 \cdot 10^{-6}$	$5.100 \cdot 10^{-7}$
N_{3312}	$1.300 \cdot 10^{-1}$	$1.300 \cdot 10^{-1}$	$1.300 \cdot 10^{-1}$	$1.300 \cdot 10^{-1}$	$1.300 \cdot 10^{-1}$	$1.300 \cdot 10^{-1}$
N_{2323}	$2.600 \cdot 10^{-1}$	$2.600 \cdot 10^{-1}$	$2.600 \cdot 10^{-1}$	$2.600 \cdot 10^{-1}$	$2.600 \cdot 10^{-1}$	$2.600 \cdot 10^{-1}$
N_{2313}	$1.300 \cdot 10^{-1}$	$1.300 \cdot 10^{-1}$	$1.300 \cdot 10^{-1}$	$1.300 \cdot 10^{-1}$	$1.300 \cdot 10^{-1}$	$1.300 \cdot 10^{-1}$
N_{2312}	$4.012 \cdot 10^{-2}$	$4.742 \cdot 10^{-3}$	$4.766 \cdot 10^{-4}$	$4.766 \cdot 10^{-5}$	$4.766 \cdot 10^{-6}$	$4.766 \cdot 10^{-7}$
N_{1313}	$2.600 \cdot 10^{-1}$	$2.600 \cdot 10^{-1}$	$2.600 \cdot 10^{-1}$	$2.600 \cdot 10^{-1}$	$2.600 \cdot 10^{-1}$	$2.600 \cdot 10^{-1}$
N_{1312}	$2.270 \cdot 10^{-2}$	$2.544 \cdot 10^{-3}$	$2.550 \cdot 10^{-4}$	$2.550 \cdot 10^{-5}$	$2.550 \cdot 10^{-6}$	$2.550 \cdot 10^{-7}$
N_{1212}	$2.600 \cdot 10^{-1}$	$2.600 \cdot 10^{-1}$	$2.600 \cdot 10^{-1}$	$2.600 \cdot 10^{-1}$	$2.600 \cdot 10^{-1}$	$2.600 \cdot 10^{-1}$

E Estimating the convergence order and the asymptotic error constant for the self-consistent method

Let us denote by $\boldsymbol{C}_A$ the apparent stiffness tensor of some tissue A, and by $\boldsymbol{C}^{(k)}$ the estimate of $\boldsymbol{C}_A$ obtained in step $k = 1, 2 \ldots, N$ of Algorithm 4.2.1. We introduce the error

$$\mathrm{err}_k = \|\boldsymbol{C}^{(k)} - \boldsymbol{C}_A\|,$$

where $\|\cdot\|$ refers to the Frobenius norm. Since $\boldsymbol{C}_A$ is not known, we approximate err_k by $\mathrm{err}_k \approx \left\|\boldsymbol{C}^{(k)} - \boldsymbol{C}^{(N)}\right\|$.

Assume that for Algorithm 4.2.1 there exist two numbers, Q and p, such that

$$\mathrm{err}_k = Q\,(\mathrm{err}_{k-1})^p, \quad k = 2, \ldots, N, \tag{E.1}$$

where Q is called asymptotic error constant and p is the convergence order. In case of linear convergence, i.e. if $p = 1$, the asymptotic error constant Q, is also called convergence rate.

Due to Eq. (E.1), the errors in step $k-1$ and step k read

$$\begin{aligned} \mathrm{err}_{k-1} &= Q\,(\mathrm{err}_{k-2})^p, \\ \mathrm{err}_k &= Q\,(\mathrm{err}_{k-1})^p, \end{aligned} \tag{E.2}$$

respectively. Taking the logarithm on both sides of Eq. (E.2), we obtain the following uniquely solvable linear system for $\log Q$ and p:

$$\begin{pmatrix} \log \mathrm{err}_{k-1} \\ \log \mathrm{err}_k \end{pmatrix} = \begin{pmatrix} 1 & \log \mathrm{err}_{k-2} \\ 1 & \log \mathrm{err}_{k-1} \end{pmatrix} \begin{pmatrix} \log Q \\ p \end{pmatrix}. \tag{E.3}$$

Solving linear system (E.3) gives an estimate of Q and p dependent on k. Denoting these estimates by $Q(k)$ and $p(k)$, respectively, we take the median of the sets $\{Q(k) \,|\, 3 \le k \le N\}$ and $\{p(k) \,|\, 3 \le k \le N\}$, to obtain

$$Q = \mathrm{median}\left(\left\{ \exp\left(\frac{(\log \mathrm{err}_{k-1})^2 - \log \mathrm{err}_{k-2} \log \mathrm{err}_k}{\log \mathrm{err}_{k-1} - \log \mathrm{err}_{k-2}} \right) \right\}_{3 \le k \le N} \right), \tag{E.4}$$

$$p = \mathrm{median}\left(\left\{ \frac{\log \mathrm{err}_k - \log \mathrm{err}_{k-1}}{\log \mathrm{err}_{k-1} - \log \mathrm{err}_{k-2}} \right\}_{3 \le k \le N} \right), \tag{E.5}$$

respectively.

F Experimental derivation of the acoustic impedance of CIR and INT tissue

We start by briefly describing the function principle of SAM. Then, we list the steps in determining the acoustic impedance of CIR and INT tissue.

Let us consider some volume element of the MTLT sample which lies near to the surface and which we denote by V. The volume element V may have size l and may be filled with heterogeneities of size d. Employing SAM, we subject our sample with ultrasound waves at a wavelength λ. The ultrasound waves interact with V; one part is reflected back, the other part is transmitted. The reflected portion of the wave depends on the materials that make up V, in particular, it depends on the size of the heterogeneities within V. The reflected portion is used to determine the acoustic impedance[1] of V. Given that $d \ll l < \lambda$ holds, we derive the acoustic impedance at scale l. In terms of the RVE-based homogenization theory, the quantities, λ, l and d, characterize the coarse, the meso and the fine scale of the investigated tissue, respectively. Moreover, the requirement $d \ll l < \lambda$ entails that these scales are sufficiently separated, see Chapter 3.

Our project partners employed 50-MHz SAM on the transverse and the longitudinal cross section of several MTLT samples. For these measurements the wavelength was $\lambda_{50} = 23 - 30\,\mu$m, the volume element V had size $l \approx 20\,\mu$m, and V consisted of several MCFBs (heterogeneities) of diameter $d_{\mathrm{CIR}} = 2.9 - 4.0\,\mu$m (CIR tissue) and $d_{\mathrm{INT}} = 3.2 - 8.9\,\mu$m (INT tissue). Since $d \ll l < \lambda_{50}$ holds, the scale separation was sufficient. Hence, the 50-MHz SAM measurements yielded the acoustic impedance of compounds of CIR and INT tissue; measurements performed on transverse cross sections yielded the axial acoustic impedance, while those on longitudinal cross sections yielded the transverse acoustic impedance.

In order to obtain the acoustic impedance of CIR and INT tissue together with the site-matched DMB in ROIs i, our project partners performed the following steps (Figures 6.2a, 6.2b and 6.2c):

1. SR-μCT measurements and light-microscopy measurements were performed to obtain the DMB and the microporosity of MTLT tissue, respectively.

2. 50-MHz and 200-MHz SAM measurements were performed. 50-MHz SAM was employed to determine the acoustic impedance of CIR/INT tissue compounds. 200-MHz SAM was employed, since it was not possible to distinguish between CIR and INT tissue in the 50-MHz maps.

3. ROIs, which either consist of CIR or INT tissue, were marked manually in the 200-MHz maps of the transverse and the longitudinal cross section. This worked well in the transverse cross sections of the sample (axial acoustic impedance), however, not so well for the longitudinal cross sections (transverse acoustic impedance), see Section 6.5.2 for a discussion of the problems.

4. The corresponding 200-MHz and 50-MHz SAM maps and the DMB map were site-matched. This yielded corresponding ROIs in the 50-MHz SAM and the DMB map.

5. Within each ROI i the values of the DMB and the axial/transverse acoustic impedance were averaged. In total, one obtained for each ROI i the values DMB_i, as well as acoustic impedance values $\widetilde{Z}^{T_i}_{(i,\nu_i)}$ for direction $\nu_i = \mathrm{axi}$ and tissue type, $T_i = \mathrm{CIR}$ or $T_i = \mathrm{INT}$, and for direction $\nu_i = \mathrm{trv}$ and tissue type $T_i = \mathrm{CIR/INT}$.

[1] The acoustic impedance is the product of the tissue density and the velocity of ultrasound in the material.

G Phase volume fractions for the MTLT model

We give below the complete set of formulas that determine the phase volume fractions of our model sequence.

G.1 MTLT tissue

The phase volume fractions of the composite MTLT (CIR and INT) tissue are given by:

$$\begin{aligned}
\mathrm{vf}_{\mathrm{mp}}^{\mathrm{MTLT}} &= \begin{cases} \text{Const}, & \text{case (C) : Const} \in [0, 0.2], \\ a \cdot \mathrm{vf}_{\mathrm{ha}}^{\mathrm{MCFB}} + b, & \text{case (MD) : for } \mathrm{vf}_{\mathrm{ha}}^{\mathrm{MCFB}} \in [0.25, 0.35], a < 0. \end{cases} \\
\mathrm{vf}_{\mathrm{MCFB}}^{\mathrm{MTLT}} &= 1 - \mathrm{vf}_{\mathrm{mp}}^{\mathrm{MTLT}}.
\end{aligned}$$

G.2 MCFB

The phase volume fractions of the MCFB are given by:

$$\begin{aligned}
\mathrm{vf}_{\mathrm{MCF}}^{\mathrm{MCFB}} &= \alpha_{\mathrm{MCF}} \cdot \mathrm{vf}_{\mathrm{ha}}^{\mathrm{MCFB}} + \mathrm{vf}_{\mathrm{col}}^{\mathrm{MCFB}} = \alpha_{\mathrm{MCF}} \cdot \mathrm{vf}_{\mathrm{ha}}^{\mathrm{MCFB}} + h(\mathrm{vf}_{\mathrm{ha}}^{\mathrm{MCFB}}), \\
\mathrm{vf}_{\mathrm{ES}}^{\mathrm{MCFB}} &= 1 - \mathrm{vf}_{\mathrm{MCF}}^{\mathrm{MCFB}}.
\end{aligned}$$

The function h is derived based on an empirical formula of Raum et al. (2006a, Eq. (10), p. 750), which connects the collagen volume fraction $\mathrm{vf}_{\mathrm{col}}^{\mathrm{MCFB}}$, the mineral volume fraction $\mathrm{vf}_{\mathrm{ha}}^{\mathrm{MCFB}}$ and the nanopores volume fraction $\mathrm{vf}_{\mathrm{np}}^{\mathrm{MCFB}}$ to each other:

$$\frac{\mathrm{vf}_{\mathrm{col}}^{\mathrm{MCFB}}}{\mathrm{vf}_{\mathrm{np}}^{\mathrm{MCFB}}} = 0.36 + 0.084 \cdot \exp(6.7 \cdot \mathrm{vf}_{\mathrm{ha}}^{\mathrm{MCFB}}) =: \gamma(\mathrm{vf}_{\mathrm{ha}}^{\mathrm{MCFB}}). \tag{G.1}$$

Since ha, col and np are the sole basic constituents of the MCFB, their corresponding volume fractions $\mathrm{vf}_{\mathrm{ha}}^{\mathrm{MCFB}}$, $\mathrm{vf}_{\mathrm{col}}^{\mathrm{MCFB}}$ and $\mathrm{vf}_{\mathrm{np}}^{\mathrm{MCFB}}$ sum up to one. We then eliminate $\mathrm{vf}_{\mathrm{np}}^{\mathrm{MCFB}}$ from Eq. (G.1) using $\mathrm{vf}_{\mathrm{np}}^{\mathrm{MCFB}} = 1 - \mathrm{vf}_{\mathrm{ha}}^{\mathrm{MCFB}} - \mathrm{vf}_{\mathrm{col}}^{\mathrm{MCFB}}$ and obtain

$$\begin{aligned}
&\frac{\mathrm{vf}_{\mathrm{col}}^{\mathrm{MCFB}}}{1 - \mathrm{vf}_{\mathrm{ha}}^{\mathrm{MCFB}} - \mathrm{vf}_{\mathrm{col}}^{\mathrm{MCFB}}} = \gamma(\mathrm{vf}_{\mathrm{ha}}^{\mathrm{MCFB}}) \\
&\qquad \Leftrightarrow \qquad \mathrm{vf}_{\mathrm{col}}^{\mathrm{MCFB}} = (1 - \mathrm{vf}_{\mathrm{ha}}^{\mathrm{MCFB}}) \cdot \frac{\gamma(\mathrm{vf}_{\mathrm{ha}}^{\mathrm{MCFB}})}{(1 + \gamma(\mathrm{vf}_{\mathrm{ha}}^{\mathrm{MCFB}}))} =: h(\mathrm{vf}_{\mathrm{ha}}^{\mathrm{MCFB}}).
\end{aligned}$$

The mineral volume fraction $\mathrm{vf}_{\mathrm{ha}}^{\mathrm{MCFB}}$ is given by

$$\mathrm{vf}_{\mathrm{ha}}^{\mathrm{MCFB}} = \frac{\mathrm{DMB}}{\rho_{\mathrm{ha}}(1 - \alpha\,\widetilde{\mathrm{vf}}_{\mathrm{mp}})}.$$

Here, ρ_{ha} is the mass density of ha, DMB is the experimental DMB value, $\alpha \in [0, 1]$, and $\widetilde{\mathrm{vf}}_{\mathrm{mp}}$ is the experimentally measured microporosity.

G.3 MCF

The phase volume fractions of the MCF are given by:

$$\mathrm{vf}_{\mathrm{ha}}^{\mathrm{MCF}} = \alpha_{\mathrm{MCF}} \cdot \frac{\mathrm{vf}_{\mathrm{ha}}^{\mathrm{MCFB}}}{\mathrm{vf}_{\mathrm{MCF}}^{\mathrm{MCFB}}},$$
$$\mathrm{vf}_{\mathrm{col}}^{\mathrm{MCF}} = 1 - \mathrm{vf}_{\mathrm{ha}}^{\mathrm{MCF}}.$$

G.4 ES

The phase volume fractions of the ES are given by:

$$\mathrm{vf}_{\mathrm{ha}}^{\mathrm{ES}} = (1 - \alpha_{\mathrm{MCF}}) \cdot \frac{\mathrm{vf}_{\mathrm{ha}}^{\mathrm{MCFB}}}{1 - \mathrm{vf}_{\mathrm{MCF}}^{\mathrm{MCFB}}},$$
$$\mathrm{vf}_{\mathrm{np}}^{\mathrm{ES}} = 1 - \mathrm{vf}_{\mathrm{ha}}^{\mathrm{ES}}.$$

Bibliography

O. Akkus. Elastic deformation of mineralized collagen fibrils: an equivalent inclusion based composite model. *Journal of Biomechanical Engineering*, 127(3):383–390, 2005.

B. Alexander, T. L. Daulton, G. M. Genin, J. Lipner, J. D. Pasteris, B. Wopenka, and S. Thomopoulos. The nanometre-scale physiology of bone: steric modelling and scanning transmission electron microscopy of collagen–mineral structure. *Journal of the Royal Society Interface*, 9(73):1774–1786, 2012.

G. Allaire. Lecture 1: Introduction to homogenization theory. CEA-EDF-INRIA school on homogenization, December 2010.

J.-L. Auriault, C. Boutin, and C. Geindreau. *Homogenization of Coupled Phenomena in Heterogenous Media*, chapter Homogenization by multiple scale asymptotic expansions, pages 75–106. London, UK: ISTE, 2010.

J.-F. Barthélémy. Compliance and Hill polarization tensor of a crack in an anisotropic matrix. *International Journal of Solids and Structures*, 46(22-23):4064–4072, 2009.

Y. Benveniste. A new approach to the application of Mori-Tanaka's theory in composite materials. *Mechanics of Materials*, 6(2):147–157, 1987.

A. Bóna, I. Bucataru, and M. A. Slawinski. Material symmetries of elasticity tensors. *Quarterly Journal of Mechanics and Applied Mathematics*, 57(4):583–598, 2004.

A. F. Bower. *Applied mechanics of solids*. Boca Raton, US: Taylor & Francis Group, 2010.

D. Braess. *Finite Elemente. Theorie, schnelle Löser und Anwendungen in der Elastizitätstheorie.* Berlin, Germany: Springer, second edition, 1997.

S. C. Brenner and C. Carstensen. Finite element methods. In E. Stein, R. de Borst, and T. J. R. Hughes, editors, *Encyclopedia of Computational Mechanics*, chapter 3. Hoboken, US: John Wiley & Sons, 2004.

S. C. Brenner and L. Scott. *The mathematical theory of finite element methods*, volume 15 of *Texts in Applied Mathematics*. New York, US: Springer, third edition, 2008.

V. Buryachenko. *Micromechanics of heterogeneous materials.* New York, US: Springer, 2007.

P. G. Ciarlet. *The finite element method for elliptic problems*, volume 4 of *Studies in Mathematics and its Applications*. Amsterdam, The Netherlands: North-Holland Publishing Company, 1978.

P. G. Ciarlet. *Mathematical elasticity. Volume I: Three-dimensional elasticity*, volume 20 of *Studies in Mathematics and its Applications*. Amsterdam, The Netherlands: North-Holland Publishing Company, 1988.

P. G. Ciarlet. *Linear and nonlinear functional analysis with applications*. Philadelphia, PA: Society for Industrial and Applied Mathematics, 2013.

D. Cioranescu and P. Donato. *An introduction to homogenization*, volume 17 of *Oxford Lecture Series in Mathematics and its Applications*. New York, US: Oxford University Press, 1999.

COMSOL Multiphysics GmbH. *COMSOL Multiphysics & LiveLink for MATLAB [Software], Versions 4.1, 4.2, 4.3*. Göttingen, Germany, 2011-2013. URL http://www.comsol.de/.

S. Cowin. *Bone Mechanics Handbook, Second Edition*. Taylor & Francis, 2001.

A. Eringen and E. S. Suhubi. *Elastodynamics. Vol. II: Linear theory.* New York, US: Academic Press, 1975.

J. Eshelby. The determination of the elastic field of an ellipsoidal inclusion, and related problems. *Proceedings of the Royal Society of London. Series A. Mathematical and Physical Sciences*, 241:376–396, 1957.

G. E. Fantner, T. Hassenkam, J. H. Kindt, J. C. Weaver, H. Birkedal, L. Pechenik, J. A. Cutroni, G. A. G. Cidade, G. D. Stucky, D. E. Morse, and P. K. Hansma. Sacrificial bonds and hidden length dissipate energy as mineralized fibrils separate during bone fracture. *Nature Materials*, 4:612–616, 2005.

J. Francu. Homogenization of linear elasticity equations. *Aplikace Matematiky*, 27:96–117, 1982.

G. Franzoso and P. K. Zysset. Elastic anisotropy of human cortical bone secondary osteons measured by nanoindentation. *Journal of Biomechanical Engineering*, 131(11):1–11, 2009.

P. Fratzl. Collagen: Structure and mechanics, an introduction. In P. Fratzl, editor, *Collagen - Structure and Mechanics*. New York, US: Springer, 2008.

P. Fratzl and R. Weinkamer. Nature's hierarchical materials. *Progress in Materials Science*, 52(8):1263–1334, 2007.

F. Ghahremani. Numerical evaluaton of the stresses and strains in ellipsoidal inclusions in an anisotropic elastic material. *Mechanics Research Communications*, 4(2):89–91, 1977.

Q. Grimal, K. Raum, A. Gerisch, and P. Laugier. A determination of the minimum sizes of representative volume elements for the prediction of cortical bone elastic properties. *Biomechanics and Modeling in Mechanobiology*, 10(6):925–937, 2011.

D. Gross and T. Seelig. *Bruchmechanik. Mit einer Einführung in die Mikromechanik*. Berlin, Germany: Springer, fourth edition, 2007.

M. E. Gurtin. *An introduction to continuum mechanics*, volume 158 of *Mathematics in Science and Engineering*. London, UK: Academic Press, 1981.

E. Hamed, Y. Lee, and I. Jasiuk. Multiscale modeling of elastic properties of cortical bone. *Acta Mechanica*, 213(1-2):131–154, 2010.

Z. Hashin and S. Shtrikman. A variational approach to the theory of the elastic behaviour of multiphase materials. *Journal of the Mechanics and Physics of Solids*, 11(2):127–140, 1963.

C. Hellmich, J.-F. Barthélémy, and L. Dormieux. Mineral-collagen interactions in elasticity of bone ultrastructure – a continuum micromechanics approach. *European Journal of Mechanics - A/Solids*, 23(5): 783–810, 2004.

P. Helnwein. Some remarks on the compressed matrix representation of symmetric second-order and fourth-order tensors. *Computer Methods in Applied Mechanics and Engineering*, 190(22-23):2753–2770, 2001.

R. Hill. A self-consistent mechanics of composite materials. *Journal of the Mechanics and Physics of Solids*, 13(4):213–222, 1965.

R. Hill. The essential structure of constitutive laws for metal composites and polycrystals. *Journal of the Mechanics and Physics of Solids*, 15(2):79–95, 1967.

H. Hogan. Micromechanics modeling of Haversian cortical bone properties. *Journal of Biomechanics*, 25 (5):549 – 556, 1992.

M. Hori and S. Nemat-Nasser. On two micromechanics theories for determining micro-macro relations in heterogeneous solids. *Mechanics of Materials*, 31(10):667–682, 1999.

C. Huet. Application of variational concepts to size effects in elastic heterogeneous bodies. *Journal of the Mechanics and Physics of Solids*, 38(6):813–841, 1990.

V. I. Kushch. *Effective properties of heterogeneous materials*, chapter Multipole expansion method in micromechanics of composites, pages 97–197. Dordrecht, The Netherlands: Springer Science+Business Media, 2013.

W. J. Landis, M. J. Song, A. Leith, L. McEwen, and B. F. McEwen. Mineral and organic matrix interaction in normally calcifying tendon visualized in three dimensions by high-voltage electron microscopic tomography and graphic image reconstruction. *Journal of Structural Biology*, 110(1):39–54, 1993.

S. Lees, K. S. Prostak, V. K. Ingle, and K. Kjoller. The loci of mineral in turkey leg tendon as seen by atomic force microscope and electron microscopy. *Calcified Tissue International*, 55(3):180–189, 1994.

G. Li and J. R. Gladden. High temperature resonant ultrasound spectroscopy: A review. *International Journal of Spectroscopy*, 2010, 2010. doi:10.1155/2010/206362.

R. B. Martin and J. Ishida. The relative effects of collagen fiber orientation, porosity, density, and mineralization on bone strength. *Journal of Biomechanics*, 22(5):419 – 426, 1989.

R. Masson. New explicit expressions of the Hill polarization tensor for general anisotropic elastic solids. *International Journal of Solids and Structures*, 45(3-4):757–769, 2008.

MathWorks. *MATLAB [Software], Versions 7.10, 7.14, 8.3*. Natick, MA (US), 2010-2014. URL http://www.mathworks.com/.

M. M. Mehrabadi and S. C. Cowin. Eigentensors of linear anisotropic elastic materials. *Quarterly Journal of Mechanics and Applied Mathematics*, 43(1):15–41, 1990.

J. E. Michaels. An inverse source problem for elastic waves. Doctoral thesis, May 1984. Faculty of the Graduate School of Cornell University.

M. Moakher. Fourth-order Cartesian tensors: Old and new facts, notions and applications. *Quarterly Journal of Mechanics and Applied Mathematics*, 61(2):181–203, 2008.

T. Mori and K. Tanaka. Average stress in matrix and average elastic energy of materials with misfitting inclusions. *Acta Metallurgica*, 21(5):571–574, 1973.

M. D. Morris. Factorial sampling plans for preliminary computational experiments. *Technometrics*, 33 (2):161–174, 1991.

T. Mura. *Mircomechanics of defects in solids*. Dordrecht, The Netherlands: Martinus Nijhoff Publishers, second edition, 1987.

S. Nemat-Nasser and M. Hori. *Micromechanics: Overall properties of heterogeneous materials*, volume 37 of *North-Holland Series in Applied Mathematics and Mechanics*. Amsterdam, The Netherlands: Elsevier, second edition, 1999.

S. Nikolov and D. Raabe. Hierarchical modeling of the elastic properties of bone at submicron scales: The role of extrafibrillar mineralization. *Biophysical Journal*, 94(11):4220–4232, 2008.

S. Nuzzo, F. Peyrin, P. Cloetens, J. Baruchel, and G. Boivin. Quantification of the degree of mineralization of bone in three dimensions using synchrotron radiation microtomography. *Medical Physics*, 29(11): 2672–2681, 2002.

O. Oleĭnik, A. Shamaev, and G. Yosifian. *Mathematical problems in elasticity and homogenization.* Amsterdam, The Netherlands: North-Holland, 1992.

W. J. Parnell. *Homogenization techniques for wave propagation in composite materials*. PhD thesis, Faculty of Science and Engineering, University of Manchester, 2004.

W. J. Parnell and I. D. Abrahams. Dynamic homogenization in periodic fibre reinforced media. Quasi-static limit for SH waves. *Wave Motion*, 43(6):474–498, 2006.

W. J. Parnell and I. D. Abrahams. Homogenization for wave propagation in periodic fibre-reinforced media with complex microstructure. I. Theory. *Journal of the Mechanics and Physics of Solids*, 56(7): 2521–2540, 2008.

W. J. Parnell and Q. Grimal. The influence of mesoscale porosity on cortical bone anisotropy. Investigations via asymptotic homogenization. *Journal of the Royal Society Interface*, 6(30):97–109, 2009.

K. Raum. Microscopic elastic properties. In P. Laugier and G. Haïat, editors, *Bone quantitative ultrasound*, chapter 16, pages 409–440. Dordrecht, The Netherlands: Springer, first edition, 2011.

K. Raum, R. O. Cleveland, F. Peyrin, and P. Laugier. Derivation of elastic stiffness from site-matched mineral density and acoustic impedance maps. *Physics in Medicine and Biology*, 51(3):747–758, 2006a.

K. Raum, I. Leguerney, F. Chandelier, M. Talmant, A. Saïed, F. Peyrin, and P. Laugier. Site-matched assessment of structural and tissue properties of cortical bone using scanning acoustic microscopy and synchrotron radiation μCT. *Physics in Medicine and Biology*, 51:733–746, 2006b.

K. Raum, T. Hofmann, I. Leguerney, A. Saïed, F. Peyrin, L. Vico, and P. Laugier. Variations of microstructure, mineral density and tissue elasticity in B6/C3H mice. *Bone*, 41:1017–1024, 2007.

K. Raum, Q. Grimal, and A. Gerisch. Insight into the structure-function relationship of the bone lamellar unit through finite element modelling based on high-frequency SAM data. In O. Dössel and W. Schlegel, editors, *World Congress on Medical Physics and Biomedical Engineering, September 7 - 12, 2009, Munich, Germany*, volume 25/4 of *IFMBE Proceedings*, pages 2246–2249. Springer Berlin Heidelberg, 2010.

K. Raum, Q. Grimal, P. Laugier, and A. Gerisch. Multiscale structure-functional modeling of lamellar bone. *Proceedings of Meetings on Acoustics*, 9(1):020005, 2011.

A. G. Reisinger, D. H. Pahr, and P. K. Zysset. Sensitivity analysis and parametric study of elastic properties of an unidirectional mineralized bone fibril-array using mean field methods. *Biomechanics and Modeling in Mechanobiolgy*, 9(5):499–510, 2010.

A. G. Reisinger, D. H. Pahr, and P. K. Zysset. Elastic anisotropy of bone lamellae as a function of fibril orientation pattern. *Biomechanics and Modeling in Mechanobiology*, 10(1):67–77, 2011.

A. Reuss. Berechnung der Fließgrenze von Mischkristallen auf Grund der Plastizitätsbedingung für Einkristalle. *ZAMM - Journal of Applied Mathematics and Mechanics / Zeitschrift für Angewandte Mathematik und Mechanik*, 9(1):49–58, 1929.

D. Rohrbach, S. Lakshmanan, F. Peyrin, M. Langer, A. Gerisch, Q. Grimal, P. Laugier, and K. Raum. Spatial distribution of tissue level properties in a human femoral cortical bone. *Journal of Biomechanics*, 45 (13):2264–70, 2012.

F. Rupin, A. Saïed, D. Dalmas, F. Peyrin, S. Haupert, K. Raum, E. Barthel, G. Boivin, and P. Laugier. Assessment of microelastic properties of bone using scanning acoustic microscopy: A face-to-face comparison with nanoindentation. *Japanese Journal of Applied Physics*, 48(7):07GK01, 2009.

A. Saltelli, M. Ratto, T. Andres, F. Campolongo, J. Cariboni, D. Gatelli, M. Saisana, and S. Tarantola. *Global sensitivity analysis. The primer*. Chichester, UK: John Wiley & Sons, 2008.

E. Sanchez-Palencia. Homogenization in mechanics. A survey of solved and open problems. *Rendiconti del Seminario Matematico (già "Conferenze di Fisica e di Matematica"). Università e Politecnico di Torino*, 44(1):1–45, 1986.

A.-M. Sändig. Mathematische Methoden in der Kontinuumsmechanik. Lecture notes, 2005. Institut für Angewandte Analysis und Numerische Simulation, Universität Stuttgart.

N. Sasaki, A. Tagami, T. Goto, M. Taniguchi, M. Nakata, and K. Hikichi. Atomic force microscopic studies on the structure of bovine femoral cortical bone at the collagen fibril-mineral level. *Journal of Materials Science: Materials in Medicine*, 13(3):333–337, 2002.

E. M. Spiesz, P. Roschger, and P. K. Zysset. Influence of mineralization and microporosity on tissue elasticity: Experimental and numerical investigation on mineralized turkey leg tendons. *Calcified Tissue International*, 90(4):319–329, 2012a.

E. M. Spiesz, P. Roschger, and P. K. Zysset. Elastic anisotropy of uniaxial mineralized collagen fibers measured using two-directional indentation. Effects of hydration state and indentation depth. *Journal of the Mechanical Behavior of Biomedical Materials*, 12:20–28, 2012b.

A. P. Suvorov and G. J. Dvorak. Rate form of the Eshelby and Hill tensors. *International Journal of Solids and Structures*, 39(21-22):5659–5678, 2002.

S. Tiburtius, S. Schrof, F. Molnár, P. Varga, F. Peyrin, Q. Grimal, K. Raum, and A. Gerisch. On the elastic properties of mineralized turkey leg tendon tissue: multiscale model and experiment. *Biomechanics and Modeling in Mechanobiology*, 13(15):1003–1023, 2014. doi: 10.1007/s10237-013-0550-8.

P. Varga, A. Pacureanu, M. Langer, H. Suhonen, B. Hesse, Q. Grimal, P. Cloetens, K. Raum, and F. Peyrin. Investigation of the three-dimensional orientation of mineralized collagen fibrils in human lamellar bone using synchrotron X-ray phase nano-tomography. *Acta Biomaterialia*, 9(9):8118 – 8127, 2013.

T. J. Vaughan, C. T. McCarthy, and L. McNamara. A three-scale finite element investigation into the effects of tissue mineralisation and lamellar organisation in human cortical and trabecular bone. *Journal of the Mechanical Behavior of Biomedical Materials*, 12:50–62, 2012.

A. Vercher, E. Giner, C. Arango, J. Tarancón, and F. Fuenmayor. Homogenized stiffness matrices for mineralized collagen fibrils and lamellar bone using unit cell finite element models. *Biomechanics and Modeling in Mechanobiology*, 13(2):437–449, 2014.

W. Voigt. Ueber die Beziehung zwischen den beiden Elasticitätsconstanten isotroper Körper. *Annalen der Physik und Chemie, Neue Folge*, 38:573–587, 1888.

W. Wagermaier, H. S. Gupta, A. Gourrier, M. Burghammer, P. Roschger, and P. Fratzl. Spiral twisting of fiber orientation inside bone lamellae. *Biointerphases*, 1(1):1–5, 2006.

P. C. Waterman and R. Truell. Multiple scattering of waves. *Journal of Mathematical Physics*, 2(4): 512–537, 1961.

C. Weinberger and W. Cai. Lecture note 2. Eshelby's inclusion I. Lecture notes, January 2004. Mechanical Engineering, Mechanics & Computation, Stanford University.

S. Weiner and H. D. Wagner. The material bone: Structure-mechanical function relations. *Annual Reviews of Materials Science*, 28:271–298, 1998.

Y. Yoon and S. Cowin. An estimate of anisotropic poroelastic constants of an osteon. *Biomechanics and Modeling in Mechanobiology*, 7(1):13–26, 2008.

A. Zaoui. Structural morphology and constitutive behaviour of microheterogeneous materials. In P. Suquet, editor, *Continuum micromechanics*, pages 291–347. New York, US: Springer, 1997.

A. Zaoui. Continuum micromechanics: Survey. *Journal of Engineering Mechanics*, 128(8):808–816, 2002.

T. I. Zohdi and P. Wriggers. *An introduction to computational micromechanics*. Berlin, Germany: Springer, second edition, 2008.

Wissenschaftlicher Werdegang:

Sara Tiburtius,
geboren am 18.07.1982 in Berlin

10/2009 - 02/2015	**TU Darmstadt**, Fachbereich Mathematik Promotionsstudentin im DFG Schwerpunktprogramm 1420 auf dem Projekt: Hierarchische Struktur-Funktions-Modellierung muskuloskelettaler mineralisierter Gewebe Betreuer: Dr. Alf Gerisch, Prof. Dr. Jens Lang Thema: *Homogenisierung für die Multiskalen-Analyse von muskuloskelettalem mineralisiertem Gewebe* Abschluß: Dr. rer. nat.
10/2009 - 03/2014	**TU Darmstadt**, Fachbereich Mathematik Wissenschaftliche Mitarbeiterin in der AG Numerik und wissenschaftliches Rechnen
04/2005 - 03/2009	**TU Darmstadt**, Studium der Mathematik Schwerpunkte: Numerik und Optimierung, Nebenfach: Informatik Thema der Diplomarbeit: *Globale Fehlerschätzung und Fehlerkontrolle für gewöhnliche Differentialgleichungen mithilfe der Richardson-Extrapolation* Betreuer: Prof. Dr. Jens Lang Abschluß: Dipl.-Math.
10/2001 - 03/2005	**FU Berlin** und **TU Darmstadt**, Studium der Physik Nebenfach: Informatik Abschluß: Vordiplom
06/2001	**Dreilinden-Oberschule (Berlin)**, Abitur

Darmstadt, den 18. Februar 2015